

Design of Photonic Crystals by FDTD Method and Fabrication of High- Q Three-Dimensional Photonic Crystal Nanocavities

(有限差分時間領域法によるフォトニック結晶の設計と
高 Q 値 3 次元フォトニック結晶ナノ共振器の作製に関する研究)

A Dissertation
Submitted to the Graduate School of
the University of Tokyo
in Partial Fulfillment of the Requirements
for the Degree of
Doctor of Philosophy

タンデーシーヌラット アニワット

Tandaechanurat Aniwat

December 2008

To my family and my wife

Acknowledgement

First of all I would like to express my deep and sincere gratitude to my supervisor, Professor Yasuhiko Arakawa for giving me a great opportunity to join this laboratory and agreeing to supervise this thesis. His knowledge, experience, and vision have stimulated my enthusiasm for pushing the forefront of research. Without his guidance and mentorship, this work would not have come to fruition.

I would like to thank Professor Yoshiaki Nakano, Professor Kazuhiko Hirakawa, Professor Masaaki Tanaka, Professor Takuji Takahashi, and Professor Satoshi Iwamoto for their useful comments and advices as members of the thesis defense committee.

In particular I would like to thank Professor Satoshi Iwamoto for all of his support and important guidance. Working with him from pretty much the beginning of this work has shaped my path toward a university career, and I want to thank him for that. His editing on papers and ideas expressed there were always the best check. His wide knowledge and his logical way of thinking have been of great value for me.

I would like to thank the former and current members of the Professor Arakawa group for their input and companionship on this long journey. Their intelligence, dedication, and fantastic personalities have made it a great learning experience. First of all, I wish to express my warm and sincere thanks to Professor Masatoshi Kitamura and Professor Toshihiro Nakaoka for their advices and supports. I have had great luck to work with some very talented and motivated people on research. In particular, I want to thank my close collaborators on the three-dimensional photonic crystal project, Satomi Ishida – it has been really great working with him. Many great suggestions and different perspectives of him on our collaboration works have enlightened me a lot. Also, I would like to thank Professor Denis Guimard for his tireless effort on growth of samples. His quantum dots are always in best quality. I greatly thank Dr. Kanna Aoki for her pioneer work in micromanipulation. Without her establishment, I could not have made any three-

dimensional structures. I learned a lot working with Dr. Masahiro Nomura in the fabrication processes and optical measurements and want to thank him for the consistent positive attitude and all the help.

Also, I would like to thank Mr. Masao Nishioka, Dr. Katsuyuki Watanabe, Dr. Naoto Kumagai, Dr. Damien Bordel for the growth of epitaxy wafer. I also want to acknowledge all of my colleagues and friends in the group: Dr. Toshio Saito, Dr. Satoshi Kako, Dr. Munetaka Arita, Mr. Toshiyuki Miyazawa, Dr. Tetsuo Kodera, Dr. Katsuaki Tanabe, Dr. Jong Ho Na, Mr. Christian Kindel, Mr. Takeshi Kawano, Mr. Mohan Rajesh, Mr. Yuki Wakayama, Mr. Hiroaki Oishi, Mr. Yasutomo Ota, Mr. Kenichi Ohno, Mr. Shigeru Nakayama, Mr. Kazumasa Miyagawa, Ms. Ayako Suzuki, Mr. Satoru Nakagawa, Mr. Ryo Morihara, Mr. Kihyun Choi, Mr. Woogun Kang, and Mr. Naoya Shinomori. It has been great working and hanging out with them. I would like to thank our group's secretary: Ms. Mio Ono, Ms. Keiko Okumura, Ms. Masako Ogawa, and Ms. Chieko Sasakawa. Their kindness and supports help me do research smoothly.

I would like to acknowledge financial support from Special Coordination Funds for Promoting Science and technology.

On more personal grounds, my special gratitude is due to my family: dad, mom, Yui, and Lek. Without them, life would be an aimless wander without direction. They have served as a basis for everything I do and everything I am today.

Last and most importantly of all, I owe my loving thanks to my wife, Pim, for being with me at all the good and bad time. I could not have finished this thesis without my wife's support. She always gives me joyful home environments and makes me smile every single day. I would like to dedicate this thesis to her.

Abstract

Photonic crystal with a defect as a nanocavity has been attracting much interest as a promising platform to manipulate light and light-matter interaction on wavelength-sized length scale due to existence of photonic bandgap. The Finite-Difference Time-Domain (FDTD) method has been widely exploited as a powerful tool to simulate Maxwell's equations in photonic crystal structures, enabling ones to design novel devices. After two decades of intense development, performance of *two-dimensional* photonic crystal cavities, in term of quality (Q) factor, has reached saturation, in which experimental Q factors exceed a million with mode volume in the order of cubic wavelengths. However, there are still two issues needed to be considered. The first one is that those high Q cavities are usually sensitive to change in the cavity geometry inflicted by fabrication imperfections. The other one is their flexibility in applications. Generally, they can only be applied to material systems with sufficiently high index-contrast and with proper polarization, in which a photonic bandgap exists. On the other hand, progress in *three-dimensional* photonic crystal cavities is far behind that in two-dimensional system due to the difficulty in fabrication, in which a number of photonic crystal periods surrounding the cavity that can be fabricated is limited. This suggests that, considering current fabrication technologies, designs of high Q cavities that can be achieved even with small structural size, which is practical in fabrication, are required in order to demonstrate high Q cavities. This thesis aims to fill in the abovementioned gaps. Original research work on designs and fabrications of high Q nanocavities in both two- and three-dimensional photonic crystals are presented.

In Chapter 2, basic principles of photonic crystals that are necessary for understanding the research background and motivation of this thesis are introduced. Two-dimensional photonic crystal slabs with both triangular and square lattices and three-dimensional woodpile photonic crystal structures are described in details as they are basic building blocks of all the work in this thesis. The influence of cavity

geometry and structural parameters on the behavior of characteristics of photonic crystals, such as photonic bandgap, resonant frequencies, is discussed. Finally, defects are introduced by adding dielectric materials to perfect crystals to form nanocavities.

In Chapter 3, details on computational methods used in this thesis, which are all based on the FDTD method, are described. The FDTD simulations are categorized into two classes with different boundary conditions, depending on the types of calculations to obtain efficient and accurate solution of electromagnetic waves. The applications of the 3D FDTD calculations to investigate photonic band structures, equi-frequency contours, resonant frequencies, field distributions, quality factors, mode volumes, and effective refractive indices are shown.

In Chapter 4, a significant increase of Q -factor of dipole modes in photonic crystal H1-defect nanocavity after closing of the photonic bandgap are numerically and experimentally demonstrated by optimizing the slab thickness. The optimal slab thickness is equal to a wavelength of light confined in the cavity. The strong light confinement of the cavity in the in-plane direction is not caused by the photonic bandgap effect due to a lack of the photonic bandgap but resulted from the decoupling between the cavity mode and the guided mode in the momentum space. Because the slab thickness, which is the design parameter, can be precisely controlled by using epitaxial growth techniques, the parameter of the best fabricated cavity and that of the predicted one are almost exactly the same. This finding will contribute to extending the freedom of cavity design, such as that for the application to polarization entangled photon source, where it is required to form cavity modes with prescribed Q factor and polarization.

In Chapter 5, a photonic crystal nanocavity with an ultra-high Q and small mode volume even there is no bandgap is presented. The air hole radii are modulated with a quadratic profile to decouple the cavity mode from possible losses consisting of guiding loss and radiation loss, resulting in doubly-degenerated modes with a ratio of Q to mode volume of two times higher than the highest value reported so far for doubly-degenerated modes. Therefore, this cavity is very promising for the realization of entangled photon sources. The designed cavity is also shown to be successfully applied to achieve high Q cavities for material with low index and for quantum cascade lasers, in which a lack of photonic bandgap usually hinders them from applications. The results achieved in this chapter extend the scope of optical devices that can utilize

photonic crystal cavities to improve their performances, while the photonic bandgap is no longer a preliminary requirement to achieve high Q .

In Chapter 6, three designs of high- Q cavities in three-dimensional photonic crystals with finite structural size that can be practically fabricated are presented. High- Q cavity modes in square-shaped and rectangular-shaped nanocavities are achieved by tuning their frequencies to midgap frequency of a complete photonic bandgap, where light confinement is strongest, by means of optimizing size of the defects to gain an advantage from the photonic bandgap effect as much as possible. Apart from tuning cavity modes to the midgap frequency, the Q factor can be further improved by modifying cavity structure through shifting of dielectric rods surrounding the cavity. 4.3-time improvement of Q compared with the structure without modification of the cavity structure is obtained with a value of 73,300. Importantly, this high Q cavity only needs 17 stacked layers to obtain such high Q . These designed cavities show a great promise in the realization of high Q cavities using current fabrication technologies.

In Chapter 7, experimental demonstrations of two high- Q cavities coupled with quantum dots in three-dimensional photonic crystals fabricated by using micromanipulation techniques are presented. The structures are shown to have very small stacking errors in order of 50 nm, in spite of their large number of the stacked layers. The square-shaped defect cavity in a 25-layer woodpile layer exhibits a cavity mode with Q factor of more than 8,600, which is the highest Q among those for three-dimensional photonic crystal cavities reported so far. The high- Q nature of the cavity has been confirmed to be originated not only from a large number of the stacked layers, but also from the strong localization of the cavity mode when it was tuned to the midgap frequency of the complete photonic bandgap. The obtained cavity- Q can still be improved to more than 10,000 by finer tuning the cavity mode to the exact midgap. For the rectangular-shaped cavity, a cavity mode with Q factor of more than 7,700 is obtained by choosing a cavity mode with high theoretical Q and tuning it to the midgap. The cavity mode has mode volume as small as 2 cubic half-wavelengths, approaching the diffraction limit value. These high Q/V_{eff} cavities will give three-dimensional photonic crystals a wide-open opportunity for the realization of the applications concerning the full control of light-matter interaction and an ultra-small optical three-dimensionally-integrated circuit.

In Chapter 8, conclusions to this thesis are presented. Implications of the results presented in this thesis are discussed. The outlook for future research and development is also given.

One may expect it to take quite some time for an ultra-small optical three-dimensionally-integrated circuit based on photonic crystals to be realized and implemented. Nevertheless, the results obtained in this thesis provide one important step towards the acquisition of complete manipulation of light.

Contents

Acknowledgements	i
Abstract	iii
1 Introduction	1
1.1 Research background	1
1.2 Thesis objectives	5
1.3 Thesis outline	6
2 Basis for Theoretical Analysis of Photonic Crystal	11
2.1 Maxwell's equations and the Bloch-Floquet theorem	11
2.2 Origin of photonic bandgap	14
2.3 Types of photonic crystal	17
2.4 Two-dimensional photonic crystal slabs	18
2.4.1 Comparison between square and triangular photonic crystal lattices	21
2.4.2 Effect of slab thickness and radius of air holes on photonic bandgap	23
2.5 Woodpile structures	27
2.6 Photonic crystal defect nanocavities	29
2.7 Summary	33
3 Finite-Difference Time-Domain Method	35
3.1 The Yee algorithm	35
3.2 Boundary conditions	38
3.2.1 Absorbing boundary condition	38
3.2.2 Periodic boundary condition	42
3.3 FDTD-simulations of photonic crystals	44

3.3.1	Band structures and equi-frequency contours	44
3.3.2	Cavity characteristics	45
3.4	Summary	51
4	High-Q Photonic Crystal Nanocavity after Closing of Photonic Bandgap with Optimal Slab Thickness	53
4.1	Introduction	53
4.2	Structural parameters and defect modes	54
4.3	Increase of cavity Q of H1 dipole modes by optimizing slab thickness	58
4.4	Fabrication Processes	67
4.5	Optical characterization	71
4.5.1	Experimental setup of photoluminescence measurements	71
4.5.2	Experimental results	71
4.6	Summary	78
5	High-Q Photonic Crystal Nanocavity without Photonic Bandgap by Modulating Air Hole Radii in Square Lattice	79
5.1	Introduction	79
5.2	Cavity structures and defect modes	80
5.3	High cavity Q in graded photonic crystal structure by mode decoupling	85
5.3.1	Graded photonic crystal nanocavity with modulating air hole radii	85
5.3.2	Improvement of cavity Q in graded structure by mode decoupling	87
5.4	Applications of high- Q graded photonic crystal cavities	96
5.4.1	High- Q graded photonic crystal nanocavity with low refractive index	96
5.4.2	Reduction of threshold current of quantum cascade lasers by graded photonic crystal cavity	98
5.4.3	Prospects of graded photonic crystal nanocavity for highly efficient entangled photon sources	100
5.5	Summary	101
6	Designs of High-Q Nanocavities in Three-Dimensional Photonic Crystals with Finite Structural Sizes	103

6.1	Introduction	103
6.2	Designs of high- Q nanocavities in woodpile photonic crystals by tuning cavity modes to photonic midgap	105
6.2.1	Square-shaped defect nanocavity	105
6.2.2	Rectangular-shaped defect nanocavity	113
6.3	Further improvement of cavity Q by shifting rods in cavity neighborhood	118
6.3.1	Structural parameters and cavity mode	119
6.3.2	Enhancing Q factor by fine shifting dielectric rods	121
6.3.3	Comparison with double-heterostructure three-dimensional photonic crystal nanocavity	125
6.4	Summary	127
7	Fabrication and Characterization of High-Q Three-Dimensional Photonic Crystal Nanocavities	129
7.1	Introduction	129
7.2	Fabrication of three-dimensional photonic crystal nanocavities by micromanipulation techniques	131
7.2.1	Principles of micromanipulation techniques	131
7.2.2	Preparations of micromanipulation components and samples	133
7.2.2.1	Probe and posts	133
7.2.2.2	Plates	136
7.2.3	Assembly into three-dimensional structures by micromanipulation	141
7.3	Experimental setup of photoluminescence measurements	144
7.4	Results of photoluminescence measurements	145
7.4.1	Square-shaped defect nanocavity	145
7.4.2	Rectangular-shaped defect nanocavity	149
7.5	Summary	153
8	Conclusions and Future Outlook	155
8.1	Conclusions	155
8.2	Future Outlook	158
	References	159

Chapter 1

Introduction

1.1 Research background

Photonic crystals are periodic structures made of dielectric materials. Regions with different dielectric constants alternate periodically and the period is of the order of the wavelength of light. Then, as light propagates inside the periodic material, it reflects at each interface of the different dielectric materials, in the same way as electron experiencing a periodic potential in a semiconductor crystal [1]. As a result of interference, total reflection occurs at specific wavelength-period combinations. Light with this specific wavelength cannot propagate or exist inside the photonic crystal. These forbidden wavelengths or frequencies form a bandgap for light, which is the basis of operation of photonic crystals, in analogy with forbidden energy bands in electronic system. This phenomenon is also present in the nature, for example, the wings of certain butterflies and moths are covered with periodic microscopic structures, which act as photonic crystals [2-4]. The wings reflect light that has a wavelength in the bandgap of the photonic crystal. This effect is seen as the color of the wings. Classes of photonic crystals are distinguished depending on the dimensionality of spatial periodicity. While the one-dimensional structures have been adopted for various lasers for more than three decades such as distributed feedback laser diodes [5-7] and vertical cavity surface-emitting lasers (VCSELs) [8,9], the extension of photonic crystals to two and three dimensions was simultaneously proposed by Yablonovitch and John in 1987 [10,11]. The first one dealt with the possibility of inhabiting spontaneous emission of electromagnetic radiation using three-dimensionally periodic structure. The latter paper discussed the strong localization of photons in defect intentionally introduced into the perfect lattice, resulting in trapping of electromagnetic radiation in the forbidden gap. Their works

have stimulated attention of researchers from all over the world in these new prospects in photonics. In the first decade after the proposal, most of work on photonic crystals has been concentrated on efforts to realize structures with a complete photonic bandgap, in which light is prohibited to propagate in all three directions. Such structures, of course, needs to be periodic in three dimensions. Three criteria were considered to seek for the structure and material that were capable to open the gap. A lattice with a first Brillouin zone closest to a spherical shape would help since gap for different directions would appear at similar energies. The best lattice for a photonic bandgap is thus the triangular lattice in two-dimensional structure and the face-centered-cubic in three-dimensional structure. In addition, an asymmetry lattice was necessary to break the degeneracy of the three-dimensional photonic band and open the gap [12]. As a consequence, most of all the three-dimensional photonic bandgap structures realized up to now are based on the diamond structure [12,13]., an fcc structure with two optical atoms per unit cell. And in order to achieve an overlapping of the gaps at every point of the Brillouin zone boundary, a high refractive index contrast between the composing materials was required [10]. The first experimental demonstration of complete-photonic-bandgap materials appeared in 1991, which was based on a face-center-cubic (fcc) lattice, presented by Yablonovitch *et al.* [13,14]. The structural size was in centimeter order for the microwave regime. Since then many efforts have been concentrated to scale the various three-dimensional structures down to the visible or near-infrared regime [15-20]. In application points of view, three-dimensional photonic crystals have been something disappointing, in spite of their ideal capability to fully control the light. One of the most promising goals of photonic crystals is an ultra-small optical three-dimensionally-integrated circuit [21], which combines ultra-low threshold lasers arrays, sharp bend waveguides, an optical modulator, wavelength selectors, and so on, on one *optical chip*. However, only sharp bend waveguides in line-defect-embedded three-dimensional photonic crystals with low losses have been implemented so far [18,22-24]. Although three-dimensional photonic crystals offer a promise to realize an efficient nanocavity, by introducing a three-dimensionally-localized defect into a perfect crystal, because light can be strongly confined in very small volume for a long period of time due to Bragg reflection in all three directions, quality (Q) factors of cavities in three-dimensional photonic crystals are still modest. This deficiency mainly results from the difficulty in fabrication of the three-dimensional photonic

crystals. Especially when a light-emitting element and an artificial defect cavity are to be introduced into the three-dimensional structure to generate a light-emitting device, a fabrication technique that can simultaneously fulfil requirements of introduction of an artificial defect and a light-emitting element into the three-dimensional structure is essential. The existing techniques, such as colloidal self-assembly [25-31], direct writing by two-photon polymerization [32-35], and multibeam interference lithography [36-39], can carry out each of the requirement, but not both at the same time. Layer-by-layer method [15-17,40] and wafer-fusion method [18,19,41,42] have been shown to have a capability to accomplish the task. Nevertheless, their complicated procedures together with damage inflicted on the fine structure by multiple etching and heat treatment preclude them from making three-dimensional structures with large number of periods and with good quality, leading to a cavity with low Q factor of no more than several hundreds [40,43,44]. In contrast, micromanipulation techniques do not undergo such problem [45,46]. All photonic crystal components used to construct three-dimensional structure can be prepared using a single semiconductor processing sequence and no heating, enables components to be assembled with high precision and minimum damage to their fine structure irrespective of materials or complexity of photonic patterns. Therefore, micromanipulation technique is capable of introducing a defect cavity and light-emitting elements into the structure at arbitrary positions. Recently, a cavity in woodpile structure with a record- Q of 2,300 has been reported with 17 stacked layers using micromanipulation techniques [47]. Yet, this Q seems to be insufficient to pursue ultimate applications, such as thresholdless lasers [48]. High- Q cavity in three-dimensional photonic crystals still poses a great challenge to be realized. The low value of Q is partly resulted from the restricted structural size of photonic crystals that can be fabricated. There are two approaches, which should be done in parallel, to enhance the Q . One is the development of the fabrication techniques, which allow a larger size of photonic crystals to be made. The other one is to improve the cavity designs to be able to have high Q even with a limited size. If such a cavity can be achieved, not only the ultimate lasers, but also an ideal semiconductor system for demonstrating *genuine* strong coupling between three-dimensionally confined photon and electron may be obtained by introducing a single quantum dot [49] into the cavity [50,51].

Fabrication of three-dimensional photonic crystal structures is still a difficult process, and a more appealing approach is based on the use of lower-dimensional photonic crystals. Therefore, many of researchers have turned their attention to two-dimensional photonic crystals, whose periodicity is in two dimensions [52-56]. However, because such structures must be infinitely long in the direction perpendicular to the plane in which two-dimensional periodicity exists, they are not practical for applications since only finite height structures can be fabricated. A structure that have been attracted a lot of attention is a finite-thick semiconductor slab perforated with a two-dimensional lattice of holes [57-62]. Then, the two-dimensional photonic crystal slab can be easily fabricated following the standard microlithographic techniques and still retain most of the important features of full three-dimensional photonic crystals. In photonic crystal slabs, the localization of light in the vertical direction is controlled by the total internal reflection resulting from the high index contrast between the high-index slab and the low-index environment. On the other hand, the confinement in the in-plane direction is controlled by the Bragg reflection resulting from the photonic crystal lattice. Light in the photonic crystal slab cavity that does not fulfill the condition for the total internal reflection radiates vertically out of the cavity and thus limits Q factor of the cavity, while losses into the in-plane direction can be reduced exponentially with the number of photonic crystal layers surrounding the cavity. In 1999, when first photonic crystal defect cavity lasers was demonstrated, a Q of around 250 was reported for a single point defect [63]. Since then there have been various attempts to improve the Q factor. Thanks to the excellent suitability of the Finite-Difference Time-Domain (FDTD) method [64] to simulate light field dynamics and propagation in photonic crystal structures and the flexibility in the design of two-dimensional photonic crystal slab nanocavities, various designs of ultra-high Q nanocavities have already been succeeded by, such as fine tuning of shape, size, and position of air holes near the cavity site [65-71] and exploiting a photonic crystal waveguide mode confined in a mode gap [72,73]. Designed Q s in the order of 10^7 - 10^8 has been achieved [72,73]. With the maturation of nanometer-size photonic crystal fabrication technology in past ten years, photonic crystal nanocavities with a passive Q factor of more than one million have been experimentally demonstrated [74,75]. However, most of designs of those structures are based on the modification of the defect structures, in which the high Q modes are very sensitive to their surrounding structural parameters. Thus, these designs require a precise control

of the cavity geometry in practical fabrication to achieve high Q s. Small variations in the geometry could easily reduce the Q by a factor of 10 [76]. This lack of robustness to changes in the cavity geometry becomes a great difficulty to practically fabricate the device with quality as good as the simulation results.

Photonic bandgap has been shown above to be a great implement for confining light. There is a restrict rule of thumb in design of high- Q photonic crystal cavities, in which cavity modes must be properly designed to fall in the photonic bandgap to assure the strong light confinement in the in-plane direction, otherwise the light mode could couple with guided modes and leak out of the cavity. However, in some material systems, such as low-index materials [77-79] and quantum cascade lasers [80-82], which also desire to couple with localized optical modes in photonic crystal cavities with high Q to improve their performances, the photonic bandgap does not exist in a frequency range of interest, i.e., the photonic bandgap for the structure with low refractive index only exists in very high frequency range, while there is no photonic bandgap for light polarized in transverse magnetic (TM) -like mode, where photons are polarized in quantum cascade lasers, in the photonic crystal slab with air holes [60]. Search for cavity designs suitable for these material systems is still ongoing.

1.2 Thesis objectives

After more than two decades since the proposal of photonic crystals, the performance of two-dimensional photonic crystal slab cavities, in term of cavity- Q , has reached saturation, in which experimental Q factors exceed a million with mode volume in the order of cubic wavelengths. It is thus interesting to divert the development of cavity designs to robustness of cavities to fabrication imperfections, which usually degrade the cavity performance from the design. In addition, a predesignated condition, in which a photonic bandgap is essential to achieve high Q , should be compromised to extend the scope of optical devices that can utilize photonic crystal cavities to improve their performance. Compared to the two-dimensional system, progress in three-dimensional photonic crystal cavities is far behind due to the limitation in fabrication. This suggests that, considering current fabrication technologies, designs of high Q cavities that can be achieved even with

small structural size, which can be practically fabricated, should be realized in order to demonstrate high Q cavities.

This thesis aims to fill in the abovementioned gaps. Regarding to the two-dimensional photonic crystal cavities, a cavity design based on simulations using FDTD computational method, in which its principal parameter of design used to boost Q factor is fabrication-tolerant and can be precisely controlled, is to be realized. This is the first objective of this thesis. Another key objective of this thesis is to show how to achieve high Q cavities even there is no photonic bandgap. In order to do so, mechanisms of losses of light when the bandgap is absent and a way to suppress them must be explicitly understood. In addition, experimental demonstrations should be performed on the designed cavities to confirm the availability of the strong light confinement in such counter-intuitive photonic crystal cavities. The last and most important objective is to demonstrate a high Q cavity in three-dimensional photonic crystals, which is one important step towards the acquisition of complete manipulation of light-matter interaction, by means of proposing new designs of high Q cavities with finite structural size. The author's original contributions to the field are briefly summarized in the following thesis outline.

1.3 Thesis outline

This thesis presents original research work on designs and fabrications of high Q nanocavities in both two- and three-dimensional photonic crystals. It is organized into eight chapters. Figure 1.1 shows how the eight chapters are logically related to one another. Chapter 1 gives the research background and thesis objectives. It also provides the reader with the thesis outline.

In Chapter 2, basic principles of photonic crystals are discussed to understand the behavior of light in photonic crystals and the origins of photonic band structures and bandgaps. Two-dimensional photonic crystal slabs with both triangular and square lattices and three-dimensional woodpile photonic crystal structures are then described in details as they are the basic building blocks of all the work in this thesis. The influence of structural parameters, such as slab thickness and radius of air holes of two-dimensional photonic crystal slabs, which are the important parameters of the designs of high Q nanocavities in Chapters 4 and 5, on the behavior of photonic

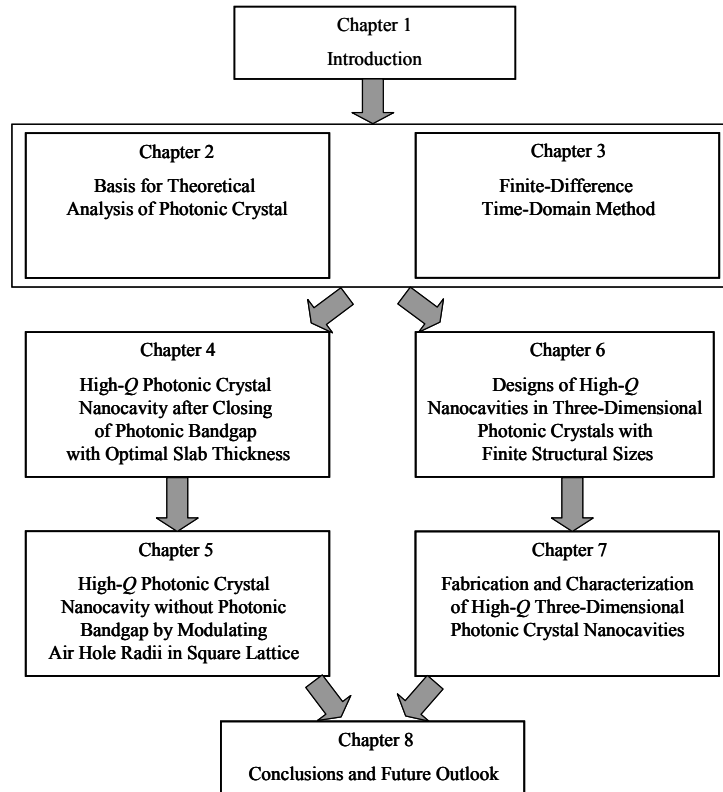


Figure 1.1 Thesis organization.

bandgap is preliminarily discussed. Finally, photonic crystal nanocavities formed by introducing artificial defects into a perfectly periodic system are introduced.

Chapter 3 describes computational methods used in this thesis, which are all based on the FDTD method. The FDTD simulations are categorized into two classes with different boundary conditions. To calculate the fields in the infinitely extended periodic system, i.e., to calculate photonic band diagram, periodic boundary condition reduces the computational domain to a primitive cell of the crystal. In the case of a finite structure, i.e., a photonic crystal structure with defect cavity, the entire structure has to be set up in the core region of the simulation and perfectly matched layer is exploited to enclose the region as a nonreflecting absorber, so that outgoing energy is not reflected back to the core region. Then applications of the FDTD method, together with the fast Fourier transformation, to the investigation of the characteristics of photonic crystal nanocavities, such as resonant frequencies, field distributions, Q factors, mode volumes of the cavity modes are presented.

Chapters 4 and 5 concern work on the two-dimensional photonic crystal slab nanocavities. Chapter 4 serves for the first thesis objective regarding to a proposal of achievement of high Q cavity by optimizing slab thickness. A significant increase of Q factor of dipole modes in photonic crystal H1-defect nanocavity after closing of the photonic bandgap by tuning the slab thickness is numerically and experimentally demonstrated. It is shown that the optimal slab thickness is equal to a wavelength of light confined in the cavity, which is approximately two times thicker than that of conventional structures. Interestingly, the strong light confinement of the cavity in the in-plane direction is not caused by the photonic bandgap effect due to a lack of the photonic bandgap but resulted from the decoupling between the cavity modes and the guided modes in the momentum space yielding only weak coupling between these two modes. This finding contributes to extending the freedom of cavity design. It is also suggested that because the only parameter of this cavity that needs to be adjusted is the slab thickness which can be precisely controlled by using epitaxial growth techniques such as molecular beam epitaxy (MBE) or metal-organic chemical vapor deposition (MOCVD), discrepancy of structural parameters between the designed and the fabricated structures can be very small.

Chapter 5 deals with the second objective aiming to extend the scope of applications of high Q photonic crystal cavities to structures where a photonic bandgap does not exist. The concept of mode decoupling established in Chapter 4 is extended to design a cavity with higher Q and more flexible in applications by gradually modulating air hole radii in square lattice photonic crystals. An ultra-high ratio of Q factor to mode volume, desired for applications such as entangled photon source, of these modes has been achieved and this value is about two times higher than the highest value reported so far. In addition, the designed cavity has been applied to achieve high Q cavities for material with low index and for quantum cascade lasers, in which a lack of photonic bandgap usually hinders them from applications. These results emphasize a flexibility of the cavity, while the photonic bandgap is no longer a preliminary requirement to achieve high Q .

The topic is then turned to discussions on three-dimensional structures. In Chapter 6, three designs of high Q cavities in three-dimensional photonic crystals with finite structural size that can be practically fabricated are presented. Two of them are achieved by tuning resonant frequencies of their cavity modes to the middle frequency of the complete photonic bandgap, where the mode localization is strongest

to gain an advantage from the photonic bandgap effect as much as possible, and thus highest Q s, by means of optimizing size of the defect cavities. Apart from tuning cavity modes to the midgap frequency, it is also theoretically predicted that the Q factor can be further increased more than four times in magnitude compared with that of the unperturbed structure by slightly modifying the arrangement of dielectric rods surrounding the cavity site.

In Chapter 7, the fabrication of the three-dimensional woodpile photonic crystal nanocavities designed in Chapter 6 using micromanipulation techniques and their optical characteristics are presented. Firstly, principles of the micromanipulation techniques and how to use them to assemble three-dimensional structures are described. The structures with a large number of stacked layers have been achieved with high alignment accuracy. After that, experimental results are given on optical characterization of the fabricated cavities coupled with quantum dots by means of photoluminescence measurements. For the cavity with square-shaped in the 25-layer woodpile structure, a cavity mode with Q factor of more than 8,600, which is the highest Q among those for three-dimensional photonic crystal cavities reported so far, has been achieved. This result is consistent with the calculation results discussed in Chapter 6, in which a cavity mode locating closest to the midgap possesses the highest Q . Moreover, for a cavity with rectangular-shaped and smaller size, a cavity mode with Q factor of more than 7,700 with an ultra-small mode volume of 2 cubic half-wavelengths has been obtained. The results presented in this chapter give three-dimensional photonic crystals a wide-open opportunity for the realization of the applications concerning the control of light-matter interaction.

Chapter 8 is the conclusion to this thesis. Implications of the results presented in this thesis are discussed. The outlook for future research and development is also given

Chapter 2

Basis for Theoretical Analysis of Photonic Crystal

Photonic crystal, which is a periodic arrangement of dielectric media, introduces a periodic potential to photons propagating through it in the same way as a crystal, in which electron experiences a periodic potential due to a periodicity of atoms or molecules, in electronic systems. This “optical potential” leads to the development of a band structure for photons in photonic crystals. Resulting photonic bandgaps which disallow the propagation of light in the crystal for frequencies inside the gap and artificially introduced defects can be applied to construct, for example, mirror, waveguide, or nanocavity structures. In order to accurately describe the behavior of light in photonic crystals, the full vector nature of light has to be taken into account using the Maxwell’s equations.

2.1 Maxwell’s equations and the Bloch-Floquet theorem

The macroscopic electromagnetic fields are described by the Maxwell’s equations

$$\vec{\nabla} \times \vec{E} = -\frac{1}{c} \frac{\partial \vec{H}}{\partial t} \quad (2.1)$$

$$\vec{\nabla} \times \vec{H} = \frac{4\pi}{c} \vec{J} + \frac{1}{c} \frac{\partial \epsilon \vec{E}}{\partial t} \quad (2.2)$$

$$\vec{\nabla} \cdot \epsilon \vec{E} = 4\pi \rho \quad (2.3)$$

$$\vec{\nabla} \cdot \vec{H} = 0 \quad (2.4)$$

where $\vec{E}(\vec{r}, t)$ and $\vec{H}(\vec{r}, t)$ are the electric and magnetic fields, which can be expressed by:

$$\vec{E}(\vec{r}, t) = \vec{E}(\vec{r}) e^{i\omega t} \quad (2.5)$$

$$\vec{H}(\vec{r}, t) = \vec{H}(\vec{r})e^{i\omega t} \quad (2.6)$$

\vec{J} is the free current density, ρ is the free charge density, and ε is the dielectric function. In the case that light propagating within a dielectric medium without any light sources, \vec{J} and ρ can be set to zero. In addition, it is acceptable to restrict the dielectric function ε to the case of linear dielectrics. And also, ε is assumed to be independent of frequency and being a real number.

According to these assumptions, by substituting Eq. (2.5) and Eq. (2.6) into Eq. (2.1) and Eq. (2.2) and then combining them into one equation, which contains only $\vec{H}(\vec{r})$ components, called the master equation:

$$\vec{\nabla} \times \left(\frac{1}{\varepsilon(\vec{r})} \vec{\nabla} \times \vec{H}(\vec{r}) \right) = \left(\frac{\omega}{c} \right)^2 \vec{H}(\vec{r}) \quad (2.7)$$

Then use Eq. (2.2) to regain $\vec{E}(\vec{r})$:

$$\vec{E}(\vec{r}) = \left(\frac{-ic}{\omega \varepsilon(\vec{r})} \right) \vec{\nabla} \times \vec{H}(\vec{r}) \quad (2.8)$$

It can be observed from Eq. (2.7) that it is a Hermitian eigenvalue problem an eigenfunction $\vec{H}(\vec{r})$ and an eigenvalue $(\omega/c)^2$. The eigenfunctions $\vec{H}(\vec{r})$ are the allowed fields in the structure, i.e., the electromagnetic modes of the system.

An important feature of the electromagnetic modes is that there is no specified length scale involved. Once the eigenvalues and eigenfunctions of Eq. (2.7) are solved, they can be scaled to any physical size or wavelength range. This can be understood by defining $\vec{r}' = s\vec{r}$, $\vec{\nabla}' = \vec{\nabla}/s$, and $\varepsilon'(\vec{r}') = \varepsilon(\vec{r}/s)$, and substituting them into Eq. (2.7). This results in

$$s\vec{\nabla} \times \left(\frac{1}{\varepsilon(\vec{r}/s)} s\vec{\nabla} \times \vec{H}(\vec{r}/s) \right) = \left(\frac{\omega}{c} \right)^2 \vec{H}(\vec{r}/s) \quad (2.9)$$

where $\varepsilon(\vec{r}/s) = \varepsilon'(\vec{r}')$. Thus

$$\vec{\nabla}' \times \left(\frac{1}{\varepsilon'(\vec{r}')} \vec{\nabla}' \times \vec{H}(\vec{r}'/s) \right) = \left(\frac{\omega}{cs} \right)^2 \vec{H}(\vec{r}'/s) \quad (2.10)$$

It can be seen that when the dimensions are scaled by a factor of s , the electromagnetic mode is the same, but has to be scaled as $\vec{H}(\vec{r}/s)$ and the frequency has to be scaled as ω/s . Due to the scalability, photonic crystal components can be

designed without specifying the dimensions and subsequently fabricated in an scale to perform experiments in varying wavelength ranges.

Because a photonic crystal is a periodically ordering dielectric media, its dielectric function $\varepsilon(\vec{r})$ becomes a periodic function of positions. The solution of the Hermitian eigenvalue problem shown in Eq. (2.7) can always be shown in the form of $e^{i\vec{k}\cdot\vec{r}}$ (periodic function), where \vec{k} is the wave vector. This is commonly known as Bloch-Floquet theorem [83]. A periodic function is expressed as:

$$\vec{u}_{\vec{k}}(\vec{r}) = \vec{u}_{\vec{k}}(\vec{r} + \vec{R}) \quad (2.11)$$

for any lattice vector \vec{R} . If the function is periodic in all three dimensions, lattice vector \vec{R} can be formed in:

$$\vec{R} = l\vec{a}_1 + m\vec{a}_2 + n\vec{a}_3 \quad (2.12)$$

where (l, m, n) are integers and \vec{a}_1 , \vec{a}_2 and \vec{a}_3 are primitive lattice vectors.

Therefore, the solution of Eq. (2.7) for a periodic dielectric function ε is given by:

$$\vec{H}_{\vec{k}}(\vec{r}) = e^{i\vec{k}\cdot\vec{r}} \vec{u}_{\vec{k}}(\vec{r}) = e^{i\vec{k}\cdot\vec{r}} \vec{u}_{\vec{k}}(\vec{r} + \vec{R}) \quad (2.13)$$

This Bloch state indicates each electromagnetic mode through its wave vector \vec{k} and periodic function $\vec{u}_{\vec{k}}(\vec{r})$. To solve for $\vec{u}_{\vec{k}}(\vec{r})$, Eq. (2.13) is substituted into Eq. (2.7), another Hermitian eigenvalue problem is then obtained:

$$(\vec{\nabla} + i\vec{k}) \times \frac{1}{\varepsilon} (\vec{\nabla} + i\vec{k}) \times \vec{u}_{\vec{k}}(\vec{r}) = \left(\frac{\omega}{c}\right)^2 \vec{u}_{\vec{k}}(\vec{r}) \quad (2.14)$$

Due to the periodicity of $\vec{u}_{\vec{k}}(\vec{r})$, Eq. (2.14) can be considered as the eigenvalue problem over a unit cell of the photonic crystal. Corresponding to quantum mechanics, eigenvalue problem with a finite domain leads to a discrete set of eigenvalues. That is, there is a set of modes, denoted by $\omega_n(\vec{k})$ (for band number $n = 1, 2, 3, \dots$), which are discretely spaced in frequencies and continuously varied as \vec{k} varies. The plot of these frequency bands as a function of \vec{k} is called the band structure of photonic crystal.

Another important property of the Bloch states is that, in order to solve the eigenvalue problem for a wavevector \vec{k} , it is adequate to only solve the eigenvalue problem for \vec{k} in a finite zone called the first Brillouin zone. By considering the Bloch state shown in Eq. (2.10), an eigensolution with wave vector \vec{k} is identical to

an eigensolution with wave vector $\vec{k} + \vec{G}$, where \vec{G} is a reciprocal lattice vector and defined as:

$$\vec{G} = l\vec{b}_1 + m\vec{b}_2 + n\vec{b}_3 \quad (2.15)$$

where (l, m, n) are integers and \vec{b}_1 , \vec{b}_2 and \vec{b}_3 are primitive reciprocal lattice vectors. This vector can be evaluated from $\vec{G} \cdot \vec{R} = N2\pi$ (for $N = 1, 2, 3, \dots$). This means that, in order to solve the eigenvalue problem for \vec{k} , \vec{k} will be bounded to only the region in reciprocal space where \vec{k} cannot have any other values of itself by adding any \vec{G} . This restricted region is called the first Brillouin zone. Furthermore, if additional symmetries, e.g., rotational symmetry, are applied to photonic crystals, it is unnecessary to solve for every \vec{k} point in the first Brillouin zone. Only the region, in which those symmetries do not have any effects on $\omega_n(\vec{k})$, is required. This region is called the irreducible Brillouin zone.

2.2 Origin of photonic bandgap

In certain structures of photonic crystal there can be a range of ω , in which no propagating states $\omega_n(\vec{k})$ corresponding to the restricted wave vector \vec{k} are allowed and all incident radiation is reflected. This frequency range is known as the photonic band gap. In order to understand the origin of the gap, two properties of Hermitian eigenvalue problem have to be concerned. Firstly, because the operator of Eq. (2.7) is Hermitian, its eigenvalue must be real and positive and its harmonic modes must be orthogonal:

$$\langle \vec{H}_1 | \vec{H}_2 \rangle = 0 \quad (2.16)$$

That is, an inner product of any two harmonic modes with different frequencies is zero. Secondly, corresponding to the electromagnetic variational theorem, the lowest frequency mode is the field pattern that minimizes the electromagnetic energy functional:

$$E_f(\vec{H}) = \left(\frac{1}{2(\vec{H}, \vec{H})} \right) \int d\vec{r} \frac{1}{\varepsilon} |\nabla \times \vec{H}|^2 = \left(\frac{1}{2(\vec{H}, \vec{H})} \right) \int d\vec{r} \frac{1}{\varepsilon} \left| \frac{\omega \varepsilon}{c} \vec{E} \right|^2 \quad (2.17)$$

Other higher bands, e.g., the second band, also satisfy Eq. (2.17), but orthogonality of harmonics mode according to Eq. (2.16) must be fulfilled as well. From this expression, in order to minimize E_f , the field of the first band must be concentrated in

the regions of high dielectric constant ε to lower its potential energy. This yields to have a lower frequency. Additionally, the curl of field $\nabla \times \vec{H}$ should be small, in other words, the field is varying slowly inside the high dielectric constant regions and containing no nodal plane, in order to lower its kinetic energy. When the case comes to the second band, this mode also wants to be concentrated in the high dielectric constant regions and contain no nodal plane inside those regions to obtain the minimum E_f . However, from Eq. (2.16), this mode must be orthogonal to the mode of the first band. As a result, the second band has to be concentrated in the regions of low dielectric constant and restrictedly have nodal plane in those regions to make the integral zero. This results in a difference in frequencies of these two bands and the band gap occurs. This can be understood by an example shown in Fig. 2.1(a). Applying the relation in Eq. (2.17), two equally symmetric modes, $\sin(\pi x/a)$ and $\cos(\pi x/a)$, are forced in a one-dimensional photonic crystal. The bandgap between the top of dielectric band and bottom of air band is visualized for a one-dimensional photonic crystal in Fig. 2.1(b).

Unlike the simple one-dimensional photonic crystal, in which any nonzero periodic dielectric variation will result in a complete bandgap, achieving a photonic bandgap in higher-dimensional photonic crystal becomes complicated. This is because the forbidden gaps for all possible directions in reciprocal space are needed to be overlapped in some frequency. Therefore, with a fairly large contrast in ε between the high and low dielectric regions, a proper geometry of the periodic structure should be selected to create the photonic bandgap. Figure 2.2(a) shows the Brillouin zone of the face-centered-cubic lattice. A point on the surface of the Brillouin zone closest to the center is the L point, oriented toward the body diagonal of the cube. A point in the cubic direction is the X point. Considering a plane wave in the X direction as done in the case of the one-dimensional photonic crystal, it will sense the periodicity in the cubic direction, forming a standing wave and opening a forbidden gap as indicated by the shading in Fig. 2.2(b). Supposing, on the other hand, that the plane wave is going in the L direction, it will sense the periodicity along the cubic-body diagonal, and a gap will form in that direction as well. But the wave vector to the L point is $\sim 14\%$ smaller than the wavevector to the X point. Therefore, the gap at L is likely to be centered at a 14% smaller frequency than the gap at X. If the two gaps are not

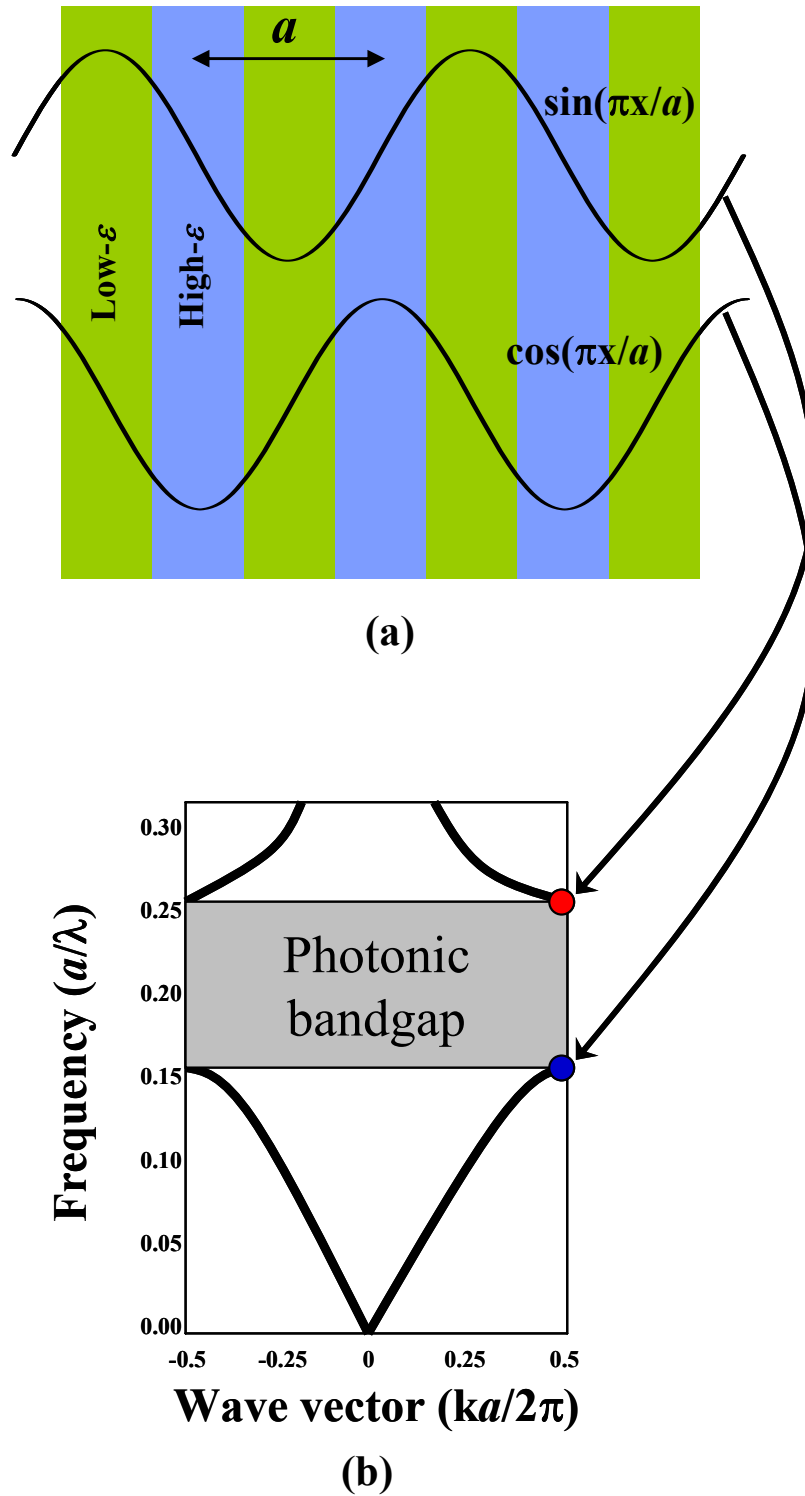


Figure 2.1 (a) Schematic illustration of the electric fields of mode at air and dielectric bandedges in a multilayer film with lattice constant a . (b) Photonic band structure of the structure shown in (a).

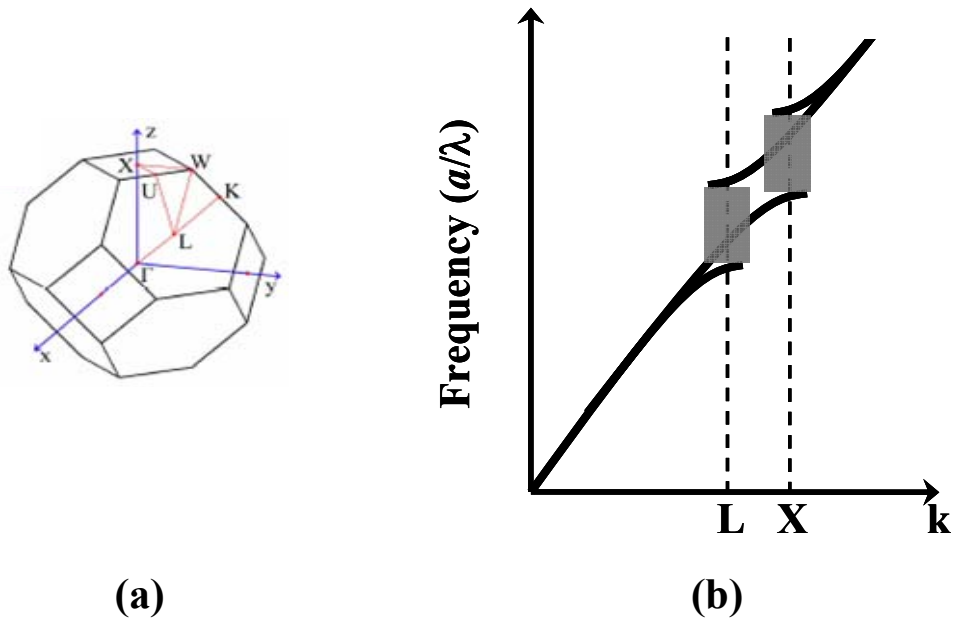


Figure 2.2 (a) Brillouin zone of face-centered-cubic lattice. (b) Forbidden gap (shaded) at point L, which is centered at a frequency $\sim 14\%$ lower than X-point forbidden gap.

wide enough, they will not overlap in frequency. As a result, for three-dimensional photonic crystal, the Brillouin zone should most closely resemble a sphere in order to increase the likely hood of a frequency overlap in all directions of space. In this case, the face-centered-cubic lattice has the highest potential among any other types of lattice to achieve a photonic bandgap due to its least percentage deviation of the Brillouin zone from a sphere.

In the same way as in the three-dimensional system, the two-dimensional photonic crystals whose the Brillouin zone more closely resemble a circle will lead to a larger gap. This will be discussed in details in next subsection.

2.3 Types of photonic crystals

According to the order of dimensions that they periodically alter, photonic crystals can be classified into three categories, which are one-dimensional, two-dimensional, and three-dimensional photonic crystals. These three types of photonic crystal are shown in Fig. 2.3. In one- and two-dimensional photonic crystals,

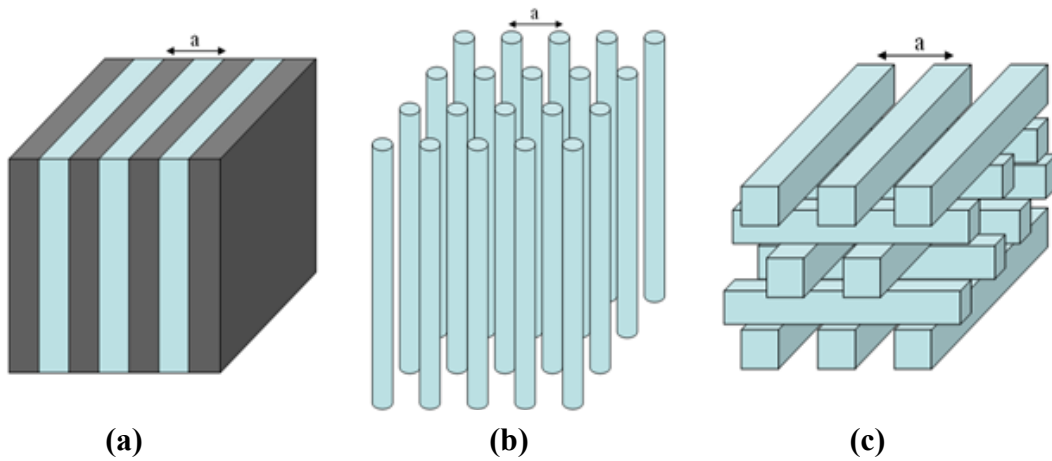


Figure 2.3 Schematic illustrations of photonic crystal (a) one-dimensional (b) two-dimensional (c) three-dimensional.

band structure diagrams and bandgaps are limited to the directions of periodic dielectric modulation. Unaffected propagation of electromagnetic waves is possible along those lattice directions showing no periodicity [84]. One-dimensional photonic crystals are known as Bragg mirrors. These structures have been used for a long time before the concept of photonic crystals was established, but the same concepts and principle apply to the one-dimensional structures also. They consist of periodically stacked layers of different refractive indices [85]. Two-dimensional photonic crystals have a periodicity in two dimensions and are infinitely extended in the third dimensions. They are often realized in practice by a periodic arrangement of air cylinders in a dielectric or by cylinders consisting of a dielectric material in air organized in a square or triangular lattice. [86-89]. Three-dimensional photonic crystals are the only true photonic crystals in the strict sense since in them light propagation can be forbidden in all directions. In the following subsections, only two-dimensional photonic crystal slabs with both triangular and square lattices and three-dimensional (woodpile) photonic crystal structures will be discussed as they are the basic building blocks of the work described in this thesis.

2.4 Two-dimensional photonic crystal slabs

While the theoretical treatment of two-dimensional photonic crystals is relatively easy, their fabrication procedure is not straightforward since they are

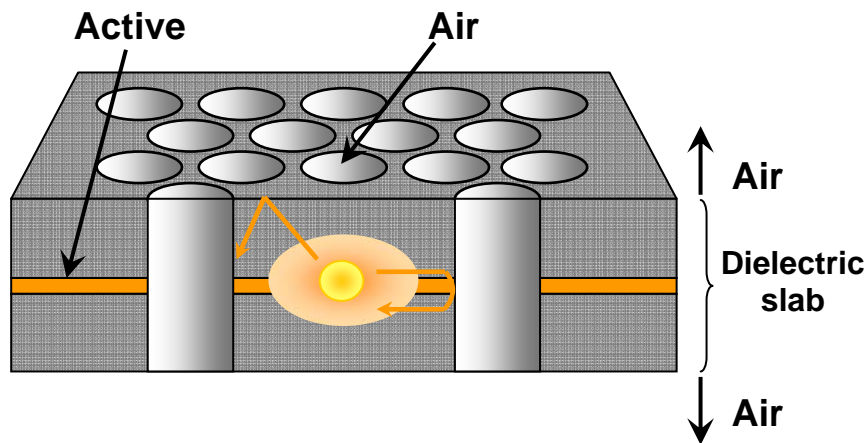


Figure 2.4 Schematic illustration of photonic crystal slab.

infinite structures in the third dimension. Therefore, the concept of a two-dimensional photonic crystal slab was proposed to overcome this obstacle [57]. Two-dimensional photonic crystal slab is essentially a two-dimensional photonic crystal with a finite third dimension. One typical structure is a membrane based photonic crystal shown in Fig. 2.4. An optically thin semiconductor slab (thickness is roughly $\lambda/2$) is surrounded with a low-refractive index material (usually air), and perforated with a two-dimensional lattice of holes. When the slab is cladded by air on both sides, the structure is called a two-dimensional air-bridge photonic crystal. In such structure, the localization of light in all three dimensions is made possible by the combination of two mechanisms: in the vertical direction, light is confined to the slab by means of total internal reflection due to high index contrast between the high-index slab and the low-index environment, while in the in-plane direction light is controlled by means of distributed Bragg reflection due to the presence of two-dimensional lattice of holes. In the two-dimensional air-bridge photonic crystal shown in Fig. 2.4 the third dimension is not periodic nor infinite, and therefore photons incident to the surface between the semiconductor slab and air with smaller angles than the critical angle for total internal reflection can escape from the slab and couple into the continuum of radiation modes. These photons leak energy from the slab and therefore represent the loss mechanism of the two-dimensional photonic crystal slab. In order to take these losses into account, the notion of light cone is introduced in the analysis of photonic crystal by the light line. The light cone, where the leaky modes exist, is the region over the light line.

The light cone, where the leaky modes exist, is the region over the light line. Concretely, examining the energy-momentum dispersion relation for a homogeneous dielectric cladding with refractive index n :

$$\left(\frac{n\omega}{c}\right)^2 = k_z^2 + k_\perp^2 \quad (2.18)$$

where ω is the angular frequency, k_z is the in-plane wave vector, k_\perp is the wave vector normal to the slab, and c is the speed of light. Light line can be confined as:

$$k_z^2 = \left(\frac{n\omega}{c}\right)^2 \quad (2.19)$$

Since radiative modes exist at all frequencies, including the bandgap region, they close the bandgap, and the complete bandgap does not exist in two-dimensional photonic crystal slab. The forbidden frequency range still exists, however, for the guided modes of the slab, which is for the photons confined in the patterned slab and just decayed exponentially into the claddings. The gap for guided modes is shown by shaded region in Fig. 2.5. Therefore, in the case of two-dimensional photonic crystal slab, the bandgap is not complete and it exists only for the guided modes of the patterned slab. The properties of two-dimensional photonic crystal slab, such as position and width of the bandgap, depend strongly on several important parameters: the type of lattice (e.g., triangular, square), the thickness of the slab (d), the refractive of both slab and claddings, the periodicity of the lattice (a) and the radius of the holes (r).

In two-dimensional photonic crystal, due to the mirror reflection symmetry in the direction perpendicular to the plane of periodicity, modes of every two-dimensional photonic crystal can be classified into two non-interacting classes of polarizations: TE polarized modes (electric field in plane of periodicity) and TM polarized modes (magnetic field in plane of periodicity). As in two-dimensional system, guided modes in photonic crystal slab can be also decomposed into two distinct classes. These are not purely TE and TM polarized as in the two-dimensional photonic crystal due to the finite extent of slab in the direction normal to the plane of slab. However, they are classified by whether they transform to be even or odd with respect to a horizontal mirror plane bisecting the slab. These even and odd states have the strong similarities with TE and TM modes, respectively, in two-dimensional

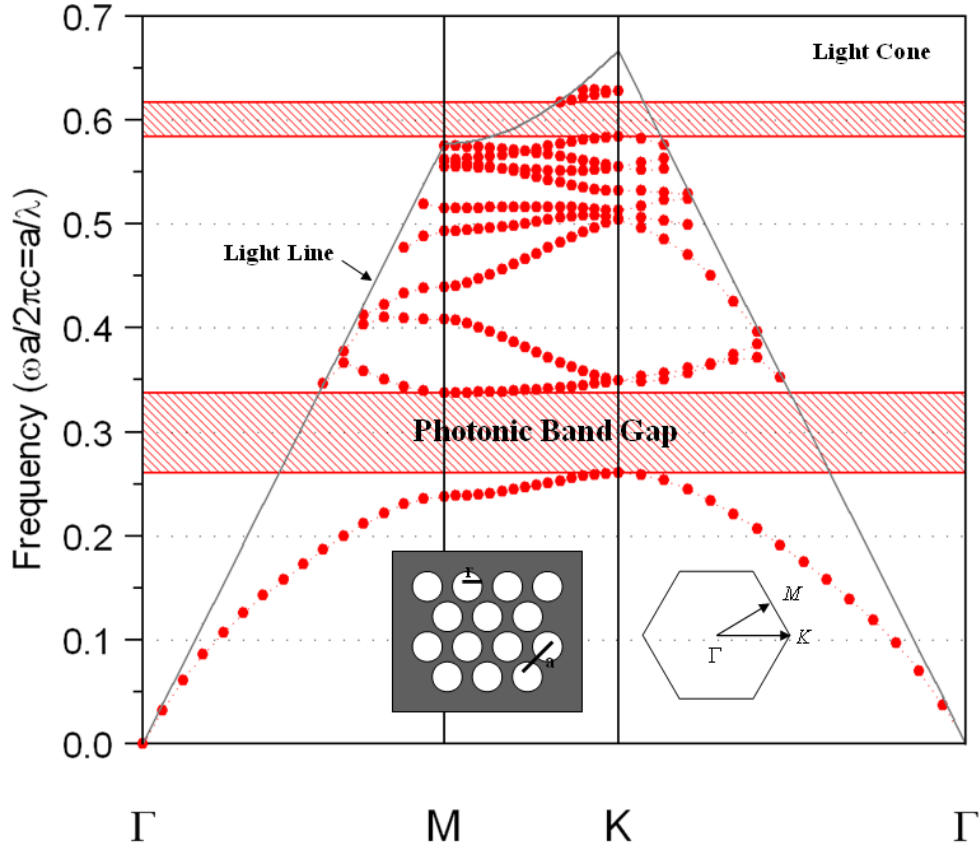


Figure 2.5 Band diagram for the air-bridge slab structure with $r = 0.30a$ and $d = 0.60a$. The insets show triangular lattice of air holes in dielectric with refractive index of 3.4 and its first Brillouin zone.

photonic crystal. In addition, within the slab they are TE- and TM-like, and closely resemble the TE and TM modes in two-dimensional system.

2.4.1 Comparison between square and triangular photonic crystal lattices

Since in this thesis, two-dimensional photonic crystal slabs with two types of lattice, square and triangular, are concerned, they will be discussed in details in this subsection. The structure that is a GaAs slab, suspended in air, and patterned with square or triangular lattice of holes as illustrated in Fig. 2.6 and 2.7. The Three-dimensional Finite-Difference Time-Domain method (3D-FDTD) was used to calculate the band diagrams (details on the computational method are discussed in Chapter 3). The thickness of the slab was $d = 0.60a$ and hole radius was $r = 0.40a$. The refractive index of GaAs is assumed to be 3.4.

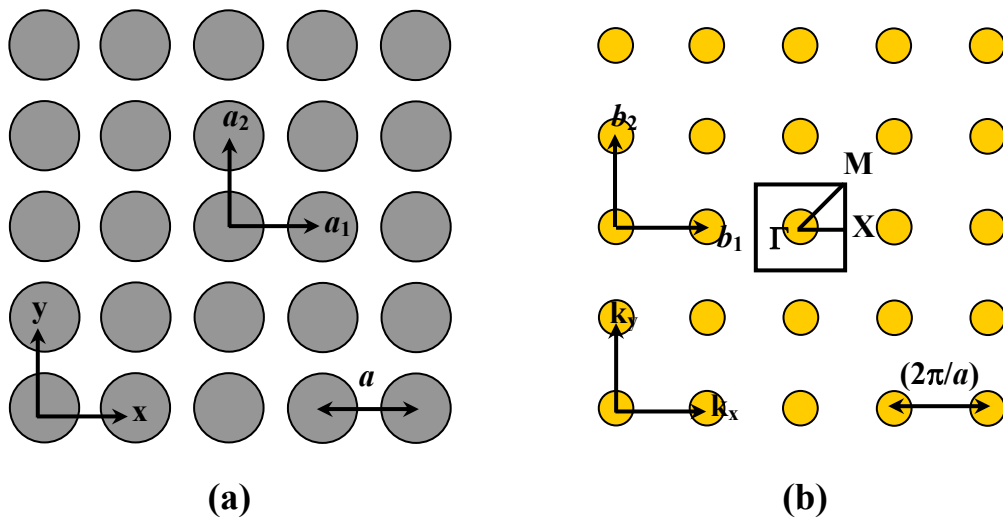


Figure 2.6 The square lattice shown in (a) real space and (b) reciprocal space with their corresponding lattice vectors. The square represents the first Brillouin zone, and Γ , X and M are the high-symmetry points.

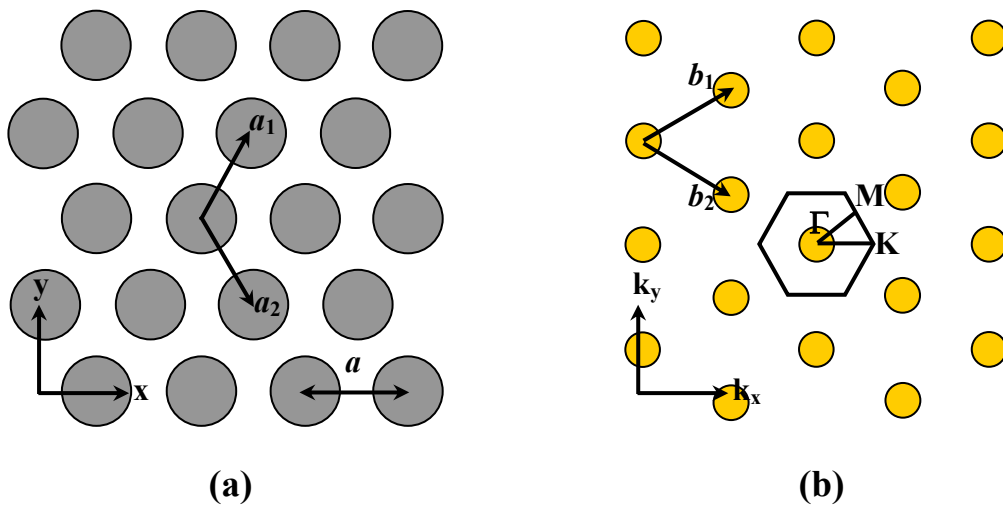


Figure 2.7 The triangular lattice shown in (a) real space and (b) reciprocal space with their corresponding lattice vectors. The hexagon represents the first Brillouin zone, and Γ , K and M are the high-symmetry points.

Figure 2.6 (a) and (b) illustrate the square lattice in real space and reciprocal space, respectively. The lattice vectors in real space are $\vec{a}_1 = a \cdot (1,0,0)$ and $\vec{a}_2 = a \cdot (0,1,0)$, and reciprocal lattice vectors are $\vec{b}_1 = (2\pi/a) \cdot (1,0,0)$ and $\vec{b}_2 = (2\pi/a) \cdot (0,1,0)$. The square in Fig. 2.6(b) represents the first Brillouin zone, and Γ , X and M are the high-symmetry points with coordinates in reciprocal space: $\Gamma = (0,0,0)$, $X = (\pi/a,0,0)$, $M = (\pi/a,\pi/a,0)$. In the case of the photonic crystal slab with triangular lattice, lattice vectors in the real space can be expressed as $\vec{a}_1 = a \cdot (1/2, \sqrt{3}/2, 0)$ and $\vec{a}_2 = a \cdot (1/2, -\sqrt{3}/2, 0)$, and reciprocal lattice vectors are $\vec{b}_1 = (2\pi/a) \cdot (\sqrt{3}/2, 1/2, 0)$ and $\vec{b}_2 = (2\pi/a) \cdot (\sqrt{3}/2, -1/2, 0)$. The hexagon in Fig. 2.7(b) represents the first Brillouin zone, and the coordinates of high-symmetry points are $\Gamma = (0,0,0)$, $M = (\pi/a) \cdot (1, 1/\sqrt{3}, 0)$, $K = (\pi/a) \cdot (4/3, 0, 0)$.

Band diagram for the vertically even (TE-like) eigenmodes of the two-dimensional photonic crystal slab structure with square and triangular symmetry are shown in Fig. 2.8. Only band diagram for TE-like modes are concerned here since active materials adopted in this work are quantum dots, which have electronic states predominantly coupled to the TE modes. As it can be seen, in both structures the first-order bandgap is open for the guided modes of the slab. The bandgap is formed only for the guided modes as discussed above. The photonic crystal slab with triangular lattice has a much wider bandgap than the square lattice, a result of the greater symmetry and the smoother Brillouin zone in that geometry, in other words, the Brillouin zone more closely resemble a circular shape. Therefore, the triangular lattice is in many ways a more promising geometry for the realization of photonic crystal devices. However, in many cases it is not necessary to work with photonic crystals that have wide bandgap. In Chapter 4 and 5, it will be shown that high quality factor cavity can be realized in the structures with a very small bandgap or even no bandgap at all.

2.4.2 Effect of slab thickness and radius of air holes on photonic bandgap

Because high quality factor photonic crystal nanocavities by optimizing the slab thickness and by modulating air hole radii will be presented in Chapter 4 and 5, respectively, in this subsection the influence that slab thickness and radius of air holes have on the behavior of photonic bandgap is discussed. A triangular lattice

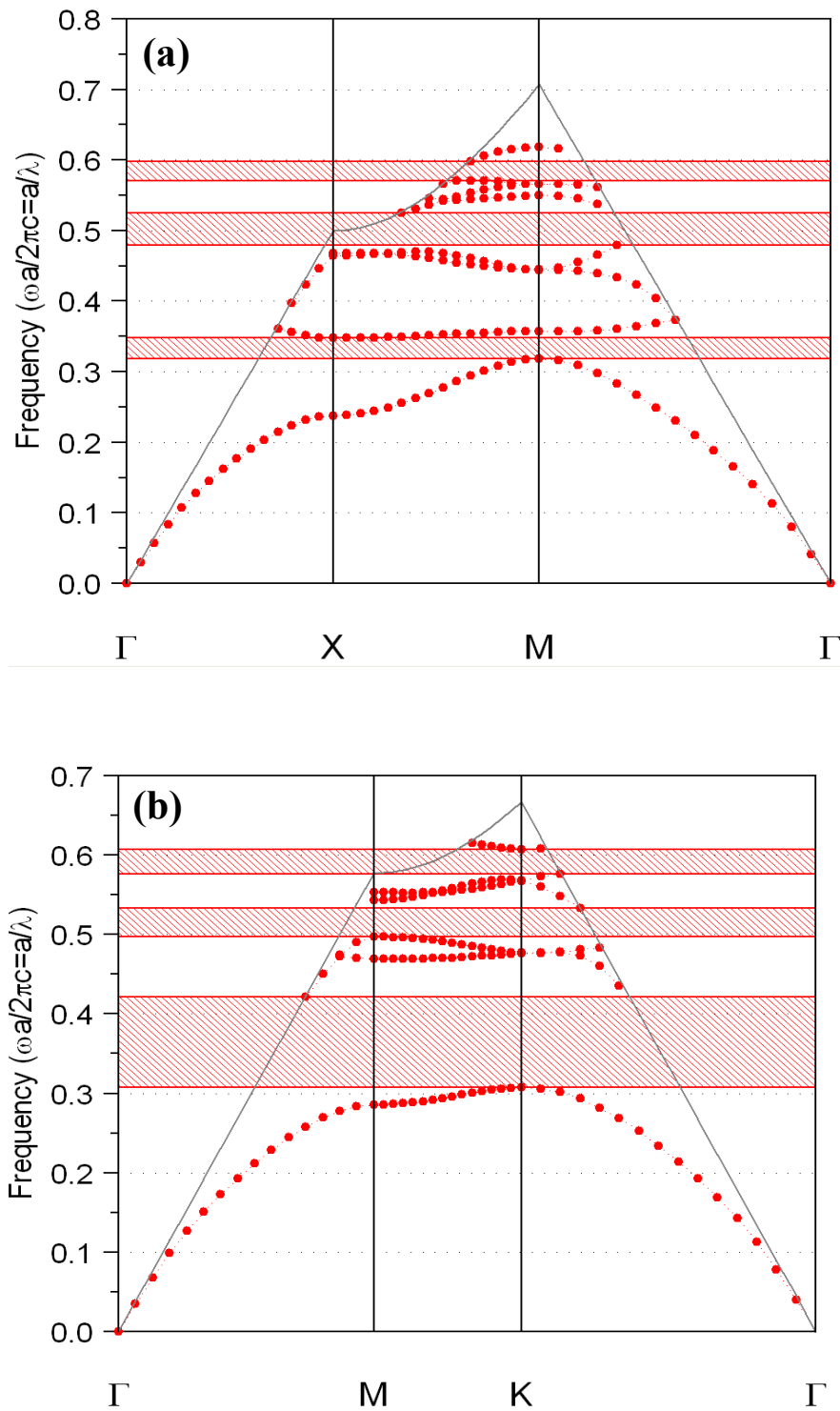


Figure 2.8 Band diagrams for the air-bridge slab structure with (a) square and (b) triangular lattice. Slab thickness $d = 0.60a$, radius of air holes $r = 0.40a$, refractive index = 3.4 for both structures.

two-dimensional photonic crystal slab is studied, but results can be generalized to the square lattice photonic crystal slab as well.

As previously mentioned, a two-dimensional photonic crystal slab has a band gap for its guided modes. Among many photonic band gaps that can occur, the lowest-order photonic band gap that emerges between the lowest-order mode, a so-called dielectric band, and the second-order mode, a so-called air band, is the most interesting due to lower density of radiation states in low frequency region, leading to lower radiation losses. However, this band gap can occur only when some of parameters of the slab are suitable. More concretely, if radius of the air holes r is large enough as well as appropriate slab thickness d is fulfilled, the gap may appear [60,90]. The radius of air holes has an important effect on the propagation of light in the slab, as it determines the width of the gap. Figure 2.9 shows the plots between the gap-mid gap ratio, which designates the band gap size, for and the slab thickness for TE-like modes in the air-bridge structure with r equal to $0.30a$, $0.35a$, and $0.40a$ indicated by boxed dots, circular dots, and triangular dots, respectively. The bandgap becomes wider as the holes become bigger. Because bandedges are shifted towards higher frequencies when the hole size is increased due to increased overlap with low-dielectric material (air), the air-band modes that localize their energy in the air holes are more sensitive to changes in the hole size, and they experience larger blue shift than the dielectric-band modes, when holes are made bigger. This results in widening of the photonic bandgap. This is obvious over the range of the slab thickness less than $0.60a$. When the slab thickness is over $0.60a$, the tendency of gap size becomes complex. This is because when the slab is thick, the gap is determined by the frequency range between the dielectric-band edge and the second-order guided mode cutoff, instead of the frequency range between the dielectric-band edge and the air-band edge at K point of the first Brillouin zone as in the case of the slab thinner than $0.60a$. Figure 2.10 shows the band diagram when $r = 0.40a$ and $d = 1.10a$. To achieve accurate values of the cutoff frequency, high-resolution and time-consuming computations are needed. As a result, the exact results are slightly inconsistent.

The existence of the gap and the gap size also strongly depends on the slab thickness as shown in Fig. 2.9. It is obvious that there is an optimal slab thickness, which can yield the largest gap between the first two bands. When the slab is too thin, air holes are just like a weak perturbation on the bare slab. Guided modes still exist,

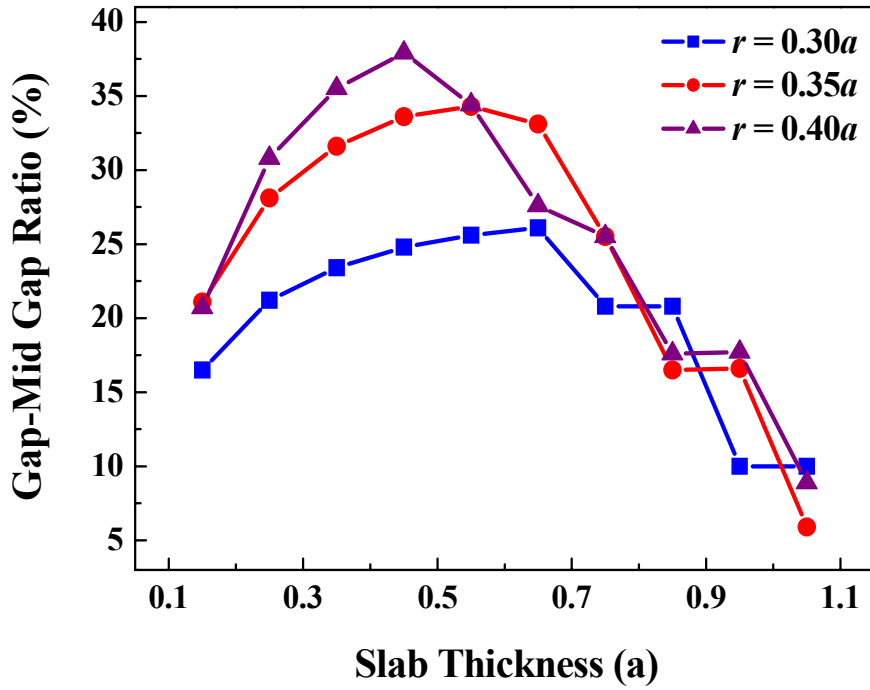


Figure 2.9 Dependence of Gap-mid gap ratio on slab thickness for air-bridge slab structure with $r = 0.30a$ (square), $r = 0.35a$ (circle), and $r = 0.40a$ (triangle).

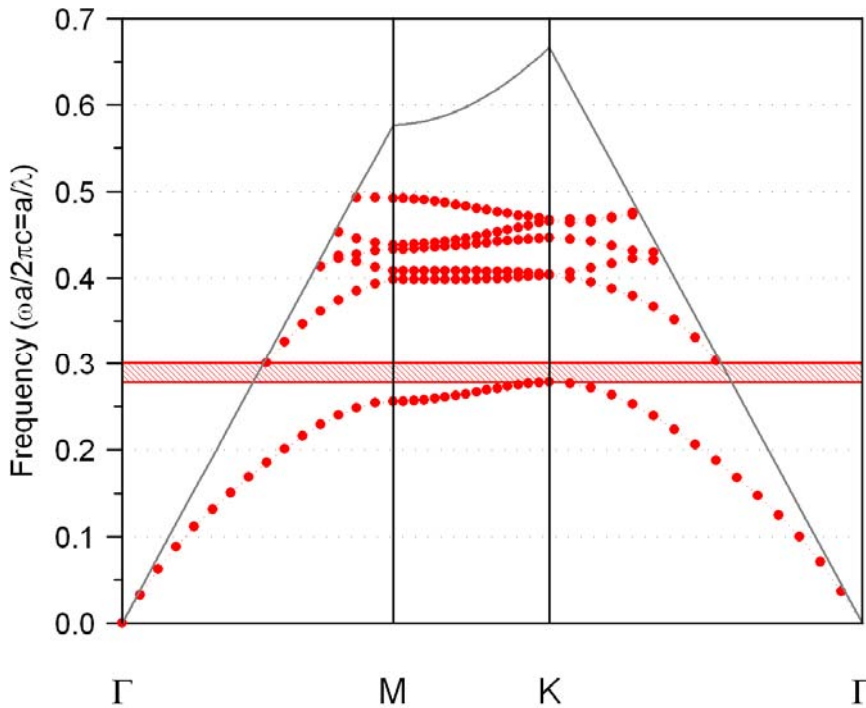


Figure 2.10 Band diagrams for the air-bridge slab structure with triangular lattice. The slab thickness is $1.10a$.

but they cannot be strongly confined within the slab. As a result, the gap is very small. On the other hand, if the slab is too thick, the second-order modes will be created at low frequency, which may locate at frequencies very near to the lowest-order mode. If the slab is thick enough, the air band falls below the dielectric-band edge and is responsible for destroying the photonic bandgap. The photonic bandgap is closed at the slab thickness $d = 1.10a$, $1.25a$, and $1.20a$ for the structure with $r = 0.30a$, $0.35a$, and $0.40a$, respectively. In the aspect of localized modes, which are confined in the photonic crystal slab defect cavity and have frequencies within the band gap, larger gap means the ability of the cavity to achieve better in-plane confinement for the localized modes. On the other hand, when the gap is closed, localized modes are able to couple to slab guided modes and then be guided through the slab in in-plane direction, resulting in very poor confinement in in-plane direction. With these reasons, conventional photonic crystal slab cavity structures usually have the slab thickness in the order of half wavelength of light confined in the cavity, which is about $0.60a$. However, in Chapter 4, a design of high quality factor photonic crystal nanocavity with a wavelength-thick slab, where the bandgap is closed, will be shown. This has been achieved by decoupling the cavity mode from the leaky modes.

2.5 Woodpile structures

The so-called “woodpile” geometry is a well-established three-dimensional photonic crystal lattice designed to provide a complete photonic bandgap in a structure with a straightforward fabrication process [91]. The woodpile has a narrower complete photonic bandgap than most of other types of three-dimensional photonic crystal structure [92], however, it is relatively easier to fabricate. Therefore, in this thesis, only this structure will be concentrated. The illustration of the woodpile structure is illustrated in Fig. 2.11. The structure is made of layers of dielectric rods with a stacking sequence that repeats itself every four layers with a periodicity $c (= 4d)$, where d is the layer thickness) in stacking direction (z direction). Within each layer, the rods are arranged with their axes parallel and separated by an in-plane periodicity pitch a (in x and y directions). The orientations of the axes are rotated by 90° between adjacent layers and offset by a distance $0.5a$ from the layer two below. As discussed in Section 2.2, the face-centered-cubic lattice has the highest potential among any

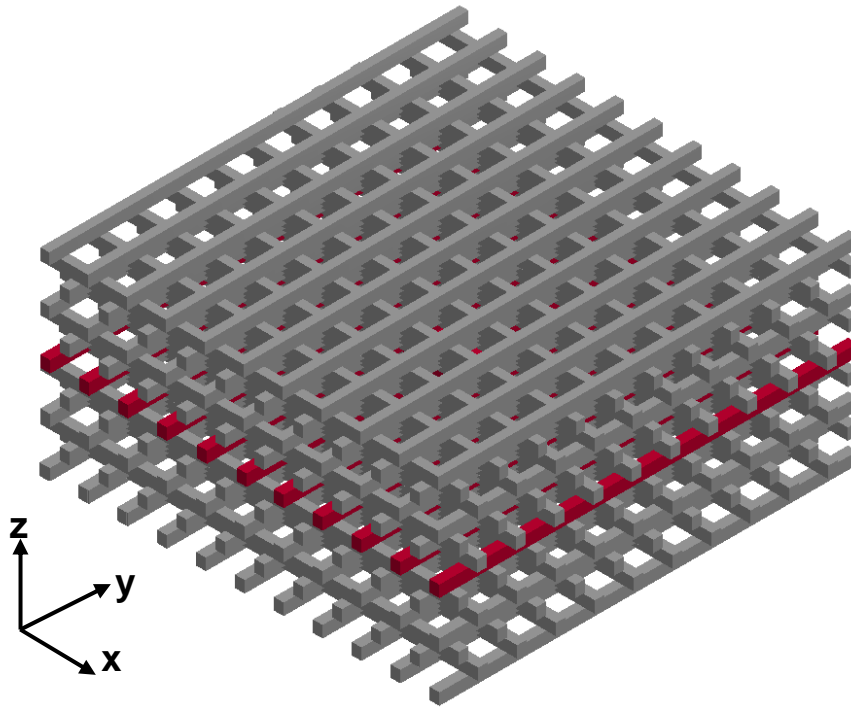


Figure 2.11 Schematic illustration of woodpile structure with 11 in-plane periods and 17 vertical layers

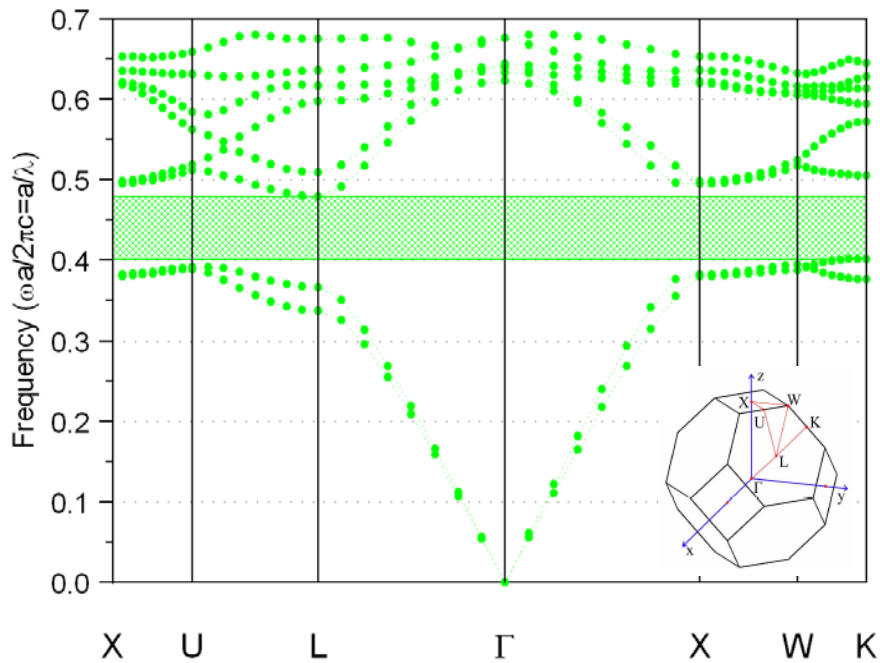


Figure 2.12 Band diagram for the woodpile structure showing a complete bandgap between $a/\lambda = 0.40-0.48$. The layer thickness and the rod width are $0.25a$ and $0.25a$, respectively. The refractive index is 3.4.

other types of lattice to achieve a photonic bandgap due to its least percentage deviation of the Brillouin zone from a sphere. The woodpile structure appears to have a simple tetragonal lattice structure, with $(a\hat{x}, a\hat{y}, c\hat{z})$ as the lattice basis. However, the lattice in fact has a more complex crystal structure. In addition to symmetry under translation by the lattice basis vectors given above, the woodpile lattice is also symmetric under translation by half a period in each direction. While this symmetry immediately implies a body-centered tetragonal structure, the lattice also has face-centered tetragonal structure under a different orthogonal basis. Consider the basis $(a\hat{X}, a\hat{Y}, c\hat{Z})$, where $\hat{X} = \hat{y} + \hat{x}$, $\hat{Y} = \hat{y} - \hat{x}$ and $\hat{Z} = \hat{z}$. This is an orthogonal basis, and the woodpile lattice is certainly symmetric under translations by the lattice vectors. The lattice is also symmetric under translation by the vectors:

$$\begin{aligned}\frac{1}{2}(a\hat{X} + a\hat{Y}) &= a\hat{y}, \\ \frac{1}{2}(a\hat{X} + c\hat{Z}) &= \frac{a}{2}\hat{x} + \frac{a}{2}\hat{y} + \frac{c}{2}\hat{z}, \\ \frac{1}{2}(a\hat{Y} + c\hat{Z}) &= \frac{a}{2}\hat{y} - \frac{a}{2}\hat{x} + \frac{c}{2}\hat{z}.\end{aligned}$$

Thus the woodpile lattice has face-centered tetragonal structure. In particular, if $c = \sqrt{2}a$, the orthogonal basis given above is cubic, therefore the lattice has face-centered-cubic structure. This layered structure can be derived from the diamond lattice by replacing the (110) chains in the diamond structure by rods. The Brillouin zone of the face-centered-cubic lattice is shown in the inset of Fig. 2.12. Figure 2.12 shows a calculated band diagram of the woodpile structure along the symmetry points which bound the irreducible Brillouin zone. The refractive index, rod width, and layer thickness were set to 3.4, $0.25a$ and $0.25a$, respectively. The lattice exhibits an omnidirectional bandgap—a range of frequencies in which no mode, of any wavevector or polarization, exists.

2.6 Photonic crystal defect nanocavities

A very promising application of photonic crystals is to realize optical nanocavities that can trap the light in very small mode volumes and for a long period of time (proportional to the cavity quality factor). The strong light localization in photonic crystal nanocavities can dramatically increase the light-matter interaction

and the photon-photon interaction, which are important for a wide range of applications, ranging from basic science to engineering.

Photonic crystal nanocavities can be formed by perturbing periodic components of perfect crystals (i.e., by adding or removing dielectric material). Such a break in the periodicity of the lattice introduces new energy levels within the photonic bandgap. This is analogous to the creation of energy levels within the semiconductor energy band gap by the addition of dopant atoms in semiconductor crystals. According to the perturbation theory applied to Maxwell's equations, removing dielectric material, i.e., increasing the hole sizes of the two-dimensional photonic crystal slab, increases the energy of the modes supported in the slab and pulls up defect states from the dielectric band into the bandgap. Such bound states exist close to the dielectric band and shows similarity to the acceptor levels in semiconductors. Because of that, the modes created in this way are called the acceptor modes. Similarly, the reduction of the hole sizes decreases the energy of the mode and pulls down defect states from the air band into the bandgap. Such types of defect modes are called referred to as the donor modes. It shall be mentioned that, strictly speaking, the discrete translational symmetry of the lattice is already broken by one defect and the crystal could no longer be characterized by the concept of a \vec{k} -vector. But, as the periodic remainder of the ideally infinite lattice still works effectively as a perfect mirror, defect modes cannot penetrate the unperturbed crystal and is then confined in the defect region. Because the defect mode of the donor defect is typically more strongly localized in the dielectric material than that of the acceptor defect, throughout this thesis only donor defects will be discussed in consideration of introducing a light emitter, such as quantum dots, into the dielectric material. Figure 2.13 shows illustrations of three kinds of defect structures, which are mainly studied throughout this thesis. The first two are H1-defect nanocavity in triangular lattice air-bridge photonic crystal and square lattice air-bridge photonic crystal nanocavity with modulating air hole radii. The other one is square-shaped point-defect in woodpile structure. They will be discussed in details in the following Chapters.

In the case of cavities defined in photonic crystal slabs, in which only bandgaps for guided modes exist, cavity modes will suffer from radiation losses due to the coupling into the continuum of radiation modes that exist within the light cone.

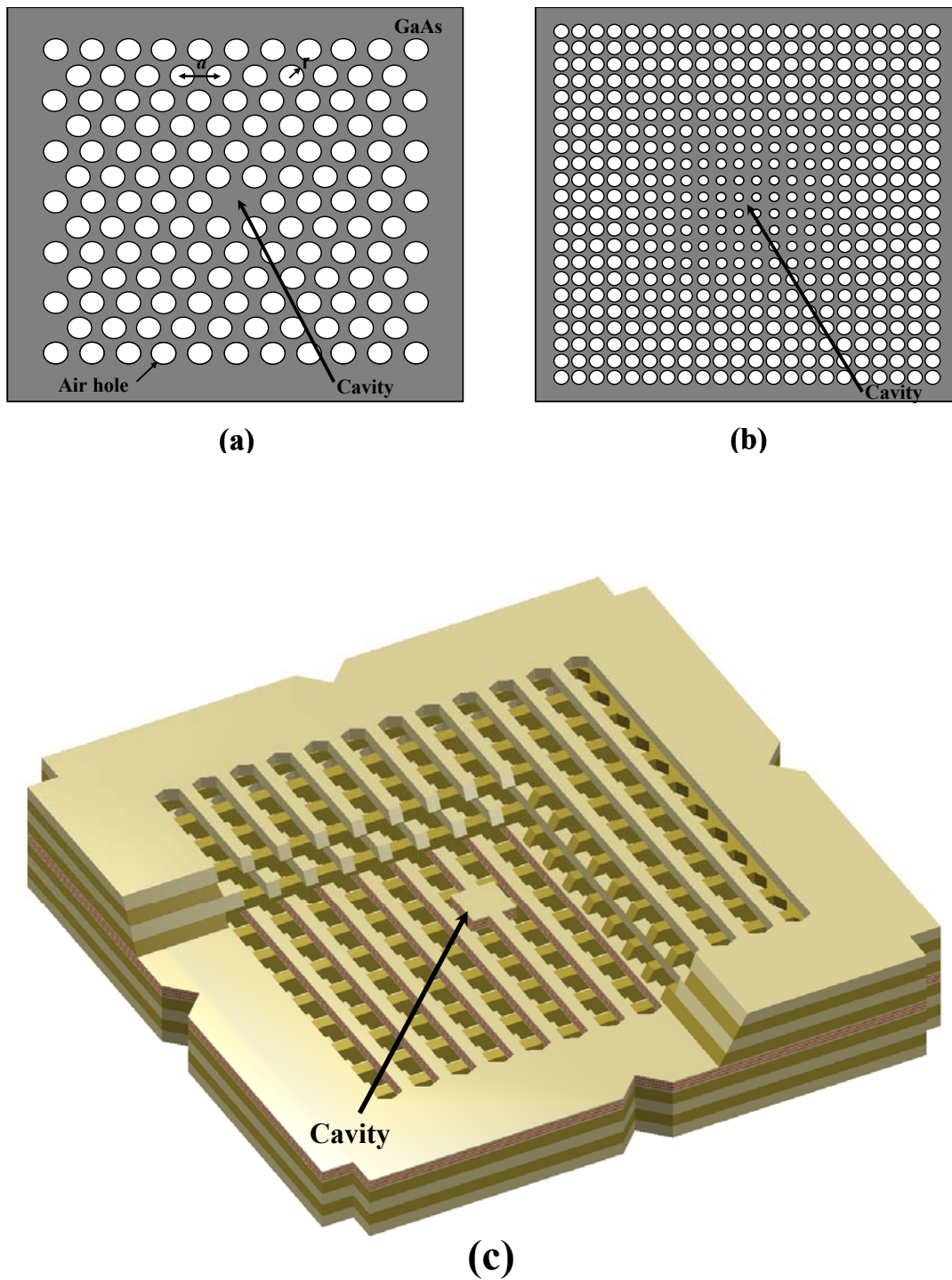


Figure 2.13 Three defect structures studied in the thesis. (a) H1-defect nanocavity in triangular lattice air-bridge photonic crystal. (b) Square lattice air-bridge photonic crystal nanocavity with modulating air hole radii (c) Square-shaped defect nanocavity in woodpile photonic crystal.

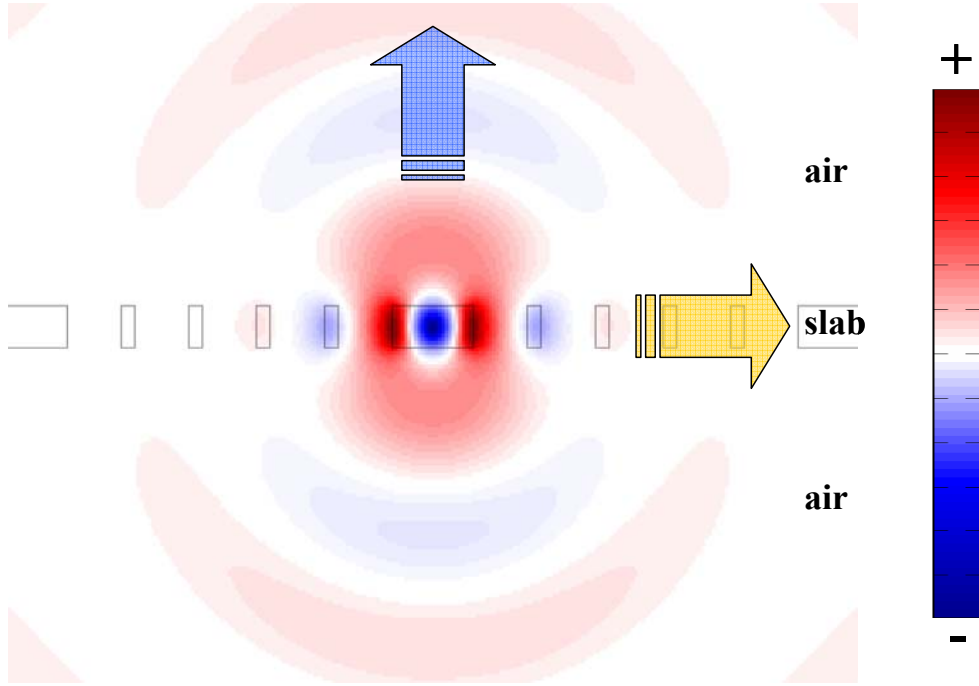


Figure 2.14 Field distribution of dipole mode in the H1-defect photonic crystal slab nanocavity viewed in cross section. Blue arrow indicates the radiation loss and yellow arrow represents in-plane loss.

Light coupled with these radiation modes radiate out of the cavity into the vertical direction. These components contribute to the out-of-plane losses of the cavity, as shown in Fig. 2.14. At the same time, light can leak laterally due to the finite number of the photonic crystal layers surrounding the cavity contributing to the in-plane losses of the resonator. On the other hand, cavities in three-dimensional photonic crystals can have a complete photonic bandgap, in which cavity modes are confined by photonic bandgap effect in all directions; no radiation losses exist. Only losses due to the finite number of periodicity surrounding the cavity take place. The efficiency of a cavity, described by a quality (Q) factor, can be expressed as the ratio of energy stored in the cavity (U) and power P dissipating from the cavity at a center frequency ω_0 as:

$$Q = \omega_0 \frac{U}{P} \quad (2.20)$$

Taking into account that the power dissipating is the negative of the time rate of energy stored in the resonator, it is found that:

$$\frac{dU}{dt} = -P = -\omega_0 \frac{U}{Q} \quad (2.21)$$

and thus

$$U(t) = U_0 e^{-\frac{\omega_0 t}{Q}} \quad (2.22)$$

The time dependence of the stored energy implies that oscillations of the field inside the cavity are damped as follows:

$$E(t) = E_0 e^{-\frac{\omega_0 t}{2Q}} e^{i(\omega_0 + \delta\omega)t} \quad (2.23)$$

Assuming that the resonant frequency does not change in presence of the losses, i.e., $\delta\omega \approx 0$, and transforming the time dependence field into frequency, the relation can be shown in the following equation:

$$E(\omega) = E_0 \frac{1}{-i(\omega - \omega_0) + \frac{\omega_0}{2Q}} \quad (2.24)$$

Therefore an exponentially as $e^{-\frac{\omega_0 t}{2Q}}$ decaying field at the frequency ω_0 has a frequency spectrum of Lorentzian intensity shape centered at ω_0 with the full width at half maximum (FWHM) of $\Delta\omega = \frac{\omega_0}{Q}$, which leads to another expression of the quality factor:

$$Q = \frac{\omega_0}{\Delta\omega} \quad (2.25)$$

To describe the spatial confinement of the cavity field, its effective volume with respect to the spatial distribution of the dielectric constant $\epsilon(\vec{r})$ is defined. This leads to the definition of the cavity mode volume:

$$V_{eff} = \frac{\iiint \epsilon(\vec{r}) |\vec{E}(\vec{r})|^2 d^3\vec{r}}{\max[\epsilon(\vec{r}) |\vec{E}(\vec{r})|^2]} \quad (2.26)$$

Details on calculation of these parameters will be discussed in next chapter.

2.7 Summary

In this chapter, the principle of photonic crystal has been reviewed theoretically. By cooperating of Maxwell's equations and solid-state physics, the propagation of light in a photonic crystal can be studied. Due to a periodic dielectric

function of photonic crystal, the Bloch-Floquet theorem can then be applied to solve the Hermitian eigenvalue problem over a unit cell of the photonic crystal. The solution results in a discrete set of modes, which originates a band structure of the photonic crystal. In addition, by considering the electromagnetic variation theorem, the origin of the photonic band gap, in which no propagating modes can be existed, has been revealed. After that, two-dimensional photonic crystal slabs with both triangular and square lattices and three-dimensional woodpile photonic crystal structures have been described in details as they are the basic building blocks of all the work in this thesis. The influence of slab thickness and radius of air holes of two-dimensional photonic crystal slabs, important parameters of the design of high- Q nanocavities in the following chapters, on the behavior of photonic bandgap have been preliminarily discussed. Finally, photonic crystal nanocavities formed by introducing defects to a perfectly periodic system have been introduced.

Chapter 3

Finite-Difference Time-Domain Method

The Finite-Difference Time-Domain (FDTD) method is a general method for numerically solving the time-dependent Maxwell's equations in media that is structured on the scale of the wavelength. It is therefore particularly well suited to simulate light field dynamics and propagation in finite photonic crystal defect structures like nanocavities. Photonic band structures and spectra can be obtained via Fourier transformation of the time-dependent simulation data. The FDTD method therefore directly complements spectral methods in photonic band structure calculation and makes it an important tool for photonic band structure physics and engineering. This chapter summarizes the basic concepts of FDTD with respect to its application on photonic crystal simulations, including the calculations of band diagrams, equi-frequency contours, and several cavity characteristics such as resonant frequencies, field distributions, and Q factor of defect modes in photonic crystal nanocavities.

3.1 The Yee algorithm

FDTD method [64] is based on a discretization of the Maxwell's time dependent curl equations, i.e., Eq. (2.1) and (2.2), for both the \vec{E} and \vec{H} fields. A schematic shown in Fig. 3.1 corresponds to the Yee's algorithm, which represents positions in space of the \vec{E} - and \vec{H} -field vector components in a way what every \vec{E} component is surrounded by four circulating \vec{H} components and every \vec{H} component is surrounded by four circulating \vec{E} components, respectively. All field components are updated at discrete timesteps Δt in a leapfrog manner: At times $t = (n+1/2)\Delta t$ the new \vec{E} field components are calculated using the spatial derivatives

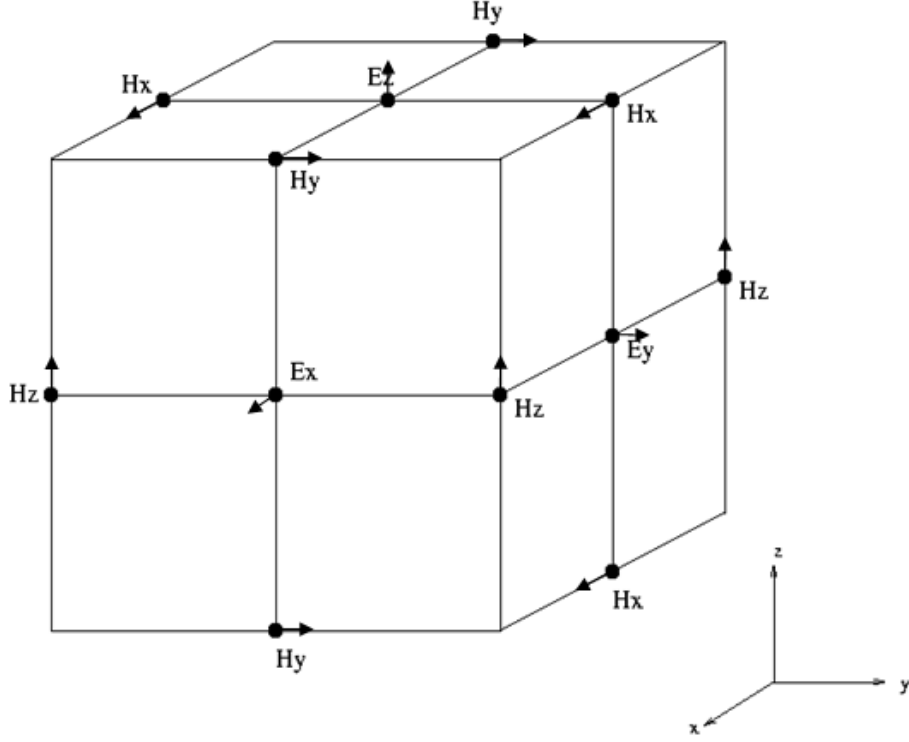


Figure 3.1 Positions of field components using Yee's cell.

of the surrounding \vec{H} vectors at times $t = n\Delta t$ and the former electric field at time $t = (n-1/2)\Delta t$, while at times $t = (n+1)\Delta t$ the new \vec{H} field components are calculated using the spatial derivatives of the surrounding \vec{E} vectors at times $t = (n+1/2)\Delta t$ and the former magnetic field at time $t = n\Delta t$. A Cartesian spatial grid is defined with increments Δx , Δy , and Δz . Δt is a time increment. Any field u of space (i,j,k) and time t is evaluated at a discrete point in space and time as:

$$u_{i,j,k}^n = u(i\Delta x, j\Delta y, k\Delta z, n\Delta t) \quad (3.1)$$

where n defines the point in time. The partial derivatives in the discretized system can be written as

$$\frac{\partial u}{\partial x}(i\Delta x, j\Delta y, k\Delta z, n\Delta t) = \frac{u_{i+1/2,j,k}^n - u_{i-1/2,j,k}^n}{\Delta x} \quad (3.2)$$

Applying Eq. (3.2) to Maxwell's curl equations, six finite-difference equations for each of the electromagnetic fields are then solved and shown as [93]:

$$E_x \Big|_{i,j+1/2,k+1/2}^{n+1/2} = E_x \Big|_{i,j+1/2,k+1/2}^{n-1/2} + \frac{\Delta t}{\mathcal{E}_{i,j+1/2,k+1/2}} \left[\frac{H_z \Big|_{i,j+1,k+1/2}^n - H_z \Big|_{i,j,k+1/2}^n}{\Delta y} - \frac{H_y \Big|_{i,j+1/2,k+1}^n - H_y \Big|_{i,j+1/2,k}^n}{\Delta z} \right] \quad (3.3)$$

$$E_y \Big|_{i-1/2,j+1,k+1/2}^{n+1/2} = E_y \Big|_{i-1/2,j+1,k+1/2}^{n-1/2} + \frac{\Delta t}{\mathcal{E}_{i-1/2,j+1,k+1/2}} \left[\frac{H_x \Big|_{i-1/2,j+1,k+1}^n - H_x \Big|_{i-1/2,j+1,k}^n}{\Delta z} - \frac{H_z \Big|_{i,j+1,k+1/2}^n - H_z \Big|_{i-1,j+1,k+1/2}^n}{\Delta x} \right] \quad (3.4)$$

$$E_z \Big|_{i-1/2,j+1/2,k+1}^{n+1/2} = E_z \Big|_{i-1/2,j+1/2,k+1}^{n-1/2} + \frac{\Delta t}{\mathcal{E}_{i-1/2,j+1/2,k+1}} \left[\frac{H_y \Big|_{i,j+1/2,k+1}^n - H_y \Big|_{i-1,j+1/2,k+1}^n}{\Delta x} - \frac{H_x \Big|_{i-1/2,j+1,k+1}^n - H_x \Big|_{i-1/2,j,k+1}^n}{\Delta y} \right] \quad (3.5)$$

$$H_x \Big|_{i-1/2,j+1,k+1}^{n+1} = H_x \Big|_{i-1/2,j+1,k+1}^n + \frac{\Delta t}{\mu_0} \left[\frac{E_y \Big|_{i-1/2,j+1,k+3/2}^{n+1/2} - E_y \Big|_{i-1/2,j+1,k+1/2}^{n+1/2}}{\Delta z} - \frac{E_z \Big|_{i-1/2,j+3/2,k+1}^{n+1/2} - E_z \Big|_{i-1/2,j+1/2,k+1}^{n+1/2}}{\Delta y} \right] \quad (3.6)$$

$$H_y \Big|_{i,j+1/2,k+1}^{n+1} = H_y \Big|_{i,j+1/2,k+1}^n + \frac{\Delta t}{\mu_0} \left[\frac{E_z \Big|_{i+1/2,j+1/2,k+1}^{n+1/2} - E_z \Big|_{i-1/2,j+1/2,k+1}^{n+1/2}}{\Delta x} - \frac{E_x \Big|_{i,j+1/2,k+3/2}^{n+1/2} - E_x \Big|_{i,j+1/2,k+1/2}^{n+1/2}}{\Delta z} \right] \quad (3.7)$$

$$H_z \Big|_{i,j+1,k+1/2}^{n+1} = H_z \Big|_{i,j+1,k+1/2}^n + \frac{\Delta t}{\mu_0} \left[\frac{E_x \Big|_{i,j+3/2,k+1/2}^{n+1/2} - E_x \Big|_{i,j+1/2,k+1/2}^{n+1/2}}{\Delta y} - \frac{E_y \Big|_{i+1/2,j+1,k+1/2}^{n+1/2} - E_y \Big|_{i-1/2,j+1,k+1/2}^{n+1/2}}{\Delta x} \right] \quad (3.8)$$

Numerical instability of the Yee algorithm with a rectangular grid occurs for

$$\Delta t > \frac{1}{c_0 \sqrt{\frac{1}{(\Delta x)^2} + \frac{1}{(\Delta y)^2} + \frac{1}{(\Delta z)^2}}} \quad (3.9)$$

where c_0 is the velocity of light in vacuum [93]. Considering the case of a three-dimensional cubic-cell space lattice with $\Delta x = \Delta y = \Delta z = \Delta$ which we are exploiting, Eq. (3.9) becomes

$$\Delta t > \frac{\Delta}{c_0 \sqrt{3}} \quad (3.10)$$

Here we set the Δt to be $\Delta/(2c_0)$ to assure the stability of the method.

3.2 Boundary conditions

As for FDTD all field components are updated in every timestep, the whole amount of spatial components needs to be stored in the computational memory. Unfortunately no computer can store an unlimited amount of data. Therefore, a computational domain must be limited in size, but large enough to enclose the structure of interest. As a result, it is necessary to apply suitable boundary conditions the edges of the computational domain to simulate the behavior and to calculate the spatial derivatives at the edges. In this thesis, two types of boundary conditions have been exploited depending on the calculations. Absorbing boundary conditions are used to calculate a finite structure, such as photonic crystals with defects, in which the perfect periodicity is broken. On the other hand, periodic boundary condition is used to calculate the fields in the infinitely extended periodic system, such as a calculation of photonic band structure.

3.2.1 Absorbing boundary condition

When defects are present or introduced to generate a cavity the periodicity of the perfect photonic crystal is no longer available and one has to resort to open boundaries. In order to obtain efficient and accurate solution of electromagnetic waves as if the computational domain is unbounded and stretches to the infinity, the perfectly matched layer (PML) backed by perfect electric conductor must be introduced at all outer boundaries as a nonreflecting absorber [94]. The basic computational domain is embedded in a perfectly matched additional medium which

is just a half of lattice thick as shown in Fig. 3.2. The yellow cubic is a three-dimensional computational domain, while the gray regions are the PML layers. In the PML medium, each component of the electromagnetic field is split into two parts yielding 12 subcomponents denoted as E_{xy} , E_{xz} , E_{yz} , E_{yx} , E_{zx} , H_{xy} , H_{xz} , H_{yz} , H_{yx} , H_{zx} , H_{zy} , and the Maxwell equations are replaced by 12 equations,

$$\varepsilon \frac{\partial E_{xy}}{\partial t} + \sigma_y E_{xy} = \frac{\partial(H_{zx} + H_{zy})}{\partial y} \quad (3.11)$$

$$\varepsilon \frac{\partial E_{xz}}{\partial t} + \sigma_z E_{xz} = -\frac{\partial(H_{yz} + H_{yx})}{\partial z} \quad (3.12)$$

$$\varepsilon \frac{\partial E_{yz}}{\partial t} + \sigma_z E_{yz} = \frac{\partial(H_{xy} + H_{xz})}{\partial z} \quad (3.13)$$

$$\varepsilon \frac{\partial E_{yx}}{\partial t} + \sigma_x E_{yx} = -\frac{\partial(H_{zx} + H_{zy})}{\partial x} \quad (3.14)$$

$$\varepsilon \frac{\partial E_{zx}}{\partial t} + \sigma_x E_{zx} = \frac{\partial(H_{yz} + H_{yx})}{\partial x} \quad (3.15)$$

$$\varepsilon \frac{\partial E_{zy}}{\partial t} + \sigma_y E_{zy} = -\frac{\partial(H_{xy} + H_{xz})}{\partial y} \quad (3.16)$$

$$\mu \frac{\partial H_{xy}}{\partial t} + \sigma_y^* H_{xy} = -\frac{\partial(E_{zx} + E_{zy})}{\partial y} \quad (3.17)$$

$$\mu \frac{\partial H_{xz}}{\partial t} + \sigma_z^* H_{xz} = \frac{\partial(E_{yz} + E_{yx})}{\partial z} \quad (3.18)$$

$$\mu \frac{\partial H_{yz}}{\partial t} + \sigma_z^* H_{yz} = -\frac{\partial(E_{xy} + E_{xz})}{\partial z} \quad (3.19)$$

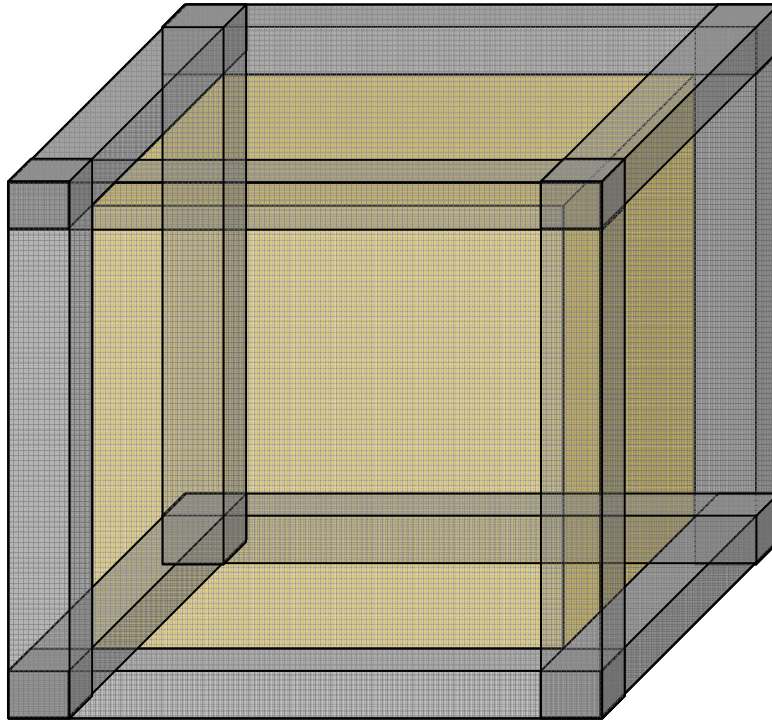


Figure 3.2 Three-dimensional computational domain (yellow) bounded by PML layers (gray).

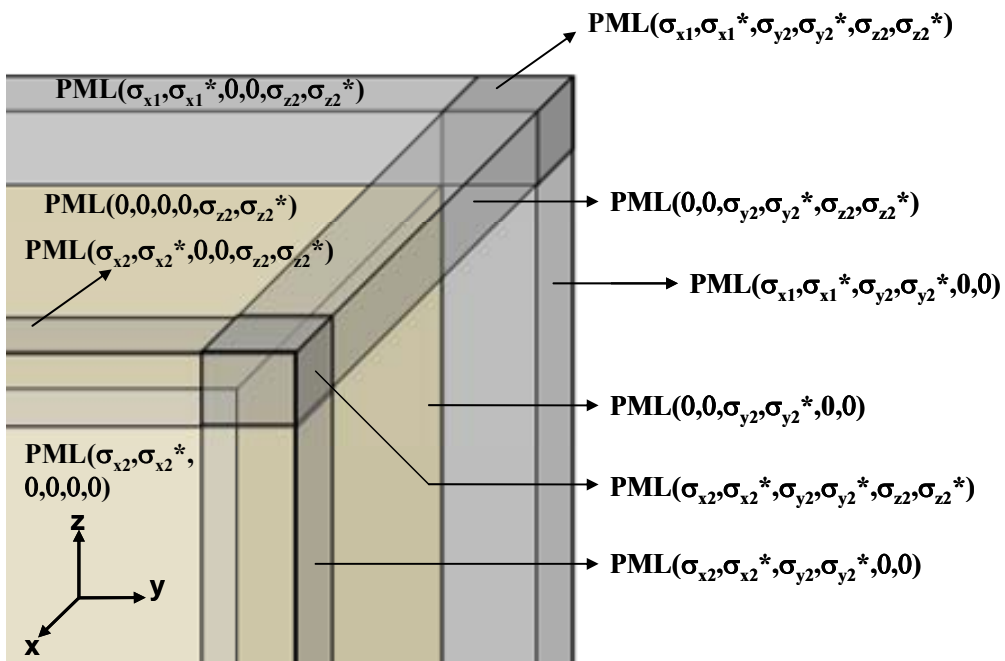


Figure 3.3 Upper right part of a computational domain surrounded by PML layers.

$$\mu \frac{\partial H_{yx}}{\partial t} + \sigma_x^* H_{yx} = \frac{\partial(E_{zx} + E_{zy})}{\partial x} \quad (3.20)$$

$$\mu \frac{\partial H_{zx}}{\partial t} + \sigma_x^* H_{zx} = -\frac{\partial(E_{yz} + E_{yx})}{\partial x} \quad (3.21)$$

$$\mu \frac{\partial H_{zy}}{\partial t} + \sigma_y^* H_{zy} = \frac{\partial(E_{xy} + E_{xz})}{\partial y}, \quad (3.22)$$

where the parameters $(\sigma_x, \sigma_y, \sigma_z, \sigma_x^*, \sigma_y^*, \sigma_z^*)$ are homogeneous to electric and magnetic conductivities.

Numerical implementation of the PML layer in a three-dimensional (3D) FDTD domain is straightforward. In the inner vacuum (the computational domain), the finite-difference equations are the usual discretizations of the Maxwell's equations derived in Eq. (3.3)-(3.8). In the PML layer, there are 12 subcomponents expressed in Eq. (3.11)-(3.22) to be computed in place of the six components. The Yee's grid is unchanged, the only change is that two subcomponents are computed at each point of the grid, i.e., E_{xy} and E_{xz} at E_x point. For instance, E_{xy} is computed by the equation derived from Eq. (3.11),

$$E_{xy} \Big|_{i+1/2, j, k}^{n+1} = e^{-\sigma_{y, i+1/2, j, k} \Delta t / \epsilon} E_{xy} \Big|_{i+1/2, j, k}^n + \frac{1 - e^{-\sigma_{y, i+1/2, j, k} \Delta t / \epsilon}}{\sigma_{y, i+1/2, j, k} \Delta y} \cdot \left[H_{zx} \Big|_{i+1/2, j+1/2, k}^{n+1/2} + H_{zy} \Big|_{i+1/2, j+1/2, k}^{n+1/2} - H_{zx} \Big|_{i+1/2, j-1/2, k}^{n+1/2} - H_{zy} \Big|_{i+1/2, j-1/2, k}^{n+1/2} \right] \quad (3.23)$$

where σ_y depends on the location in the layer. In the six sides of the domain, the absorbing media are matched PML media of transverse conductivities equal to zero. In the twelve edges, the conductivities are selected in such a way that the transverse conductivities are equal at the interfaces located between edge media and side media. This is obtained by means of two conductivities equal to zero and the other four equal to the conductivities of the adjacent side media, as shown in Fig. 3.3. In the eight corners of the domain, the conductivities are chosen equal to those of the adjacent edges, so that the transverse conductivities are equal at the interfaces between edge layers and corner layers. Therefore, the reflection equals zero from all the edge-corner interfaces in principle. However, due to the discretization of the PML equations, a

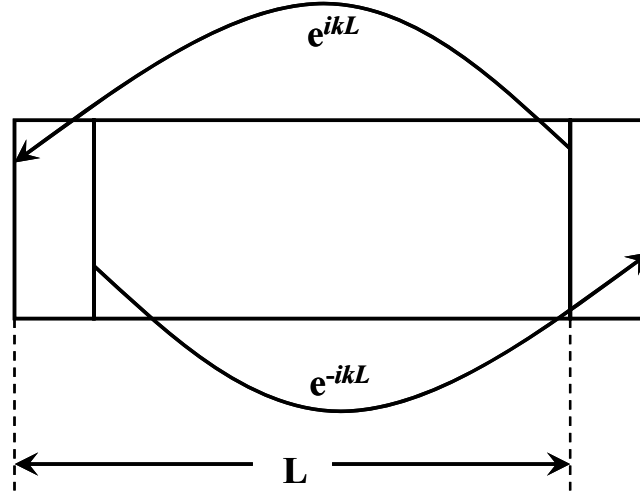


Figure 3.4 Lower and upper bound field values copied to the position next to each other by shifting the phase back and forth by $k \cdot L$.

certain amount of numerical reflection occurs from sharp variations of conductivities at the interfaces. In order to reduce this reflection the conductivities must be increased from a small value in the vacuum-layer interfaces to a great value on the outer boundaries.

3.2.2 Periodic boundary condition

Although a computational domain is bounded to be finite, it is also possible to simulate infinite structures as long as they are periodic. The Bloch-Floquet discussed in Section 2.1 is then used.

$$\vec{E}(\vec{r} + \vec{R}) = \vec{E}(\vec{r})e^{i\vec{k} \cdot \vec{R}} \text{ and } \vec{H}(\vec{r} + \vec{R}) = \vec{H}(\vec{r})e^{i\vec{k} \cdot \vec{R}} \quad (3.24)$$

In a simulation the boundary values of the fields are exchanged as illustrated in Fig. 3.4, where bound field values are copied to the position next to each other by shifting the phase back and forth by $k \cdot L$ (L is length of the cell). It is obvious that the shift in phase requires complex field values. To implement this in FDTD, the computational domain is chosen to be one and two unit cells of the periodic structure in the case of the calculation of triangular and square photonic crystal lattices. Figure 3.5 shows a top view of the square and triangular photonic crystal lattices indicating unit cells of the photonic crystals with boundary conditions. These structures are periodic in two dimensions, the in-plane direction, however their third dimension lack of translational

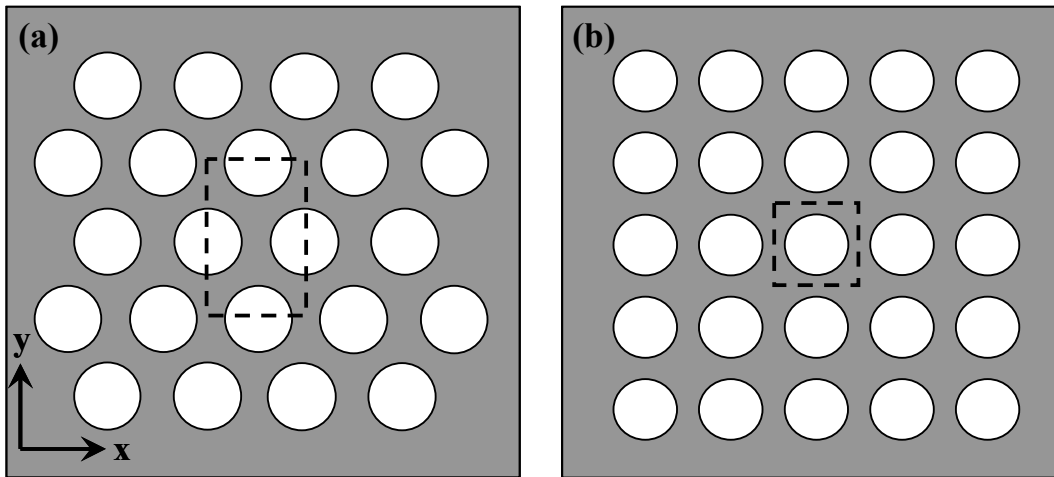


Figure 3.5 Top view of the photonic crystal slabs with (a) triangular lattice and (b) square lattice of air holes. Dotted squares indicate unit cells of each structure with periodic boundary condition.

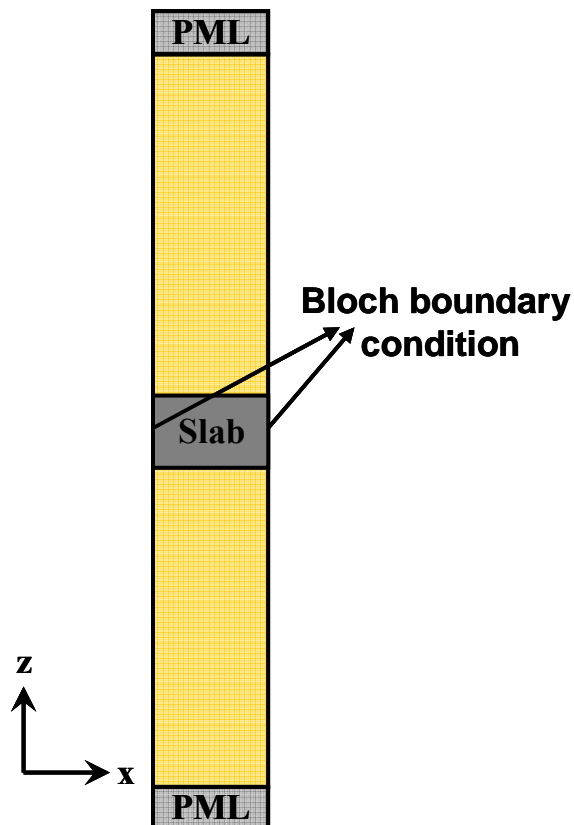


Figure 3.6 Cross-section view of the unit cell showing a mixing of boundary conditions used to calculate band structures. The domain is wrapped by Bloch boundary condition in the in-plane direction and PML in the vertical direction

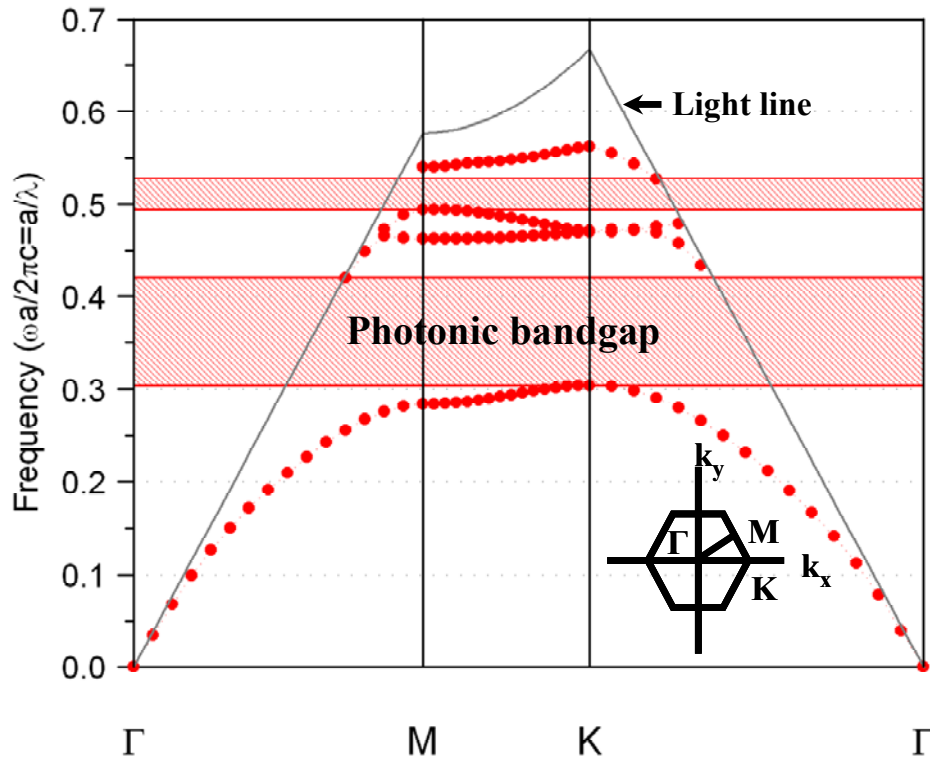


Figure 3.7 Band diagram for the air-bridge slab structure with $r = 0.40a$ and $d = 0.60a$. The insets show its first Brillouin zone and corresponding high-symmetry directions.

symmetry. As a result, the periodic boundary condition cannot be applied to the edge of computational domain in the vertical direction. In this case, the PML is introduced to absorb the waves propagating into the vertical direction as shown in Fig. 3.6.

3.3 FDTD-simulations of photonic crystals

In this subsection, methods to calculate various characteristics of photonic crystals, such as photonic band structures, equi-frequency contours, cavity's resonance frequencies, field distributions, quality factor, and etc., are shown.

3.3.1 Band structures and equi-frequency contours

The starting point for the investigation of any photonic crystal devices is the calculation of a dispersion diagram for the modes supported in the structure. Figure 3.7 shows a band diagram for the case of a triangular lattice photonic crystal slab. The band diagram is calculated only along the high-symmetry directions in the first Brillouin zone for the first four bands. The light line is also represented. In some

applications, for example, study of coupling between cavity modes and guided modes in momentum space, which will be realized in next Chapter, it is necessary to calculate not only along the high-symmetry directions in the first Brillouin zone but the full band diagram for all k -vectors in the first Brillouin zone. Figure 3.8 shows such a dispersion diagram for the first four bands of the structure with the same parameters as that in Fig. 3.7 for all k -vectors in the first Brillouin zone. The plot indicates a large gap between the first two bands. The light cone is represented by an unshaded area. It is obvious that the band diagram shown in Fig. 3.7 is a projected plot of the full band along the high-symmetry directions in the first Brillouin zone. For quantitative analysis, it is better to make equi-frequency contour plots, which are projections of the full band diagram cut at each frequency. An example is shown in Fig. 3.8, which are equi-frequency contours of the first band at each frequency with an increment of 0.02. These plots are very useful for the analysis of the coupling of multiple modes at a frequency because they contain information of the modes at the frequency in the momentum space.

3.3.2 Cavity characteristics

By using the 3D FDTD calculation, resonant frequencies, field distributions, quality (Q) factor, mode volume of defect modes in photonic crystal cavities can be evaluated. In all calculations, lattice constant (a) is set to be equal to 20 space steps ($20 \cdot \Delta x$), where $\Delta x = \Delta y = \Delta z$ (cubic lattice). The time step Δt is chosen to be equal to $(\Delta x/2c)$, where c is speed of light in free space. These values of steps ensure numerical stability as previously discussed. To obtain field distributions and Q factor of the defect modes, resonant frequencies of those modes must be calculated first. In order to do this, a pulse source with a Gaussian-shaped bandpass is excited in the at the point of low symmetry in the vicinity of the cavity, then the fields are subsequently evolved in time. The frequency bandwidth of this pulse source is broad enough to cover the total modes of interest. The profile of the excitation source in frequency domain is illustrated in Fig. 3.10(a). The time evolution of the fields is recorded at a point of low symmetry, and is calculated by the fast Fourier transform to obtain the cavity mode spectra in normalized frequency unit. As shown in Fig. 3.10(b), which is an example for a point defect cavity in two-dimensional photonic crystal slab

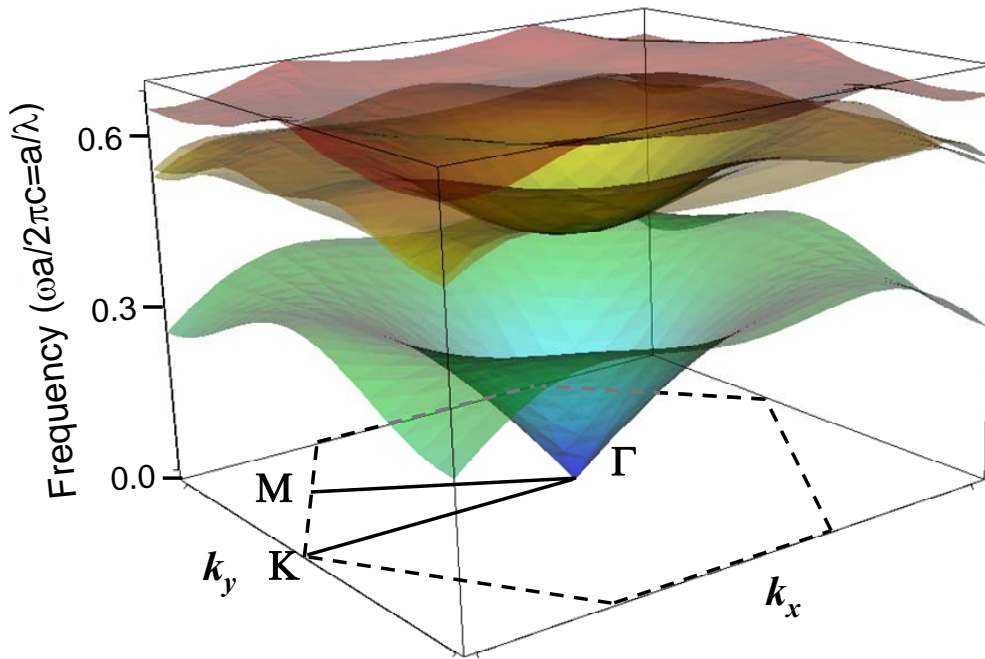


Figure 3.8 The band diagram for the first four bands for the air-bridge slab structure with $r = 0.40a$ and $d = 0.60a$, calculated for all k -vectors in the first Brillouin zone shown in dotted hexagon.

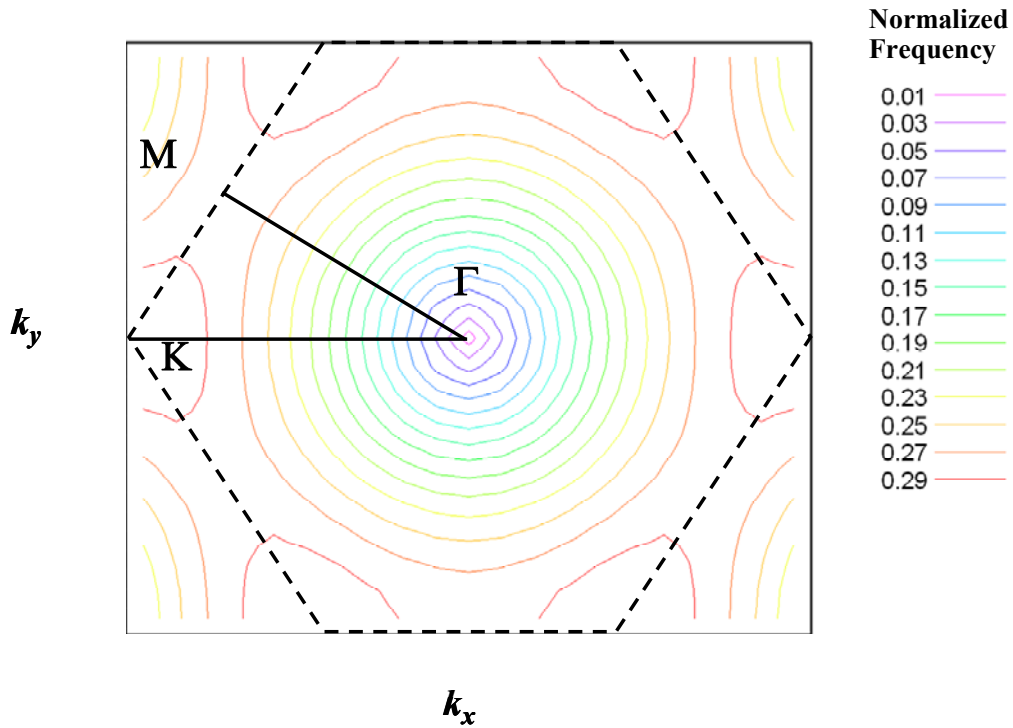


Figure 3.9 The equi-frequency contours for the first band. The step of increment of frequency is 0.02.

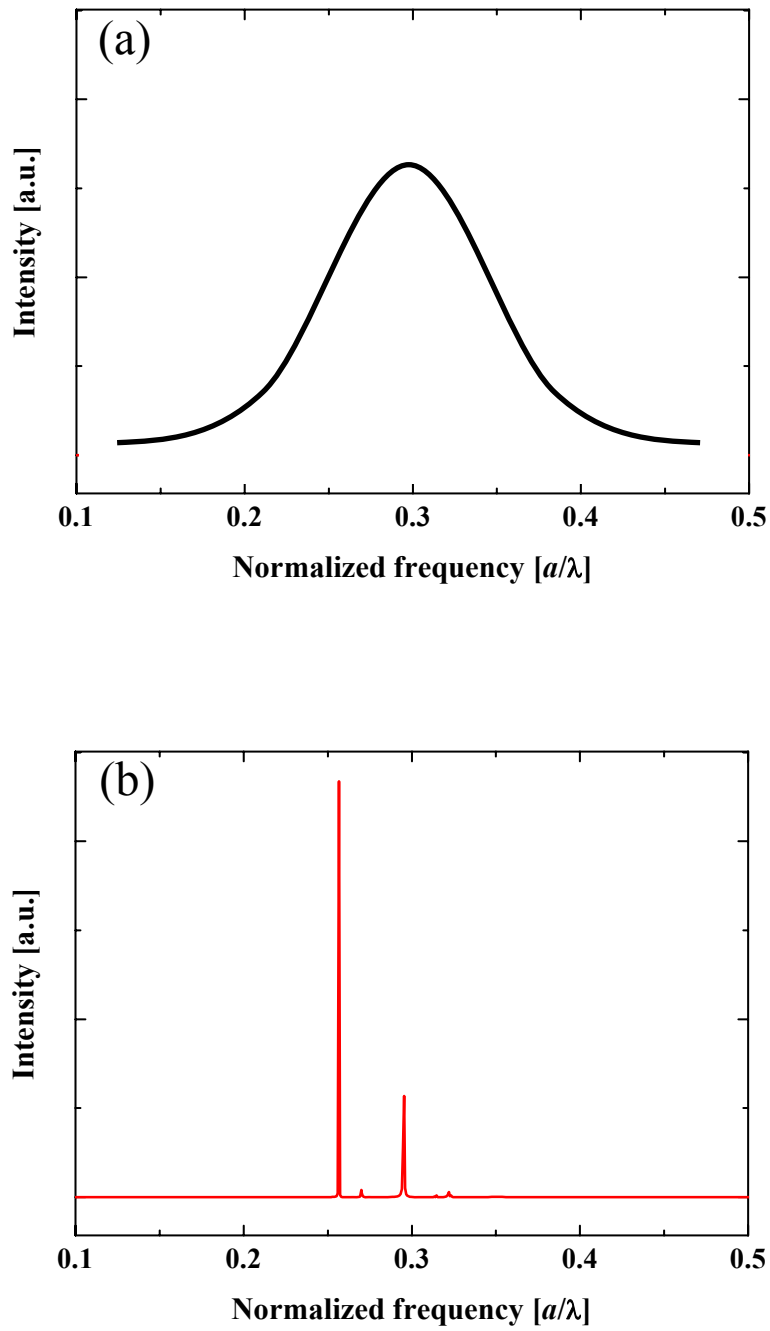


Figure 3.10 (a) Wide-band Gaussian-shaped excitation pulse shown in normalized frequency domain. (b) Spectra of cavity modes for a point defect photonic crystal obtained by Fourier transforming the time response of the cavity field.

there are many sharp peaks occurred within the bandwidth of the source. They are cavity modes. Then, another single pulse, which has the frequency bandwidth narrow enough to excite only one cavity mode of interest, is applied to the cavity. An example for one of the modes achieved in Fig. 3.10(b), is shown in Fig. 3.11. The time dependence of the intensity shows the excitation pulse and then exponential decay of the energy inside the cavity after turning off the excitation pulse.

Snap-shot of each time-varying field components can be recorded to illustrate the point-in-time view of field distributions of the resonant mode. The field profile can be viewed in any arbitrary cut plane of the computational model. The Q factor is obtained by measuring the exponential decay of electromagnetic energy after turning off the oscillation of the source [95]:

$$U(t) = U(0) \exp(-t / \tau_{ph}) = U(0) \exp[-(\omega_0 t) / Q] \quad (3.25)$$

where $U(t)$ is the electromagnetic energy in the mode at time t , and ω_0 is the frequency of the cavity mode. The total Q factor is evaluated by measuring the slope of the logarithm plot of this energy-time relation. In fact, the Q factor can also be calculated by measuring spectrum linewidth of the cavity mode. However, the value calculated by this method is not accurate limited by the resolution in frequency domain of the calculations. As discussed in Section 2.6 in the case of two-dimensional photonic crystal slab cavity, in order to efficiently determine what factors are limiting the Q factor of the defect modes, another calculation method is adopted to separate out losses into different directions, vertical and in-plane directions. The vertical and in-plane losses are caused by leaky modes above the light line and imperfection of Bragg reflection resulted from lack of number of photonic crystal layers that surround the defect region or cavity modes not locating inside the photonic bandgap, respectively. The total radiating power P can be divided in to vertical radiation P_{\perp} and in-plane radiation $P_{//}$. The total radiating power $P = P_{\perp} + P_{//}$ is related to the electromagnetic energy $U(t)$ by [95]:

$$P = -\frac{dU}{dt} = \frac{\omega_0 U}{Q} \quad (3.26)$$

where ω_0 is the angular frequency of the cavity mode. As a result, the total Q factor can be separated into vertical and in-plane components, denoted as Q_{\perp} and $Q_{//}$, respectively, and satisfy the following relation:

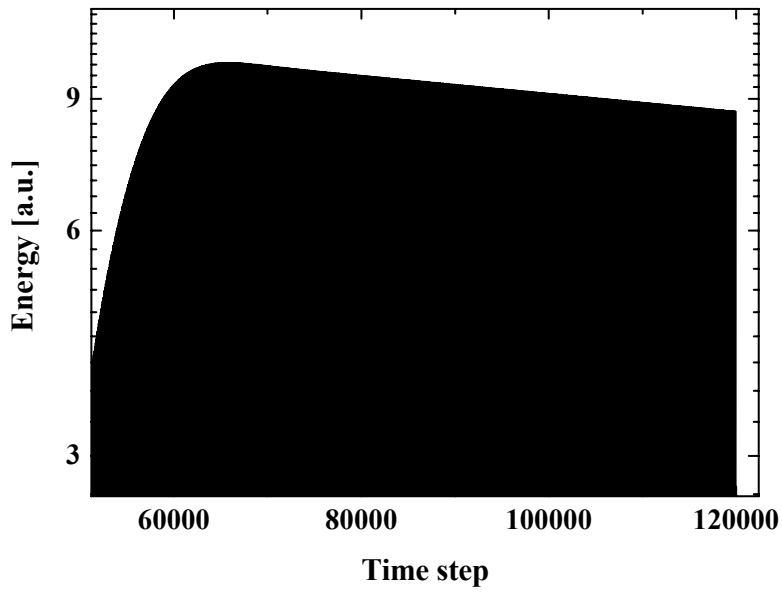


Figure 3.11 Decay of the electromagnetic intensity stored in the photonic crystal defect cavity. After the initial excitation pulse, the exponential decay of the cavity modes sets in.

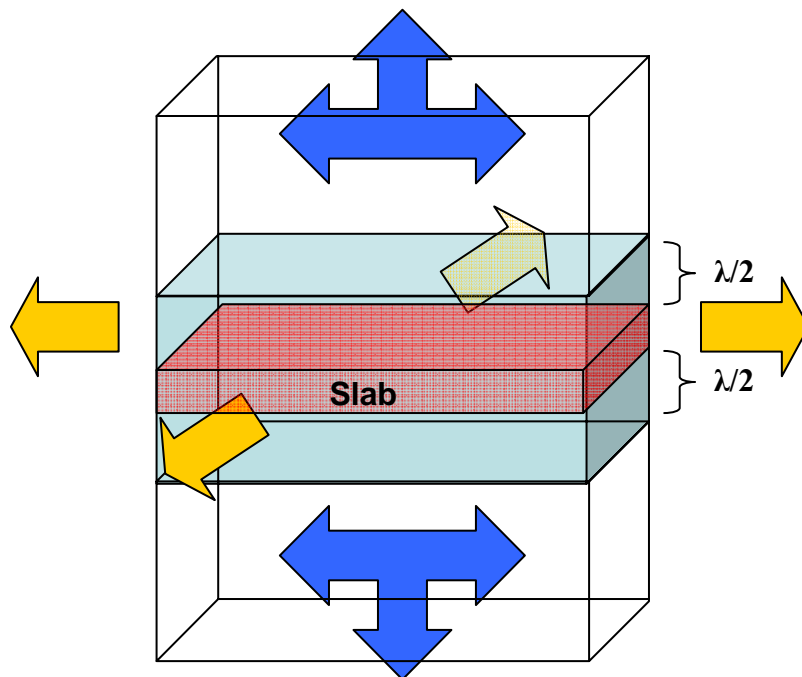


Figure 3.12 Schematic illustration of the computational domain for a two-dimensional photonic crystal slab cavity with separation of power-collecting boundaries at a half-wavelength from the slab. Yellow arrows indicate the energy losses into the in-plane direction. Blue arrows define the energy losses into radiation modes.

$$\frac{1}{Q_{total}} = \frac{1}{Q_{\perp}} + \frac{1}{Q_{//}} \quad (3.27)$$

Combine the relations in Eq. (3.26) and Eq. (3.27), the Q factor in each direction is then given by [96]:

$$Q_{\perp, //} = \frac{\omega_0 U}{P_{\perp, //}} \quad (3.28)$$

In practical calculation, these effective Q values are calculated by spatial separation of the power radiated by the mode that is absorbed in the outer boundary. The in-plane radiation $P_{//}$ is defined as the Poynting vectors that are absorbed into the sidewalls that extend from approximately a half-wavelength above the waveguide to a half-wavelength below the waveguide to separate the guiding losses from the radiation losses as shown in the illustration in Fig. 3.12. The vertical radiation P_{\perp} is defined as the Poynting vector that are absorbed into the rest of the boundaries, where the radiating power can be considered as radiation losses. With this separation of Q , the factors that limit the performance of the cavity can be understood. A proper design can then applied to improve the performance. However, this method of separation of Q is not applicable to three-dimensional structures, because in this case light is confined by Bragg reflection in all directions. As a result, proper separation boundaries cannot be simply determined.

Purcell factor [97], which indicates strength of interaction between electromagnetic field and emitters inside a cavity, and mode volume [98] are calculated using the following definition:

$$F_p = \frac{3Q}{4\pi^2 V_{eff}} \left(\frac{\lambda}{n} \right)^3 \quad (3.29)$$

$$V_{eff} = \frac{\iiint \varepsilon(\vec{r}) |\vec{E}(\vec{r})|^2 dV}{\max[\varepsilon(\vec{r}) |\vec{E}(\vec{r})|^2]} , \quad (3.30)$$

where $\varepsilon(\vec{r})$ is the dielectric constant at position \vec{r} , V is a volume of the computational domain, and $\vec{E}(\vec{r})$ is the total electric field at position \vec{r} . In addition, the effective refractive index of photonic crystal structures is determined by taking the square root of the space-averaged dielectric constant [99]:

$$n_{eff} = \sqrt{\frac{\iiint \varepsilon(\vec{r}) |\vec{E}(\vec{r})|^2 dV}{\iiint |\vec{E}(\vec{r})|^2 dV}}, \quad (3.31)$$

In next Chapter, this value of effective refractive index will play an important role to partly explain the origin of strong confinement of light in the cavity after the closing of the photonic bandgap.

3.4 Summary

In this chapter, details of the calculation method based on the three-dimensional finite-difference time-domain method have been described. Two types of boundary conditions, perfectly matched layer and periodic boundary conditions, have been selected to bound the computational domain depending on the calculations to obtain efficient and accurate solution of electromagnetic waves. The applications of the 3D FDTD calculations to investigate photonic band structures, equi-frequency contours, cavity's resonance frequencies, field distributions, quality factor, mode volume, and effective refractive index have been shown. The computational methods described in this chapter will be applied to the calculation of all structures in the following chapters.

Chapter 4

High- Q Photonic Crystal Nanocavity after Closing of Photonic Bandgap with Optimal Slab Thickness

4.1 Introduction

As mentioned in Chapter 2, complete control of light in three dimensions can be achieved in three-dimensional photonic crystal, which possesses a three-dimensional band gap. However, fabricating such an ideal structure has still been a great challenge due to the requirement of highly-advanced structural designs as well as fabrication techniques. Therefore, most of research on photonic crystal has been focused on photonic crystal slab structure, which requires only relatively easy top-down fabrication process. In order to minimize out-of-plane scattering loss, a so-called air-bridge photonic crystal slab structure, which is the photonic perforating dielectric slab cladded with air, is one of the most promising structures. However, in air-bridge slab structure, there are only gaps for guided modes not for all modes. Therefore radiation losses, which correspond to the mode locating above the light line, in the vertical direction still exist. When a defect is introduced to the slab to form a nanocavity, the vertical radiation loss will limit the Q factor in the vertical direction. While the in-plane Q factor can be increased exponentially with the number of photonic crystal layers surrounding the defect region, the vertical Q factor limits the total Q factor to only low values [96]. This is one of the most important obstacles for photonic crystal slab nanocavities to achieve high-efficiency light sources such as low threshold lasers and single-photon emitters. Much research has been done to design the structures that can reduce the vertical radiation losses. Thanks to the flexibility in the

design of two-dimensional photonic crystal slab nanocavity, various designs of ultra-high Q nanocavities have already been succeeded [65-69,72,73]. A designed Q in the order of 10^7 - 10^8 has been recently achieved [72,73]. With the maturation of nanometer-size photonic crystal fabrication technology in past ten years, photonic crystal nanocavities with a Q factor of more than one million have been experimentally demonstrated [74,75]. However, most of designs of those structures are based on the modification of the defect structures, in which the high Q modes are very sensitive to their surrounding structural parameters, that is, these designs require a precise control of position and size of air holes in practical fabrication, in which the Q -factor significantly degrades when the structural parameters are deviated from their ideal setups [76,100] This lack of robustness to changes in the cavity geometry becomes a great difficulty to practically fabricate the device with quality as good as the simulation results. On the other hand, slab thickness, which is also a parameter of design, can be precisely controlled by using epitaxial growth techniques such as molecular beam epitaxy (MBE) or metal organic chemical vapour deposition (MOCVD). So far, slab thickness of photonic crystal slab structure is usually chosen in the order of half wavelength to ensure that PBG exists and to confine cavity modes strongly within the slab [60].

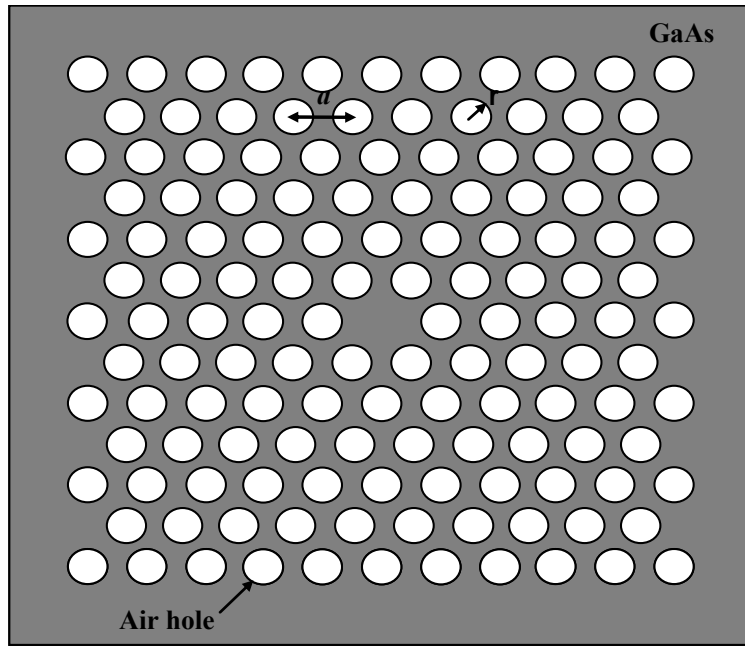
In this Chapter, a new approach to design high Q factor photonic crystal nanocavities by just simply changing slab thickness without modification of structural parameters of air holes surrounding the defect cavities is presented. Dependence of Q -factor of dipole modes in H1-defect nanocavity on slab thickness is numerically and experimentally investigated and found that high- Q can be obtained after closing of the photonic bandgap. These dipole modes in H1 cavity consist of two orthogonal polarized modes and are energetically degenerated, so the cavity possessing such modes can be applied to polarization entangled photon sources [101,102].

4.2 Structural parameters and defect modes

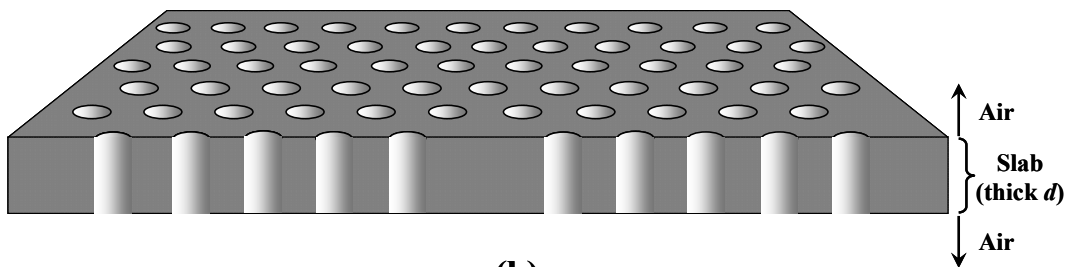
In this section, details of structural parameters exploited in the FDTD calculation and defect mode of interest are presented. The computational model of the design of the cavity is based on an air-bridge type photonic crystal slab, which is a dielectric slab thick d with refractive index of 3.4, corresponding to that of GaAs, cladded with air in both upper and lower sides. The photonic crystal geometry is a

triangular lattice of air holes with lattice constant a and radius of air hole r . The schematics of the calculation model are shown in Fig. 4.1. The calculation domain contains eleven air holes along the Γ - K direction. A defect, called a H1-defect, is formed by simply removing one air hole at the center as shown as a missing hole at the center. The defect cavity contains no modification in shape and position of the surrounding holes.

The H1-defect cavity in a triangular lattice photonic crystal slab is well-known to support doubly-degenerated dipole modes in a bandgap, in which Q factor, limited by the radiation losses, is only a few hundreds in the conventional structure with parameters $d = 0.50a$ and $r = 0.30a$ [59]. The defect mode of interest is the x -dipole mode [96], which is one of the doubly-degenerated dipole modes, and its field distributions of E_y component at the center of the slab is shown in Fig. 2(a). E_x -field distribution of the y -dipole mode is also depicted in Fig. 2(b). It can be seen that the two modes are polarized orthogonally to each other. In the FDTD calculation, a cubic lattice, in which size of grid cells in three dimensions are identical, is used as mentioned in Chapter 3.1. Therefore, the structure is not a completely perfect triangular lattice. As a result, anisotropy occurs in the x and y directions, which leads to splitting of the dipole degeneracy. The full-width at half-maximum (FWHM) of the emitter inside the cavity is ensured to be narrow enough to excite only the mode of interest when cavity Q and mode volume are calculated.



(a)



(b)

Figure 4.1 (a) Top-view and (b) schematic view of the H1-defect nanocavity in a two-dimensional photonic crystal. Circles represent air holes with refractive index of 1 etched into a slab of GaAs with refractive index of 3.4.

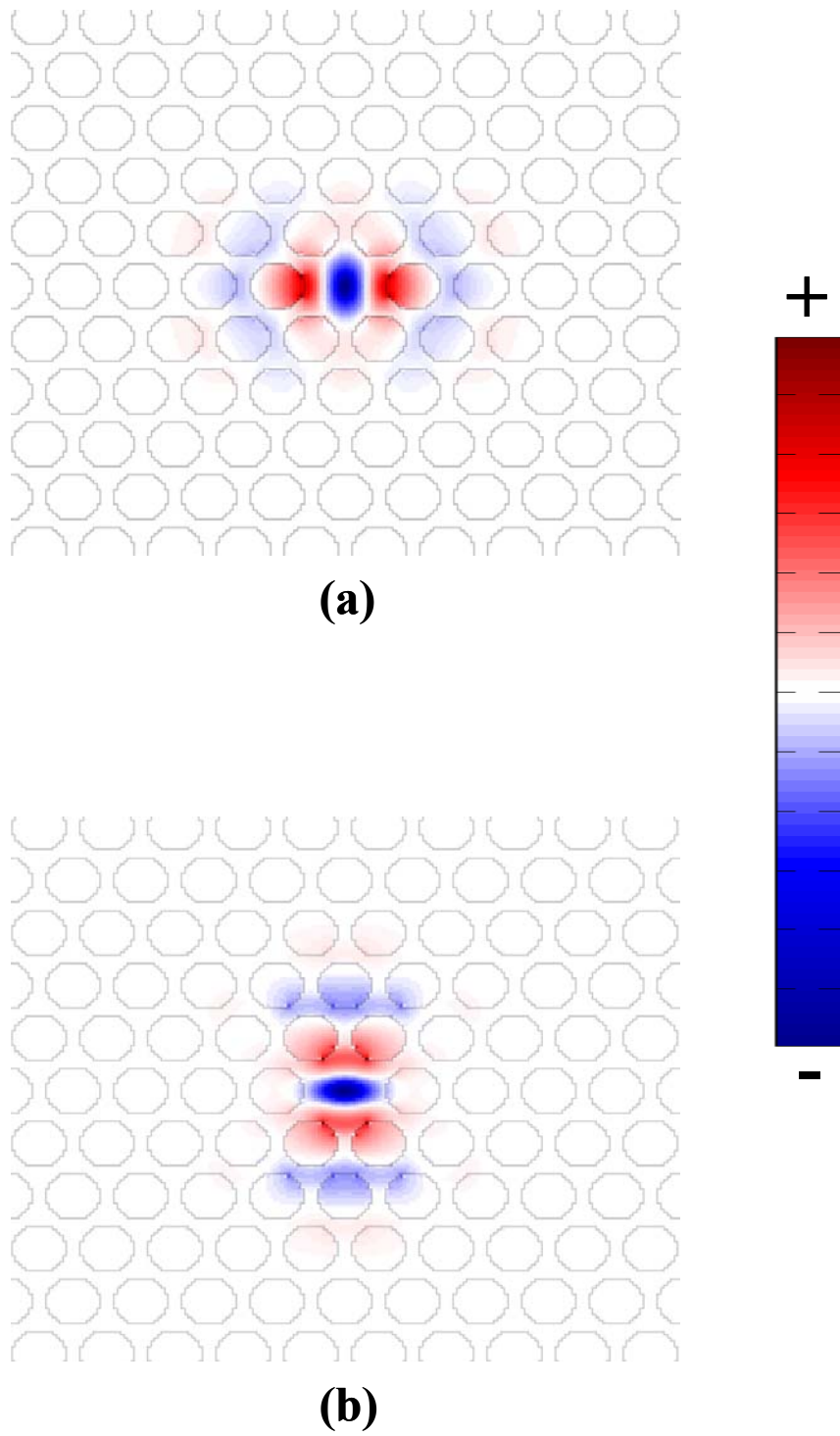
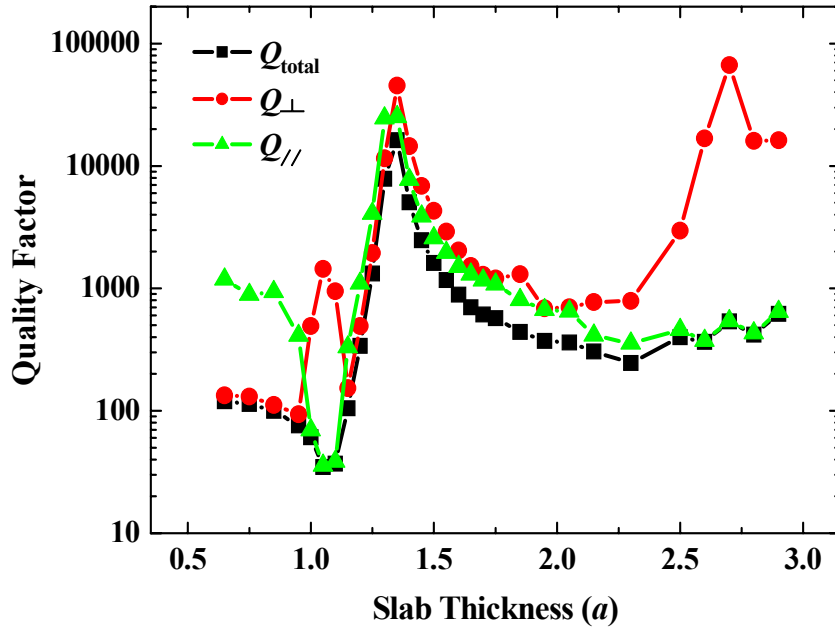


Figure 4.2 Field distributions at the center of the slab of (a) E_y component of x -dipole mode and (b) E_x component of y -dipole mode. The circular lines show boundaries of air holes.

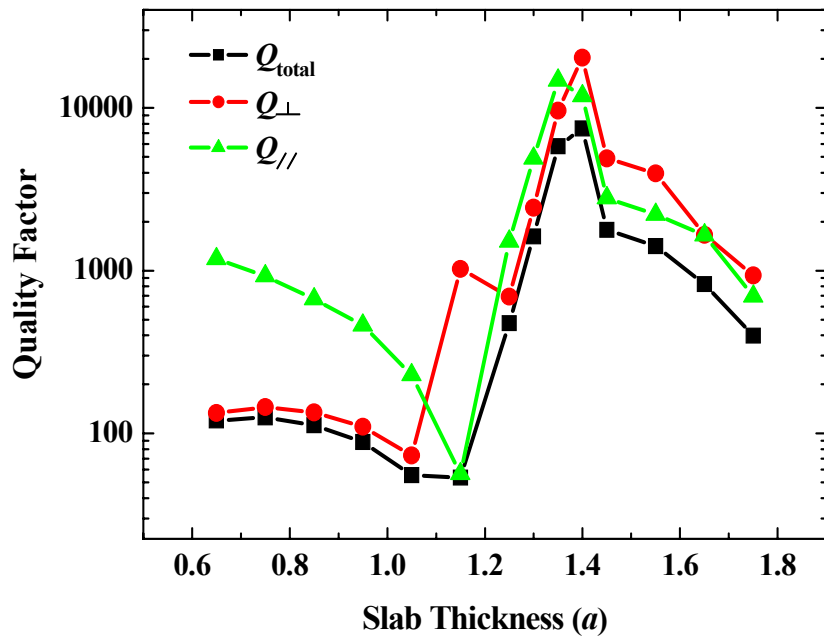
4.3 Increase of cavity Q of H1 dipole modes by optimizing slab thickness

Dependence of Q factor of the x -dipole mode on a wide range of slab thickness, from $0.65a$ to $2.90a$, for the air-bridge slab with radius of air holes $r = 0.40a$, is shown in Fig. 4.3(a). The results for the y -dipole mode are also shown in Fig. 4.3(b). Because the behavior of Q for both modes is in similar, only the x -dipole mode is discussed in this section. As seen in Fig. 4.3(a), the Q factor of the x -dipole mode is significantly improved by slightly increasing the slab thickness. The Q_{total} reaches the highest value up to 16,200 at the slab thickness $d = 1.35a$ with small mode volume $V_{\text{eff}} = 0.44(\lambda/n)^3$. Interestingly, such a high Q factor is obtained after the photonic bandgap for TE-like modes between the lowest two TE-like bands, denoted as 1st- and 2nd-guided band, is closed at $d = 1.20a$. Field distributions shown in Fig. 4.4 confirm that the cavity mode in the structure with $d = 1.35a$ is indeed more strongly confined within the cavity than that of the structure with conventional slab thickness ($d = 0.60a$). The Q_{total} was divided into two components, Q_{\parallel} and Q_{\perp} , in order to separately observe a behavior of the Q factor in each direction. Firstly, a tendency of Q -factor in a conventional range of slab thickness, before closing of the photonic bandgap, should be explained. The in-plane Q can be increased by increasing the number of air holes surrounding the cavity, however, the Q_{total} of dipole mode is limited by decay to the free space, and thus the Q_{total} is only a few hundreds. It gradually drops as the slab thickness increases resulted from the reduction of Q_{\parallel} due to the decrease in the photonic bandgap size [60]. It should be clarified that the peak of Q_{\perp} at the minimum value of Q_{total} and Q_{\parallel} has no physical significance. In that region, because of the coupling between the cavity mode and the 2nd-guided mode, the cavity mode mainly leaks into the slab guided mode. Therefore, the component of light that can radiate toward the vertical direction becomes very small, which unavoidably results in a large value of Q_{\perp} without any evidence of strong confinement of light in this direction due to the cavity.

After the gap is closed, both Q_{\perp} and Q_{\parallel} (and thus Q_{total}), increase together to their peaks at $d = 1.35a$ and then decrease when the slab thickness exceeds that value. Only Q_{\perp} significantly rises up again when the slab thickness keeps increasing and another maximum peak occurs at $d = 2.70a$. The increase of Q_{total} after closing of the

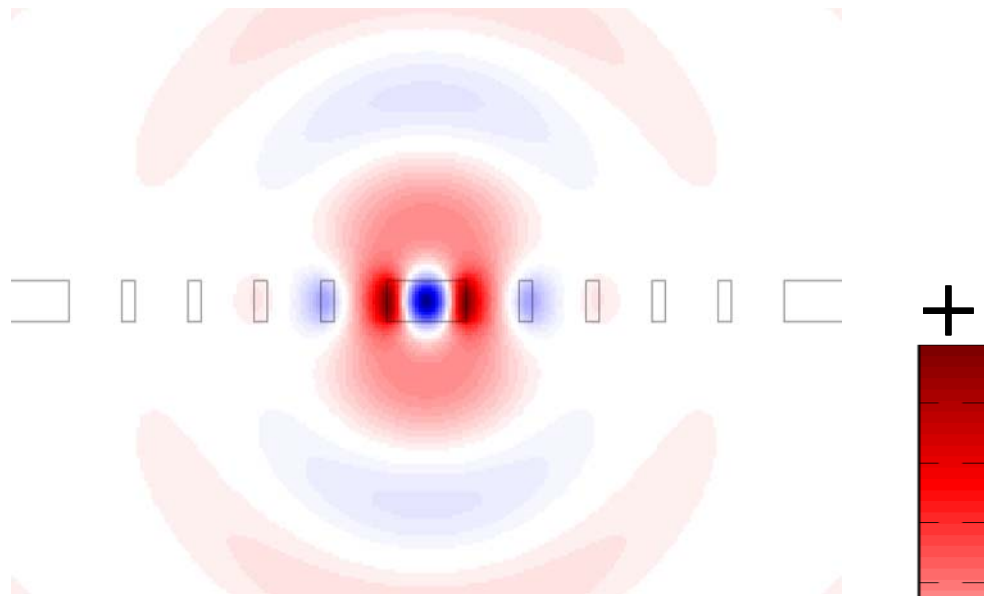


(a)

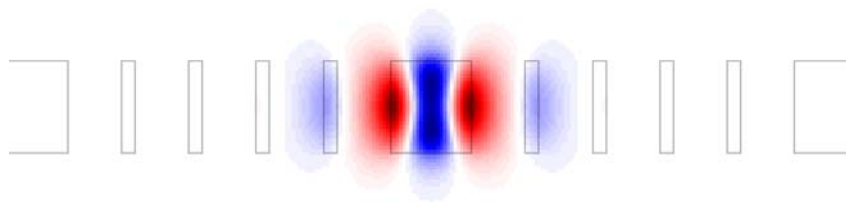


(b)

Figure 4.3 Dependence of Q factor on slab thickness for the (a) x -dipole and (b) modes in H1-defect cavity with $r = 0.40a$. The total Q factor (square), the vertical Q factor (circle) and the in-plane Q factor (triangle) are plotted separately. The photonic bandgap is closed when $d \geq 1.20a$.



(a)



(b)

Figure 4.4 Comparison of field distributions between the structures with (a) $d = 0.60a$ and (b) $d = 1.35a$. Both structures have $r = 0.40a$. The E_y -field profiles are shown in cross section at the center of the cavities along Γ - K direction.

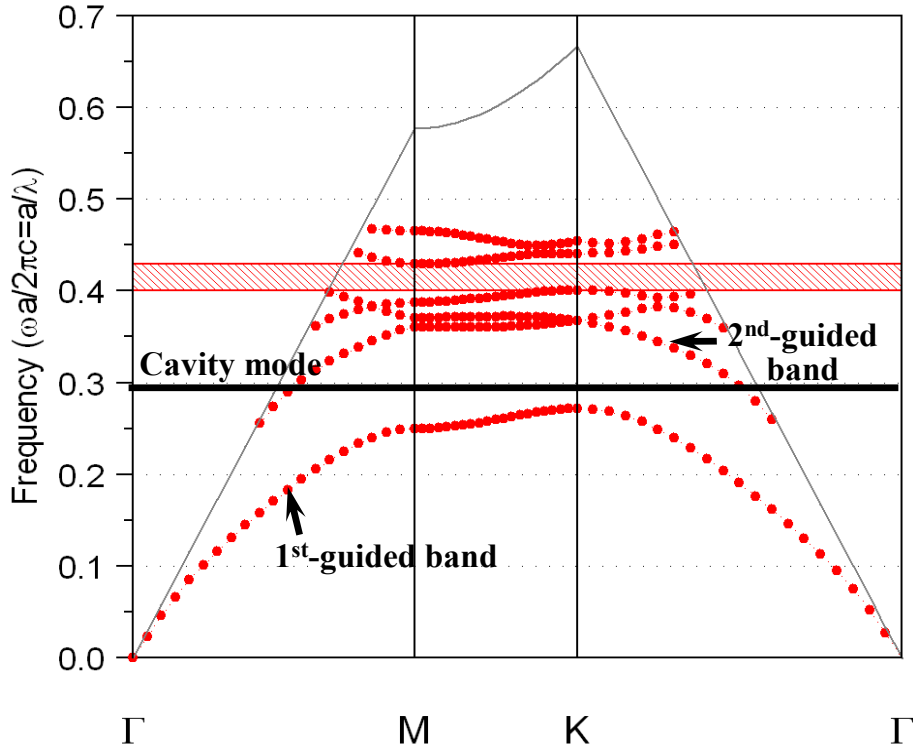


Figure 4.5 Band diagram for the structure with $d = 1.35a$ and $r = 0.40a$. The x-dipole mode with normalized frequency of 0.292 overlaps with the 2nd-guided mode.

PBG is unexpected because $Q_{//}$ is supposed to greatly drops limiting Q_{total} . The origin of the strong light confinement mechanisms at the optimized slab thickness in each direction is separately considered. In the vertical direction, there are two maximum peaks of Q_{\perp} at $d = 1.35a$ and $2.70a$. These values of slab thickness correspond to $\sim 1\lambda$ and 2λ , where the effective refractive indices of the structures were calculated to be 2.608 and 2.619, respectively, using Eq. (3.31). Therefore, the strong confinement mechanism in the vertical direction is due to the resonance of the cavity mode when the slab thickness is equal to a multiple of wavelength.

If the slab is thick enough, by more than $1.20a$, the 2nd-guided band falls below the lowest-order band edge and is responsible for destroying the photonic bandgap. As a result, the photonic bandgap effect cannot be used to explain the strong light confinement mechanism in the in-plane direction. Figure 4.5 shows a band diagram for the structure with $d = 1.35a$. The cavity mode in this structure has a normalized frequency of $a/\lambda = 0.292$, which is spectrally matched with the 2nd-guided mode near the light line. Furthermore, the cavity mode also has the same symmetry as

that of the guided mode, even symmetry about the center of the slab. If their wavevectors are additionally matched, they can be coupled with each other. In order to do that, coupling between the cavity mode and the guided mode was studied in the momentum space. The field distributions of the cavity mode in momentum space were obtained by directly taking the field distributions of the cavity mode in real space a two-dimensional spatial-Fourier transform. Figure 4.6(a) shows E_y -field distribution in momentum space for the x -dipole mode with $d = 1.35a$, which is the optimal slab thickness with high $Q_{//}$ of more than 30,000. That for the structure with $d = 1.75a$, which has low $Q_{//}$ of about 1,000, is also shown in Fig. 4.6(b) for comparison. For the guided mode, equi-frequency contour (EFC) of the 2nd-guided mode, which represents its distribution in the momentum space, at the same frequency as the cavity mode was calculated. The equi-frequency contours for both the structures with $d = 1.35a$ and $1.75a$ are in circular shape and are plotted as dotted circles in Fig. 4.6. For the optimal structure with $d = 1.35a$, the equi-frequency contour only overlaps with faint components of the cavity mode field, which leads to decoupling between the cavity mode and the 2nd-guided mode and thus high $Q_{//}$. In addition, amount of the momentum components that locates within the light line is very small, which is corresponding to small radiation losses into the vertical direction. This is consistent with the previous assumption that this structure has very high Q_{\perp} . In contrast, in the structure with $d = 1.75a$ with $Q_{//}$ of about 1,000, there are strong components of the field distribution that overlap with the equi-frequency contour of the 2nd-guided mode, especially at M point of the first Brillouin zone. As a result, the cavity mode is not strongly confined in the cavity but well guided through the slab. Amounts of overlap between the cavity mode and the equi-frequency contour of the 2nd-guided mode of each structure with the slab thickness from $1.20a$ to $1.75a$ are summarized in Fig. 4.7. These amounts of overlap were calculated by firstly normalizing the field distributions in momentum space and then taking them a line integral over the equi-frequency contour. As expected, the amounts of overlap show the opposite behavior to $Q_{//}$, while the minimum amount of overlap occurs at the slab thickness where the $Q_{//}$ is maximum. With these results, the origin of high $Q_{//}$ is concluded to be resulted from the decoupling between the cavity mode and the guided mode in the momentum space. Such a counter intuitive behavior of Q factor after closing of the photonic bandgap is also attainable in the y -dipole mode of the same cavity structure and experimental confirmations will be shown in next section.

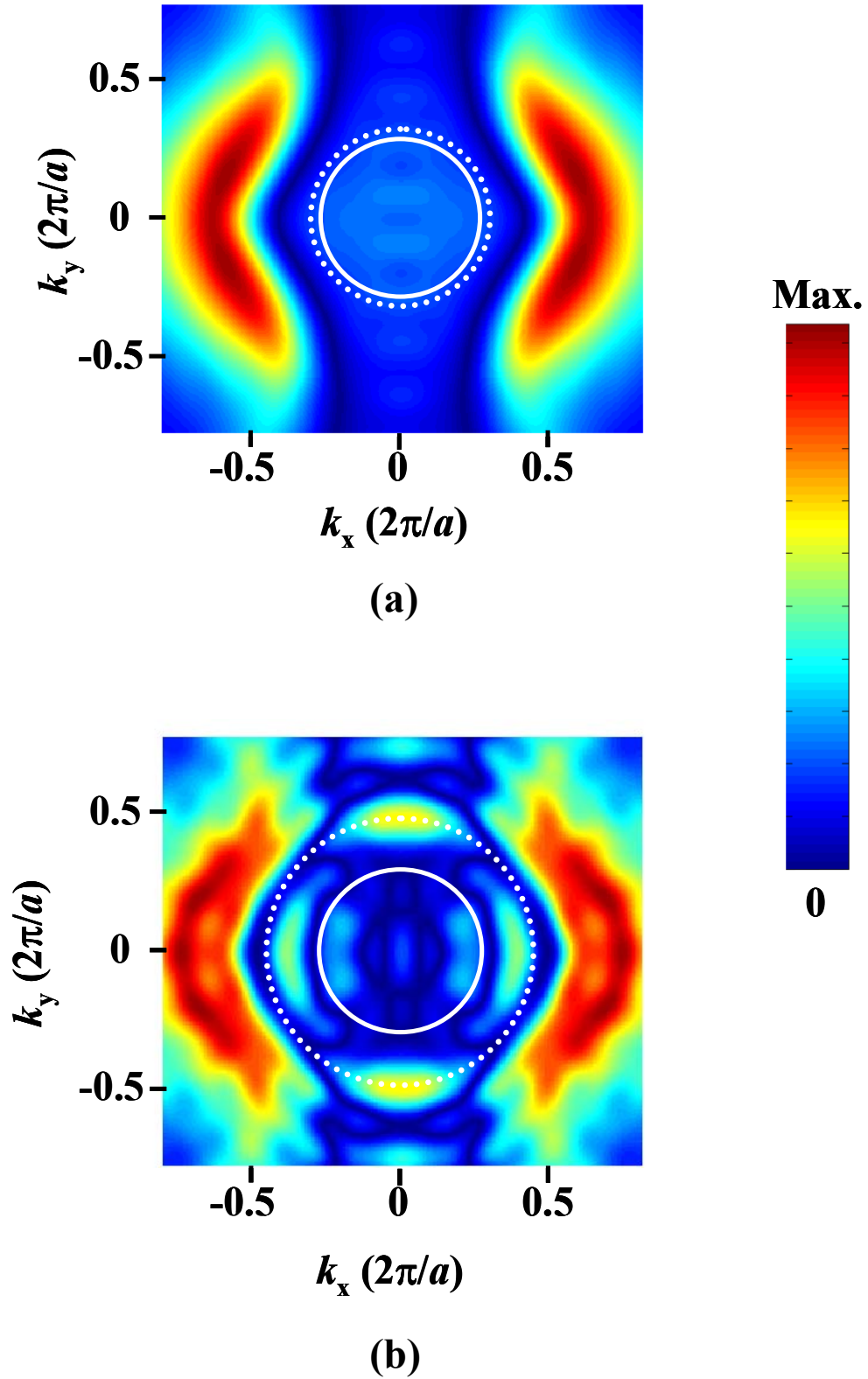


Figure 4.6 E_y -field distributions in momentum space for the cavity mode in the cavities with (a) $d = 1.35a$ and (b) $d = 1.75a$ including light lines (solid circles) and equi-frequency contours of 2nd-guided modes at the cavity mode frequencies (dotted circles).

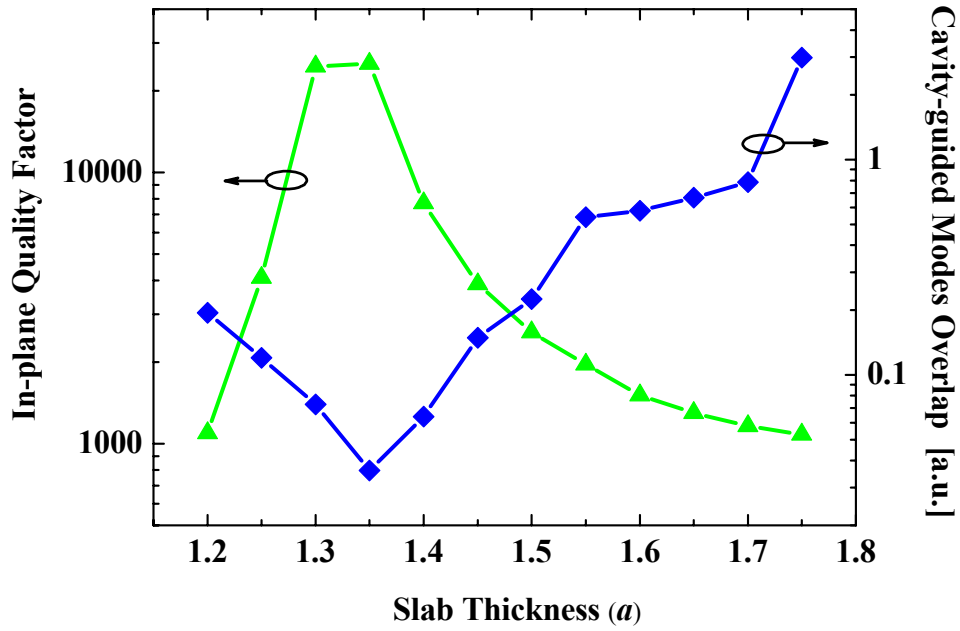
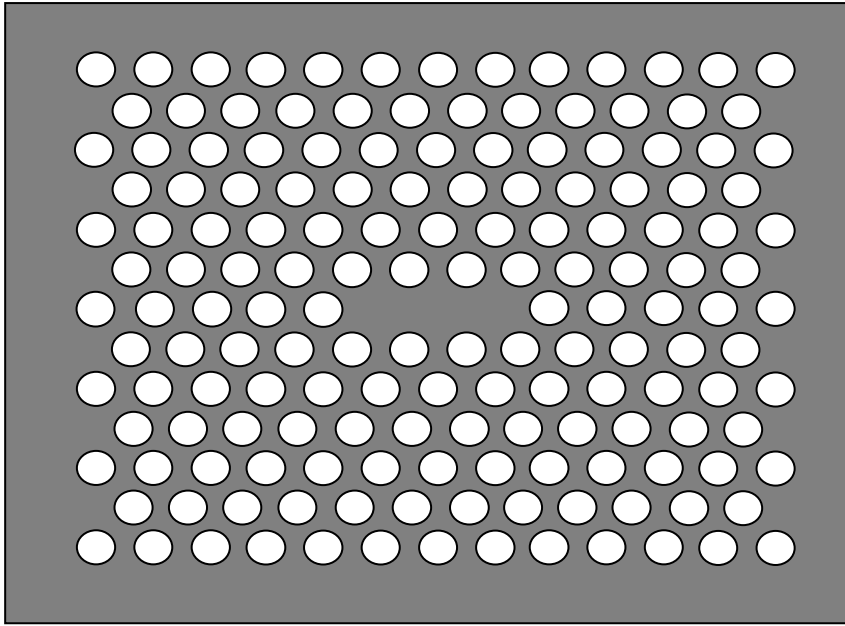
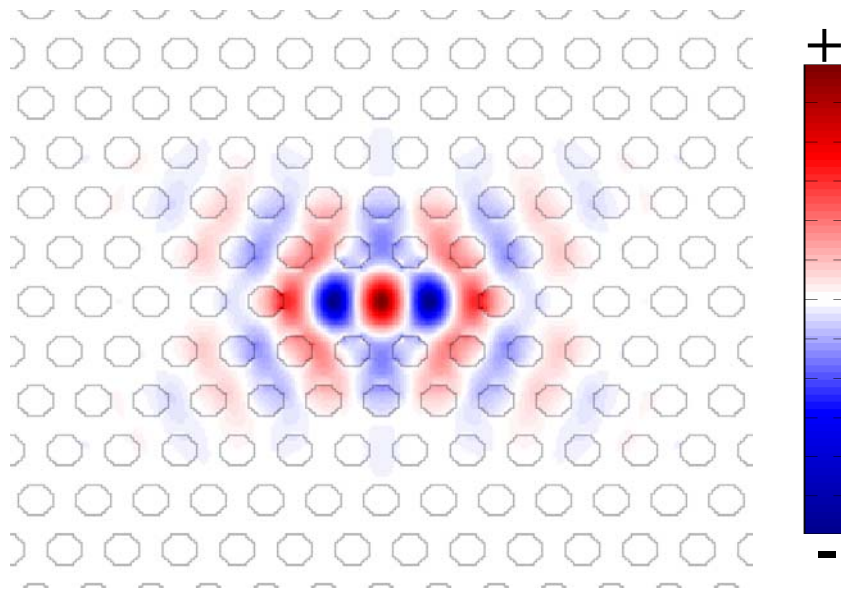


Figure 4.7 In-plane Q versus amounts of overlap between the cavity mode and the equi-frequency contour of the 2nd-guided mode of each structure with the slab thickness from 1.20 to $1.75a$.

The behavior of Q factor as a function of the slab thickness of another type of a cavity was also investigated to see whether the assumption of light confinement after closing of the photonic bandgap in the H1-cavity is available. A model of a three-missing-hole (L3) cavity [103] is shown in Fig. 4.8(a). The calculation model of the L3-defect structure contains the same number of periods of air holes surrounding the cavity as that of the H1-cavity. A fundamental mode of the L3-defect cavity was exploited as a defect mode. Its field distribution is depicted in Fig. 4.8(b). Dependence of Q factor on the slab thickness of the L3-defect structure is shown in Fig. 4.9(a). The radius of air holes was set to $0.30a$, not $0.40a$ like in the case of the H1-defect cavity, because with $r = 0.40a$ the fundamental mode is embedded in the first band. With this radius of air holes, the photonic bandgap is closed when the slab thickness is equal or more than $1.10a$. The total Q factor is highest at $d = 0.65a$, and decreases as the slab thickness increases beyond the value at the maximum Q factor due to decreasing in gap size. It can be seen that no peak of the total Q factor is observed in the range of the slab thickness after the bandgap is closed. The coupling between the cavity mode

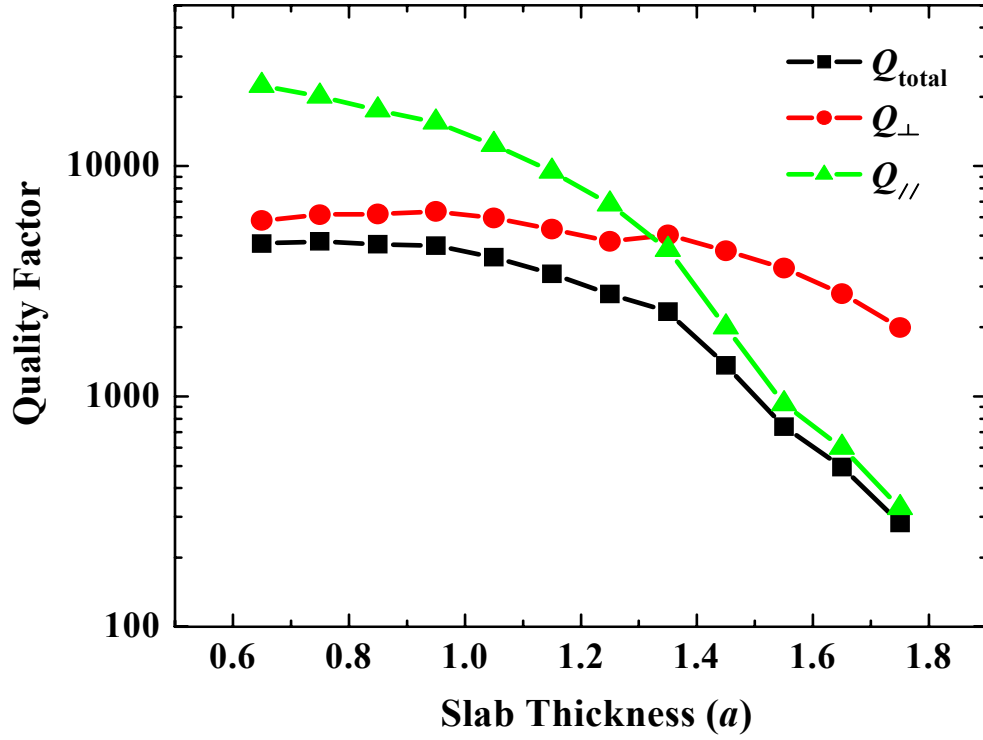


(a)

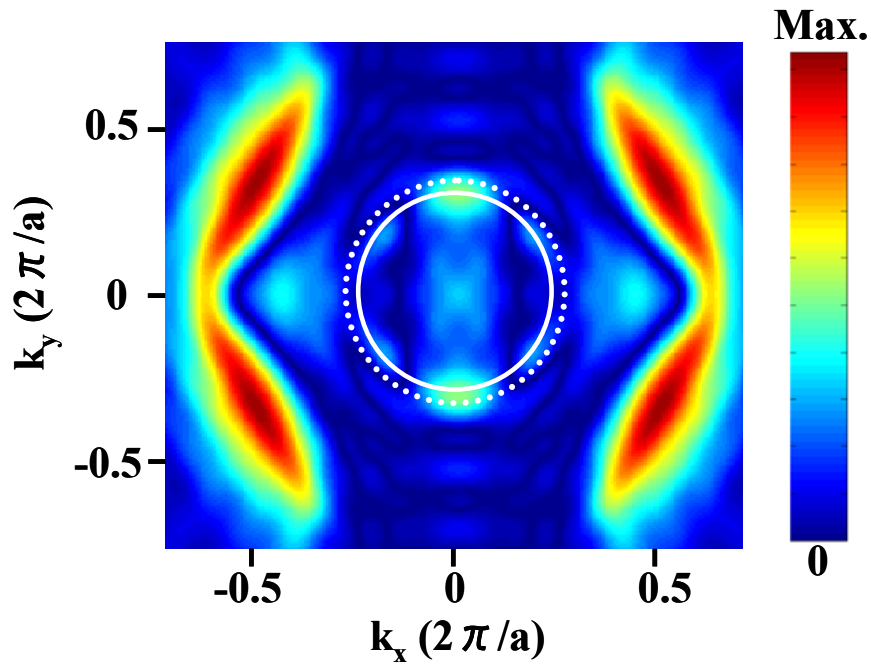


(b)

Figure 4.8 (a) Schematic of the L3-defect slab nanocavity with three missing air holes. (b) E_y -field distribution of the fundamental mode of the L3-defect structure detected at the center of the slab. The circular dotted lines show the regions of air holes for reference.



(a)



(b)

Figure 4.9 (a) Dependence of Q factor on slab thickness for the fundamental mode in L3-defect cavity with $r = 0.30a$. The photonic bandgap is closed when $d \geq 1.10a$. (b) E_y -field distribution in momentum space for the fundamental mode with $d = 1.75a$ including light line (solid circle) and equi-frequency contour of 2nd-guided mode (dotted circle).

and the guided mode in the momentum space after the closing of the photonic bandgap was then investigated. Figure 4.9(b) shows the E_y -field distribution in the momentum space for the fundamental mode with $d = 1.75a$ and equi-frequency contour of the 2nd-guided mode at the same frequency. There are strong components of the field distribution overlapping with the equi-frequency contour of the 2nd-guided mode. Therefore, the cavity mode is strongly coupled with the guided mode and laterally leaks out of the cavity, leading to very low Q factor.

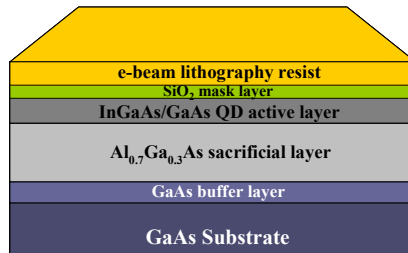
In this section, the anomalous behavior of Q factor of the modes in H1-cavity after closing of the photonic bandgap has been numerically presented. In the following sections, the numerical prediction of high- Q cavities will be experimentally confirmed and shown that the experimental results are in good agreement with the calculated results.

4.4 Fabrication processes

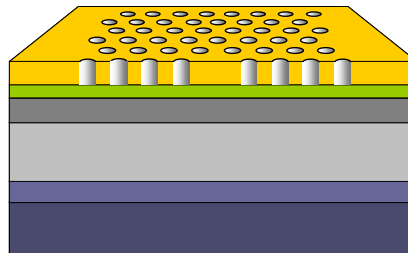
To demonstrate emissions from the designed cavity, gallium arsenide (GaAs) material system with quantum dot as an active material has been used. Four samples with different thickness of the active slab were prepared. Each sample was grown on an undoped (100)-oriented GaAs substrate by molecular beam epitaxy. First, a 300-nm-thick GaAs buffer layer was deposited on the substrate at 600°C followed by a 700-nm-thick $\text{Al}_{0.7}\text{Ga}_{0.3}\text{As}$ sacrificial layer. Finally, GaAs slab layers with the slab thickness of 190, 315, 390, and 450 nm including a self-assembled indium gallium arsenide (InGaAs) quantum dot (QD) layer at the center of the slab were grown on each sample. The quantum dot density was $\sim 10^{10} \text{ cm}^{-2}$. The emission from the QD ensemble can be used to prove the cavity characteristics because of its broad spectrum across a wide range of wavelength of 920-1050 nm at 4 Kelvin.

Figure 4.10 summarizes whole fabrication process for fabricating the designed cavities. Firstly, 150 nm of silicon-dioxide (SiO_2) was deposited on the samples by magnetron sputtering to be used as a hard mask. Sputtering condition was as follows: Argon (Ar) 12 sccm, Oxygen (O_2) 3 sccm, RF power 300 W, sputtering time 12 minutes. Because the thick active layers and large fraction of air in the photonic crystal patterns of the designed structures compared to those of conventional devices, the thickness of the SiO_2 mask layer was chosen to be thick enough to make sure that the photonic crystal patterns could be well transferred through the active

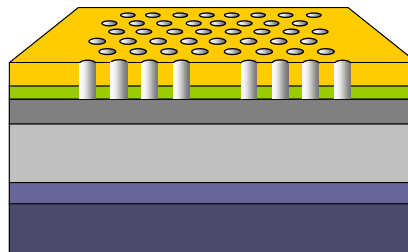
**Epitaxial growth (MBE)
and mask deposition**



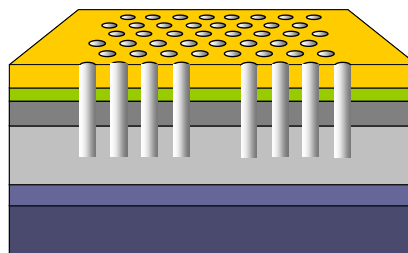
**Electron-beam lithography
and development**



**ICP/RIE (CF₄/Ar)
SiO₂ mask etching**



**ICP/RIE (Cl₂/Ar)
semiconductor etching**



**HF wet etching
Sacrificial layer & mask
removal**

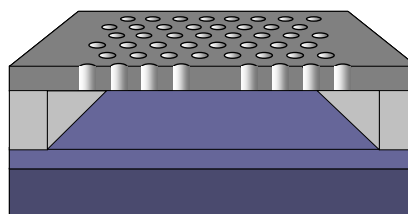
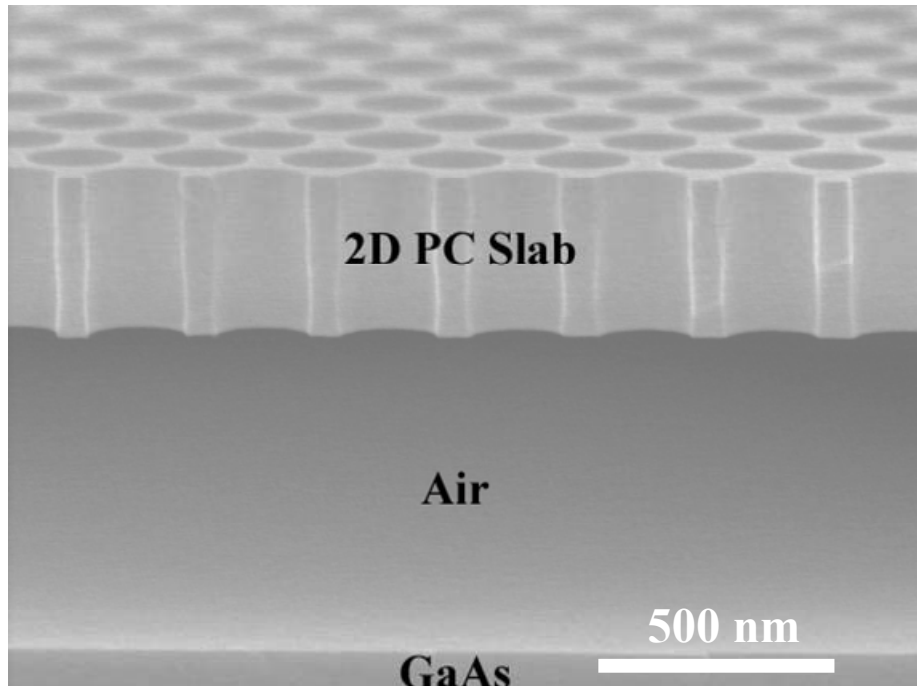
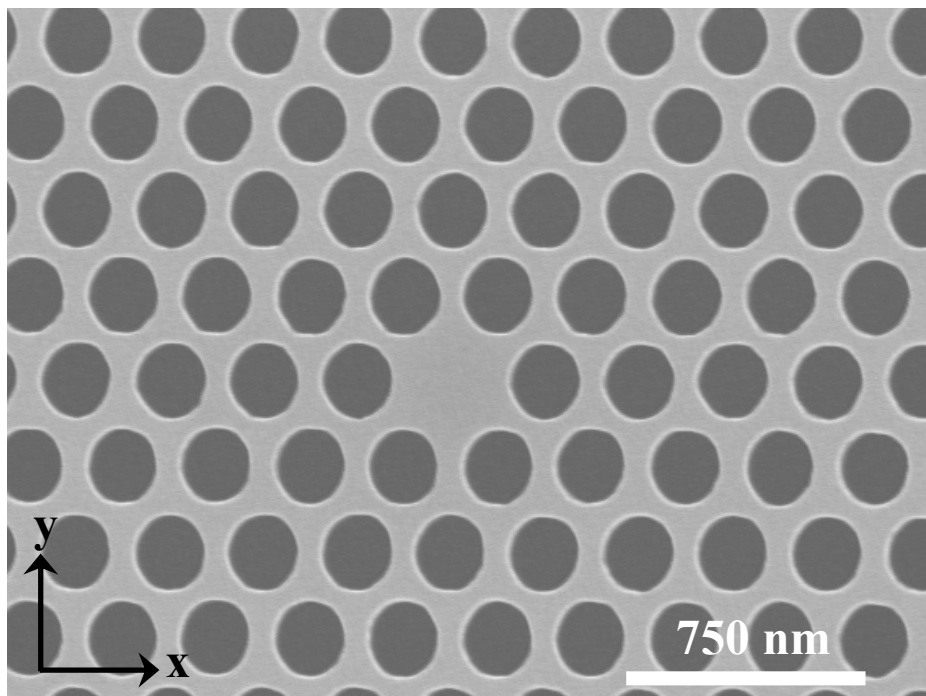


Figure 4.10 Fabrication process flow for a two-dimensional air-bridge photonic crystal nanocavity.

layer with good profile of sidewall of the air holes. Then, the samples were spin coated with electron-beam resist (ZEP-520A). The conditions for the spin coating process were as follows; spinning speed 500 rpm for 5 seconds, 4000 rpm for 60 seconds, and pre-baking at 180 °C for 20 minutes in an oven. With these conditions, the resist thickness was approximately 350 nm. Photonic crystal patterns with radius of air holes $r = 0.40a$ and various periodicities between $a = 245\text{-}360$ nm were prepared. The wide range of periodicities covers a range of the slab thickness of interest. One air hole at the center of each pattern was omitted to form the H1-defect cavity. The photonic crystal structures were patterned using an electron-beam lithography system (JEOL JBX-6000) at 50 kV, with 80 pA current and $75 \mu\text{C}/\text{cm}^2$ dose. The exposed ZEP-520A was developed in n-amyl acetate (Nihon-Zeon, ZED-N50) at 20 °C for 10 seconds, and rinsed in mixed solvent (Nihon-Zeon, ZMD-B) at room temperature for 30 seconds. The photonic crystal patterns were subsequently transferred to the SiO_2 layer by an inductive coupled plasma reactive ion etching (ICP-RIE) using a tetra fluorocarbon (CF_4) and Ar mixture. Flow rates of gases were set to 5 sccm and 6 sccm for CF_4 and Ar, respectively. The etching process was performed for 75 seconds with RF platen power of 500 W and source power of 125 W. The pressure during the process was set to 0.75 Pa and all the process was done at room temperature. Dry etching of the GaAs membrane was then performed in an ICP-RIE using a chlorine (Cl_2) and Ar mixture. Etching conditions were as follows: Cl_2 5 sccm, Ar 1.5 sccm, platen power 500 W, source power 125 W, initial pressure 1.2 Pa, final pressure 0.5 Pa, temperature 50 °C and etching times 60, 70, 75, 90 seconds for the samples with the slab thickness of 190, 315, 390, 450 nm, respectively. The active layer was intentionally over-etched into the underlying sacrificial layer to assure the slab with vertical and smooth sidewalls of etched air holes. Finally, the sacrificial layer was removed by dipping the samples in a 1:9 hydrogen fluoride solution ($\text{HF}:\text{H}_2\text{O}$) to form suspending air-bridge structures. The sample drying process after the wet etching was crucial and needed to be taken care of. To avoid the collapse of the air-bridge structures as a result of surface tension caused by trapped liquid underneath the membranes, the samples was rinsed in isopropyl alcohol (IPA), which has surface tension force relatively smaller than water, as the last rinsing solvent after the wet etching process to substitute the water. The fabricated air-bridge H1-defect nanocavity with $d = 390$ nm is shown in the scanning electron



(a)



(b)

Figure 4.11 Scanning electron micrograph of the fabricated H1-defect nanocavity with the slab thickness of 390 nm viewed in (a) Cross sectional view and (b) Top view

micrographs of Fig. 4.11 in cross sectional and top views. In spite of defining circular shapes of masks, the fabricated photonic crystal patterns have air holes slightly elongated in y direction resulted from fabrication errors occurred during the dry etching process. This elongation of air holes will play an important role in breaking of degeneracy of the doubly-degenerated dipole modes in the H1-cavity as will be shown in the next section.

4.5 Optical characterization

4.5.1 Experimental setup of photoluminescence measurements

To investigate optical properties of the nanocavities, photoluminescence (PL) measurements were performed in a temperature-controlled liquid-helium cryostat at 4 K. Figure 4.12 illustrates schematics of the measurement setup. The cryostat was pumped down to vacuum. A continuous-wave (CW) titanium:sapphire laser operated at 780 nm was used as an excitation source. The pump laser beam was focused to a 4 μm -diameter spot on the sample surface by a microscope objective [50 \times , numerical aperture = 0.42], and was positioned on the photonic crystal regions using piezo-electric nanopositioners. For imaging purpose, white light from a lamp was illuminated on the sample and a charge-coupled device (CCD) camera was used to image the positions of the photonic crystals. The photoluminescence from the QDs was collected by the same microscope objective and analyzed with both a monochromator equipped with a cooled InGaAs multichannel detector array and a triple grating monochromator equipped with a cooled Si CCD for high-resolution measurements. A mirror located in front of the monochromator can be flipped to select the detections, image of photonic crystals or luminescence. A polarizer was located just before the monochromator to filter the different in-plane polarization components of the emitted light from the cavity.

4.5.2 Experimental results

Figure 4.13(a) shows PL spectrum for the H1-cavity with $a = 280$ nm, $r = 0.40a$, and $d = 390$ nm. The cavity modes shown as sharp peaks are clearly distinguishable from the broad background emission range of the quantum dot

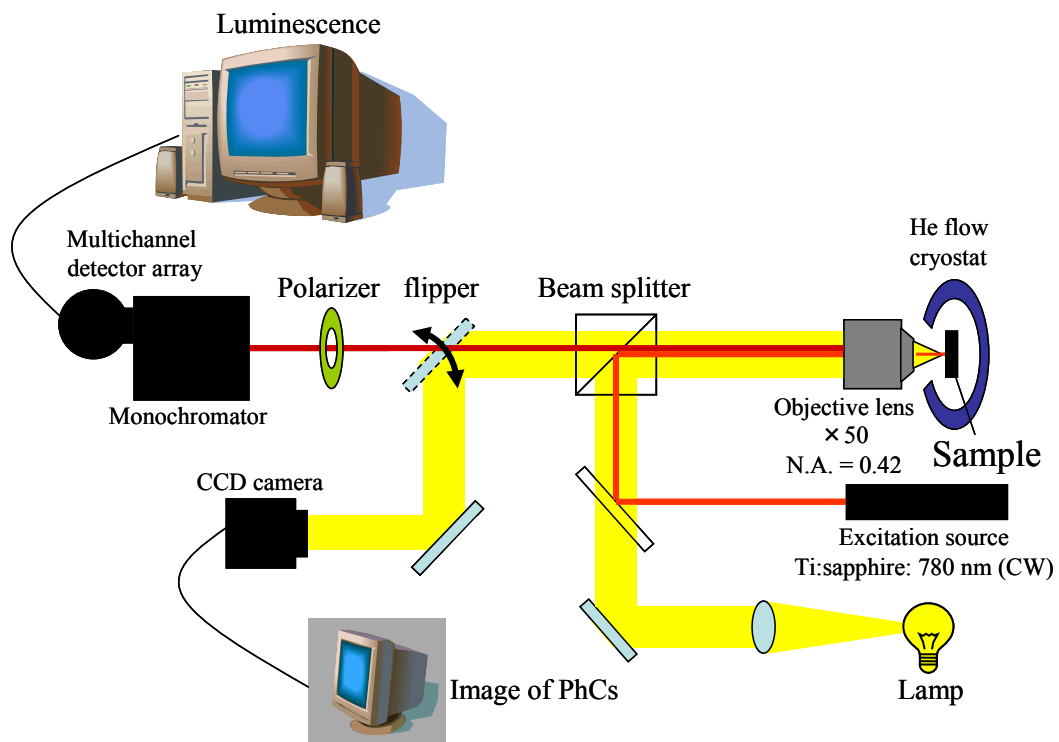
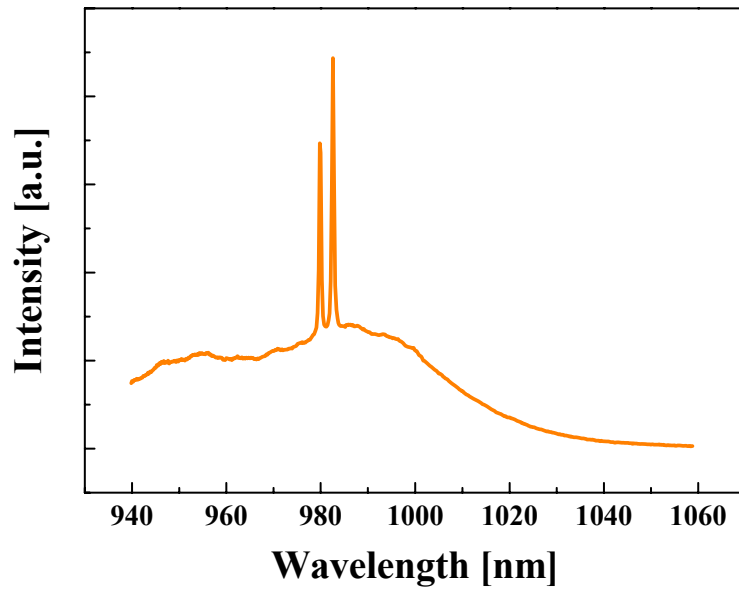
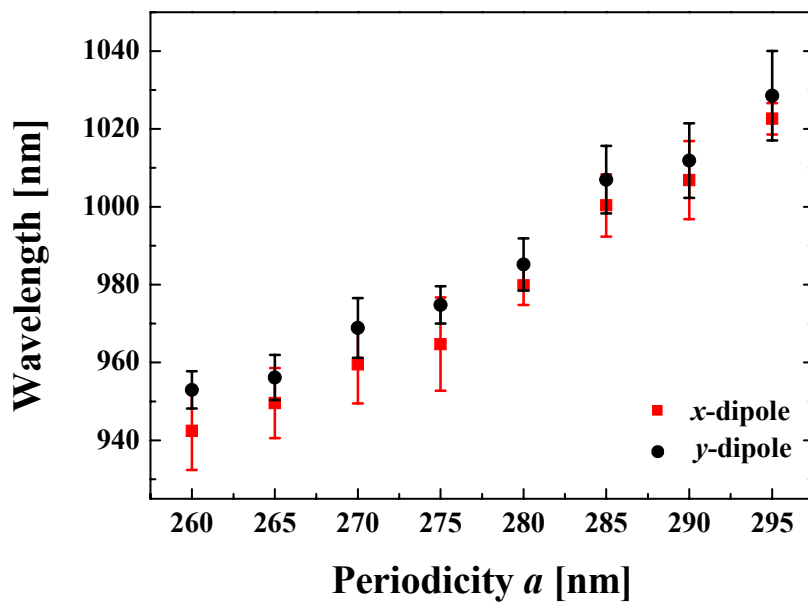


Figure 4.12 Schematic illustration of photoluminescence measurement setup.



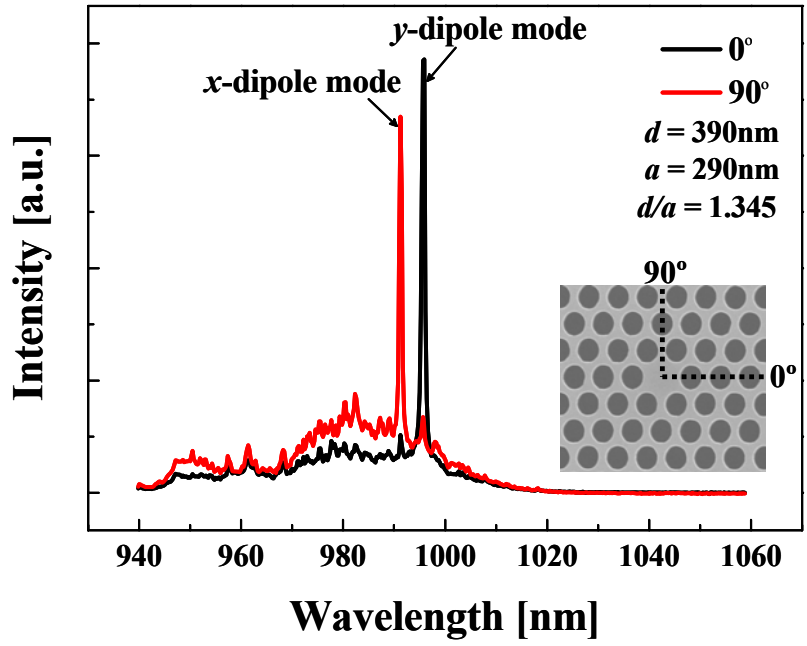
(a)



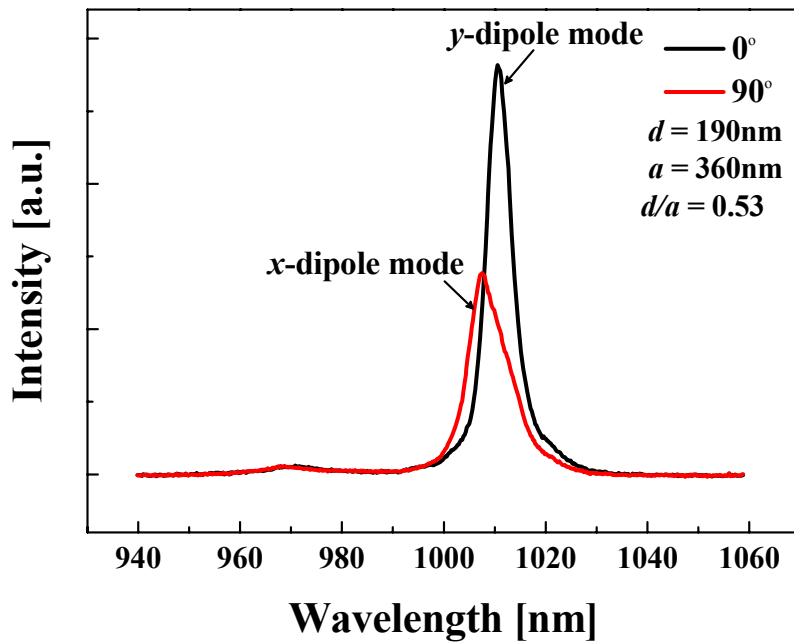
(b)

Figure 4.13 (a) PL spectrum from the H1-nanocavity with $a = 280$ nm, $r = 0.40a$, and $d = 390$ nm. (b) Periodicity dependence of wavelength of the cavity modes. All the cavities have $r = 0.40a$ and $d = 390$ nm. Error bars are also shown.

ensemble. The spectra of the cavity modes can be tuned throughout the emission range of the quantum dots by changing the periodicity of the photonic crystals [105]. The periodicity dependence of wavelength of the cavity modes are plotted in Fig. 4.13(b) with the separation between the two modes of approximately 10 nm. All the cavities have $r = 0.40a$ and $d = 390$ nm. The pair of modes observed in Fig. 4.13(a) is a result of the two perpendicular dipole modes in this cavity. When filtering the spectrum with a polarizer, they are linearly polarized and orthogonal to each other as shown in Fig. 4.14. The mode at the shorter wavelength corresponds to the x -dipole mode, while the other is y -dipole mode. Spectral splitting of the modes does not occur in a completely symmetric H1-defect cavity within a two-dimensional photonic crystal, since the structure with a 60° rotational symmetry leaves two degenerated eigenmodes. Therefore the measured mode splitting of around 1% relative to the wavelength in the figure is expected to result from fabrication fluctuations within the photonic crystals [105]. One possible fluctuation is the elongation of air holes as can be observed in the SEM image of the fabricated structure shown in Fig. 4.11(b). Such a degeneracy lifting occurs even in 3D-FDTD simulations as discussed in Chapter 4.2. Sharp peaks of both x -dipole and y -dipole modes of the structure with the slab thickness $d = 390$ nm and periodicity $a = 290$ nm, which is corresponding to $d = 1.345a$, reflect their high Q . In contrast, the cavity with $d = 190$ nm and $a = 360$ nm, which is corresponding to $d = 0.53a$, shows much broader linewidths of both modes. Figure 4.15 shows a high-resolution PL spectrum for the x -dipole mode of the cavity with $d = 1.345a$, fitted with a Lorentzian function. The linewidth of 0.34 nm corresponds to the estimated Q factor of about 3,000 calculated from ratio of the center wavelength of the peak to its full width at half maximum (FWHM). Figure 4.16 summarizes the measured- Q over a wide range of the slab thickness for both the x -dipole mode and y -dipole mode compared with the calculation results extracted from Fig. 4.3. The experimental results were obtained from all four samples and were plotted in the graphs with their corresponding d/a . The Q s at each d/a shown in the figure were measured from more than ten identical cavities. The square symbols representing the measured- Q s are the averaged values with the error bars. It can be seen that the measured- Q s have tendencies very close to that of the calculated- Q s. In the range of the slab thickness before closing of the photonic bandgap (at $d = 1.20a$),



(a)



(b)

Figure 4.14 Polarization dependence of the cavity modes from the nanocavities with (a) $d = 1.345a$ and (b) $d = 0.53a$. The radius of air holes is fixed to $0.40a$ for both structures. The polarization directions are defined in the inset of (a).

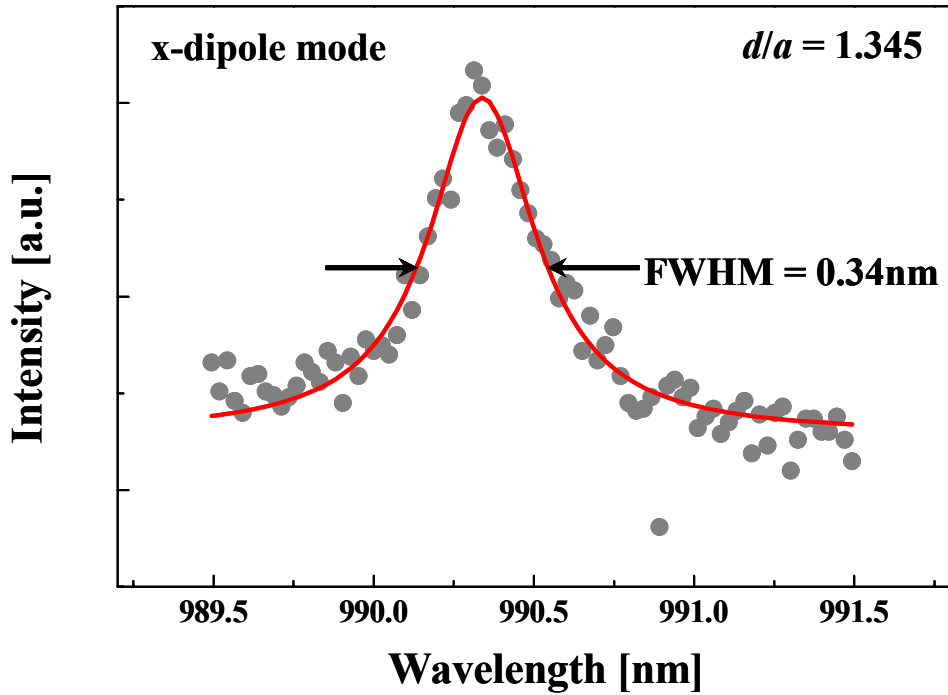
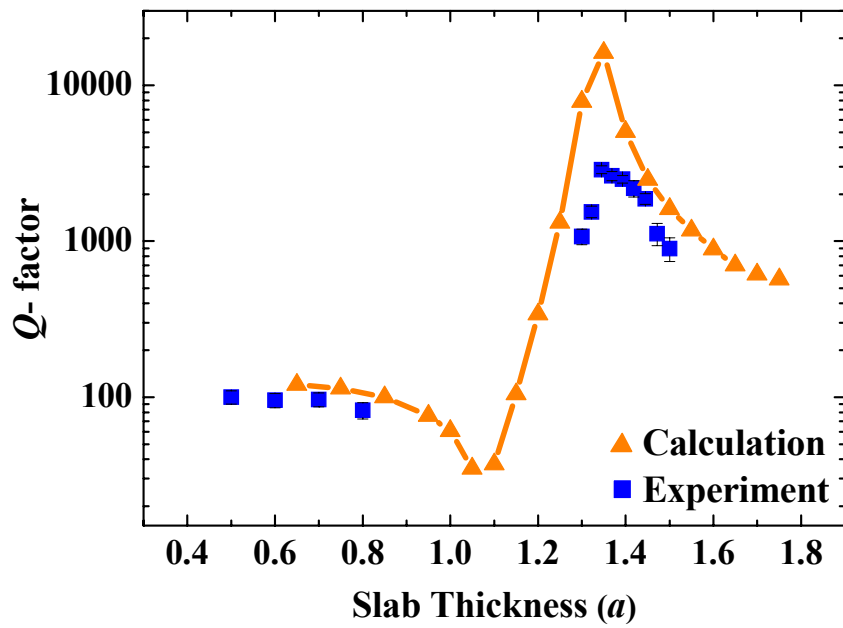
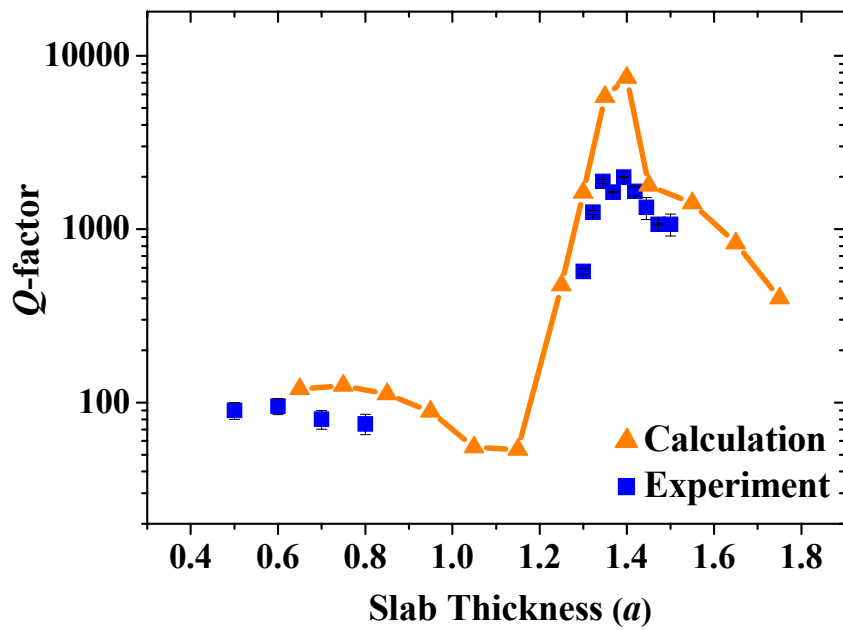


Figure 4.15 High-resolution PL spectrum for the x-dipole mode shown in Fig. 4.14(a) fitted with a Lorentzian function (red curve).

the measured- Q s for both x - and y -dipole modes are very low, and they gradually drop as the slab thickness increases due to the reduction of the photonic bandgap size. These results are consistent with the results of previous studies on the dipole modes of the H1-cavity with no modification of the defect structure [59,105]. However, they significantly increase by more than an order of magnitude after closing of the photonic bandgap with the highest measured- Q being approximately 3,000 at $d = 1.345a$ for the x -dipole mode and about 2,000 at $d = 1.393a$ for the y -dipole mode. The calculated- Q for the x -dipole and y -dipole modes are 16,200 at $d = 1.35a$ and 7,500 at $d = 1.40a$, respectively. These differences between the measured and calculated values can be attributed to the quantum dot absorption and the fabrication errors causing the roughness of the sidewall and the fluctuation of shape and size of the etched air holes. The results clearly show that the structural parameters of the best fabricated cavity and those of the predicted one are almost exactly the same, in which the slab thickness $d = 1.345a$ of the experimental results is close to $d = 1.35a$ of the calculated ones, because the only parameter that needs to be adjusted is the slab thickness which can



(a)



(b)

Figure 4.16 Dependence of the measured- Q (square) on the slab thickness compared with the calculated- Q (triangle) for (a) x -dipole mode and (b) y -dipole mode.

be precisely controlled by using epitaxial growth techniques such as MBE and MOCVD. The cavity modes in the samples with the slab thickness around $1a$ cannot be recognized due to their very low Q .

4.6 Summary

In summary, a significant increase of Q -factor of dipole modes in photonic crystal H1-defect nanocavity after closing of the photonic bandgap were numerically and experimentally demonstrated in this Chapter by tuning the slab thickness. The optimal slab thickness is equal to a wavelength of light confined in the cavity confirmed by calculating effective refractive index of the porous structure. The maximum calculated- Q and measured- Q are $\sim 16,200$ at $d = 1.35a$ and $\sim 3,000$ at $d = 1.345a$, respectively. They were obtained after closing of the photonic bandgap. In this cavity, the strong light confinement of the cavity in the in-plane direction is not caused by the photonic bandgap effect due to a lack of the photonic bandgap but resulted from the decoupling between the cavity mode and the guided mode in the momentum space yielding only weak coupling between these two modes. As a result, the light can be strongly confined within the cavity despite of no photonic bandgap. The results clearly show that the structural parameters of the best fabricated cavity and those of the predicted one are almost exactly the same, in which the slab thickness $d = 1.345a$ of the experimental results is close to $d = 1.35a$ of the calculated ones, because there is no modification of the defect structure and the only parameter that needs to be adjusted to achieve high Q is the slab thickness which can be precisely controlled by using epitaxial growth techniques such as MBE and MOCVD. This finding will contribute to extending the freedom of cavity design, such as that for the application to polarization entangled photon source, where it is required to form cavity modes with prescribed Q factor and polarization.

Chapter 5

High- Q Photonic Crystal Nanocavity without Photonic Bandgap by Modulating Air Hole Radii in Square Lattice

5.1 Introduction

In the previous Chapter, high quality factor dipole modes in photonic crystal H1-defect nanocavity were shown to be achieved even there was no photonic bandgap at the frequencies of the cavity modes. These have been numerically and experimentally proved to be a result of decoupling between the cavity modes and the losses in the momentum space. However, the cavity used in the previous section requires definite structural parameters in order to achieve high Q factor. That means, if some of the parameters are different, for example, refractive index is different or the structure is not an air-bridge slab, the cavity is needed to be re-designed from the starting point to have high Q or is even impossible to achieve high Q after all due to the restriction of the design. In addition, the maximum designed Q factor of 16,200 of the dipole mode in H1-cavity is still preferable to be further increased with consideration of many applications, such as cavity quantum electrodynamics (cavity-QED) and quantum information processing [100,106-112]. In a strong coupling cavity-QED system [106-108], a large figure of merit $Q/\sqrt{V_{eff}}$ is desired for improving the quantum coherence, while high Q/V_{eff} is preferable in a weak coupling regime [100,109-112]. Therefore, a cavity with large Q factor is required with mode volume being kept small. Moreover, in some applications, such as structures with

low refractive index and quantum cascade lasers, there is no photonic bandgap in a frequency region of interest, i.e., photonic bandgap for the structure with low refractive index only exists in very high frequency range, while the photonic bandgap is not open for light polarized in transverse magnetic (TM) -like mode, where photons are polarized in quantum cascade lasers. So far, there is no appropriate design of photonic crystal cavities that can achieve high Q for both structures.

In this Chapter, the concept of mode decoupling that allows one to have high Q cavities despite of no existence of photonic bandgap, obtained in the previous Chapter, is applied to design high Q photonic crystal nanocavities with square lattice. The high Q cavities are achieved by modulating air hole radii surrounding the cavities with proper modulation profile. Although there is no photonic bandgap at the cavity mode frequency, the maximum Q factor of the doubly-degenerated modes in the designed cavity exceeds 120,000 with the mode volume of $0.79(\lambda/n)^3$, leading to a large figure of merit Q/V_{eff} in the weak coupling regime of about two times higher than the highest value reported so far for doubly degenerated modes in photonic crystal cavities. Therefore, the designed cavity is very promising for realizing entangled photon sources. In addition, it is shown that the designed cavity can also be effectively applied to achieve high Q cavity in low index material and high Q cavity for quantum cascade lasers, in which a lack of photonic bandgap usually hinders them from applications.

5.2 Cavity structures and defect modes

Because the concept of mode decoupling obtained in the previous Chapter directly deals with the distribution of cavity field and losses in the momentum space, a photonic crystal structure with a square lattice is adopted to design a high Q cavity rather than a triangular lattice. This is because the square lattice has lower symmetry, and hence simplifies the cavity design. There are three symmetry points in a square lattice where a defect can be introduced to form a cavity. Two of them possess a 90° rotational symmetry (points d and f) and the other has 180° rotational symmetry (point e) as shown in Fig. 5.1. A designed cavity is chosen to have a defect located at point f, in which the cavity is surrounded by four innermost holes and doubly-degenerated modes are expected to exist. The computational model of the design of the cavity is

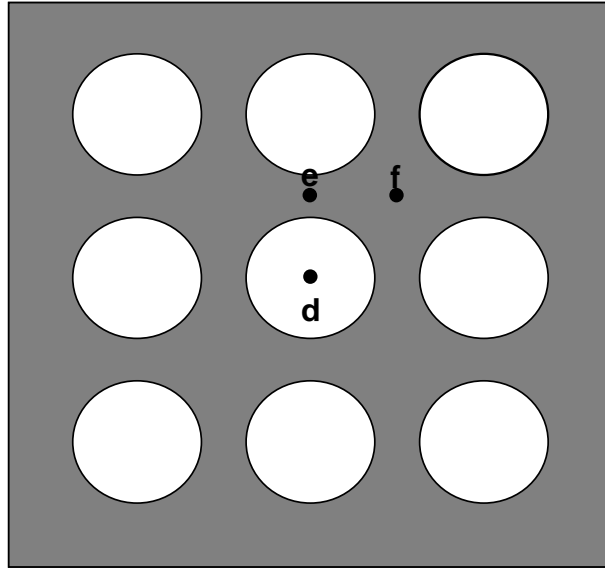
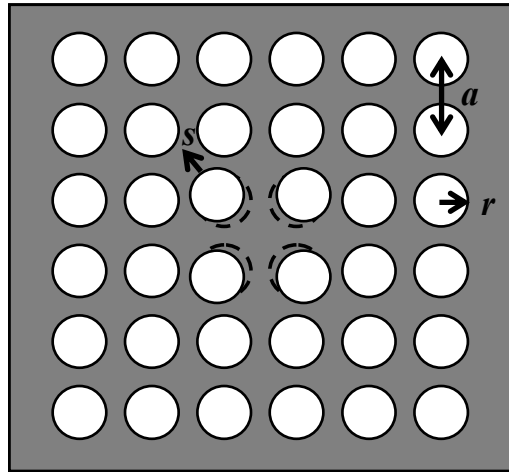
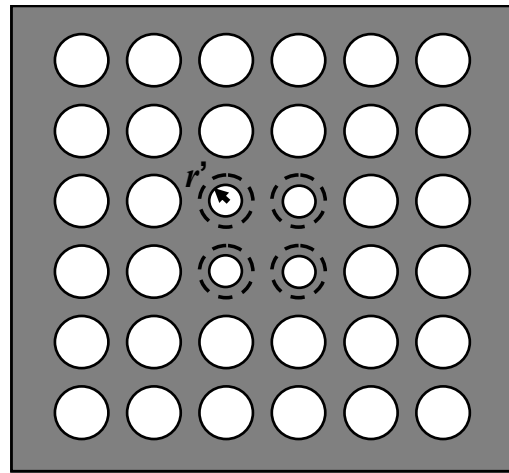


Figure 5.1 Real space lattice of a two-dimensional square lattice. High symmetry points about which a defect can be formed are also shown. Points d, e, and f correspond to 90° , 180° , and 90° rotational symmetry points, respectively.

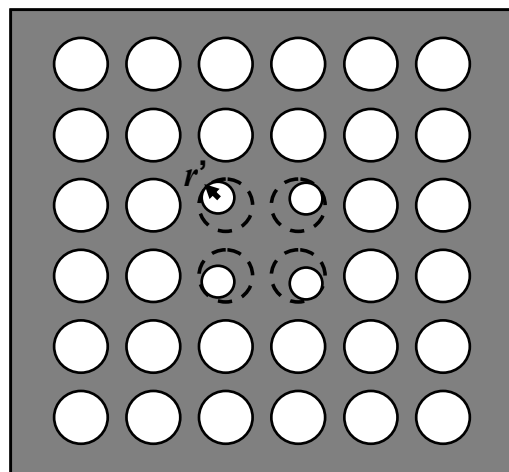
based on an air-bridge type photonic crystal slab, which is a dielectric slab thick d with refractive index of 3.4, corresponding to that of GaAs, cladded with air in both upper and lower sides. Air holes have a lattice constant a and radius r . In order to form a cavity, periodic components of the square lattice photonic crystals are perturbed to introduce a defect. The simplest ways to do this are shown in Fig. 5.2. A defect can be generated by shifting positions, reducing sizes, or both of the innermost air holes without removing of any hole. Such kinds of perturbations result in cavities with donor defect modes as discuss in Chapter 2. Doubly-degenerated modes existing in this cavity are shown in Fig. 5.3, where the defect cavity is formed by shifting the innermost holes outward for $0.05a$. E_x component field distribution at the center of the slab of x -mode is shown in Fig. 5.3(a), and E_y component field distribution of y -mode is depicted in Fig. 5.3(b). It is worth noting that these x - and y -modes are a new type of doubly-degenerated modes in photonic crystal cavities. In the FDTD calculation, as same as in Section 4.2, a cubic lattice, in which size of grid cells in three dimensions are identical, is used. However, unlike in the case of the triangular lattice, the cubic grid cell can well be exploited to model the structure with the square lattice without adding any anisotropy to the structure. As a result, resonant frequencies of the x - and y -mode are completely coincided in the spectrum. In order to selectively excite only one mode at a



(a)



(b)



(c)

Figure 5.2 Three types of defect cavities generated at a symmetry point Γ in photonic crystals with a square lattice.

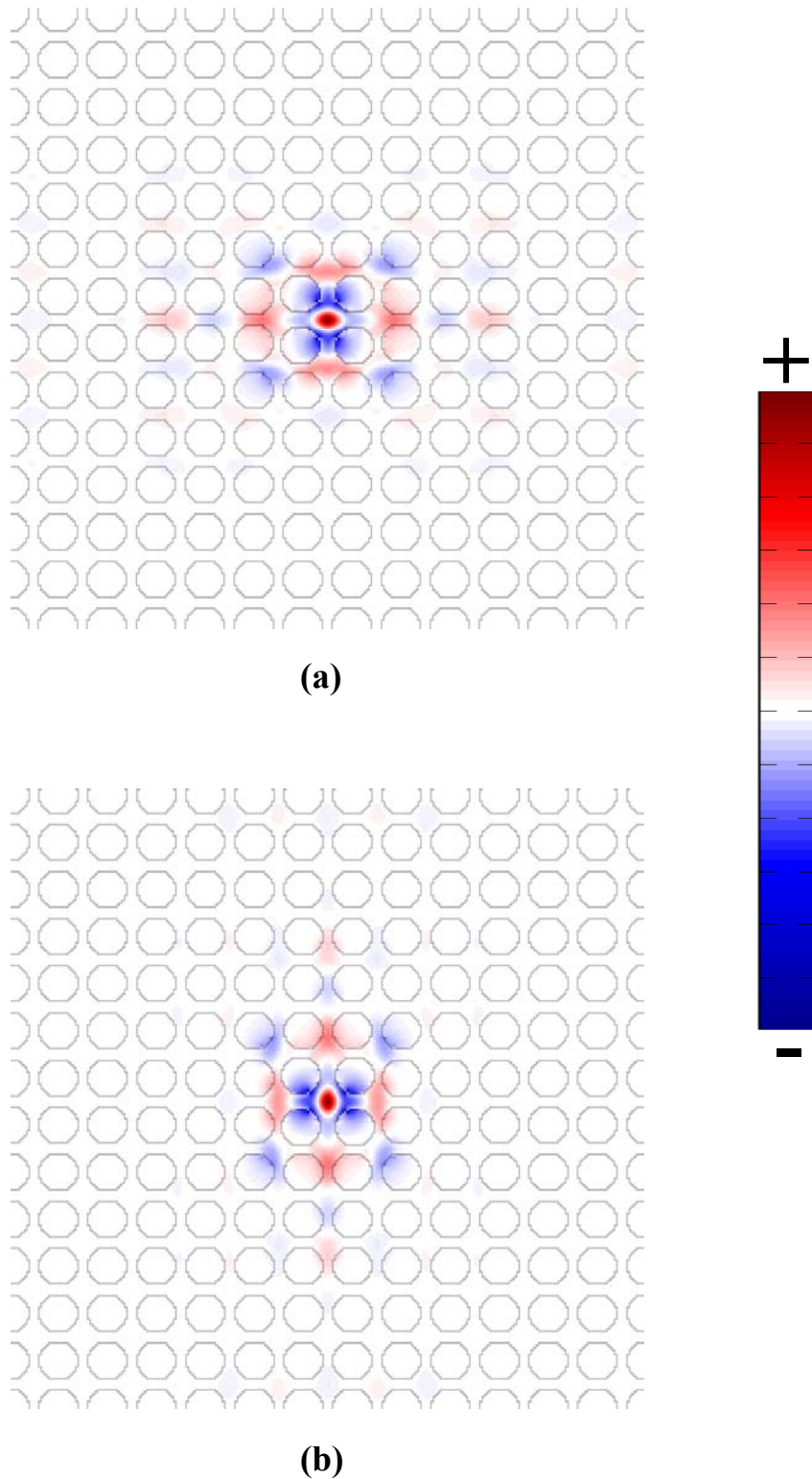


Figure 5.3 Field distributions at the center of the slab of (a) E_x component of x -mode and (b) E_y component of y -mode. The circular lines show boundaries of air holes. Radius and thickness of the structure are set to $0.40a$ and $0.5a$, respectively. Nearest neighbor holes are shifted outward for $0.05a$ to form a cavity.

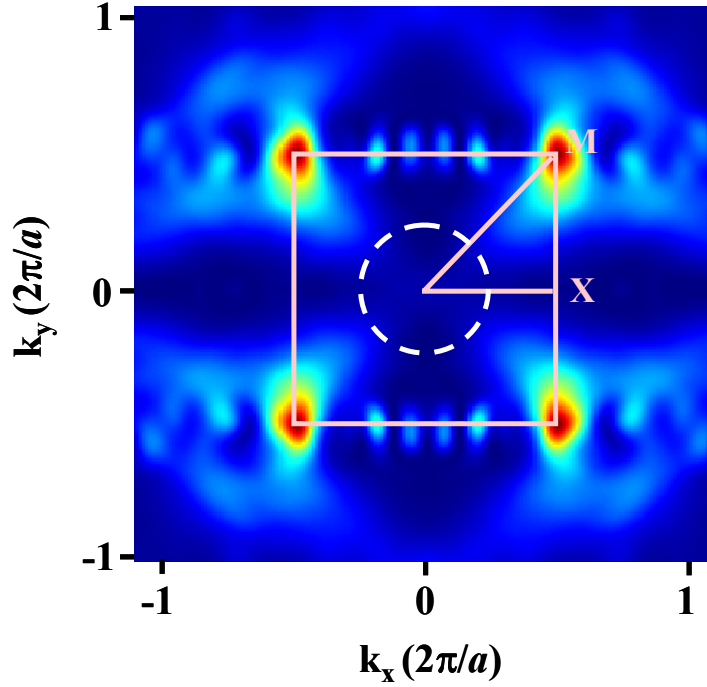


Figure 5.4 Absolute value of the electric field distribution of the x -mode shown in Fig. 5.3(a) in momentum space. Solid square and dotted circle represent the corresponding first Brillouin zone and light line, respectively.

time, a pulse source is intentionally located at a symmetry point where one mode has its antinode at that position, while the other mode has its node. And thus, only the mode with its antinode at the position of the source is excited.

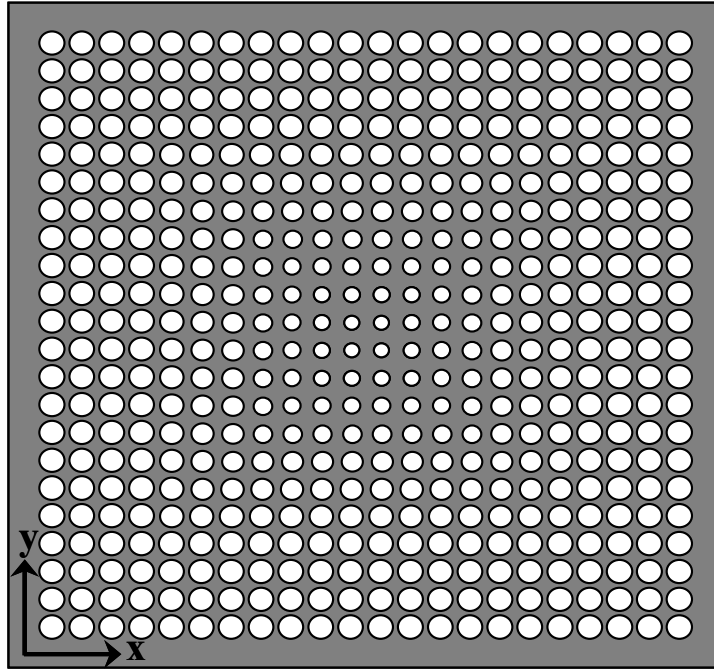
Because the behavior of Q for the x - and y -modes is in similar, only the x -mode is discussed in this section. As can be expected, Q factors of these modes are very low. In this cavity both the vertical Q and in-plane Q are only a few hundreds and thousands, respectively. Figure 5.4 illustrates total electric field distribution in momentum space of the x -mode shown in Fig. 5.3(a). The low Q in the vertical direction roots from two mechanisms. The first one is that the modes have an antinode of their fields at the center of the cavity and this plays an important role in coupling out of the slab. Like in the case of the dipole modes in the H1-cavity, the antinode of the cavity mode field leads to large components of wavevectors located inside the lightcone, and these components couple to the radiation modes and radiated out of the cavity. The other reason is that the mode is well confined in a small region of the cavity in real space, leading to delocalization of the mode in momentum space [113]. As can be seen, the dominant momentum components of the x -mode locating around M -point of the first Brillouin zone

strongly leak into the light cone. In the in-plane direction as previously mentioned, the photonic bandgap of the square lattice is at best very narrow, consequently, it requires a lot of effort to design a cavity with cavity modes inside the bandgap. Because the x -mode locates very close to the M -point of the valence bandedge, it is necessary to reduce coupling between the cavity mode and neighborhoods surrounding the M -point, especially when the cavity mode is embedded in the valence band and is strongly coupled to the guided mode, to obtain high in-plane Q .

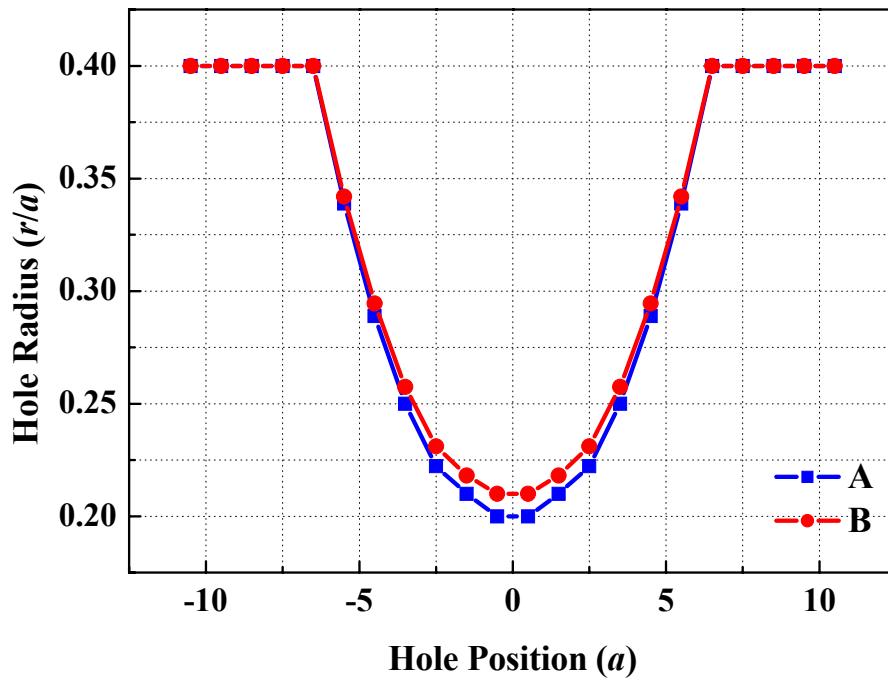
5.3 High cavity Q in graded photonic crystal structure by mode decoupling

5.3.1 Graded photonic crystal nanocavity with modulating air hole radii

Figure 5.5(a) shows a top-view showing in-plane pattern of the designed cavity. This kind of structure is called a graded lattice structure [114]. The cavity is centered at point Γ surrounded by four innermost holes with $r = 0.20a$ (cavity A). The air hole radii are then increased quadratically outwards from the innermost holes over six periods from $r = 0.21a$ to $0.40a$. The graded area is surrounded by four periods of air holes with a fixed air hole radius of $0.40a$. The air hole radii profile is the same in both x and y directions in order not to break the degeneracy of the modes (Fig. 5.5(b)). The radius of the second nearest air holes is increased a little bit, approximately 2% from the value of the quadratic distribution. This jump of air hole size acts like a potential well and thus helps confine the mode in real space. However, too quick jump of holes leads to delocalization of the mode in momentum space, consequently, the mode undesirably couples to the losses. The size of jump is well selected to compromise the mode localization in real space and momentum space. In addition, the grading profile is also important. A Q -degradation is observed for gradings which occur too slowly or too quickly. The radii profile with too sharp modulation results in the stronger mode localization in real space and subsequent Fourier space broadening of the mode. On the other hand, too slow modulation destroys the mode confinement and the in-plane losses increase. In order to compare the Q factors and to thoroughly study the confinement mechanisms of the mode later, another cavity (cavity B) with different air hole radii profile is also investigated. Its radii profile compared with that of cavity A is plotted in Fig. 5.5(b). Both cavities have the same slab thickness of $0.60a$.



(a)



(b)

Figure 5.5 (a) Photonic crystal nanocavity with modulating air hole radii. (b) Hole radii profile in the center cut-plane in both x and y directions for two cavities, A and B, for comparison.

5.3.2 Improvement of cavity Q in graded structure by mode decoupling

Figure 5.6 (a) and (b) show the absolute value of the electric field distribution of the x - and y -modes in cavity A. They are doubly-degenerated and orthogonally-polarized. Both modes are a little expanded from the cavity site but still strongly confined within the grading region. It is also shown that the modes are well confined within the slab in the vertical direction, implying very high vertical Q . The Q factor reaches the highest value of more than 120,000 with mode volume $V_{eff} = 0.79(\lambda/n)^3$ for both modes with the slab thickness $d = 0.60a$. This Q value is more than two orders of magnitude higher than the structure without grading. The figure of merit Q/V_{eff} in the weak coupling regime is about two times higher than the highest value reported so far for doubly-degenerated modes [115]. In addition, such a high ratio of Q/V_{eff} of cavity A is obtained even the modes are not located inside the photonic bandgap. The cavity modes slightly embed in the valence band near the M-point of the irreducible 1st Brillouin zone as shown in Fig. 5.7. On the other hand, the x - and y -modes in cavity B have Q factor of only 12,000, about an order of magnitude lower than that of cavity A. It is worth noting that the cavity modes in cavity B also locate outside the photonic bandgap. The Q factors of cavity A and B are divided into the vertical Q of 175,000 and 16,300, respectively, and into the in-plane Q of 336,000 and 53,000, respectively. This means that both vertical and in-plane Q s of cavity A are higher than those of cavity B. Details on the reasons why cavity A has very high Q even the cavity modes are not in the photonic bandgap, and why Q factors of the two cavities are so different are discussed in the followings.

Figure 5.8(a) describes the distribution of the cavity mode, radiation mode and waveguide mode in momentum space. As aforementioned, the cavity mode is embedded in the valence band near point M, resulting in a circular shape of field distribution extracted from the equi-frequency contour of the 1st-guided mode at frequency of the cavity mode. It can be seen that the field distribution of the guided mode is very close to the cavity mode. Therefore, they are needed to be decoupled from each other in order to have strong confinement of the cavity mode in the in-plane direction. In the vertical direction, components of the cavity mode field that expand into the light cone will be coupled out of the cavity. As a result, the cavity mode and the radiation mode must also be decoupled to have high vertical Q . Couplings of the modes to other modes (losses) can be considered through the

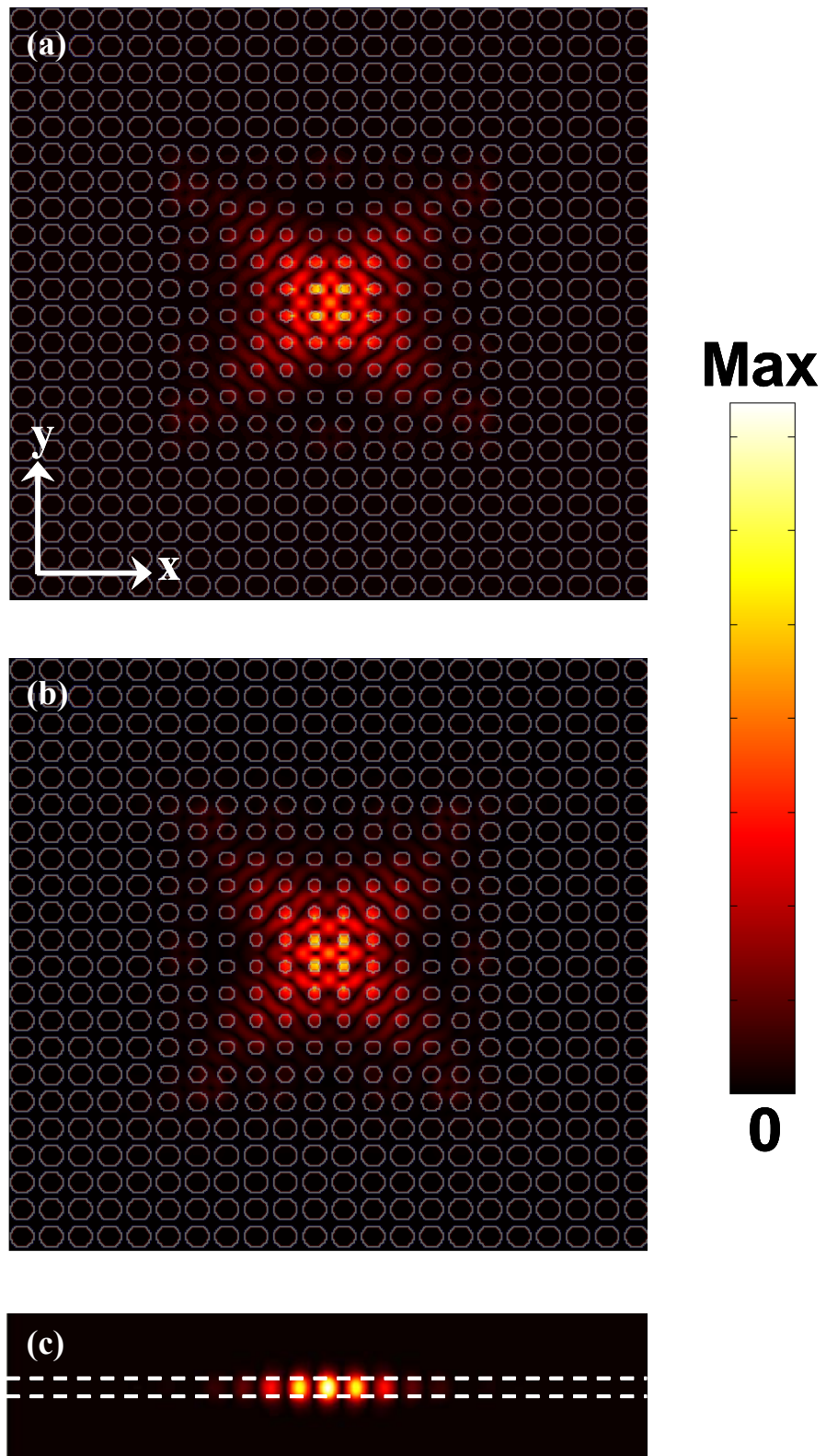


Figure 5.6 Total electric field intensities of the (a) x -mode and (b) y -mode in cavity A. (c) Cross sectional view of field intensity of the x -mode in xz plane. Broken lines represent the boundaries of the slab.

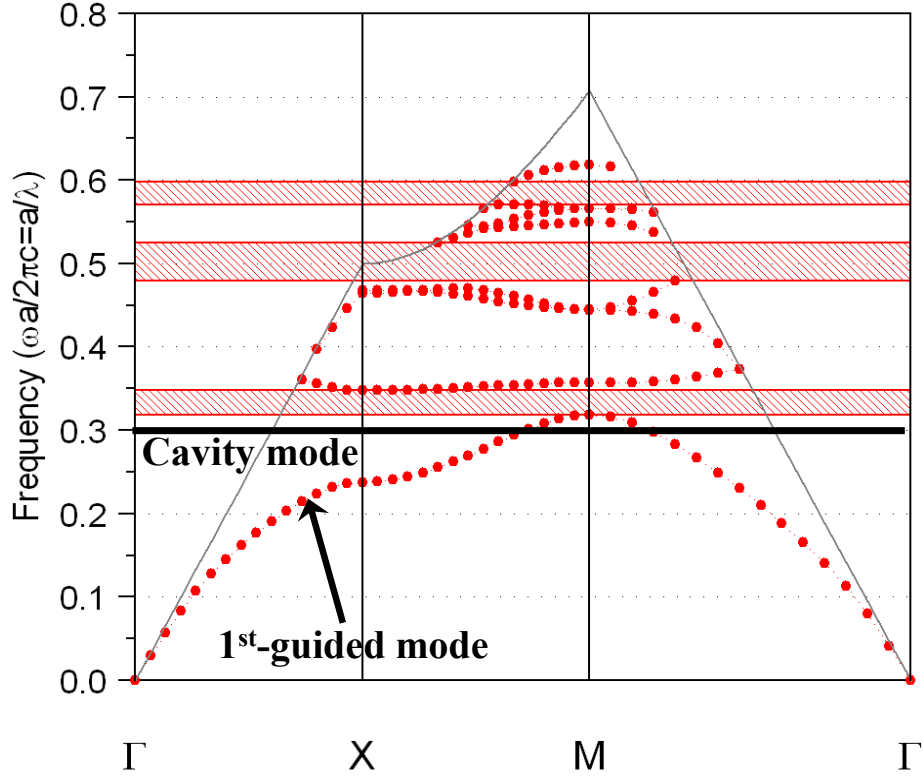
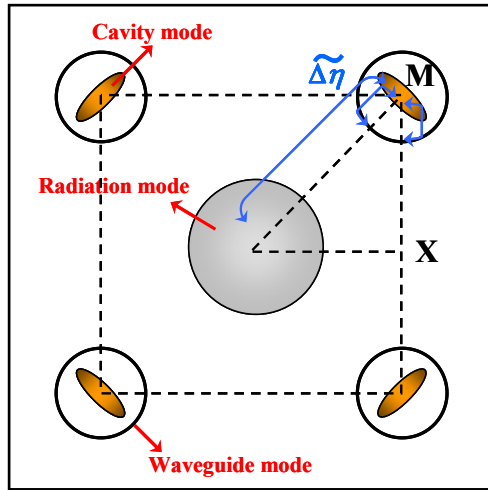
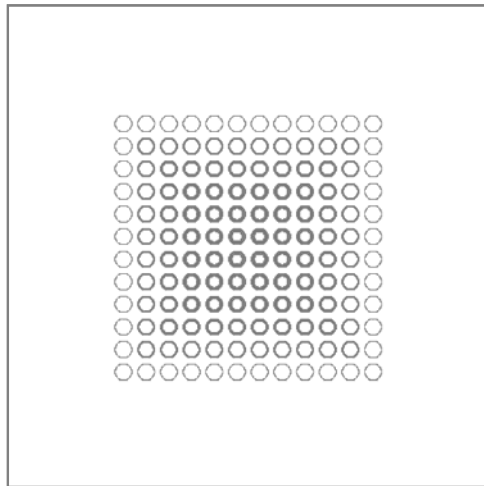


Figure 5.7 Band diagram for cavity A. The cavity modes with normalized frequency of 0.298 overlap with the 1st-guided mode near point M.

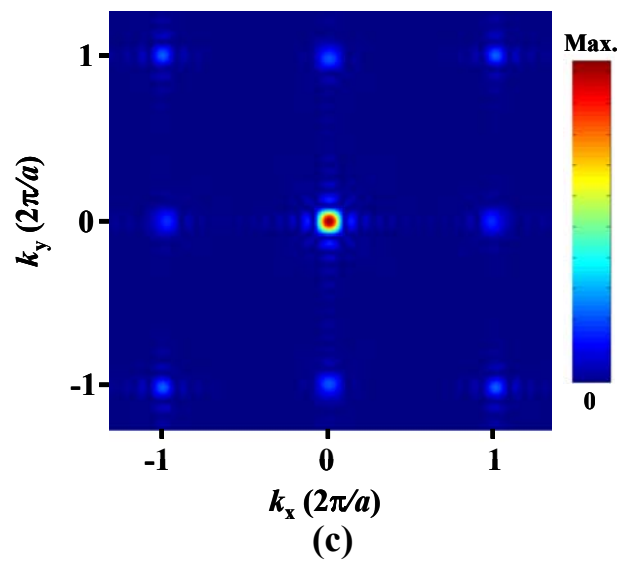
dielectric perturbation $\Delta\eta(\mathbf{r})$, where $\eta = 1/\varepsilon$ is the inverse of the dielectric profile of the lattice and \mathbf{r} is the in-plane coordinate [114]. $\Delta\eta(\mathbf{r})$ induces the change of cavity mode field and the coupling amplitude between the cavity mode and the leaky modes is determined by the Fourier amplitude of the dielectric perturbation $\Delta\tilde{\eta}(k)$. Therefore, by reducing $\Delta\tilde{\eta}(k)$ at the corresponding vectors from the dominant Fourier components of the cavity modes to the leaky modes in momentum space, leakages into in-plane and vertical directions can be limited. As can be seen in Fig. 5.8(a), for the designed cavity modes, the modes mainly couple to the guided mode with the momentum components along the Γ -M and M-X directions, while they dominantly couple to the radiation mode along the Γ -M direction. Consequently, it is necessary to reduce the quantity of $\Delta\tilde{\eta}(k)$ at points where the guided mode is along the Γ -M and M-X directions and at region of light cone along the Γ -M direction. Figure 5.8(b) and (c) show the distributions of the dielectric perturbation for cavity A in real space and momentum space. The perturbation distribution in real space is firstly obtained by



(a)



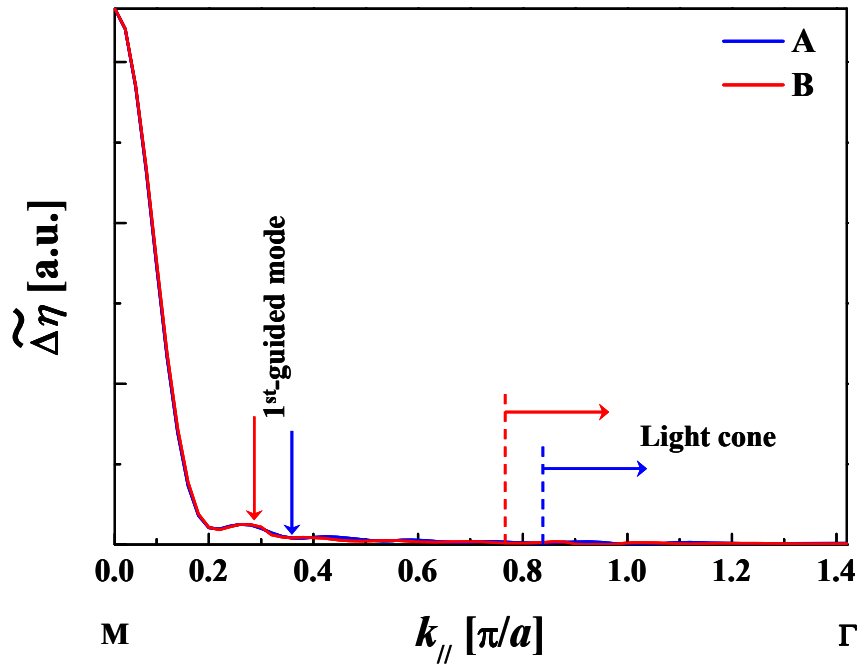
(b)



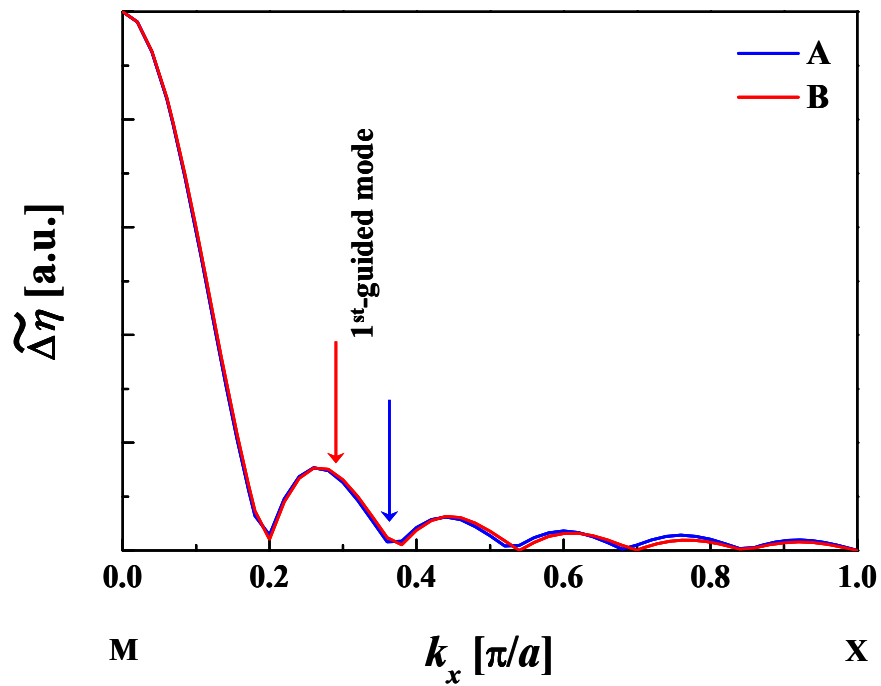
(c)

Figure 5.8 (a) Schematic illustration of mode distributions of cavity, radiation, and waveguide modes in momentum space. (b), (c) Distributions of the dielectric perturbation in real space and momentum space, respectively.

calculating the difference between the hole radii profile of cavity A and that of the structure with fixed r/a of $0.40a$. Then the distribution in momentum space is achieved by taking the real space distribution two-dimensional spatial Fourier transform. Figure 5.9(a) and (b) are one dimensional line scans of $\Delta\tilde{\eta}(k)$ along Γ -M and M-X, respectively. The values of momentum components of the 1st-guided mode and the light cone are extracted from the photonic band diagram. The 1st-guided mode only overlaps with very small amplitudes of $\Delta\tilde{\eta}(k)$ for cavity A in both directions, while it locates at the regions where the amplitudes of $\Delta\tilde{\eta}(k)$ are large for cavity B. This is because cavity B has the radii of air holes in the vicinity of the cavity larger than cavity A, and this increases the frequency of the cavity mode. Thus the cavity mode goes closer to the bandedge at the M point than that of cavity A. Therefore, the cavity mode of cavity B tends to more strongly couple to the guided mode and thus low in-plane Q . For the vertical direction, the amplitudes of $\Delta\tilde{\eta}(k)$ are likely to be small near the Γ point for both cavities. However, the size of light cone plays an important role here. Because the frequency of the cavity mode in cavity B is higher than that in cavity A, the size of light cone becomes bigger, consequently resulting in larger components of the amplitudes of $\Delta\tilde{\eta}(k)$ that lies within the light cone. Therefore the vertical Q of the mode in cavity B decreases. These are the reasons why the total Q factor of the mode in cavity A is much higher than that of cavity B. These results are then confirmed by concretely investigating and comparing the coupling behaviors of the modes in both cavities. Figure 5.10(a) and (b) shows the total electric field distributions in momentum space and their magnifications around the light cone region for the x -mode of cavity A and B including. Their magnitudes are normalized in order to accurately compare with each other. For the guided mode, equi-frequency contours of the 1st-guided modes at the same frequencies as the cavity modes are calculated. They are in circular shape and are plotted as solid circles in the figure. The equi-frequency contours only overlap with faint components of the cavity mode field for cavity A compared with that of cavity B, resulting in decoupling between the cavity mode and the 1st-guided mode and thus higher in-plane Q . Moreover, because of the localization of the mode in Fourier space and smaller size of light cone, the cavity mode in cavity A has a smaller number of momentum components falling inside the light cone and thus higher vertical Q than that of cavity B. These results



(a)



(b)

Figure 5.9 Comparison between the dielectric perturbations of cavity A and B along (a) Γ -M and (b) M-X directions with arrows indicating positions of the guided mode and the light cone.

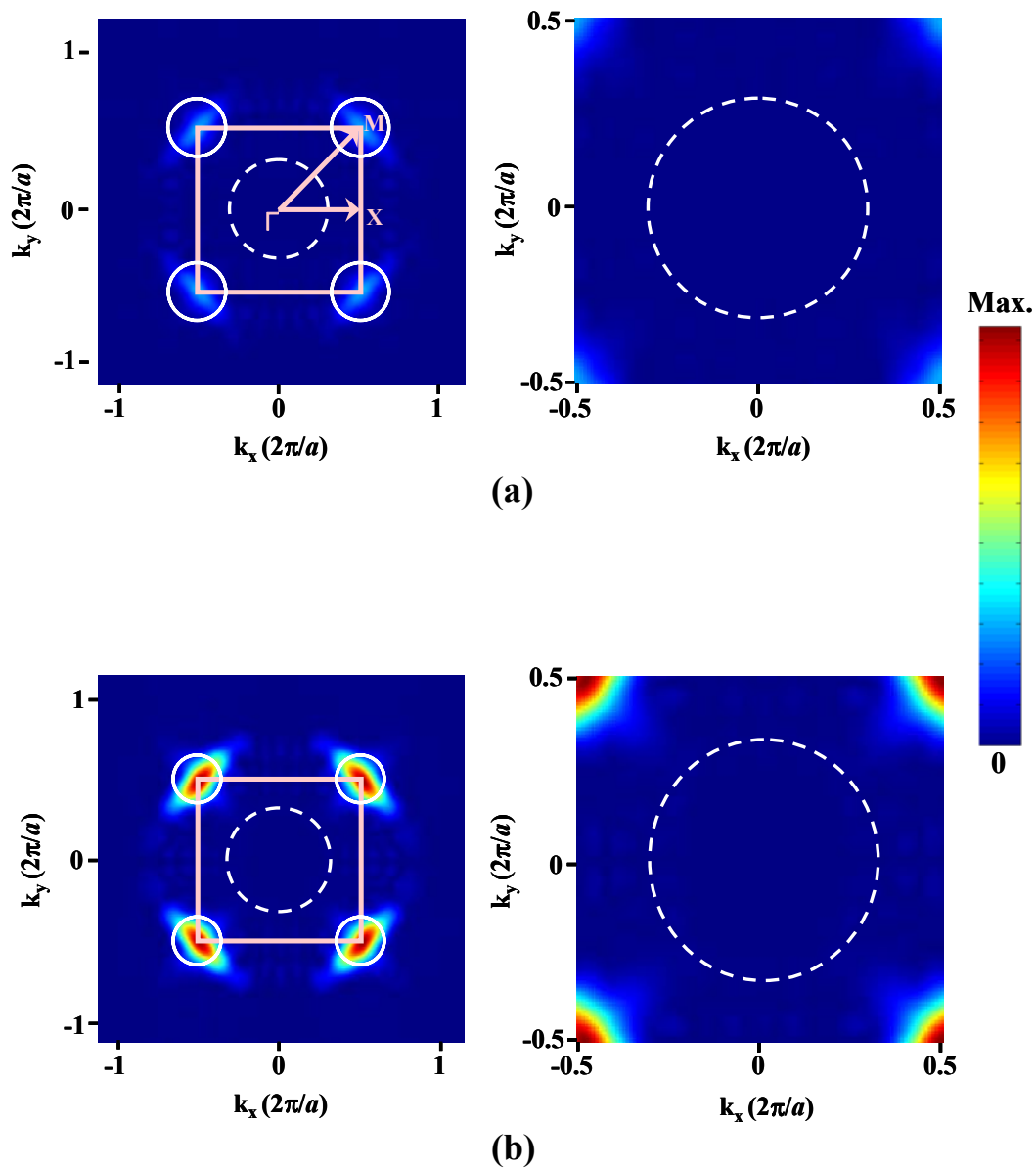
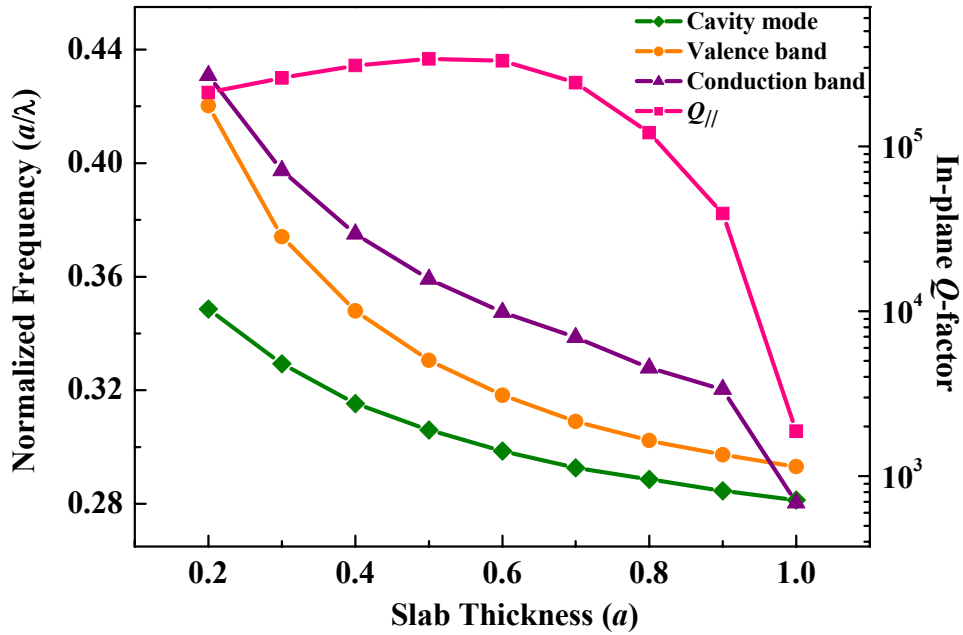


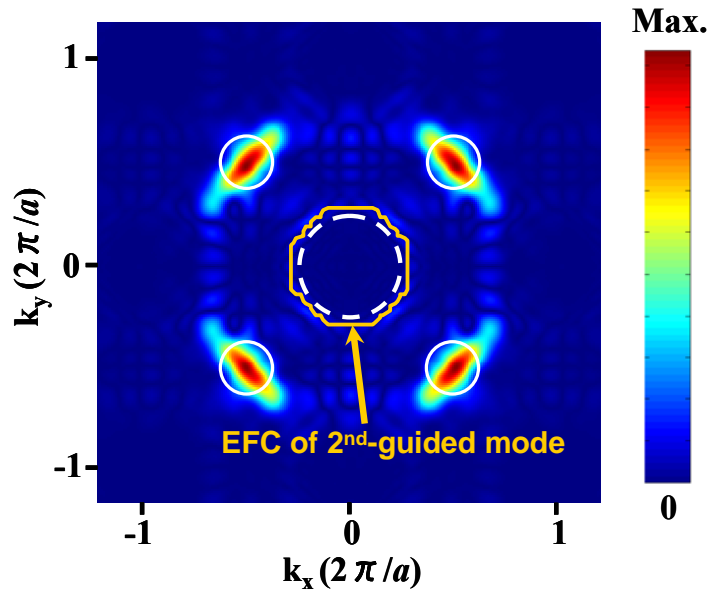
Figure 5.10 Total electric field distributions in momentum space and their magnifications around the light cone for the x -mode of (a) cavity A and (b) cavity B including light lines (broken circles) and equi-frequency contours of 1st-guided modes at the cavity mode frequencies (solid circles). They are presented in normalized unit.

agree well with the results from the study of couplings through the amplitudes of the dielectric perturbation in momentum space.

Another important parameter that requires a great intention to have high Q cavity is the slab thickness. Figure 5.11(a) shows dependence of the in-plane Q factor of the cavity mode in cavity A as a function of the slab thickness. The normalized frequencies of the cavity mode, conduction bandedge, and valence bandedge are also plotted in the graph. The frequencies of the bandedges decrease as the slab thickness increase due to a larger fraction of dielectric. The conduction bandedge comes down more quickly than the valence band resulting in the reduction of bandgap size. However, that does not concern the case here, because the cavity mode is always below the valence bandedge. However, the in-plane Q factor decreases as the slab is thicker. This comes from two reasons. The first one is the effect from the losses induced by the valence band (1st-guided mode). As the slab becomes thicker, the cavity mode and the valence bandedge come closer to each other. This results in a smaller diameter of the equi-frequency contour of the 1st-guided mode near point M. As a result, the equi-frequency contour tends to overlap with stronger components of the cavity mode whose its peak intensity is at point M. The other reason comes from the coupling between the cavity mode and the conduction band (2nd-guided mode). The conduction bandedge falls down as a function of the slab thickness and comes below the valence bandedge when the slab thickness is more than $0.90a$. And the in-plane Q abruptly degrades when the cavity mode starts to couple to this additional guided mode. Total electric field distribution in the momentum space of cavity A with the slab thickness $d = 1.0a$ with the equi-frequency contours confirms these assumptions as shown in Figure 5.11(b). The equi-frequency contour of the 1st-guided mode becomes very small and overlaps with strong components of the cavity mode near the point M. Moreover, because the cavity mode spectrally overlaps with the 2nd-guided mode, the coupling between the two modes must also be taken into account. The equi-frequency contour of the 2nd-guided mode exists in the vicinity of the light line and it overlaps with expanded components of the cavity mode as seen in the figure, leading to additional loss of the cavity mode into the in-plane direction. From these results, it is preferable to restrict the slab thickness around $0.60a$ to assure the high in-plane Q . It is worth noting that the vertical Q just slightly increases as the slab thickness increase due to a decrease in the frequency of the mode, thus reducing the size of the light cone.



(a)



(b)

Figure 5.11 (a) Dependence of normalized frequencies of the cavity mode, valence bandedge, and conduction bandedge of cavity A on the slab thickness. The in-plane Q as a function of the slab thickness is also plotted on the axis on the right hand side. (b) Total electric field distribution in momentum space of cavity A with the slab thickness $d = 1.0a$, including light lines (broken circles) and equifrequency contours of 1st-guided modes (solid circles) and 2nd-guided mode (orange closed figure) at the cavity mode frequency.

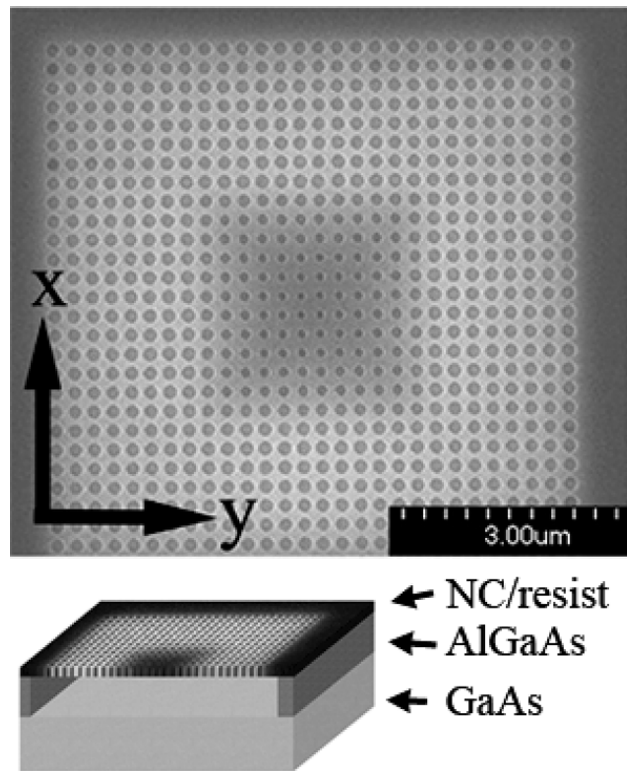
In this section, it has been shown that a cavity with an ultra-high Q can be obtained even cavity modes do not locate within the gap or even no bandgap at all. This has been achieved by decoupling the cavity mode from possible losses, consisting of guiding loss and radiation loss, by appropriately design the distribution of them in the momentum space. In the following section, various applications of the designed cavity, such as materials with low refractive index and quantum cascade lasers, will be presented. Those results will prove a promising performance and flexibility of the cavity.

5.4 Applications of high- Q graded photonic crystal cavities

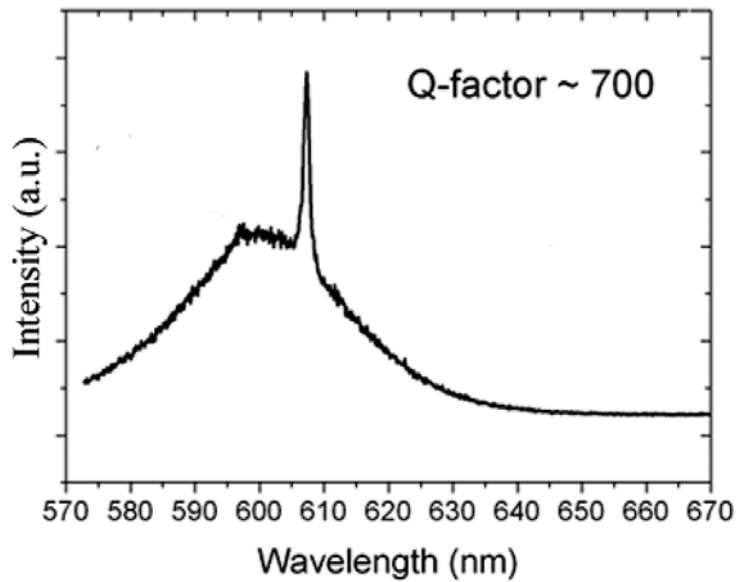
Light emitters confined in photonic crystal cavities are promising candidates for the development of various high performance optical devices. However, there are some applications that have been hindered from the utilization of photonic crystals to improve their performances, such as materials with low refractive index, and quantum cascade lasers, due to a lack of photonic bandgap in a frequency region of interest. In the previous section, the designed cavity has been shown that it can have an ultra-high Q in a GaAs-based (refractive index = 3.4) air-bridge structure for transverse electric (TE) polarized light. In this section, it is shown that the designed cavity can also be applied to achieve high Q s in colloidal nanocrystals with low index of only 1.575 and in transverse magnetic (TM) -like polarized quantum cascade lasers. In addition, the designed cavity is shown to be very promising for realization of highly-efficient entangled photon sources.

5.4.1 High- Q graded photonic crystal nanocavity with low refractive index

Figure 5.12(a) shows an in-plane scanning electron microscope image of a patterned structure after development and a sketch of the final air-bridge structure after wet etching. The slab is an electronic resist (ZEP520-12) embedding colloidal nanocrystals with a refractive index of 1.575 [116,117]. Due to the low index contrast between the slab and the surrounding air cladding, strong light confinement cannot be achieved with conventional cavity structures. Both vertical and in-plane Q s in such cavities are very low resulted from high frequencies of cavity modes and very small size of photonic bandgap locating at very high frequency range. The designed graded cavity was then utilized to improve the Q factor. The air hole radii profile was the same as that of cavity A, which is the optimized cavity, in both x and y direction. The slab thickness



(a)



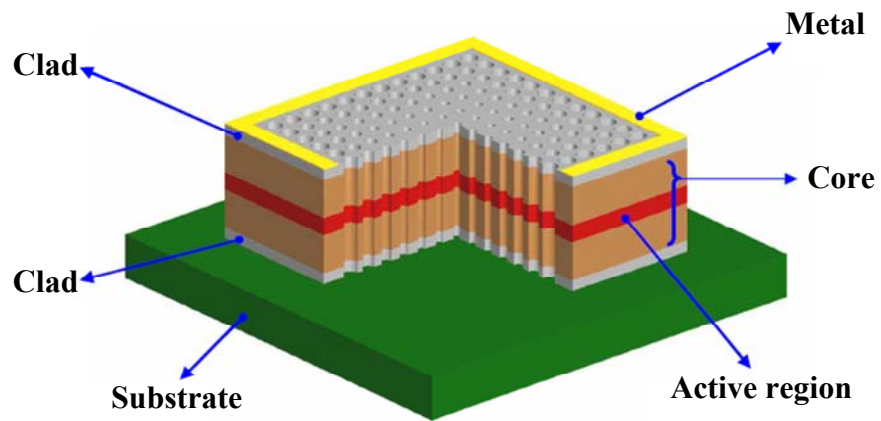
(b)

Figure 5.12 (a, above) Scanning electron microscope image of the patterned nanocavity. (a, below) Sketch of the final air-bridge structure. (b) Photoluminescence spectra from the nanocavity at room temperature.

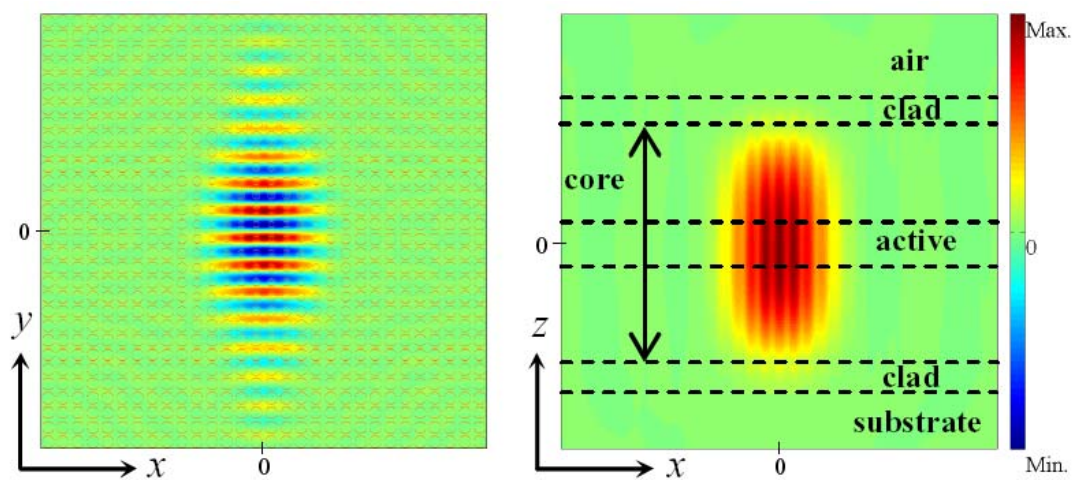
was increased from $0.60a$ of cavity A to around $1.20a$ to reduce the cavity mode frequency, and thus the size of light cone, to assure a strong localization in the vertical direction. The highest theoretical Q for the cavity was equal to 5,700 with mode volume of $1.8(\lambda/n)^3$. The large difference in the theoretical Q between this structure and the GaAs-based structure roots from the difference in the refractive index. Figure 5.12(b) shows a typical spectrum collected from the suspended resist cavity. A sharp peak, with a Q factor of ~ 700 , is present in the emission spectrum, which is in a visible range. This value of Q is the highest value reported so far in low index materials coupled with photonic crystal cavities. These results reveal that the designed graded cavity is very flexible. It can be applied to the structure with much less refractive index without any major change of the design in order to achieve high Q .

5.4.2 Reduction of threshold current of quantum cascade lasers by graded photonic crystal cavity

In quantum cascade lasers, whose light emission is resulted from intersubband transitions, photons are polarized in TM-like modes. Unfortunately, two-dimensional photonic crystal with air holes does not possess a photonic bandgap for such modes in a frequency region of interest. As a result, with conventional cavity structures light dominantly leaks out of the cavity in the in-plane direction. Moreover, structure of the quantum cascade laser is not an air-bridge. Since it is necessary to inject electrical current to drive a quantum cascade laser, cladding layers have to be semiconductors as shown in Fig. 5.13(a). These cladding layers generate an additional leaky channel of light into substrate, and thus decreasing vertical Q . These problems can be solved by exploiting the designed graded cavity. The air hole radii profile of cavity A was adopted in both x and y direction. The slab thickness was optimized to be $6a$ to improve the light confinement in the vertical direction. Cavity mode field distributions for vertical component of electric field (E_z) are shown in Fig. 5.13(b). The mode is well confined in the graded region within the core layer with the maximum calculated Q of 2,200, which is 18-time higher than the value of conventional cavities designed for TM-like modes [118]. The Q factor is lower than that of cavity A due to the additional leak into the substrate direction. This improvement of Q with consideration of effect of material absorption allows the threshold current of the designed structure to be reduced to at least one fifteenth of



(a)



(b)

Figure 5.13 (a) Schematics of a graded photonic crystal quantum cascade lasers microcavity. (b) Mode distributions of vertical electric field component (E_z) with $d = 5a$ in in-plane view and cross sectional view.

that of a conventional Fabry-Perot quantum cascade lasers. These results suggest a new way of cavity designs for TM-like polarized light, which have been an unexplored field up to now.

5.4.3 Prospects of graded photonic crystal nanocavity for highly-efficient entangled photon sources

It has been suggested that embedding a quantum dot in a cavity supporting doubly-degenerated cavity modes can improve the degree of entanglement of polarization-entangled photon sources based on biexciton-exciton cascade emissions [101,102] by increasing a photon emission rate through a so-called Purcell effect [97]. And because the emission rate enhancement factor is proportional to a ratio of Q and V_{eff} , a cavity with ultra-high Q/V_{eff} doubly-degenerated modes is preferable to realize highly-efficient entangled photon sources. The designed cavity discussed in Chapter 5.3 (cavity A) is then very suitable to be applied to such devices due to its ultra-high Q/V_{eff} , which is about two times higher than the record value [115]. With this cavity together with an improvement of growth technique, which can fine control a number and a position of quantum dots, the realization of entangled photon sources can be expected. Another important parameter to realize the entangled photon source is a spatial overlap between the degenerated modes, because it indicates an available area where a quantum dot should be located to undergo the effect from the fields of modes and generate entangled photon pairs. The overlapping area between two modes was defined to be the area in which their field intensities are more than a half of their maxima. Assuming the wavelength of the cavity modes to be 1 μm , the overlapping area of x - and y -modes of cavity A is shown in Fig. 5.14(a). There is a large central area of around $90 \times 90 \text{ nm}^2$ and small areas of around $30 \times 15 \text{ nm}^2$ in the vicinity of the most inner holes. These sizes of overlapping area are comparative with those reported in Ref. 115, while the Q/V_{eff} of the designed cavity is two times higher. The overlapping area tried to increase the possibility to generate the entangled photon pairs. The simplest way to increase the overlapping area, and thus the possibility to generate the entangled photon pairs, is to just remove the 4 innermost holes. As expected, the overlapping area becomes much bigger as shown in Fig. 5.14(b). The central area becomes around $300 \times 300 \text{ nm}^2$. However, there is a trade off in the degradation of Q/V_{eff} , in which Q decreases to 15,000 and V_{eff} becomes larger being about $1.267(\lambda/n)^3$.

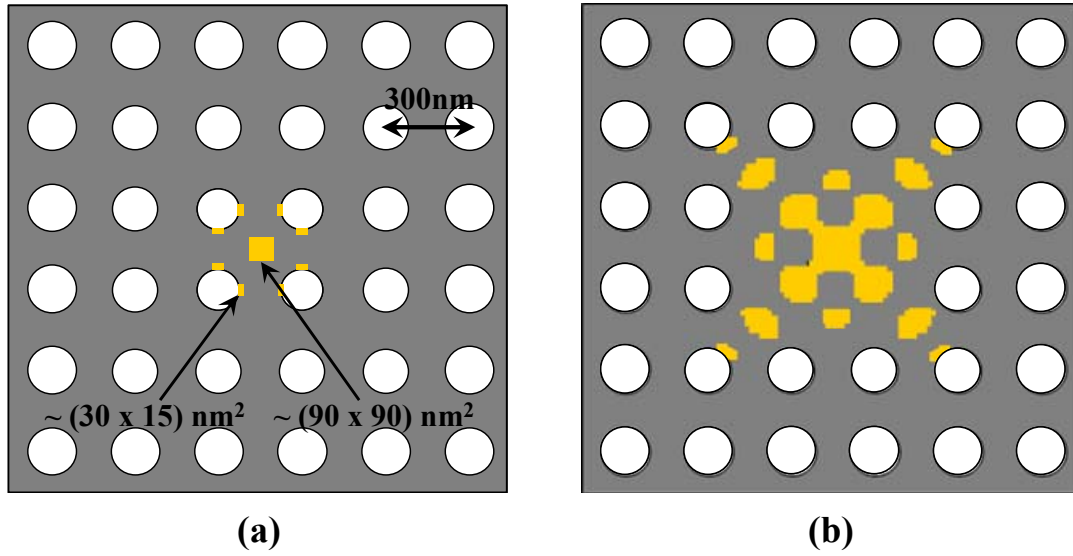


Figure 5.14 Overlapping area of the degenerated modes in (a) cavity A and (b) cavity A with the 4 innermost holes removed.

5.5 Summary

In this chapter, a photonic crystal nanocavity with an ultra-high Q and small mode volume has been achieved even cavity modes do not locate within the gap or even no bandgap at all. The air hole radii have been modulated with a quadratic profile to decouple the cavity mode from possible losses consisting of guiding loss and radiation loss, resulting in strong light confinement in all three directions. By reducing the Fourier amplitude of the dielectric perturbation, governed by the air hole radii profile, at the corresponding vectors from the dominant Fourier components of the cavity modes to the leaky modes in momentum space, leakages into in-plane and vertical directions have been limited, leading to doubly-degenerated modes with very high Q of 120,000 and mode volume V_{eff} of $0.79(\lambda/n)^3$. The figure of merit Q/V_{eff} in the weak coupling regime is about two times higher than the highest value reported so far for doubly-degenerated modes. Therefore, this cavity is very promising for the realization of entangled photon sources. Finally, the designed cavity has been applied to achieve high Q cavities for material with low index and for quantum cascade lasers, in which a lack of photonic bandgap usually hinders them from applications. These results emphasize a flexibility of the cavity. The results achieved in this chapter

extend the scope of optical devices that can utilize photonic crystal cavities to improve their performances, while the photonic bandgap is no longer a preliminary requirement.

Chapter 6

Designs of High- Q Nanocavities in Three-Dimensional Photonic Crystals with Finite Structural Sizes

6.1 Introduction

Since the concept of photonic crystals has been proposed [10,11], the use of them to manipulate light has become an active field of research due to the existence of the photonic bandgap. Thus far, the mainstream of the photonic crystal research has been focused on two-dimensional structures, including the results presented in Chapter 4 and Chapter 5, because of ease in fabrication that is based on well-established fabrication technologies. Many striking achievements, such as ultra-low threshold lasers [119-122], single photon sources [100,123,124], and cavity quantum electrodynamics in a strong coupling regime [106,125-128] have already been realized. However, in order to achieve a full control of light in all three dimensions, it is necessary to extend the photonic bandgap to the third dimension. Several three-dimensional photonic crystal structures with a complete photonic bandgap, a frequency range in which light is forbidden to propagate in all directions, have been demonstrated so far [13,18,40]. When an artificial defect is introduced into a perfect crystal, localized modes within the PBG can be generated. Therefore, light that couples to these modes can be strongly confined within a point defect cavity or guided along a line defect waveguide without loss. Because it is difficult to simultaneously fulfil the requirements of introduction of an artificial defect and a light-emitting element into a three-dimensional structure, most of research on three-dimensional photonic crystals has been concentrated on defects in passive devices [13,22-

24,40,129] or on active devices with unperturbed crystals [130]. Because of this restriction in the aspect of fabrication, study on designs of defect cavities in three-dimensional photonic crystals has been left as an almost-unexplored field of research up to now [131-136]. In fact, one may think that because the confinement mechanism of light in three-dimensional photonic crystal cavities is Bragg reflection in all three dimensions, Q factors of cavity modes embedded in the photonic bandgap can be exponentially increased with a number of photonic crystal periods surrounding the cavity. Therefore, a cavity with infinite Q can be achieved by just locating the cavity inside an infinitely-large three-dimensional photonic crystal structure without any complicated designs like in the two-dimensional case. However, with current fabrication technologies, the number of periods that can be practically fabricated is still very limited. The highest experimental Q ever reported so far for three-dimensional photonic crystal cavities is only 2,300 [47], compared with a few ten thousands in active cavities [126,127,137] and a few millions in passive cavities [74,75] in two-dimensional photonic crystal structures. The low value of Q is partly resulted from a lack of proper cavity designs, which can achieve high designed- Q even with a small size of three-dimensional structures, and this value is still needed to be improved in order to realize many promising applications including ultralow threshold lasers and quantum information processing.

In this chapter, three designs of high Q cavities in three-dimensional photonic crystals with finite structural size that can be practically fabricated are presented. Two of them are achieved by tuning resonant frequencies of their cavity modes to the middle frequency of the complete photonic bandgap, where the mode localization is strongest, and thus high Q s, by means of optimizing size of the defect cavities. Apart from tuning cavity modes to the midgap frequency, the Q factor is then further improved by modifying the cavity structure through shifting of dielectric rods surrounding the cavity. The highest designed Q is up to 73,300 which is about an order of magnitude improved, compared with the non-modified cavity with the same structural size. Therefore, by introducing an efficient light emitter into these designed cavities, ultralow threshold lasers or cavity quantum electrodynamical effects may be expected.

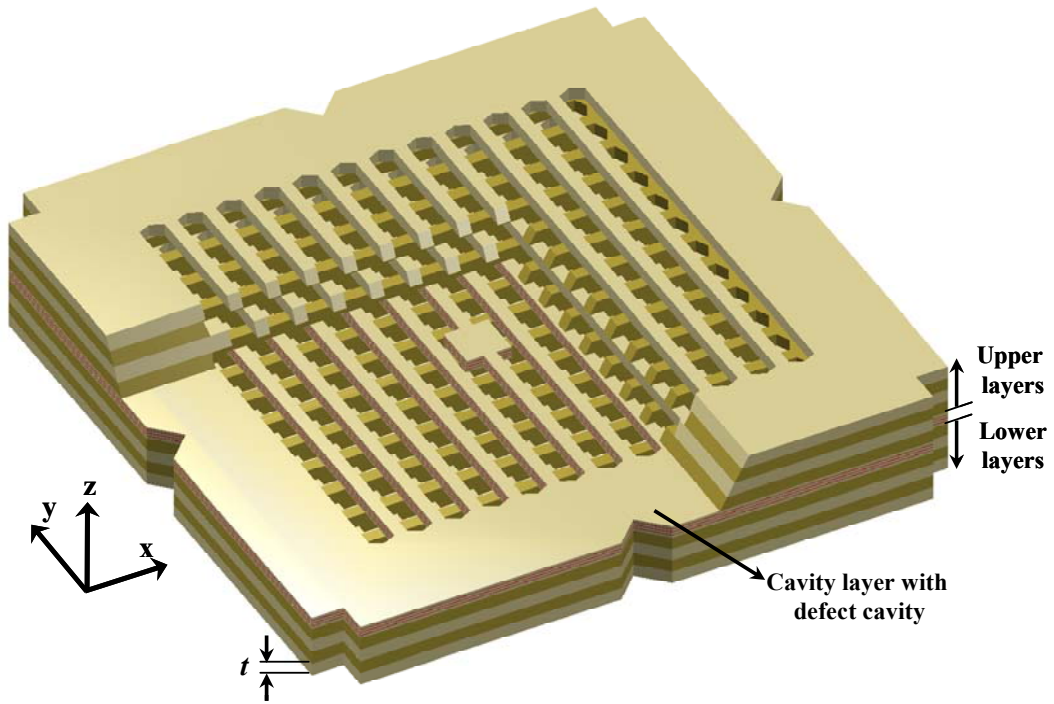
6.2 Designs of high- Q nanocavities in woodpile photonic crystals by tuning cavity modes to photonic midgap

In two-dimensional photonic crystal structures, a number of photonic crystal periods surrounding the cavities that can be fabricated can be considered as infinite. Therefore, if cavity modes is well designed to be located inside photonic bandgap, only out-of-plane losses is required to be suppressed in order to achieve high- Q cavities, while propagating losses into the plane of photonic crystal patterns can be negligible. In contrast, the size of three-dimensional structures that can be fabricated is limited. And this is the main factor that has been hindered the three-dimensional photonic crystals from the realization of high- Q cavities. Cavity mode that has a frequency inside photonic bandgap is localized in the defect region and exponentially decays once it enters the crystal. Moreover, because the rate of decay is the largest when the frequency is near the center of the gap [84], modes with frequencies at the center of the gap are then most strongly attached to the cavity. As a result, it is necessary to design the cavity to have cavity mode located closet to the middle frequency of the photonic bandgap to gain an advantage from the photonic bandgap effect as much as possible. Previous work on a design of defect cavity in a three-dimensional photonic crystal has only roughly investigated this kind of tuning [24,131].

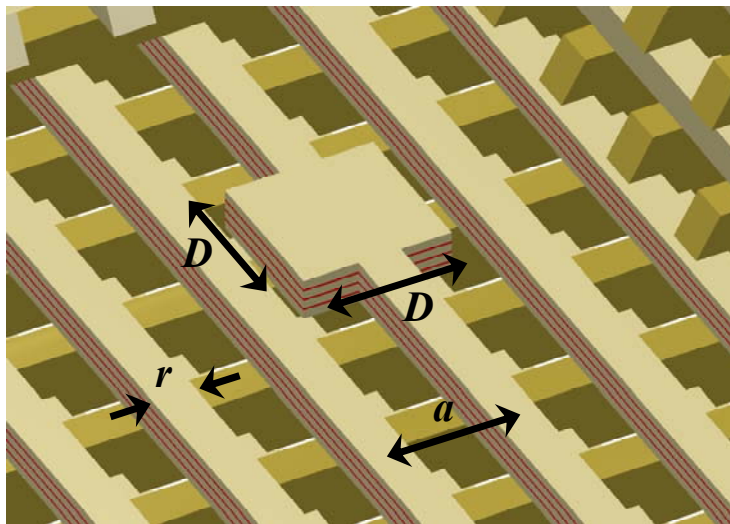
In this section, two types of cavities, square-shaped and rectangular-shaped defect nanocavities, in woodpile photonic crystal structures are designed according to the concept discussed above. Their sizes are fine optimized in order to tune the cavity modes to the midgap frequency. It is shown that a cavity mode that is nearest to the midgap frequency actually has the highest Q factor, and the Q factor decreases as the mode is detuned from the midgap.

6.2.1 Square-shaped defect nanocavity

The design structure is based on a so-called woodpile structure, which is a stack of dielectric rods. The rods of adjacent layers cross each other orthogonally, and those of the next nearest neighboring layers are aligned parallel but with a half period shift as shown in Fig. 6.1(a), in which a portion of upper stacked layers is removed to show a cross section of the stacked structure and to reveal a cavity. The dielectric rods



(a)



(b)

Figure 6.1 (a) Schematic illustration of the designed structure. A portion of upper layers is removed to show a cross section of the stacked structure and to reveal the cavity. (b) A magnification of the cavity.

that constitute the woodpile cavity have a refractive index of 3.4 corresponding to that for GaAs. The width r and thickness t of the rods are $0.25a$ and $0.40a$, respectively, where a is an in-plane periodicity (rod pitch). A number of in-plane rods for each layer is fixed at 11. This number of rods is the limited value that can be fabricated using micromanipulation techniques, which will be described in next Chapter. A cavity layer containing a defect is inserted between upper and lower stacked layers resulting in a total number of the stacked layers of $N_u + 1 + N_l$, where N_u (N_l) represents a number of the upper (lower) stacked layers. N_u is set to be equal to N_l for all structures studied in this thesis. A three-dimensional photonic crystal defect with a square shape with width of each side D is located at the center of the pattern of the cavity layer to construct a nanocavity. A magnified view of the nanocavity is depicted in Fig. 6.1(b). With these computational parameters, a complete photonic bandgap is open in a range from 0.346 to 0.408 in a normalized frequency unit. There are six cavity modes, defined as modes A to F, existing inside or in a vicinity of the bandgap. A large number of cavity modes is resulted from the large size of the cavity. The size of defect D is varied from $1.0a$ square to $1.3a$ square to tune the modes across the bandgap. The normalized frequency of each cavity mode is shown in Fig. 6.2 as a function of defect size. The complete photonic bandgap is also depicted in the figure as an unshaded region, where a dotted line represents the midgap frequency of the photonic bandgap. It can be seen that as the cavity size is increased, the frequencies of all modes decrease, because the mode fields are concentrated more and more in the high-index dielectric region. Therefore changing the defect size can be used as an effective tool to tune the cavity mode of interest to the midgap frequency. The size of the square-shaped defect D^2 is varied from $(1.0a)^2$ to $(1.3a)^2$. At $D = 1.1a$, mode D approaches the midgap, while mode C is slightly deviated from the midgap. Modes B and E get close to the bandedge. Mode A is at the bandedge, while mode F is slightly embedded within the lower bandedge. Figure 6.3(a)-(f) show field distributions of E_x component of modes A to F at the center of the cavity layer with $D = 1.1a$. Gray lines show boundaries of the dielectric rods and the cavity. Obviously, the field distributions directly associate with the position of the modes in the bandgap. The modes that are near the midgap (Modes C and D) are strongly confined within the cavity. The mode confinement becomes weakened as the mode frequency deviates

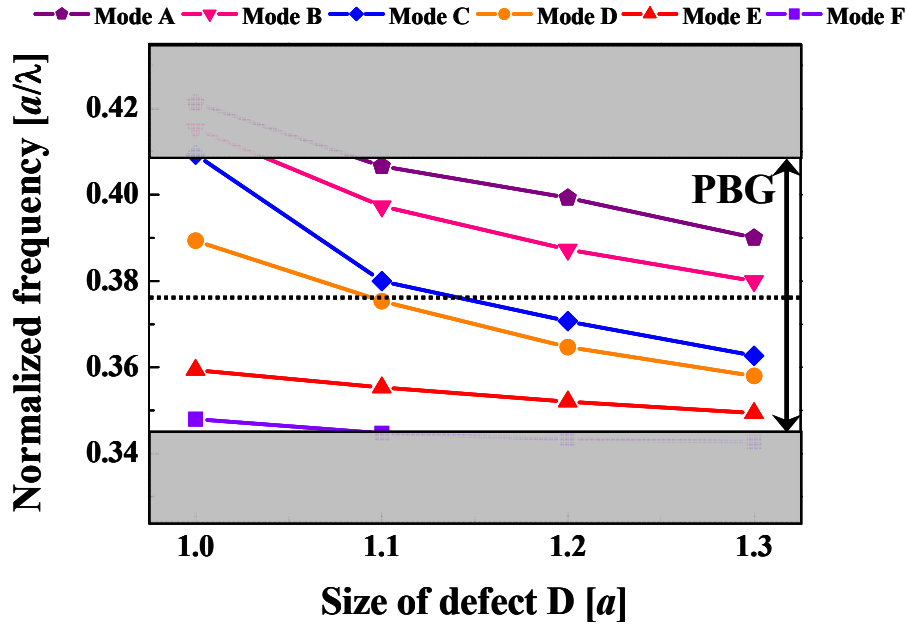


Figure 6.2 Normalized frequencies of six cavity modes (A to F) existing in the cavity as a function of the size of the square-shaped defect. Unshaded region and dotted line represent the complete photonic bandgap and midgap frequency, respectively.

from the midgap (Modes B and E). And the modes lose the strong confinement in the cavity and start to expand over a wide area when they reach the bandedge (modes A and F). These results are a direct evidence of the photonic bandgap effect. Then, the defect size is set to $D = 1.1a$ and Q factors for modes A to F are investigated as a function of the number of the stacked layers. The number of stacked layers is varied from 9 to 41. Figure 6.4 shows that total Q factors for all modes depicted in solid lines increase exponentially as the number of the stacked layers increase until their saturations. It is worth noting that dividing the total Q factor (Q_{total}) into in-plane Q (Q_{\parallel}) and vertical Q (Q_{\perp}) for three-dimensional structures is not straightforward like in the two-dimensional systems discussed in previous Chapters. Because the structure here is not based on a waveguide like in the two-dimensional systems, boundaries set at a half-wavelength above and below the structure to separate in-plane and out-of-plane losses are not available for three-dimensional systems. A possible way to separately consider losses into each direction in order to understand which factor limits the total Q is to estimate the in-plane Q to be the saturated value of the total Q when the number of stacked layers is very large, i.e., 49 layers. With such a

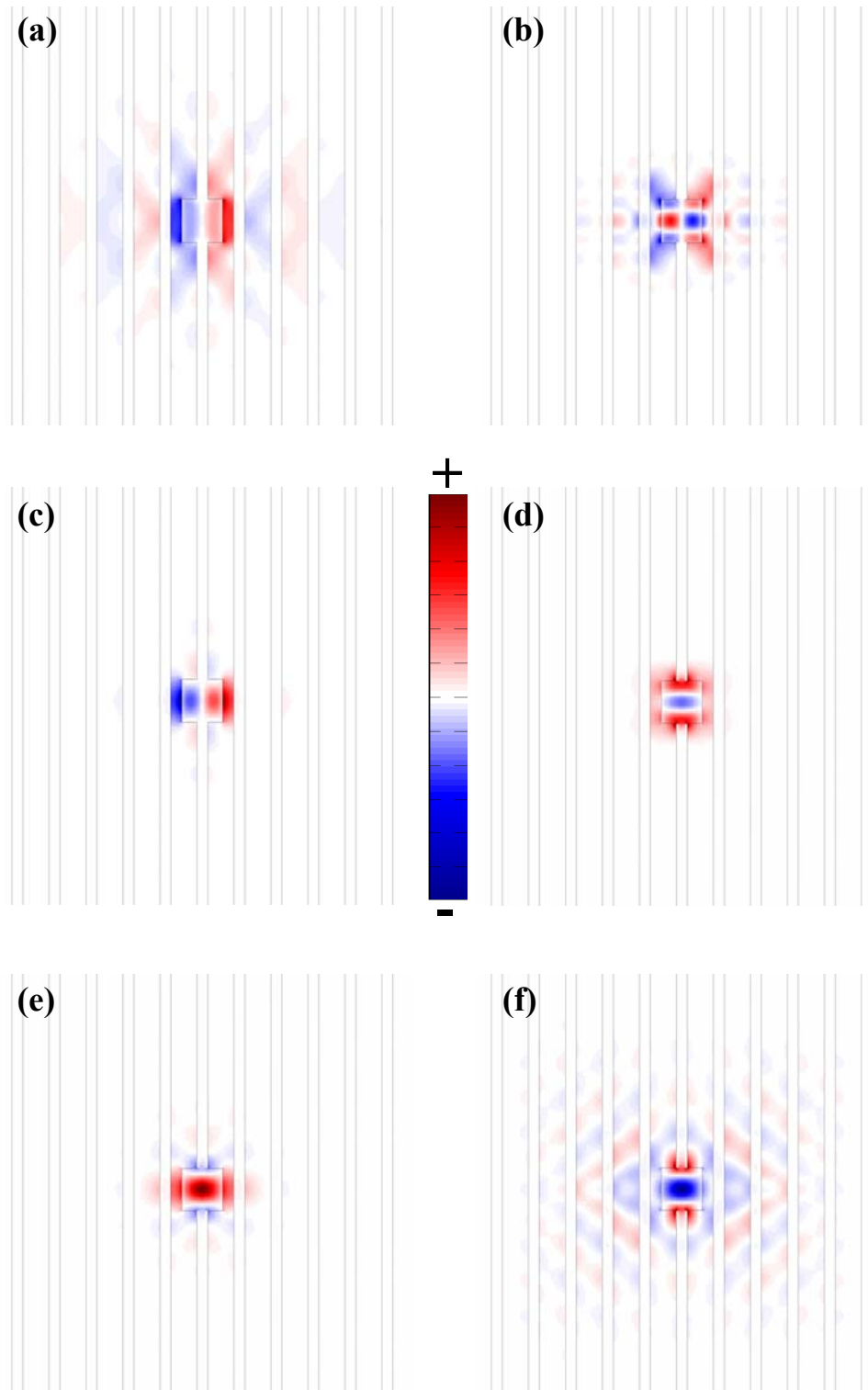


Figure 6.3 (a)-(f) Field distributions of E_x component of modes A to F, respectively, at the center of the cavity layer with $D = 1.1a$. Gray lines show boundaries of the dielectric rods and the cavity.

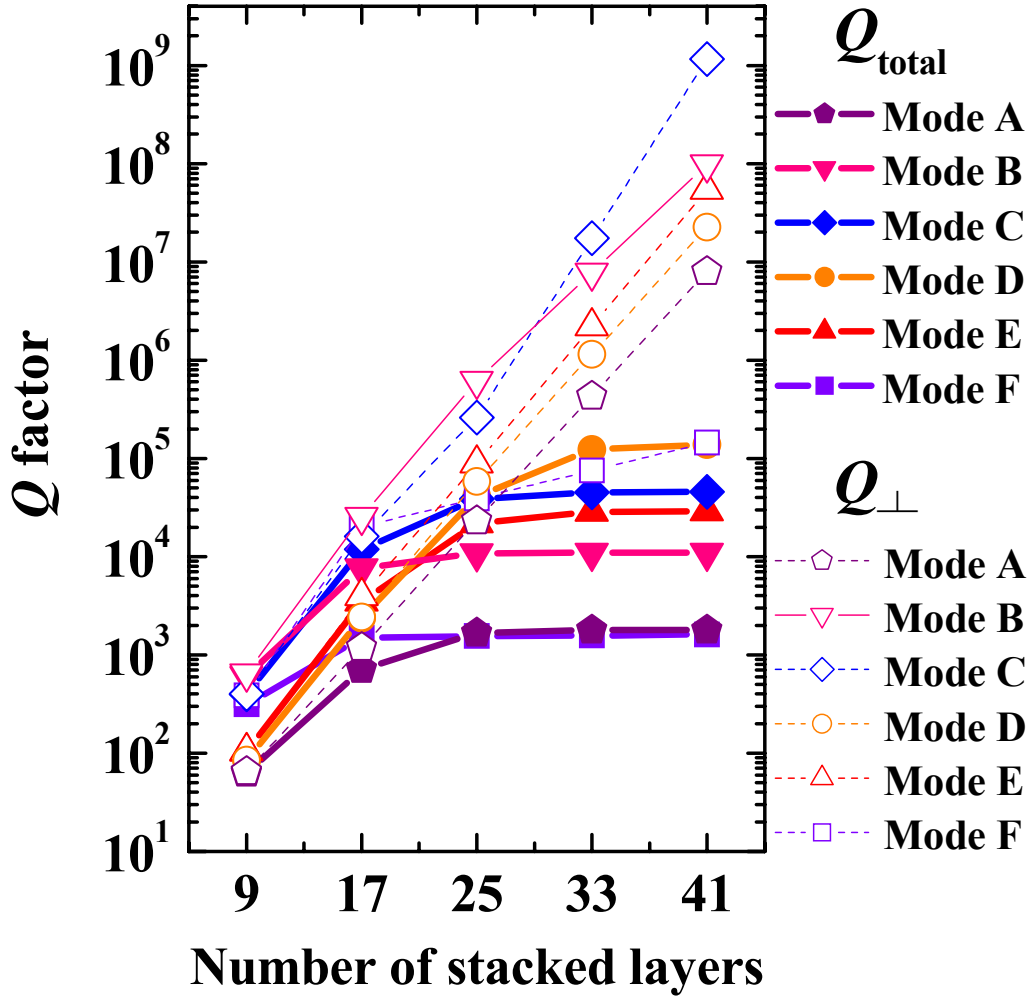


Figure 6.4 Dependences of total Q s (solid lines with closed symbols) and vertical Q s (dotted lines with open symbols) of modes A to F on the number of stacked layers with $D = 1.1a$. In-plane Q s for modes A to F are calculated to be 1800, 10970, 45460, 138540, 29000, and 1610, respectively.

large number of stacked layers, losses into the vertical direction are negligible, leading to a relation:

$$\frac{1}{Q_{//}} = \frac{1}{Q_{total}} - \frac{1}{Q_{\perp}} \approx \frac{1}{Q_{total}} \quad (6.1)$$

Therefore, the in-plane Q is obtained using this relation, where Q_{total} is the total Q of the structure with 49 stacked layers, and is set to be constant with the increase of the stacked layers. From Fig. 6.4, when the number of the stacked layers is small, the vertical Q is much lower than the in-plane Q , and thus limits the total Q . However, the vertical Q s of all modes can be increased exponentially by adding the number of the stacked layers as shown in the figure, except for that of mode F because mode F is embedded in the lower band and rarely undergoes the photonic bandgap effect. It should be noted that although the growing rate as a function of the number of the layers is the same, value of the vertical Q for each mode is different. In the vertical direction, apart from the photonic bandgap effect, the cavity field cancellation also helps confine the mode. Concretely, the mode with node of electric field at the center of the cavity results in higher vertical Q , because the field cancels out in the far field. This is why, for example, mode C has higher total Q than mode D when the number of the stacked layers is small, i.e., less than 25, due to its higher vertical Q . However, with a large number of the stacked layers, the in-plane Q becomes the factor that limits the total Q . An obvious way to break this deadlock would be to increase the number of in-plane rods to increase the in-plane Q . Nevertheless, this is still a question considering the present fabrication technique. For that reason, tuning the cavity mode to the midgap frequency to gain an advantage from the photonic bandgap effect with restricted in-plane rods as much as possible would be then the best solution unless the fabrication technique is to be developed. As shown in Fig. 6.4, the saturated Q values are inversely proportional to the distance that the modes are separated from the midgap frequency. As expected, mode D whose frequency is the closest to the midgap has the highest Q with its value exceeding 10^5 when the number of the stacked layers is more than 33.

The number of the stacked layers is then fixed at 25, which is the number of stacked layers that will be practically fabricated in later Chapter, and investigate the dependence of the Q factors on the size of the defect. Again, as shown in Fig. 6.5, all modes have their maximum Q s when their frequencies locate the nearest to the midgap frequency and decrease as they deviates from the midgap. It can be seen

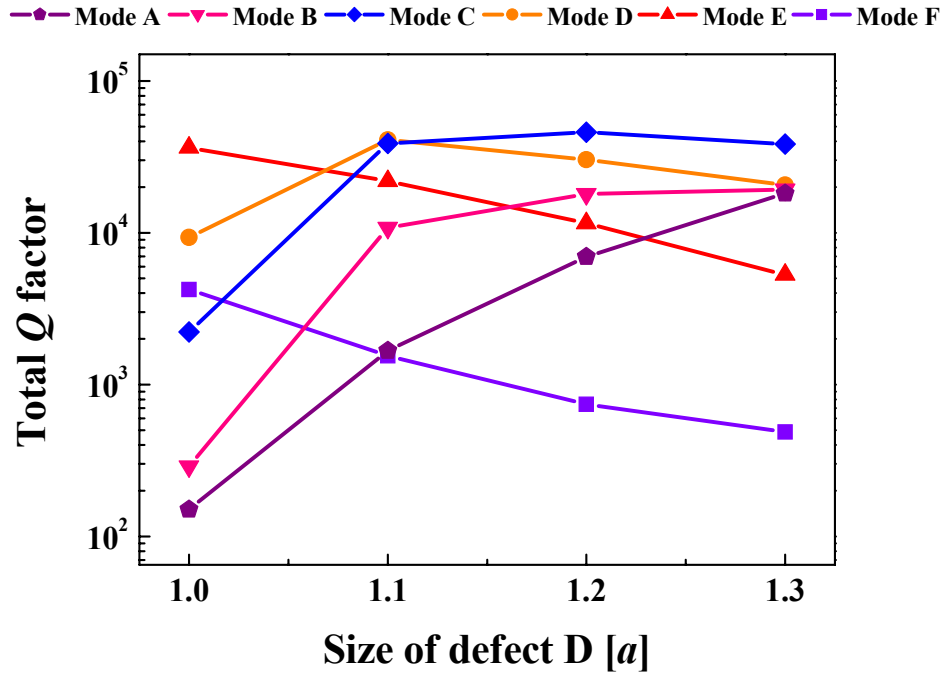


Figure 6.5 Dependences of total Q s of modes A to F on size of defect when the number of the stacked layers is fixed at 25.

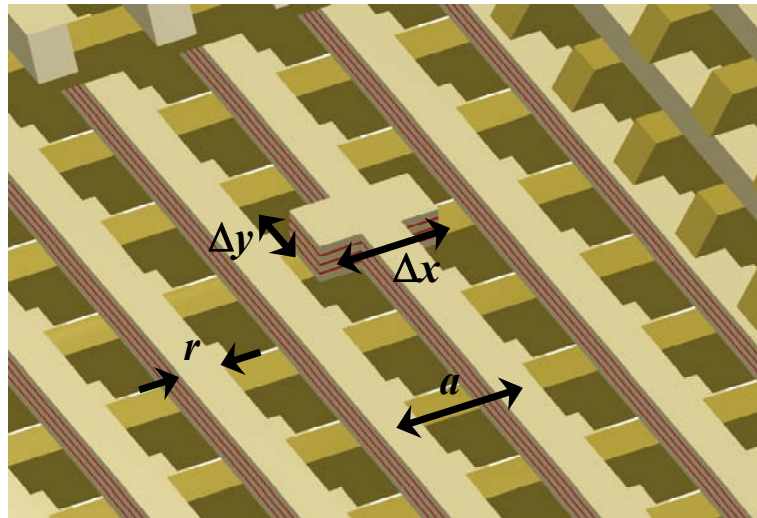
that with $D = 1.1a$, the Q factors of modes C and D are very high and comparative with each other. However, in various applications concerning light-matter interaction, such as cavity quantum electrodynamics, mode that has an antinode of electric field at the center of the cavity would be more promising. If light-emitting elements, such as quantum dots, are located at the antinode of the electric field, they can effectively interact with each other. Moreover, electron and hole densities are much lower near the surfaces of the etched patterns [96]. As a result, light modes, in which their antinodes locate near the rim of the cavity region, cannot be efficiently coupled with the emitters locating inside the cavity. From above reasons, mode D with its antinode of the field at the center of the cavity would be more suitable for applications. The Q factor of mode D is highest when $D = 1.1a$ with its value about 41,000 with mode volume of $\sim 0.441(\lambda/n)^3$. Therefore, in fabrication discussed in Chapter 7, the cavity size will be set to this value. The Q factors (mode volumes) for mode A, B, C, E, and F are $\sim 1,700 (1.462(\lambda/n)^3)$, $10,800 (0.553(\lambda/n)^3)$, $39,000 (0.668(\lambda/n)^3)$, $22,000 (0.553(\lambda/n)^3)$, and $1,550 (1.462(\lambda/n)^3)$, respectively. It should be notified beforehand that the sensitivity of Q s on the size of

the defect shown in Fig. 6.5 will play a major role in discussion of experimental Q s obtained from the fabricated devices discussed in Chapter 7.

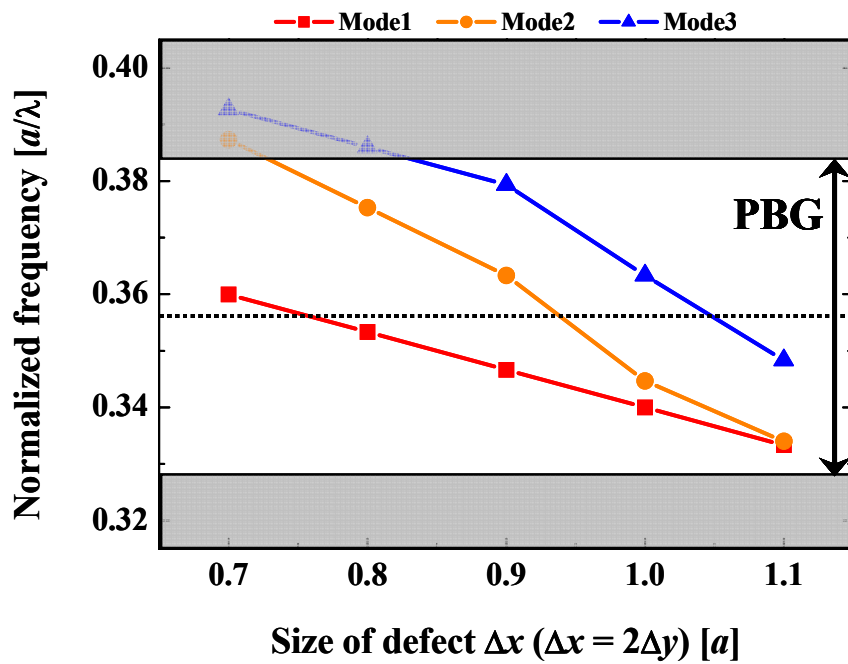
6.2.2 Rectangular-shaped defect nanocavity

In section 5.3.1, a high- Q cavity with square shape has been presented. However, the cavity is quite large and contains a lot of cavity modes with small frequency separations, as can be seen in Fig. 6.2. This may lead to multi-mode operation, which is undesirable in some applications, such as lasers, when the light emitter is introduced into the defect cavity. By changing shape and reducing size of the defect, a cavity with a small number of modes with wide frequency separation can be achieved [131].

The fundamental structure used to design is the same as that in last subsection, a woodpile structure with 11 in-plane rods, with width $r = 0.30a$ and thickness $t = 0.40a$. The same defect structure as in Ref. 131 is exploited to form a nanocavity. The cavity has a rectangular shape with its length and width defined as Δx and Δy , respectively, where a ratio of Δx to Δy is fixed to 2. A schematic illustration of the nanocavity is depicted in Fig. 6.6 (a). A complete photonic bandgap is open in a range from 0.327 to 0.384 in a normalized frequency unit. The normalized frequencies of cavity modes in the rectangular-shaped cavity are shown in Fig. 6.6(b) as a function of defect size, where $\Delta x/\Delta y$ is fixed to 2. The complete photonic bandgap is also depicted in the figure as an unshaded region, where a dotted line represents the midgap frequency of the photonic bandgap. In comparison with Fig. 6.2, the number of the cavity modes is reduced to three modes, a half of that of the square-shaped defect cavity. Only the first two lowest modes (modes 1 and 2) are investigated here, because Q factor of the highest-order mode (mode 3) is relatively low compared to those of the other two. It can be seen that the cavity modes can be tuned well by changing the size of the defect, in which modes 1 and 2 are closest to the midgap frequency when Δx is equal to $0.8a$ and $0.9a$, respectively. Figures 6.7(a) and (b) show field distributions of E_x component of modes 1 and 2 at the center of the cavity layer with $\Delta x = 0.8a$ and $0.9a$, respectively. Gray lines show boundaries of the dielectric rods and the cavity. Both modes are well confined in the cavity due to strong light confinement near the midgap frequency. Then, total Q factors of both modes are calculated as a function of the number of the stacked layers and the size of



(a)



(b)

Figure 6.6 (a) Schematic illustration of the designed rectangular-shaped nanocavity. (b) Normalized frequencies of three cavity modes (1 to 3) existing in the cavity as a function of the size of the defect, where $\Delta x/\Delta y$ is fixed to 2. Unshaded region and dotted line represent the complete photonic bandgap and midgap frequency, respectively.

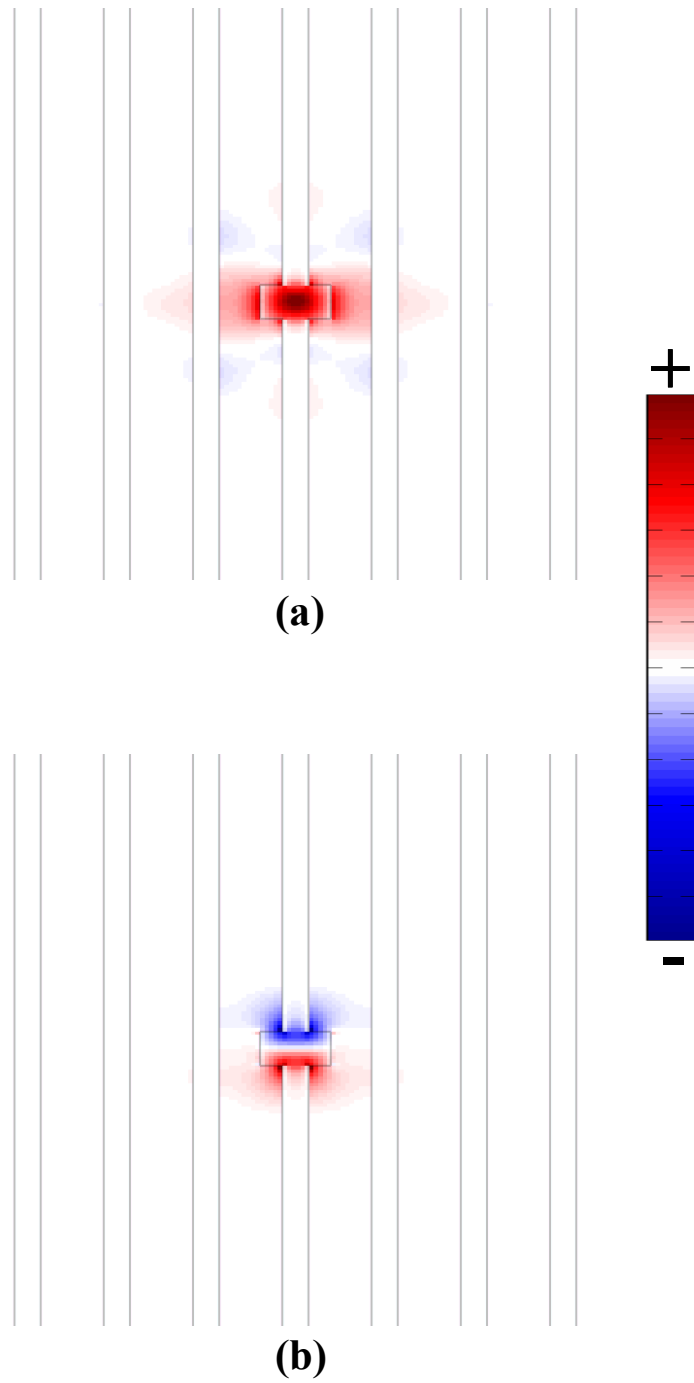
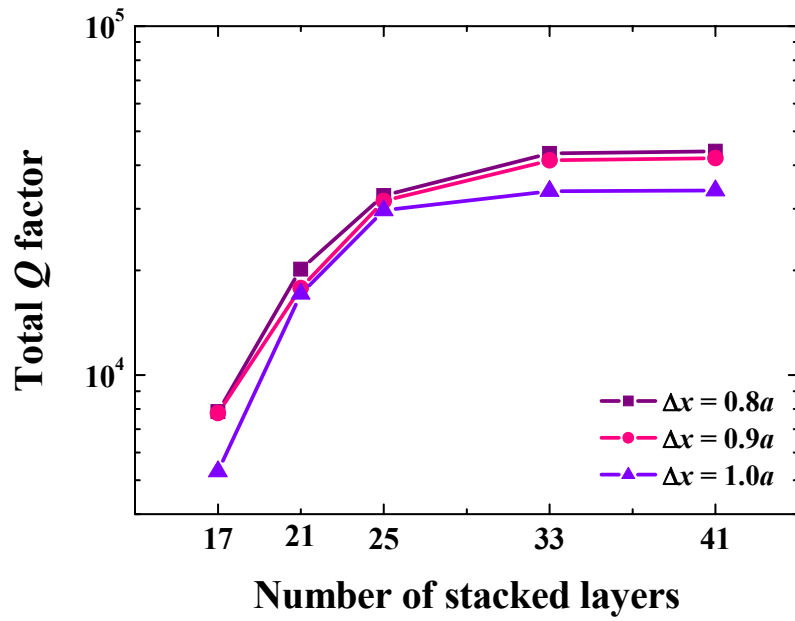


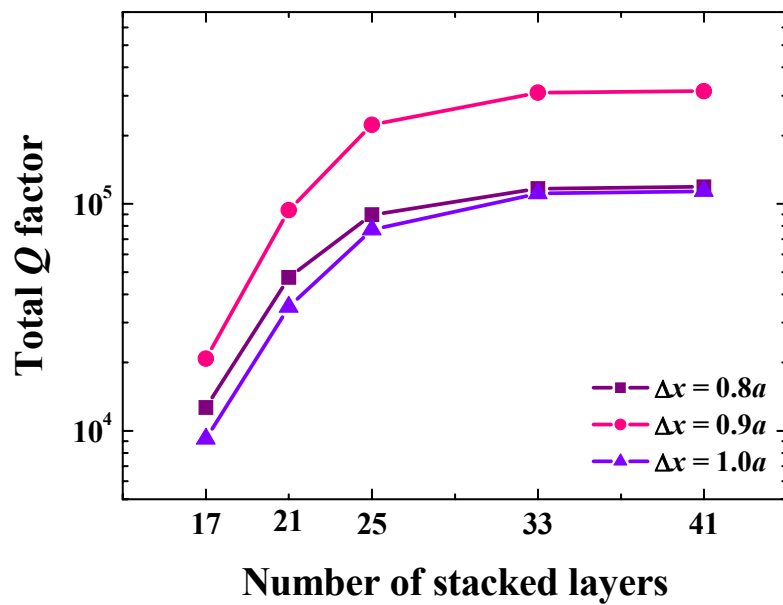
Figure 6.7 Field distributions of E_x component at the center of the cavity layer of (a) mode 1 with $\Delta x = 0.8a$ and (b) mode 2 with $\Delta x = 0.9a$. Gray lines show boundaries of the dielectric rods and the cavity.

the cavity, and plotted in Fig. 6.8. The number of stacked layers is varied from 17 to 41, while the size of the cavity is varied from $0.8a$ to $1.0a$. As can be expected, the total Q factors for both modes in all structures increase exponentially with the number of the stacked layers until their saturations determined by power losses into the in-plane direction limited by the small number of the in-plane periods. The same description in the behavior of the total Q discussed in the previous subsection can also be applied to the case here. When the number of the stacked layers is small, the total Q is limited by losses into the vertical direction, but it can be increased by enhancing the number of the stacked layer. When the number of the stacked layers is more than 25, however, the total Q becomes saturated. The differences in value of the total Q of each mode with different defect sizes can be understood by considering the separation in frequency between the mode and the midgap frequency. Both modes have their maximum Q s when their frequencies locate the nearest to the midgap frequency. The total Q of mode 1 is highest when Δx is equal to $0.8a$, and degrades more and more as the defect size is enlarged. Mode 2 has its highest Q when Δx is equal to $0.9a$ and the Q rapidly reduces when the mode is detuned from the midgap. Interestingly, the total Q of mode 2 is much higher, almost an order of magnitude, than that of mode 1 over the entire range of the number of the stacked layers. The reason for this is already discussed in the previous subsection. Mode 2 has its node of electric field at the center of the cavity leading to very high vertical Q , compared with mode 1, in which its field has antinode, as can be seen in Fig. 6.7. Therefore, if mode 2 can be well tuned to the midgap, its in-plane Q is also high, resulting in high total Q . In fact, the previous work concerning this kind of cavity [131] has only investigated mode 1, leaving mode 2 overlooked in spite of its very Q . As a result, if light-emitting elements can be introduced into the cavity and coupled with mode 2, demonstration of high- Q cavity can be expected. This will be shown in Chapter 7.

In Chapter 7, the rectangular-shaped with $\Delta x = 0.9a$, where the Q factor of mode 2 is maximum, will be fabricated to demonstrate high- Q cavity. With 21 stacked layers, the total Q factors of mode 1 and 2 are 17,800 and 94,000, respectively. It is worth pointing out that due to the small size of the cavity and the strong localization of the mode in the bandgap, the mode volumes of both modes are only $0.286(\lambda/n)^3$ and $0.217(\lambda/n)^3$ for mode 1 and 2, respectively. These values are relatively small compared with those of the square-shaped cavity, whose size is



(a)



(b)

Figure 6.8 Dependences of total Q s of (a) mode 1 and (b) mode 2 on the number of stacked layers and the size of the cavity.

almost three times larger. Therefore, the rectangular-shaped cavity is very suitable for applications to the cavity electrodynamics under both the weak coupling and strong coupling regimes, which prefers a cavity with strong optical confinement within a small volume.

In this section, it has been shown that tuning cavity modes in three-dimensional photonic crystal nanocavities to midgap frequency of a complete photonic bandgap by means of optimization of the cavity sizes is an effective tool to achieve high- Q modes in the structures with restricted sizes. Cavity modes with high Q factors can be obtained with a reasonable number of stacked layers, which can be practically fabricated. Therefore, by exploiting these designed cavities with an incorporation of efficient light-emitting elements, many promising applications, such as ultralow threshold lasers and cavity quantum electrodynamics, may be expected.

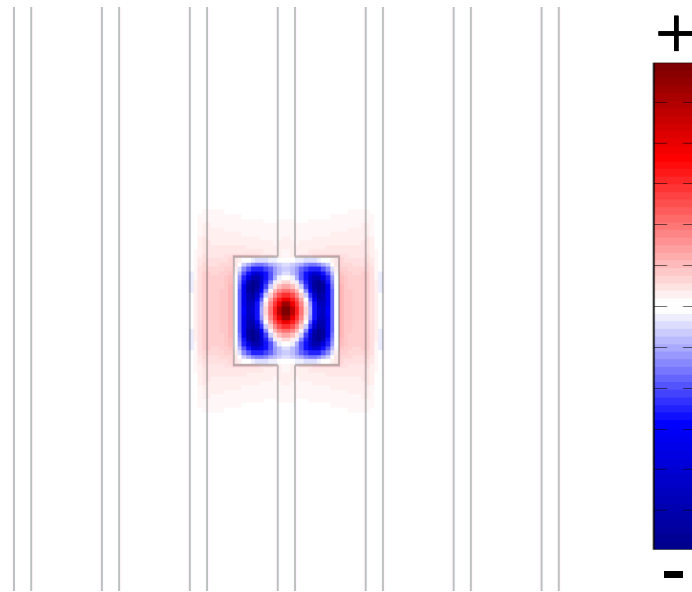
6.3 Further improvement of cavity Q by shifting rods in cavity neighborhood

From the results presented in last section, it has been shown that high- Q cavities can be achieved by tuning cavity modes to middle of a complete photonic bandgap where light confinement is strongest. However, in those designed structures, a moderately large number of stacked layers, i.e. more than 20, is needed in order to have Q factors beyond 10^4 . This number of stacked layers is still a challenge for most of present fabrication technologies [40,42,138-140]. Although a woodpile structure with this number of stacked layers can be fabricated using micromanipulation techniques, stacking errors, which usually degrade Q factor of practical devices, tend to be increased as the number of stacked layers increases. This will be discussed in next Chapter. By all means, a cavity that can have high designed Q with small number of stacked layers is preferable. It should be notified that a woodpile structure with 17 stacked layers has been successfully fabricated with precise alignment in the literature [47]. Therefore, a structure with 17 stacked layers will be concentrated in this section. Considering the designed cavities presented in previous section, the Q factor of the structure with 17 stacked layers is limited by losses into the vertical direction. Therefore, to improve the total Q , it is necessary to find a way to improve the vertical Q without adding more stacked layers.

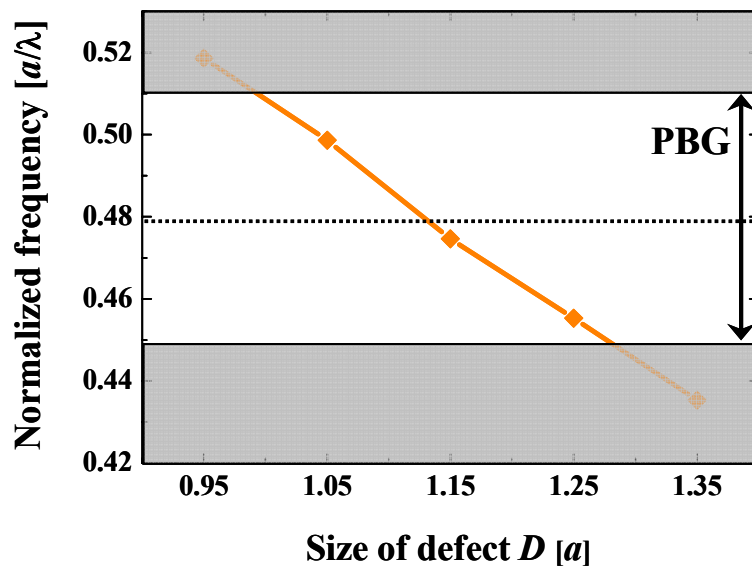
In this section, a designed of high- Q defect nanocavity in woodpile photonic crystal by shifting rods surrounding the cavity is presented. With a fixed 17 stacked layers, the total Q is more than 73,300, which is improved by more than 4 times compared with that of the unperturbed structure. The high Q of the cavity is resulted from the significant improvement of the vertical light confinement. In the last part, the designed cavity is compared with the double-heterostructure nanocavity, which is a three-dimensional photonic crystal nanocavity with highest calculated Q factor reported so far [135], and is shown that it is more promising than the double-heterostructure with the compromise between the Q factor and the difficulty in fabrication.

6.3.1 Structural parameters and cavity mode

The basic structure used to design is the same as that in last section, a woodpile structure with 11 in-plane rods, with width $r = 0.15a$ and thickness $t = 0.30a$. The numbers of stacked layers is fixed to 17 unless otherwise indicated. A square-shaped defect with width of each side D is used to form a cavity. Field distribution of H_z -component of the cavity mode of interest which is a high-order mode is shown in Fig. 6.9(a). This mode is exploited because its electric field distributions have antinodes at the center of the cavity, which leads to relatively high vertical Q by nature as discussed in previous section. At first, size of the defect is varied from $0.95a$ to $1.35a$ in order to tune the cavity mode to the midgap frequency. The mode is closet to the midgap when D is equal to $1.15a$ as shown in Fig. 6.9(b). Therefore, the defect size is set to this value in order to guarantee strong light confinement as discussed in previous section. Q factor and mode volume of the cavity are then calculated to be 17,000 and $0.66(\lambda/n)^3$, respectively. Using the method described in Section 6.2.1, the total Q is then divided to be in-plane Q and vertical Q with values of 174,000 and 19,000, respectively. Obviously, the total Q of the structure is limited by the vertical Q . It is then essential to enhance the vertical Q so as to improve the total Q .



(a)



(b)

Figure 6.9 (a) H_z -field distribution of the cavity mode at the center of the cavity layer with $D = 1.15a$. Gray lines show boundaries of the dielectric rods and the cavity. (b) Normalized frequencies of the cavity mode as a function of the size of the defect. Unshaded region and dotted line represent the complete photonic bandgap and midgap frequency, respectively.

6.3.2 Enhancing Q factor by fine shifting dielectric rods

In order to increase the vertical Q , and thus the total Q , dielectric rods at 7 positions, w_1 to w_7 , surrounding the cavity are shifted from their original positions inward and outward with respect to the cavity. The illustrations of the cross sections of the structure in xz and yz planes showing the positions of the rods are shown in Fig. 6.10. The definition of the directions is the same as that in Fig. 6.1(a). The dependence of the total Q on the shifting of rods at each position is plotted in Fig. 6.11(a). At first, the rods at position w_1 are optimized. When the total Q comes to its peak, the value of w_1 is fixed and the rods at position w_2 are then optimized. This process continues until all positions are optimized. The maximum Q of up to 73,300 with mode volume of $0.636(\lambda/n)^3$ is achieved when the shifting parameters are $w_1 = 0.25a$, $w_2 = -0.10a$, $w_3 = -0.10a$, $w_4 = 0.05a$, $w_5 = -0.05a$, $w_6 = -0.10a$, and $w_7 = -0.10a$. This value of Q is about 4.3 times higher than the value for the structure without shifting of the rods with the same structural size. As can be presumed, shifting of the rods nearer to the cavity site has a stronger effect on changing of Q than that of farther rods, e.g., the total Q depends on the shifting of rods at position w_1 , w_3 , and w_7 more strongly than the shifting of rods at position w_2 , w_4 , w_5 and w_6 . In order to understand the reason why the total Q increases when the rods are shifted, the in-plane Q and the vertical Q of the optimized structure are compared with those of the structure without shifting of the rods. The results are shown in Fig. 6.11(b). The in-plane Q of the optimized structure remains almost the same as that of the structure without shifting of any rods. However, the vertical Q is significantly improved. With 17 stacked layers, the in-plane Q of the optimized structure slightly reduces from 174,000 of the unperturbed structure to 163,000. However, the vertical Q is significantly increased from 19,000 to 133,000, which is about 7-time improvement. It means that the shift of the rods results in stronger light confinement in the vertical direction leading to the 4.3-time increase in the total Q . Figures 6.12(a) and (b) show cavity mode field distributions in the cross-sectional view of the structure without shifting of rods and the optimized structure, respectively. The amplitudes of the fields are 100-time magnified to be able to observe the evanescent field of the cavity mode. By comparing the fields in both structures, more losses that leak out of the structure in the vertical direction can be observed in the structure without shifting of rods, while the losses into the in-plane direction are almost unchanged between the two structures.

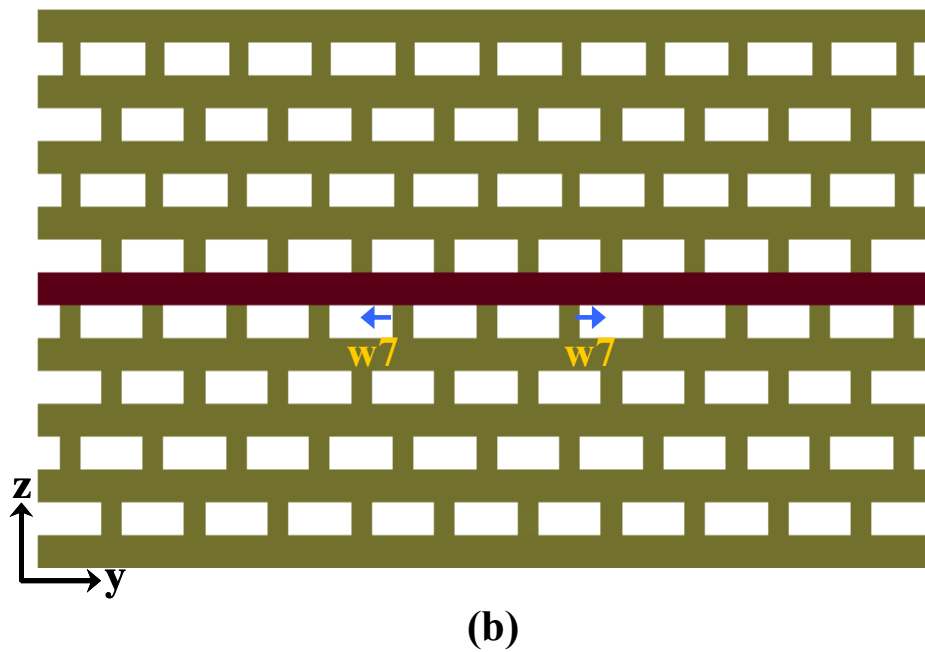
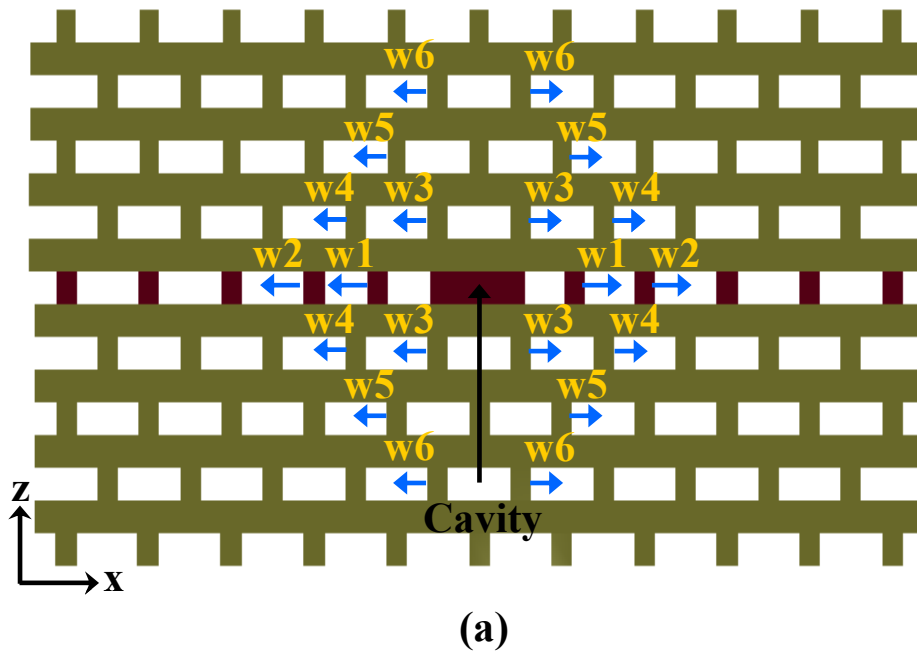


Figure 6.10 Cross-sectional views of the designed structure in (a) xz plane and (b) yz plane. Shifting of rods at 7 positions, w_1 to w_7 , surrounding the cavity is also shown.

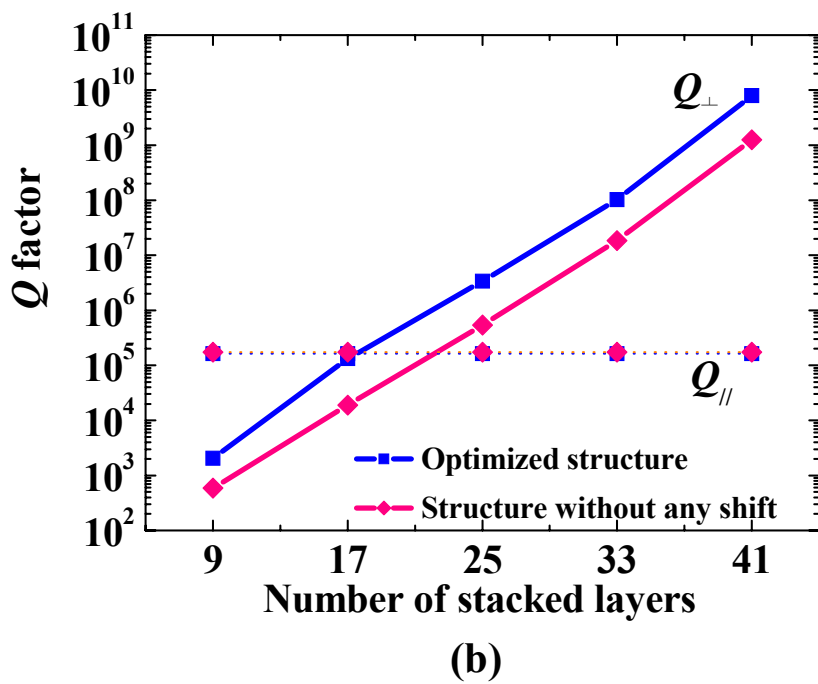
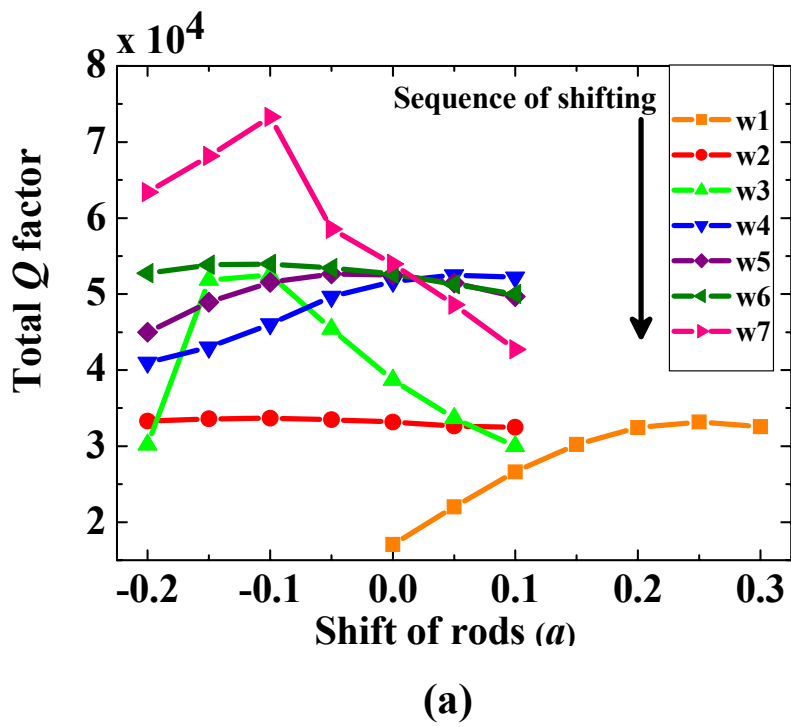


Figure 6.11 (a) Dependence of total Q factor on shifting of rods at 7 positions (w1-w7). (b) Comparison of vertical Q (solid line) and in-plane Q (dotted line) between the optimized structure (square) and the structure with no shifting of rods (diamond) as a function of number of stacked layers.

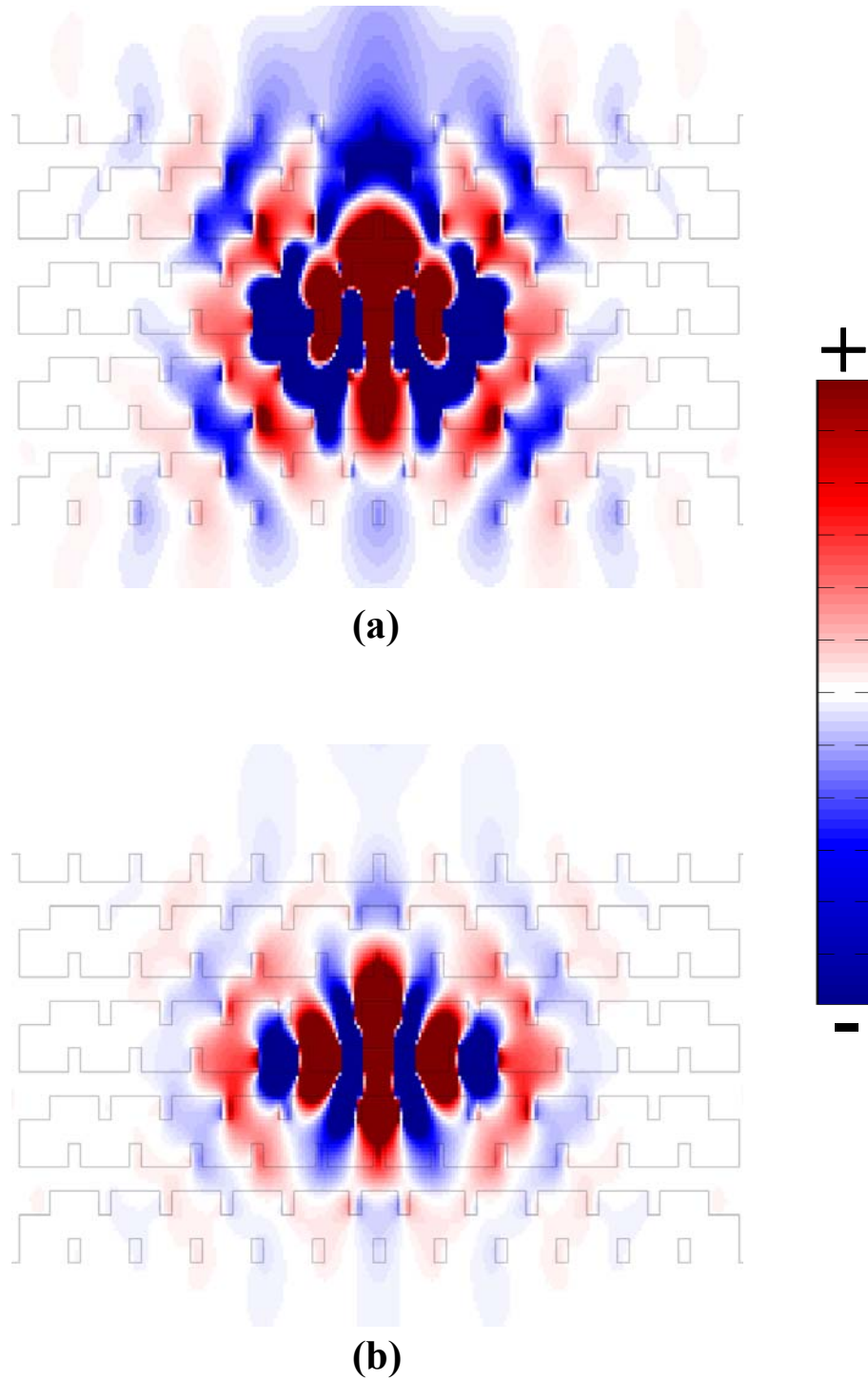


Figure 6.12 Cross sectional views of H_z -field intensities of the cavity mode of (a) structure without shifting of any rods and (b) optimized structure. The amplitudes of the fields are 100-time magnified. The lines show boundaries of dielectric rods.

These results are consistent with the calculated vertical and in-plane Q s summarized in Fig. 6.11(b).

6.3.3 Comparison with double-heterostructure three-dimensional photonic crystal nanocavity

In this subsection, the Q factor of the designed structure is compared with that of a double-heterostructure nanocavity, which possesses the highest calculated- Q for three-dimensional photonic crystals reported so far [135], with consideration of possibility in fabrication.

The structure of the double-heterostructure cavity is also based on the woodpile structure. In stead of inserting a point defect into a three-dimensionally-periodic structure to form a cavity, a line defect is used to form a cavity. Along the waveguide, unit cell length is modulated to generate localized modes with ultra-high Q in a waveguide mode gap, which is located in the complete bandgap. In order to accurately compare the designed cavity with the double-heterostructure cavity, the number of the in-plane rods of the designed structure is increased from 11 to 13 to have the same in-plane structural size as the double-heterostructure cavity. With the increased in-plane rods, the total Q of the designed cavity increases to 113,000 with the in-plane Q of 770,000, where the vertical Q remains the same, 133,000. The total Q factor of the designed cavity with optimized shifting of rods is then compared with that of the double-heterostructure cavity as a function of the number of the stacked layers in Fig. 6.13. Because the optimized structure has very high vertical Q as previously shown in Fig. 6.11(b), when the number of the stacked layers is more than 17, the total Q becomes saturated due to limited in-plane Q of 770,000. On the other hand, the total Q of the double-heterostructure cavity shows no sign of saturation with the number of the stacked layers because its in-plane Q is very high, which is $\sim 1.8 \times 10^7$, due to a combination of the mode confinements by mode gap and by the complete bandgap. However, its total Q is only $\sim 7,500$, limited by the vertical Q . This is because, in order to have high in-plane Q , the mode is needed to be tuned to the middle of the *mode gap*, which in turn detunes the mode from the middle of the *complete bandgap*, resulting in the weak confinement in vertical direction. The total Q of the double-heterostructure cavity with 17 layers is more than 15 times lower than that of the optimized cavity. In order to obtain the total Q as high as the optimized cavity with 17 stacked layers, the double-heterostructure cavity needs almost

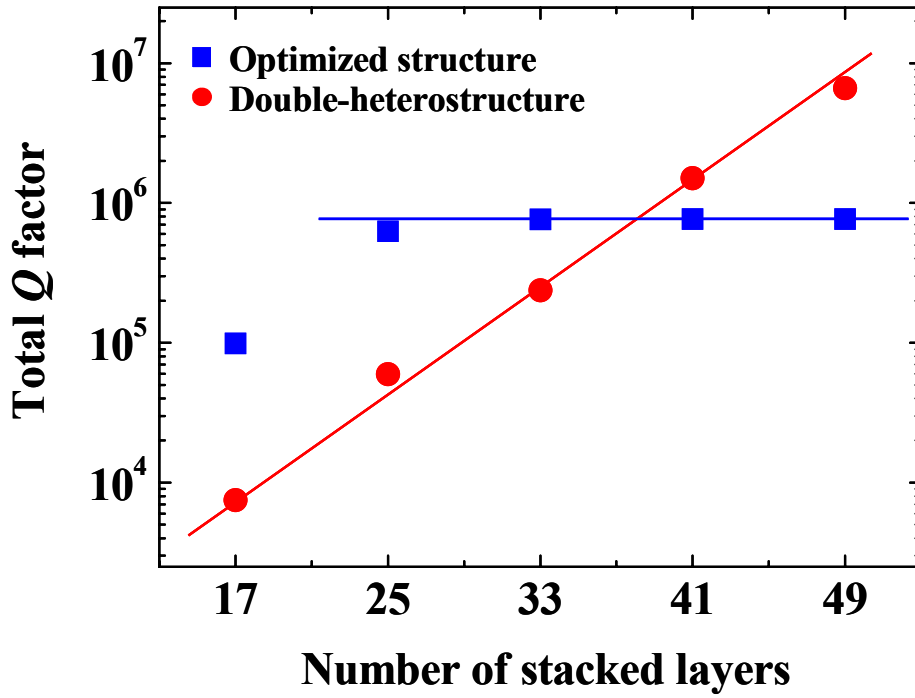


Figure 6.13 Dependence of total Q factor of the double-heterostructure nanocavity (circle) and the designed nanocavity with optimized shifting rods (square) on the number of stacked layers. Red and blue lines are guided lines for eye showing trends of increase of Q s.

30 stacked layers. In addition, it is necessary to stack almost 40 layers to build the double-heterostructure cavity with higher Q than the optimized cavity. With current fabrication techniques, such a large number of stacked layers is still a great challenge. As a result, the designed cavity structure with shifting rods is more promising to be considered as a high- Q cavity in the aspect of possibility of practical fabrication.

In this section, a design of high- Q three-dimensional photonic crystal nanocavity with small structural volume has been presented. By tuning the cavity mode in the square-shaped defect nanocavity to the midgap frequency and by optimizing the defect structure by shifting the rods surrounding the cavity, the maximum Q of up to 73,300 and mode volume of $0.636(\lambda/n)^3$ have been achieved. This value of Q is more than 4 times higher than the value for the structure without any modification of the cavity structure. This improvement of total Q has been resulted from the significantly enhanced vertical Q in the optimized structure. In the last subsection, it has been shown that when the situation comes to the practical fabrication, the designed

structure is more promising than the ultra-high- Q double-heterostructure cavity because it needs no more than 17 stacked layers to achieve very high Q of 73,300. On the other hand, the double-heterostructure cavity requires almost 30 stacked layers in order to obtain that value.

6.4 Summary

In this chapter, three designs of high- Q cavities in three-dimensional photonic crystals with finite structural size that can be practically fabricated have been presented. High- Q cavity modes in square-shaped and rectangular-shaped nanocavities have been achieved by tuning their frequencies to midgap frequency of a complete photonic bandgap, where light confinement is strongest, by means of optimizing size of the defects to gain an advantage from the photonic bandgap effect as much as possible. Apart from tuning cavity modes to the midgap frequency, the Q factor can be further improved by modifying cavity structure through shifting of dielectric rods surrounding the cavity. 4.3-time improvement of Q with a value of 73,300 has been achieved compared with the structure without modification of the cavity structure. Importantly, this high- Q cavity only needs 17 stacked layers to obtain such high Q . By introducing an efficient light emitter into these high- Q designed cavities, various promising applications including ultralow threshold lasers and cavity quantum electrodynamical effects, may be expected.

Chapter 7

Fabrication and Characterization of High- Q Three-Dimensional Photonic Crystal Nano cavities

7.1 Introduction

By the time that first experimental observation of cavity states in a three-dimensional photonic crystal at optical wavelengths was demonstrated [40], highly-advanced applications, such as electrically-driven lasers [140] and vacuum Rabi splitting in quantum dot-cavity system [106], have already been realized in two-dimensional photonic crystal cavities owing to their mature fabrication technologies and designs of high- Q cavities with tiny volume. Such a large gap in progress between two- and three-dimensional systems is directly related to difficulties in fabrications of three-dimensional structures, especially when dealing with light in optical wavelengths. In the optical characteristic point of view, Q factor of modes existing in cavities is usually regarded as an index to evaluate classes of applications that cavities can be applied to. For example, in cavity quantum electrodynamics (cavity-QED), which is the study of the interaction between light confined in a cavity and a quantum emitter, to create spontaneous emission rate enhancement through Purcell effect, the Q factor to mode volume ratio Q/V_{eff} is to be maximized. For nonlinear optical effects, a large ratio of Q^2/V_{eff} is preferable, while for the strong coupling regime of cavity QED, ratios of $g/\kappa \sim Q/\sqrt{V_{eff}}$ and $g/\gamma \sim 1/\sqrt{V_{eff}}$ are to be optimized, where g is the emitter-cavity field coupling rate, κ and γ are decay rates of cavity and emitter [51]. It can be seen that all of these applications desire a cavity with high Q and small mode volume. In Chapter 6, various designs of high- Q cavities

in three-dimensional photonic crystals with reasonably small structural size that can be practically fabricated have been presented. Bringing these complex structures from computer model to experimental reality, however, involves several unique, difficult, and interrelated challenges in the fabrication of the required precise, submicron three-dimensional structures. With a lot of efforts, various fabrication techniques for three-dimensional photonic crystals have been put forward, such as colloidal self-assembly [141-144], direct writing by two-photon polymerization [32,33,145,146], multibeam interference lithography [36-39], layer-by-layer method [15,16,40], and wafer-fusion method [19,42,148]. These techniques have been demonstrated that they are potential to make complete-photonic-bandgap structures. In order to use three-dimensional photonic crystals to manipulate light-matter interaction, in which light-emitting elements must be incorporated into a defect cavity located inside the photonic crystals, a fabrication technique that can simultaneously fulfil requirements of introduction of an artificial defect and a light-emitting element into the three-dimensional structure is essential. Colloidal self-assembly, direct writing by two-photon polymerization, and multibeam interference lithography can carry out each of the requirement, but not both at the same time. On the other hand, layer-by-layer method and wafer-fusion method have been shown to have a capability to accomplish the task. Nevertheless, their complicated procedures together with damage inflicted on the fine structure by multiple etching and heat treatment preclude them from making three-dimensional structures with large number of periods and with good quality. Hence, most of research on three-dimensional photonic crystals with defects has been concentrated on passive devices [22-24,129,149,150], or active devices with low- Q cavities [43,44]. In contrast, micromanipulation techniques do not undergo such problem [45,46]. All photonic crystal components used to construct three-dimensional structure can be prepared using a single semiconductor processing sequence and no heating, enables components to be assembled with high precision and minimum damage to their fine structure irrespective of materials or complexity of photonic patterns. Therefore, micromanipulation technique is capable of introducing a defect cavity and light-emitting elements into the structure at arbitrary positions. Recently, a cavity in woodpile structure with a record- Q of 2,300 has been reported with 17 stacked layers using micromanipulation techniques [47]. Still, this Q seems to be insufficient to pursue ultimate applications, such as thresholdless lasers [48] and strong light-matter coupling [106,125-128].

In this chapter, the fabrication of the three-dimensional woodpile photonic crystals with the square-shaped and rectangular-shaped defect nanocavities designed in Chapter 6 using micromanipulation techniques is presented. Principles of the micromanipulation techniques and preparations of their constituents and samples are described. The structures with 25 stacked layers are achieved with high accuracy and the stacking errors are shown to be 50 nm at most. After that, experimental results are given on optical characterization of the fabricated cavities coupled with InAs/Sb:GaAs quantum dots by means of photoluminescence measurements. For the cavity with square-shaped in the 25-layer woodpile structure, a cavity mode with Q factor of more than 8,600, which is the highest Q among those for three-dimensional photonic crystal cavities reported so far, was achieved. This result is consistent with the calculation results, which indicated that a high- Q cavity can be achieved in a structure with finite size by fine tuning a cavity mode to middle of a complete photonic bandgap, where the light confinement is strongest. Moreover, for the rectangular-shaped cavity, a cavity mode with Q factor of more than 7,700 with an ultra-small mode volume of 2 cubic half-wavelengths was obtained by stacking 21 layers and by tuning a cavity mode with high Q to the midgap. The results presented in this chapter give three-dimensional photonic crystals a wide-open opportunity for the realization of the applications concerning the control of light-matter interaction.

7.2 Fabrication of three-dimensional photonic crystal nanocavities by micromanipulation techniques

7.2.1 Principles of micromanipulation techniques

Because one period of a woodpile structure in the stacking direction consists of four layers, in which the rods of adjacent layers crossed each other orthogonally, and those of the next nearest neighboring layers are aligned parallel but with a half-period shift, an idea of the micromanipulation techniques is to initially slice the final three-dimensional structure into four layers. Each layer only contains a one-dimensional grating pattern prepared in a form of air-bridge plate using a conventional semiconductor processing procedure, and consequently, each layer is assembled with specific alignment at a designated position to form the final woodpile structure by micromanipulation. The micromanipulation system is installed in the specimen chamber of a scanning electron microscope (SEM) with a

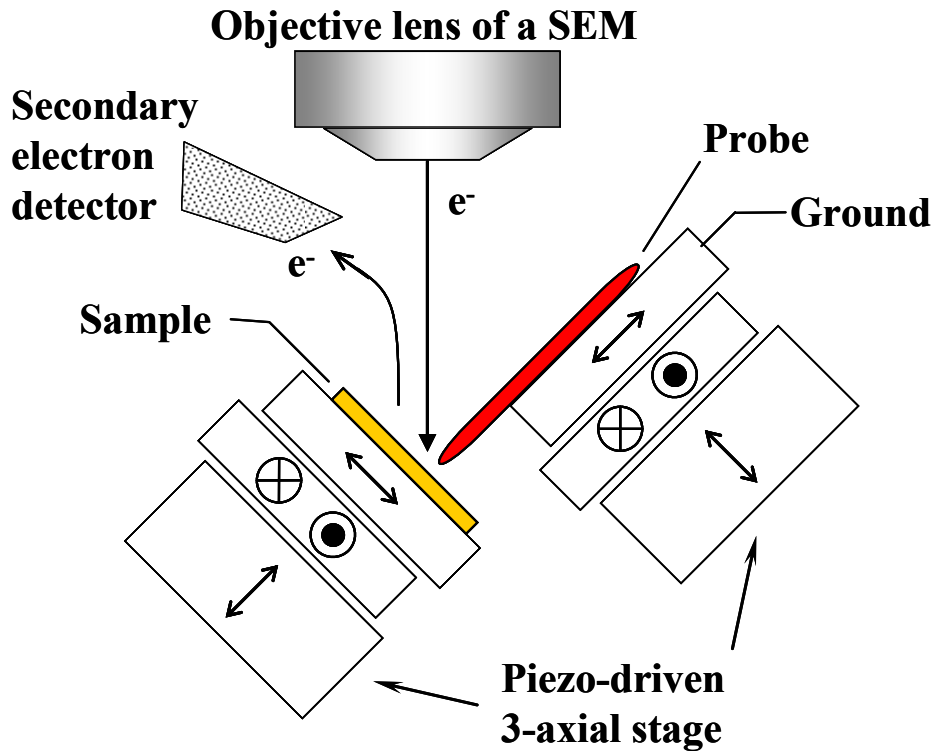


Figure 7.1 Configuration of micromanipulation system.

field-emission gun (JEOL, JSM-6460) as shown in an illustration in Fig. 7.1. In this SEM system, the magnification range is from 17 to 300,000. Image in the chamber is monitored in real-time during the process. Semiconductor samples and glass probe coated with gold are mounted on two separate Piezo-driven three-axial stages. The samples and probes are placed perpendicular to each other and at 45 degree to the direction of the electron beam. The position of both stages is controllable with a precision of within 0.1 nm. By this fine positioning configuration, fine positioning of the probe to a specific point can be done in a large working area. A voltage between charges on the surface of the plate due to the electron beam irradiation and the probe, which is grounded, make it possible to use the probe to pick and position the plate owing to electrostatic and van der Waals forces. Gravitational force is proportional to the third power of the object size, whereas the electrostatic and van der Waals forces are proportional to the first or second power of the size [152,153]. Therefore, the electrostatic and van der Waals forces are dominant compared with the gravitational force for manipulating micron-sized objects. The adhesion between the plate and

probe is controlled by adjusting the accelerating voltage and spot size of the electron beam. In addition, humidity in the chamber is important. As the relative humidity increases, water absorbs on the sample, decreasing the resistivity and increasing the rate of charge decay to the environment, which reduces the electrostatic adhesion [154]. Therefore, in order to increase the success rate of pickup, the humidity of the system is kept low by covering the SEM system with humidity control unit (APISTE, PAU-1300S-DR).

7.2.2 Preparations of micromanipulation components and samples

As described in the previous section, in order to pick the plate up and assemble it to form the final structure, a probe that is suitable for this task is necessary. Moreover, an apparatus used to assign the position of the aligned plate with high precision is also essential. In this case, aligning posts are to be developed. Of all importance, samples containing plates with and without light-emitting elements that will be assembled to constitute three-dimensional photonic crystal nanocavities must be prepared in the form that is simple to be picked up by the probe with small structural damages to preserve their nanometer-sized fine structures. In this section, fabrication processes for these components are described.

7.2.2.1 Probe and posts

The probe was a 1mm-diameter glass rod (NARISHIGE, G-1000) pulled using a micropipette puller (NARISHIGE, PC-10) while heating at 60 degree Celsius. Then it was evaporated with 40nm-thick chromium followed by 60nm-thick gold, at rate of 0.2 nm per second, to prevent chargeup and assure that voltage between the probe and plate takes place during the micromanipulation process. An SEM image of the fabricated probe is shown in Fig. 7.2. The probe is tapered with a tip in hemispherical shape with a diameter of about 200 nm. The size of the tip was predetermined to be matched well with size of frame of the plate, where there is no photonic crystal pattern, in order not to introduce any damage to the plate when it is picked up.

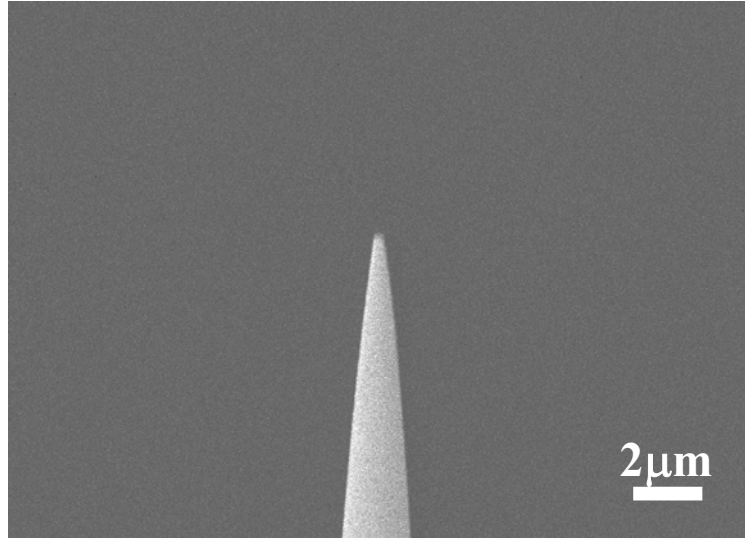
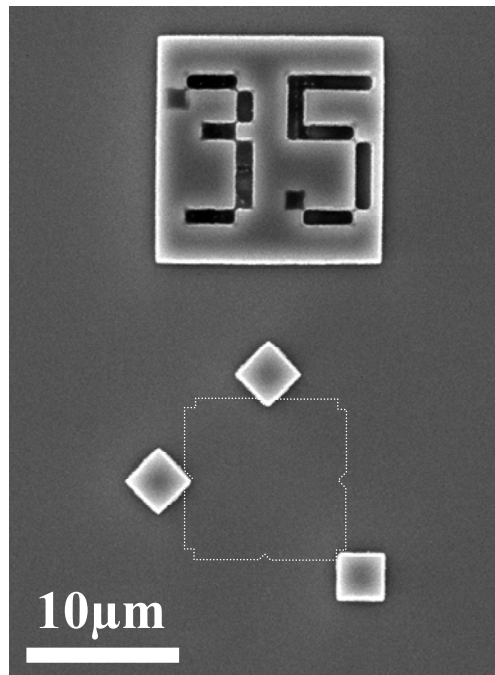
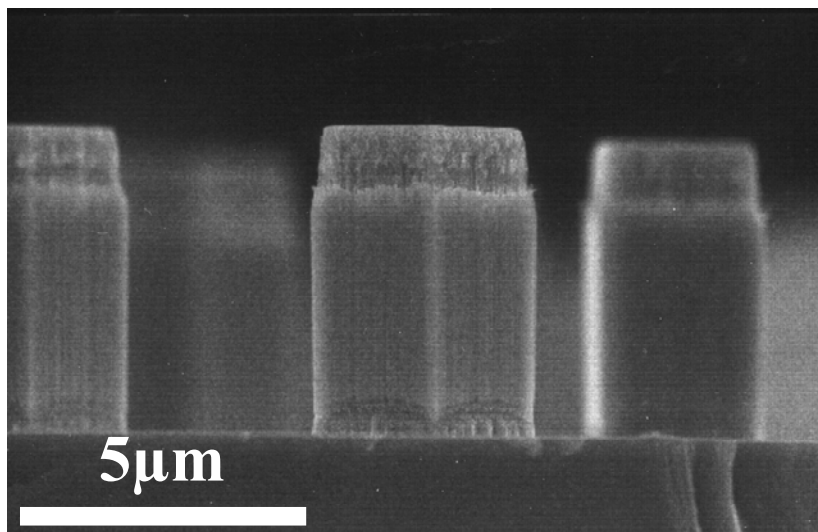


Figure 7.2 Scanning electron micrograph of probe after being coated with chromium and gold. The tip size is ~ 200 nm in diameter.

To achieve high-precision assembly of the plates, square-shaped posts were prepared on a GaAs wafer. As shown in an SEM image in Fig. 7.3(a), one positioning site consisted of three posts located at predesignated positions, which fit well with V-shaped notches introduced at the corners and sides of each plate, illustrated as dotted square in the figure. These posts allowed precise alignment of the plates, which would be aligned between these posts by the micromanipulation techniques. Firstly, 375 nm of SiO_2 was deposited on GaAs substrate by magnetron sputtering to be used as a hard mask. Sputtering condition was as follows: Ar 12 sccm, O_2 3 sccm, RF power 300 W, sputtering time 25 minutes. As will be described later, the thickness of each plate was 200 nm, which consequently needed at least 5 μm -height posts in order to assemble 25 plates. Therefore, the thickness of the SiO_2 mask layer was chosen to be thick enough to make sure that the posts could be etched to such depth. Then, the sample was spin coated with electron-beam resist (ZEP-520A). The conditions for the spin coating process were as follows; spinning speed 500 rpm for 5 seconds, 3000 rpm for 60 seconds, and pre-baking at 180 $^\circ\text{C}$ for 20 minutes in an oven. With these conditions, the resist thickness was approximately 400 nm. Post patterns with numerical label above each group of them were prepared. The size of each post was $(3 \times 3) \mu\text{m}^2$. They were then written on the sample using an electron-beam lithography system (JEOL JBX-6000) at 50 kV, with 80 pA current and 75 $\mu\text{C}/\text{cm}^2$ dose.



(a)



(b)

Figure 7.3 Scanning electron micrographs of positioning posts in (a) top view and (b) side view. Dotted square in (a) represents a plate with their notches fitted with corners of posts.

The exposed ZEP-520A was developed in n-amyl acetate (Nihon-Zeon, ZED-N50) at 20 °C for 10 seconds, and rinsed in mixed solvent (Nihon-Zeon, ZMD-B) at room temperature for 15 seconds. The post patterns were subsequently transferred to the SiO₂ layer by an ICP-RIE dry etching using CF₄ and Ar mixture. Flow rates of gases were set to 5 sccm and 6 sccm for CF₄ and Ar, respectively. The etching process was performed for 195 seconds with RF platen power of 500 W and source power of 125 W. The pressure during the process was set to 0.75 Pa and all the process was done at room temperature. Difficulty occurred in GaAs etching process, because of the strict requirement that the posts must be etched to at least 5 μm-depth with straight side walls. The sidewall profile would play a major role and determine the stacking accuracy. The optimized etching condition using an ICP-RIE with Cl₂ and Ar mixture were as follows: Cl₂ 5 sccm, Ar 2 sccm, platen power 100 W, source power 250 W, initial pressure 2 Pa, final pressure 1 Pa, temperature 50 °C and etching times 7 minutes. A key point was to etch with low platen power with long etching time to reduce physical etching by ionized gas bombarding, which would erode the entire SiO₂ mask before ending of the process. In addition, the ratio of Cl₂ to Ar was also important. With the optimized value, posts with straight sidewalls were achieved. The fabricated posts are shown in the scanning electron micrographs of Fig. 7.3(b) in side view. The posts have very straight side walls with about 5.5 μm in height. Using these posts as the positioning pins, aligning 25 plates or more with high precision can be expected. It is worth noting that the use of posts made of the same material as the stacking components (GaAs) greatly contributed to keeping both contamination and distortion of the photonic crystals to a minimum.

7.2.2.2 Plates

From the calculation results presented in previous chapter, woodpile structures with the square-shaped and rectangular-shaped defect nanocavities with optimized sizes were fabricated. Both of them had general structural parameters in common, therefore, their fabrication processes are described concurrently. As aforementioned, one unit in the stacking direction of the final woodpile structure consisted of four layers, each containing a simple line-and-space pattern with a number of in-plane rods of 11. The line-and-space patterns were set to have in-plane periodicities $a = 500$ nm and 480 nm for the structures with square-shaped and rectangular-shaped defects,

respectively. The size of plates was set to $10\mu\text{m}\times 10\mu\text{m}$, which was sufficient to contain that number of rods with those pitches. The rod widths were $0.25a$ and $0.30a$ for the structures with square-shaped and rectangular-shaped cavities, respectively. Two types of plates were fabricated. One was a normal plate with normal line and space patterns used to stack the upper and lower cladding layers, while the other one was an active plate containing light-emitting elements and cavities, located between the upper and lower layers. They were prepared on separated samples.

In the fabrication, each layer was a 200-nm-thick GaAs slab grown on a 1000-nm-thick $\text{Al}_{0.7}\text{Ga}_{0.3}\text{As}$ sacrificial layer, which was on a 300-nm-thick GaAs buffer layer, using metal organic chemical vapour deposition (MOCVD). Then, 170 nm of SiO_2 was sputter on the sample to be used as a hard mask. The sputtering condition was the same as that for the process in previous subsection, except that the sputtering time was reduced to 14 minutes. Such a thick mask layer was required despite of the thin slab to be etched. In order to increase the success rate of pickup, the patterns were needed to be etched to the substrate, as will be described in details in next section. Considering the sample used here, etching depth of more than $1.5\mu\text{m}$ was requisite. Then, the samples were spin coated with electron-beam resist (ZEP-520A). The conditions for the spin coating process were as follows; spinning speed 500 rpm for 5 seconds, 4000 rpm for 60 seconds, and pre-baking at $180\text{ }^\circ\text{C}$ for 20 minutes in an oven. With these conditions, the resist thickness was approximately 350 nm. The photonic crystal structures were patterned using an electron-beam lithography system (JEOL JBX-6000) at 50 kV, with 80 pA current and $60\mu\text{C}/\text{cm}^2$ standard dose. To compensate for the proximity effect in the lithography, a dose profile for each plate pattern was developed as shown in Fig. 7.4 to equalize the energy deposited by backscattered electrons [155]. Numbers in the figure indicate the percentage of dose deviated from the standard dose for each exposure point. The dose profile could also be well applied to the other three plate patterns and could also be used for patterns with different in-plane periods and rod widths by just slightly changing the standard dose. The exposed ZEP-520A was developed in n-amyl acetate (Nihon-Zeon, ZED-N50) at $20\text{ }^\circ\text{C}$ for 65 seconds, and rinsed in mixed solvent (Nihon-Zeon, ZMD-B) at room temperature for 60 seconds. The photonic crystal patterns were subsequently transferred to the SiO_2 layer by ICP-RIE dry etching using a CF_4 and Ar mixture. Flow rates of gases were set to 5 sccm and 6 sccm for CF_4 and

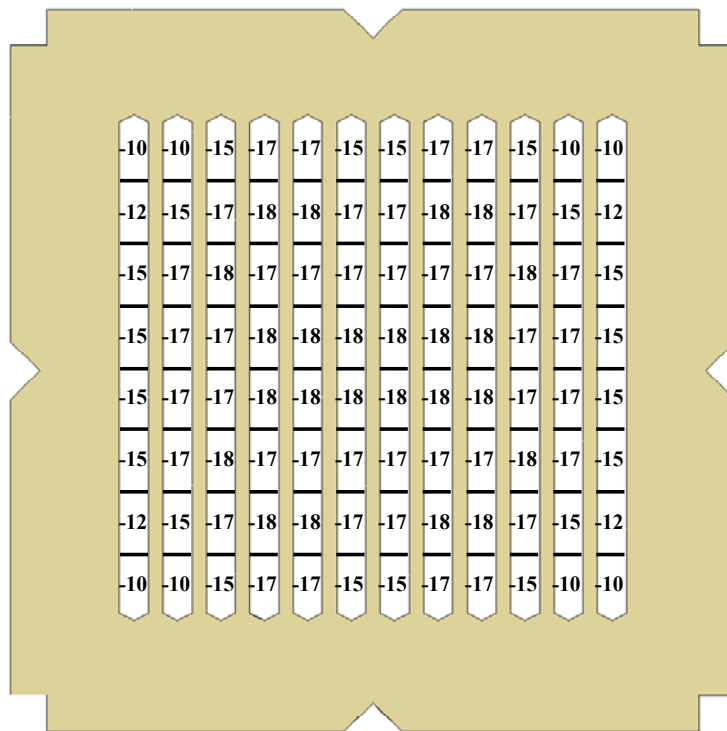
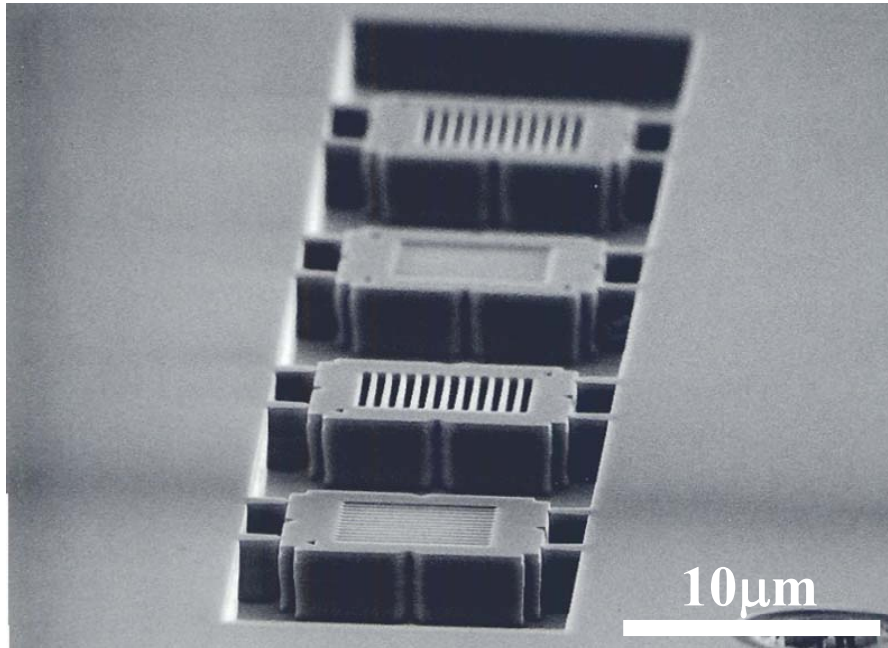
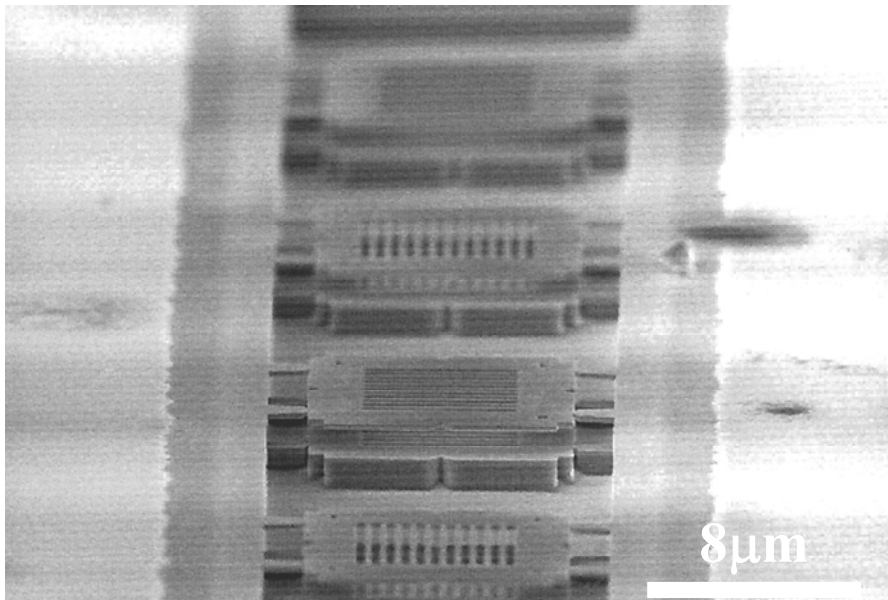


Figure 7.4 Plate pattern (gold) with electron beam dose profile to compensate for the proximity effect. Numbers indicate percentage of dose deviated from the standard dose for each exposure point

Ar, respectively. The etching process was performed for 85 seconds with RF platen power of 500 W and source power of 125 W. The pressure during the process was set to 0.75 Pa and all the process was done at room temperature. Dry etching into the semiconductor layers was then performed in an ICP-RIE dry etching using a Cl_2 and Ar mixture. Etching conditions were as follows: Cl_2 3 sccm, Ar 2 sccm, platen power 100 W, source power 300 W, initial pressure 2 Pa, final pressure 1 Pa, temperature 50 °C and etching times 100 seconds. With this condition, the patterns were etched to about 2 μm -depth as shown in Fig. 7.5(a). It should be notified that the profile of the etched sacrificial layer, which was a little indent, was insignificant as long as that of the plate slab was straight and the patterns were not deteriorated or collapsed, because it would be eventually removed after wet etching. The sacrificial layer was removed by dipping the samples in a 1:9 hydrogen fluoride solution ($\text{HF}:\text{H}_2\text{O}$) for 40 seconds to form suspending air-bridge structures. To avoid the collapse of the air-bridge structures, the sample was rinsed in isopropyl alcohol (IPA) as the last rinsing solvent after the wet etching process to substitute the water. One unit of the fabricated



(a)



(b)

Figure 7.5 Scanning electron micrographs in bird's-eye view of one unit of building blocks consisting of four plates after (a) Cl_2/Ar dry etching and (b) wet etching.

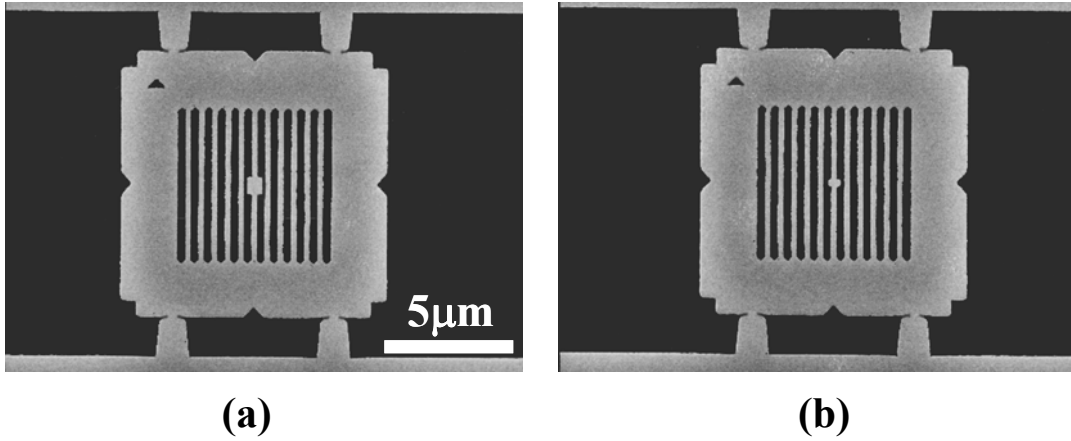


Figure 7.6 Scanning electron micrographs in top view of active plates with (a) square-shaped and (b) rectangular-shaped nanocavities after wet etching.

air-bridge building blocks consisting of four plates is shown in the scanning electron micrograph of Fig. 7.5(b) in bird's-eye view. All the plates are linked to the substrate by four small bridges to make them hung in the air.

Active plates were prepared in the same way as for the normal plates except that they contained three-layer stacked InAs/Sb:GaAs quantum dot layers, in which the middle quantum dot layer was at the center of the slab. Antimony-surfactant-mediated growth was used to grow high density quantum dots with good optical properties emitting beyond $1.3 \mu\text{m}$ [156-158]. The dot density was $2 \times 10^{10} \text{ cm}^{-2}$ per layer. The quantum dot ground state emission peaks were at $1.41 \mu\text{m}$ and $1.29 \mu\text{m}$ at room temperature for the samples for square-shaped (sample A) and rectangular-shaped (sample B) cavities, respectively. A square-shaped defect with width of each side $D = 1.1a$, which is the optimized value obtained in last chapter was located at the center of the pattern of the active plate of sample A to form a nanocavity. For sample B, a rectangular-shaped defect with dimensions $\Delta x \times \Delta y = 0.9a \times 0.45a$ was introduced as a defect cavity. SEM images of the active plates with both defect cavities are shown in top view in Fig. 7.6. The SEM-observed defect sizes and shapes, however, deviated a little from the designed values due to fabrication errors during the resists developing and etching processes. The actual square-shaped and rectangular-shaped defects became approximately $1.05a \times 1.05a$ and $1.0a \times 0.5a$, respectively, with their

corners rounded. These structural deviations will affect optical properties of the cavities as will be discussed in next chapter.

7.2.3 Assembly into three-dimensional structures by micromanipulation

The precedently prepared unit plates were assembled using micromanipulation techniques. The accelerating voltage of the primary electron beam of the SEM system was set to 6 kV. The relative humidity and temperature measured outside the chamber were controlled to 25% and 28 °C, respectively. The samples, consisting of samples of normal plates, posts, and active plates, together with probe, which was placed perpendicular to the samples, were inserted into the chamber. The chamber was then vacuumized to order of 10^{-5} Pa to start the micromanipulation. SEM images of the assembly procedure are shown in Fig. 7.7. Firstly, due to the difference in altitude between the probe and the samples, the probe was lowered down to approach the plates. After reaching the level of the plates, the probe tip was pushed to break the linking bridges in order to release the plate from the substrate. The white scratches at the interface between the plate and the linking bridges as seen in Fig. 7.7(a) indicate that the plate is already free from those linking bridges. Because the probe was quite fragile, it must not be applied with too strong tension, otherwise it would be broken. Another important point that needed a great caution was that the plate must not be dropped onto the substrate because the electrostatic and van der Waals forces between the plate and substrate were much stronger than those between the plate and probe. Plates that were fallen down on the substrate would never be able to be peeled off. This was avoided by levering the plate up to lie on the bridges after two bridges on the upper side of the plate were broken. After that, the linking bridge on the lower-right hand side of the plate was broken, while maintaining the plate not to fall down from the bridges on the upper side onto the substrate. Then, the plate was pushed from the right hand side so that it a little rotated and applied a tension to the left bridge on the lower-left hand side of the plate to break it. Consequently, the plate separated from the substrate was picked up with the probe as shown in Fig. 7.7(b). The probe should be settled at a location where there was no photonic crystal pattern in order not to damage it. The probe with the plate attached on it was then transferred to the location of the posts. After being approached to the post level, the plate was released from the probe by laying it on one of the posts as shown in Fig. 7.7(c). The

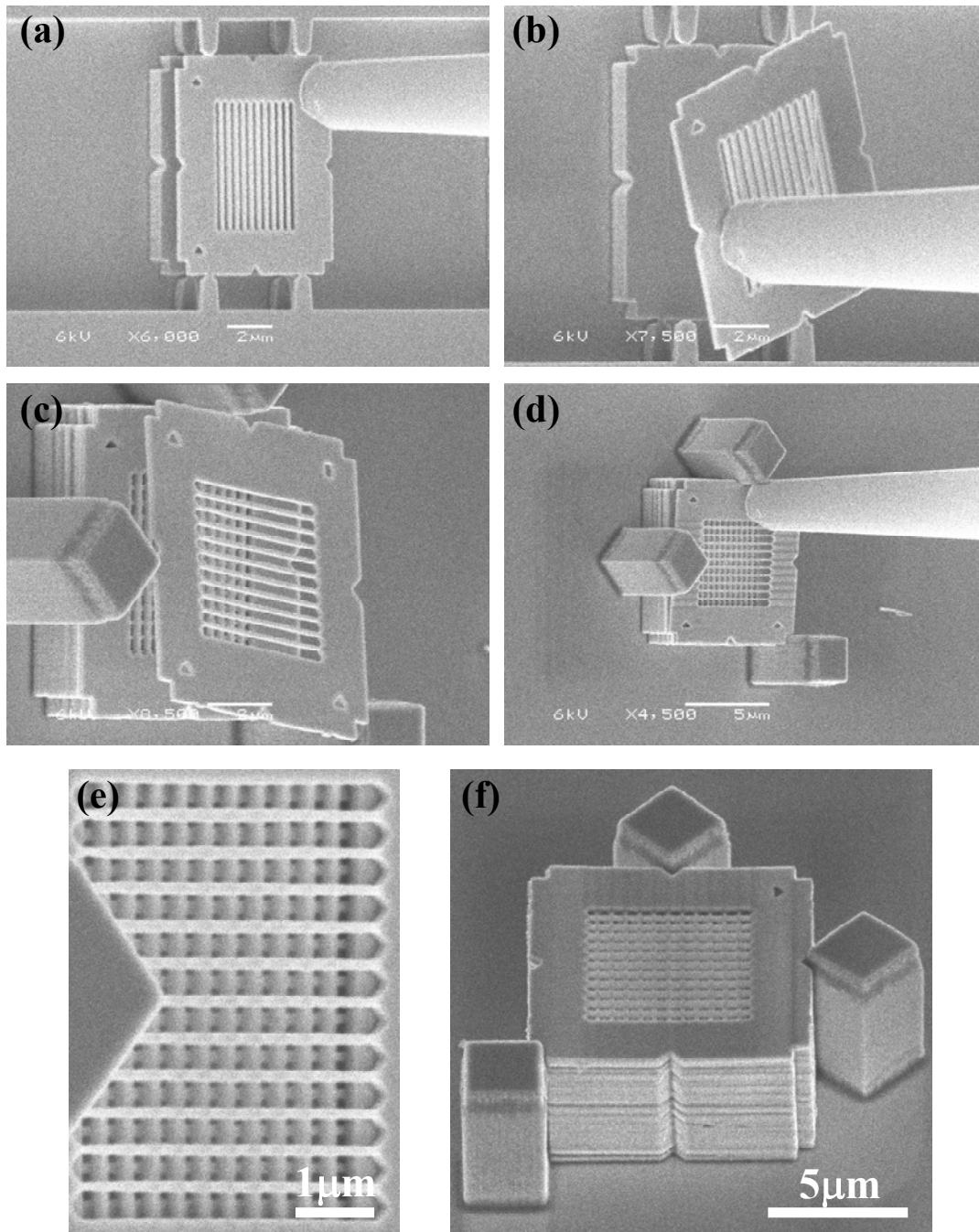


Figure 7.7 SEM images of assembly procedure by micromanipulation. (a) A bridge of a plate is broken by pushing it with a probe tip. (b) A plate is picked up with a probe. (c) A plate is released from a probe by sticking it on a post. (d) A plate is pushed and pressed down with a probe to stick with underlying layers. (e) A plate is stacked on underlying layers with high precision. (f) A final 25-layer woodpile structure.

plate tended to stick on the post rather than the probe due to stronger adhesive force between the plate and the post. The probe was used to guide the plate to the appropriate position where the notches at the corners and sides of the plate fitted with the corners of the three posts. Finally as shown in Fig. 7.7(d), the plate was pushed and pressed down for a few seconds with a probe after the arrangement in the final position to make the plate self-bonded with the underlying plates and never peeled off. Figure 7.7(e) shows a magnified SEM image of the plate after being stacked on the underlying layers. The alignment is very precise, as can be seen in the figure that the rods of the next nearest underlying layer are aligned parallel but with a half-period shift according to the topmost layer. The assembly procedures were repeated and finally formed the final multilayer three-dimensional structures. One sequence of the assembly for one plate was completed within 10 minutes in average. An SEM image of the fabricated 25-layer woodpile structure is shown in Fig. 7.7(f), where the sample is tilted up to 45° to reveal the three-dimensional structure. The stacking errors were measured from the side of the structure, and determined to be 50 nm at most. Therefore, high Q factors can be expected in these fabricated cavities. The structure with the square-shaped cavity was fabricated with 25 stacked layers, where the active layer with the defect cavity was placed between twelve upper and twelve lower normal layers, while the structure with the rectangular-shaped cavity was fabricated with 21 stacked layers with ten upper and ten lower layers. More than five structures were fabricated for each cavity with the same structural parameters. Figure 7.8 shows a 4×7 matrix of assemblies with some failed structures. Each positioning site was labelled numerically for easy recognition of the position on the substrate when performing measurements. These large number of fabricated photonic crystal components reflects the capability to achieve high fabrication throughput of the micromanipulation techniques.

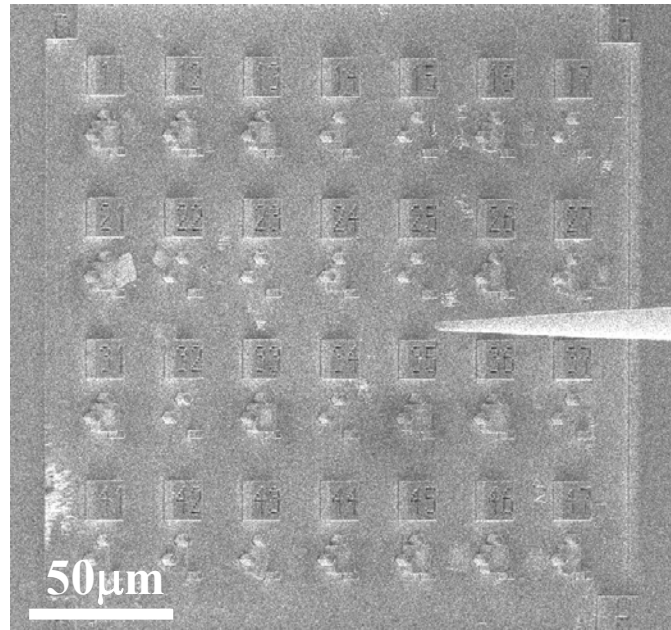


Figure 7.8 View of fabricated three-dimensional photonic crystal structures in a 4×7 matrix.

7.3 Experimental setup of photoluminescence measurements

To investigate optical properties of the nanocavities, photoluminescence (PL) measurements were performed in a temperature-controlled liquid-helium cryostat at 6 K for the square-shaped defect cavity and at room temperature for the rectangular-shaped defect cavity. Figure 7.9 illustrates schematics of the measurement setup. The cryostat was pumped down to vacuum. A continuous-wave (CW) diode laser operated at 780 nm was used as an excitation source. The pump laser beam was focused to a 4 μm -diameter spot on the samples by a microscope objective [50 \times , numerical aperture = 0.42], and was positioned on the photonic crystal regions using piezo-electric nanopositioners. Special care must be taken in adjusting the focal plane of the laser beam to the height where the cavity is in order to effectively excite the quantum dots inside the cavity. For imaging purpose, white light from a lamp was illuminated on the sample and a charge-coupled device (CCD) camera was used to image the positions of the photonic crystals. The PL from the quantum dots was collected by the same microscope objective and analyzed with both a monochromator and a triple grating monochromator equipped with InGaAs multichannel detector

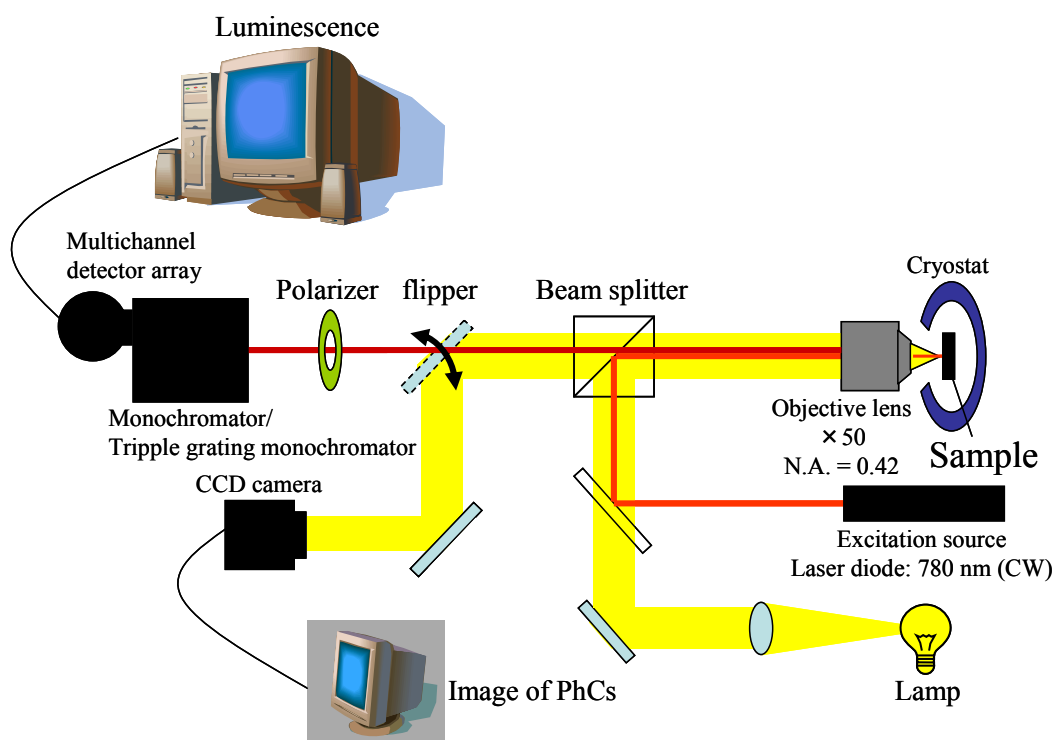


Figure 7.9 Schematic illustration of photoluminescence measurement setup.

arrays. A mirror located in front of the monochromator can be flipped to select the detections, image of photonic crystals or luminescence. A polarizer was located just before the monochromator to filter the different in-plane polarization components of the emitted light from the cavity.

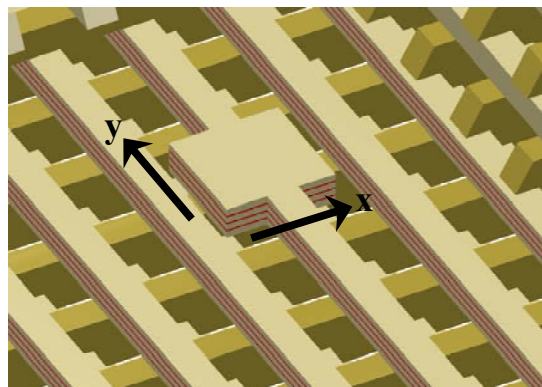
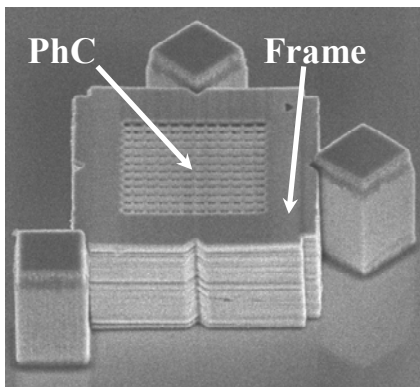
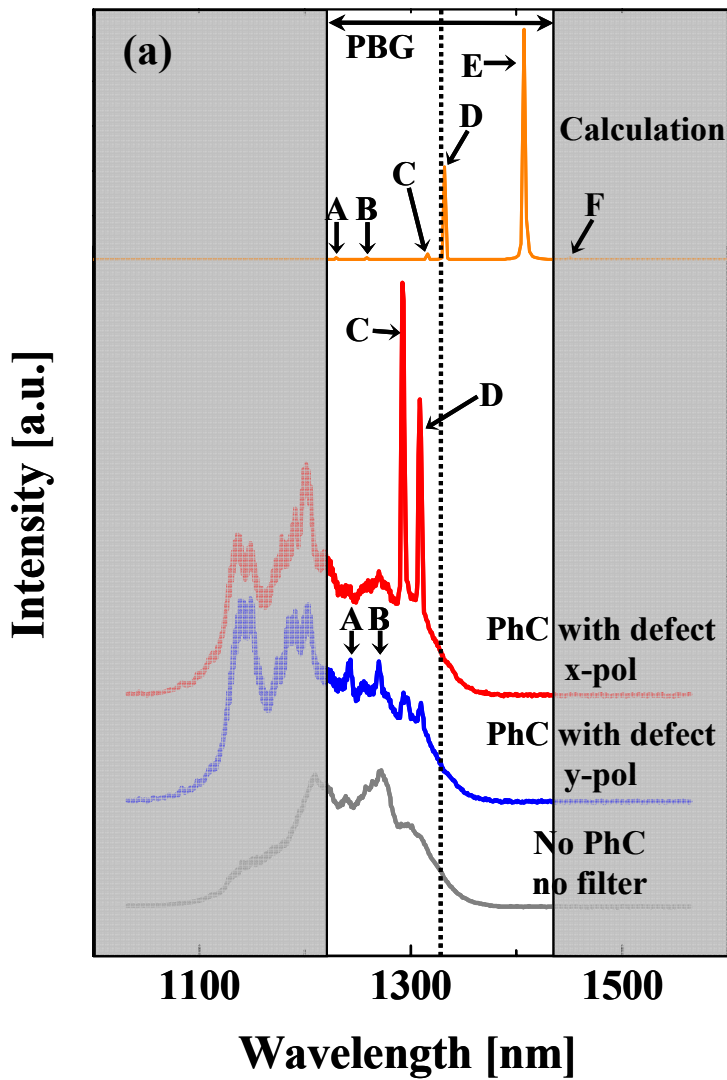
7.4 Results of photoluminescence measurements

7.4.1 Square-shaped defect nanocavity

Figure 7.10(a) shows the PL spectra for the fabricated 25-layer woodpile structure with the square-shaped defect nanocavity when measured at the regions with and without photonic crystals, which was a frame region of the plates as depicted in Fig. 7.10(b). Only broad PL from a quantum dot ensemble without any apparent sharp peak was observed outside the photonic crystal pattern. On the other hand, the spectra measured on the photonic crystal nanocavity exhibit four sharp and polarized peaks at approximately 1243, 1270, 1292, and 1308 nm. These peaks are fallen within a complete bandgap between 1225 and 1445 nm depicted in the figure as an unshaded

region, where a dotted line represents the midgap frequency of the photonic bandgap. A set of broader peaks near 1200 nm corresponds to bandedge modes, in which the emission enhancement is resulted from the high density of states at the edges of the photonic bandgap. The peaks at 1243 and 1270 nm are strongly polarized along y direction, while the peaks at 1292 and 1308 nm are polarized along the x direction. The definition of the polarization directions are given in Fig. 7.10(c), where x - and y -directions correspond to the directions perpendicular and along the rods in the defect layer. From their position-sensitive behavior and polarization dependence, these four peaks were then concluded to be originated from the cavity resonances. The Q factors of the cavity modes were then determined. Figure 7.11 shows the high-resolution PL spectrum for the peak at 1308 nm fitted with a Lorentzian function. The linewidth of 0.152 nm corresponds to the estimated Q factor of more than 8,600, which is the highest value reported so far in three-dimensional photonic crystals with almost four-time improvement [47]. Another few structures with the same configuration were also tested and found that the high Q mode was reproducible in all samples. Moreover, the peak at 1292 nm also has very high Q with value of 7,100, while the cavity Q s for the peaks at 1243 and 1270 nm are approximately 420 and 1,275, respectively.

High- Q nature of the cavity was originated not only from a large number of the stacked layers, but also from the strong localization of the cavity mode when it was tuned to the midgap frequency of the complete photonic bandgap as discussed in Chapter 6. From the measurement results, it can be seen that Q factors are high for the modes located deep inside the bandgap and become lower as the modes detuned from the midgap frequency. Considering from their wavelengths, Q factors, and polarizations, the measured peaks at 1243, 1270, 1292, and 1308 nm are, in fact, respectively corresponding to modes A, B, C, and D of the designed cavity numerically discussed in Chapter 6. The spectra of cavity modes A to F in the square-shaped cavity with width of each side $D = 1.1a$ are also plotted in Fig. 7.10 (a) for comparison. Modes E and F could not be recognized in the measured spectra, because they were out of quantum dot emission range. The polarization of modes A, B, C, and D obtained in the experiment are consistent with the FDTD calculations, which were determined by considering in-plane field parities and dominant near-field emission of the cavity modes shown in Fig. 6.3 of Chapter 6. However, the measured



(b)

(c)

Figure 7.10 (a) PL spectra from the square-shaped nanocavity with polarization filtering. Corresponding spectrum from the region without PhC structure collected with no filter is shown for comparison. The complete bandgap and midgap frequency are shown in unshaded area and dotted line, respectively. The calculated spectra of cavity modes A to F in the square-shaped cavity with width of each side $D = 1.1a$ are also plotted for comparison. (b) SEM image of the fabricated structure with excited regions indicated. (c) Definition of polarization directions.

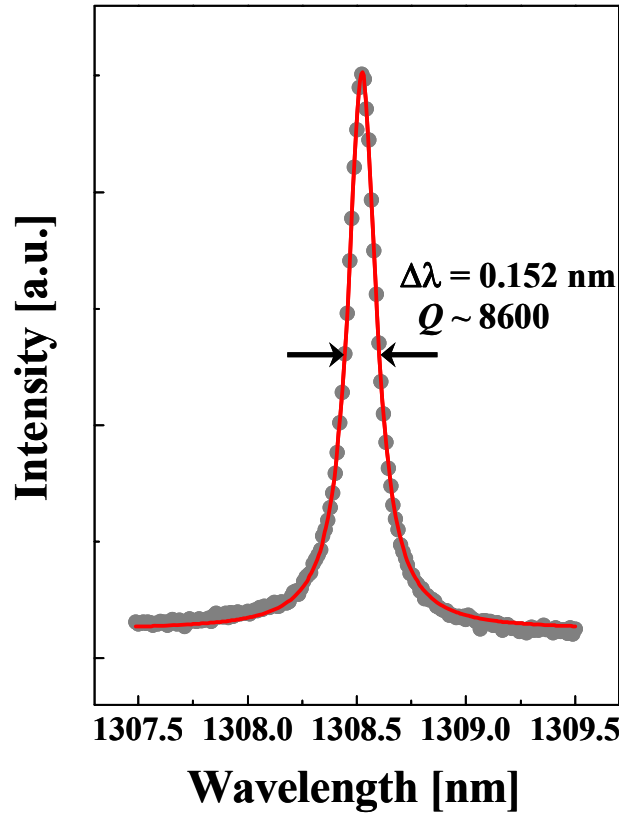


Figure 7.11 High-resolution PL spectrum for the peak at 1308 nm fitted with a Lorentzian function (red curve).

wavelengths and Q factors of those modes are deviated from the simulation results. The wavelengths of modes C and D are red-shifted, while those of modes A and B are a little shifted to longer wavelength. These changes can be attributed to structural fluctuation of the cavity caused by the fabrication processes, especially by the dry etching process. As discussed in Chapter 6, wavelengths (or normalized frequencies) of cavity modes are very sensitive to change in size and shape of the defect cavity. By observing SEM images of the fabricated structure, the actual square-shaped defect with its designed size of $1.1a \times 1.1a$ became approximately $1.05a \times 1.05a$ with their corners rounded. With this defect size, mode D, which was designed in Chapter 6 to have its resonant frequency closest to the midgap frequency, was slightly detuned from the midgap as can be seen in Fig. 7.10(a). This detuning degraded the theoretical Q of mode D in the fabricated cavity from the designed values of 41,000 to 20,000, calculated using the actual cavity size. The calculated Q s using the actual defect size for mode A, B, and C were 450, 1600, and 12,500, respectively. The tendency of the calculated Q s with 25 stacked layers using the actual defect size agrees well with that

of the measured ones. Nevertheless, there is still a large difference between the measured Q s and the calculated Q s, which can be attributed to two main reasons, material absorption and additional structural degradation due to fabrication errors, such as roughness of the rod sidewalls and stacking errors. These extrinsic losses can be related to the measured- Q ($Q_{measured}$) and calculated Q with actual size of cavity ($Q_{calculated,actual}$) by the following relation:

$$\frac{1}{Q_{measured}} = \frac{1}{Q_{calculated,actual}} + \frac{1}{Q_{absorption,fab}} \quad (7.1)$$

, where $Q_{absorption,fab}$ is the Q factor determined by material absorption and fabrication imperfections. Equation (7.1) shows that no matter how large the designed cavity- Q , its quality factor will ultimately be limited by material losses (and fabrication imperfections). For that reason, quality factors in structures containing active areas, such as quantum dots, largely lag behind passive structures. So far, two-dimensional GaAs photonic crystal cavities with quantum dots are limited to Q values of a few 10^4 [126,127,137], while photonic crystals in Si near 1550 nm, where Si appears transparent, have already passed the 1-million mark [74,75]. From Eq. (7.1), $Q_{absorption,fab}$ of the fabricated structure was calculated to be near 15,000. This means that if the structural parameters of the cavity can be kept to their designed values by, for example, compensating the cavity size in the lithography process, the cavity- Q s can still be increased to approach 15,000.

7.4.2 Rectangular-shaped defect nanocavity

Figure 7.12(a) shows the PL spectra measured at room temperature for the fabricated 21-layer woodpile structure with the rectangular-shaped defect nanocavity for different polarization filtering. There are two apparent peaks at 1392 and 1417 nm inside a photonic bandgap between 1250 and 1470 nm depicted in the figure as an unshaded region, where a dotted line represents the midgap frequency of the photonic bandgap. Both peaks are polarized along x direction, which is the longer side of the defect structure, which agree well with the FDTD calculation results. The peak at 1392 nm is very sharp reflecting its high Q factor. Figure 7.12(b) shows the high-resolution PL spectrum for the peak at 1392 nm fitted with a Lorentzian function. The linewidth of 0.1806 nm corresponds to the estimated Q factor of more than 7,700, which is more than three times higher than the previous report [47] on the same cavity structure with 17 stacked layers but without the optimization of the defect size. The

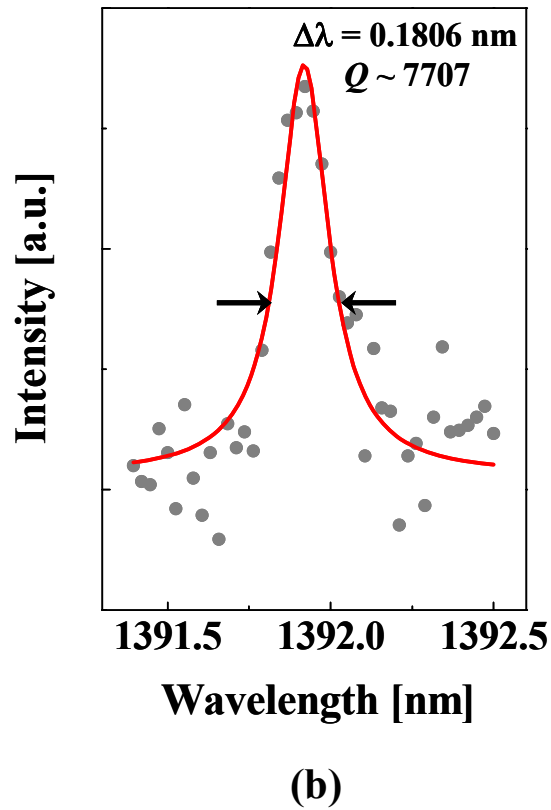
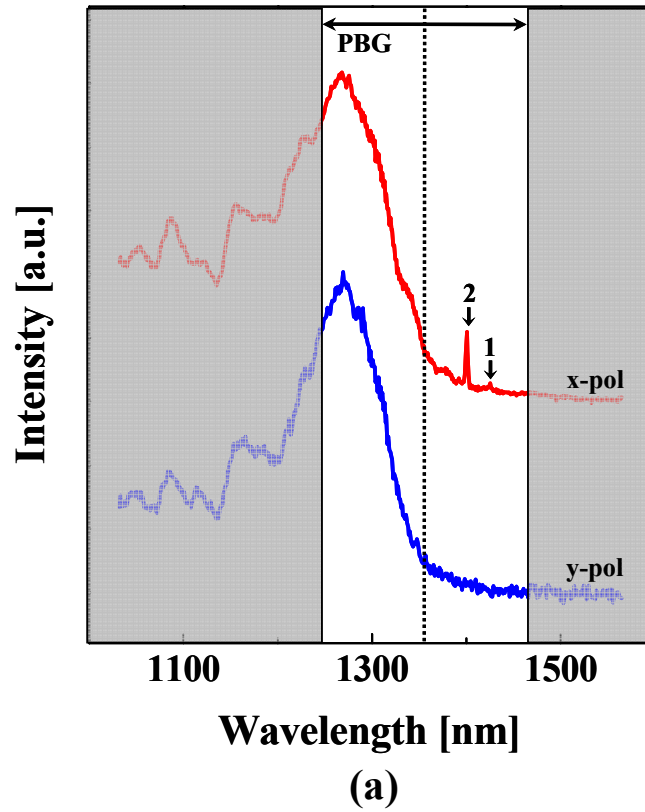


Figure 7.12 (a) PL spectra from the rectangular-shaped nanocavity collected with polarization filtering. The complete bandgap and midgap frequency are shown in unshaded area and dotted line, respectively. (b) High-resolution PL spectrum for the peak at 1392 nm fitted with a Lorentzian function (red curve).

peak at 1417 nm cannot be recognized when analysed with the triple grating monochromator to obtain high resolution PL due to its very weak signal resulted from its coupling to an emission tail of the quantum dot ensemble emission, in spite of its narrow linewidth.

The 3.3-fold improvement of Q factor compared with the previous work originated not only from a larger number of stacked layers, but it was mainly resulted from the tuning of the mode with higher theoretical Q to the midgap frequency. As discussed in Chapter 6, the second-lowest mode (mode 2) has much higher calculated- Q than the fundamental mode (mode 1) with the same number of stacked layers. Therefore, mode 1 should be tuned to the midgap in order to achieve high Q . In the previous report, mode 1 was the mode of interest and it was tuned to the midgap, leaving mode 2 largely deviated from the midgap. In contrast, the cavity studied here has its mode 2 tuned to the vicinity of the midgap as depicted in Fig. 7.12(a), resulting in higher calculated- Q , and thus higher measured- Q . The calculated- Q for mode 2 of the designed cavity was 94,000 with the cavity size $\Delta x \times \Delta y = 0.9a \times 0.45a$. It is obvious that there is a large difference between the measured- Q and the calculated- Q . As earlier discussed in the previous subsection, this large difference can be attributed to the fabrication imperfections and the material absorption. By observing SEM images of the fabricated structure, the shape of the cavity was deteriorated from the designed one with size stretched from $\Delta x \times \Delta y = 0.9a \times 0.45a$ to $1.0a \times 0.5a$ and its corners rounded. The simulation was done to calculate the spectrum and the Q factors of the cavity with actual size. Figure 7.13 shows the PL spectrum from the same fabricated cavity shown in Fig. 7.12(a) but with higher resolution, compared with the calculated spectrum obtained from the structure with actual size. In the aspect of wavelength of the cavity modes, the experimental result agrees well with the calculated one. Slight discrepancy in the value of the wavelengths is assumed to be affected from the round shape of the cavity corners, which was not included in the computational model. Broader linewidths of the calculated peaks are resulted from the limited resolution of the computations. The calculated Q of mode 2 with actual size of the cavity was degraded to 35,000. Using Eq. (7.1), $Q_{absorption, fab}$ of the fabricated structure was calculated to be near 10,000. This value of $Q_{absorption, fab}$ of the rectangular-shaped cavity is a little deviated from 15,000 of the square-shaped cavity possibly due to difference in resonant wavelengths and smaller size of the rectangular-shaped cavity,

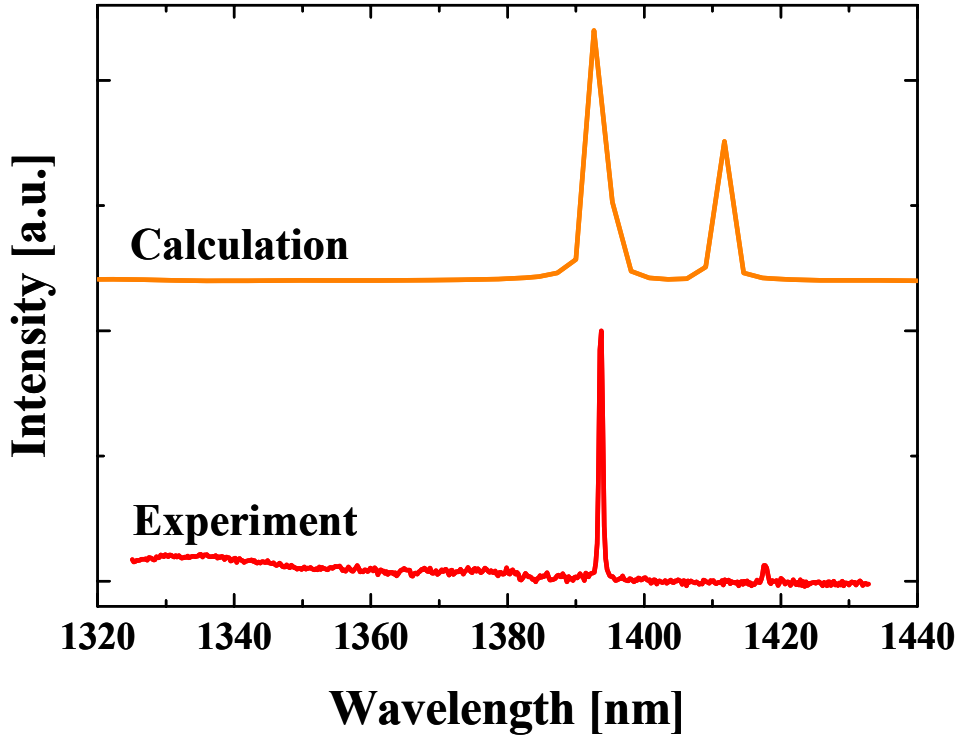


Figure 7.13 PL measured on the fabricated structure compared with calculated spectrum obtained from the structure with $\Delta x \times \Delta y = 1.0a \times 0.5a$.

which is influenced more strongly by the round shape of the cavity corners. There is still a room to improve the measured- Q of the rectangular-shaped cavity by optimizing the fabrication processes to keep the cavity to its designed size and shape. Interestingly, mode 2 in the fabricated rectangular-shaped cavity has very small mode volume of only $2(\lambda/n)^3$, approaching the diffraction limit value of $(\lambda/n)^3$. This mode volume is smaller than any of two-dimensional photonic crystal cavities reported up to now with comparative Q factors [159]. In two-dimensional photonic crystal slab cavities, the Q factor increases at a price of a larger mode volume due to the imperfect optical confinement resulting from an escaping light cone [160], in which cavity modes have to be extended in real space in order to limit wavevector components located in the light cone. Thus, it is still a challenge to build high- Q cavities as the mode volume approaches $(\lambda/n)^3$. In contrast, the Q factor in three-dimensional photonic crystal cavities can be infinitely large, while the mode volume is kept small, due to its complete photonic bandgap. Therefore, the fabricated rectangular-shaped with ultra-high Q/V_{eff} is very promising for applications, such as ultra-low threshold

lasers and nonlinear optical effects. In particular, introducing a single quantum dot in the cavity may provide us the ideal semiconductor system for demonstrating *genuine* strong coupling between three-dimensionally confined photon and electron [161].

7.5 Summary

In this chapter, experimental demonstrations of two high- Q cavities coupled with quantum dots in three-dimensional photonic crystals fabricated by using micromanipulation techniques have been presented. The structures have been shown to have very small stacking errors in order of 50 nm, in spite of their large number of the stacked layers. A square-shaped defect cavity in a 25-layer woodpile layer has exhibited a cavity mode with Q factor of more than 8,600, which is the highest Q among those for three-dimensional photonic crystal cavities reported so far. The high- Q nature of the cavity has been confirmed to be originated not only from a large number of the stacked layers, but also from the strong localization of the cavity mode when it was tuned to the midgap frequency of the complete photonic bandgap. The obtained cavity- Q can still be improved to more than 10,000 by finer tuning the cavity mode to the exact midgap. For a rectangular-shaped cavity, a cavity mode with Q factor of more than 7,700 has been obtained by choosing a cavity mode with high theoretical Q and tuning it to the midgap. The cavity mode has been shown to have mode volume as small as 2 cubic half-wavelengths, approaching the diffraction limit value of a cubic half-wavelength. These high Q/V_{eff} cavities will give three-dimensional photonic crystals a wide-open opportunity for the realization of the applications concerning the control of light-matter interaction. In addition, due to the flexibility of the micromanipulation techniques, structures that can be fabricated are not restricted to only the woodpile. By just changing patterns of plates, realization of more complicated structures, such as rod-connected diamond photonic crystal structure, which has a larger photonic bandgap than the woodpile, or a three-dimensional structure with upper layers acting as a lens, are also possible.

Chapter 8

Conclusions and Future Outlook

8.1 Conclusions

New concepts and results on designs, fabrications, and applications of high Q nanocavities in both two- and three-dimensional photonic crystals have been presented in this thesis. The results on high Q two-dimensional photonic crystal cavities have shown a great promise extending the scope of applications that can utilize photonic crystal cavities to improve their performance, where a photonic bandgap is no longer a preliminary requirement. The demonstration of high Q cavities in three-dimensional photonic crystals achieved in this thesis gives three-dimensional photonic crystals a wide-open opportunity for the realization of the applications concerning the control of light-matter interaction.

In Chapter 2, basic principles of photonic crystals that are necessary for understanding the research background and motivation of this thesis have been introduced. Two-dimensional photonic crystal slabs with both triangular and square lattices and three-dimensional woodpile photonic crystal structures have been described in details as they are the basic building blocks of all the work in this thesis. The influence of cavity geometry and structural parameters on the behavior of characteristics of photonic crystals, such as photonic bandgap, resonant frequencies, has then been discussed. Finally, donor defects have been introduced by adding dielectric materials to perfect crystals to form defect nanocavities.

In Chapter 3, details of the calculation method based on the three-dimensional finite-difference time-domain (3D FDTD) method have been described. The FDTD simulations have been categorized into two classes with different boundary conditions, depending on the types of calculations to obtain efficient and accurate solution of electromagnetic waves. The applications of the 3D FDTD calculations to investigate

photonic band structures, equi-frequency contours, resonant frequencies, field distributions, quality factors, mode volumes, and effective refractive indices have been shown.

In Chapter 4, a significant increase of Q -factor of dipole modes in photonic crystal H1-defect nanocavity after closing of the photonic bandgap have been numerically and experimentally demonstrated by optimizing the slab thickness. The optimal slab thickness is equal to a wavelength of light confined in the cavity. The strong light confinement of the cavity in the in-plane direction is not caused by the photonic bandgap effect due to a lack of the photonic bandgap but resulted from the decoupling between the cavity mode and the guided mode in the momentum space yielding only weak coupling between these two modes. The results clearly show that the structural parameters of the best fabricated cavity and those of the predicted one are almost exactly the same, in which the slab thickness $d = 1.345a$ of the experimental results is close to $d = 1.35a$ of the calculated ones, because there is no modification of the defect structure and the only parameter that needs to be adjusted to achieve high Q is the slab thickness which can be precisely controlled by using epitaxial growth techniques such as MBE and MOCVD. This finding will contribute to extending the freedom of cavity design, such as that for the application to polarization entangled photon source, where it is required to form cavity modes with prescribed Q factor and polarization.

In Chapter 5, a photonic crystal nanocavity with an ultra-high Q and small mode volume has been achieved even cavity modes do not locate within the gap or even no bandgap at all. The air hole radii were modulated with a quadratic profile to decouple the cavity mode from possible losses consisting of guiding loss and radiation loss. The Fourier amplitude of the dielectric perturbation, governed by the air hole radii profile, at the corresponding vectors from the dominant Fourier components of the cavity modes to the leaky modes in momentum space was suppressed, resulting in doubly-degenerated modes with very high Q of 120,000 and mode volume V_{eff} of $0.79(\lambda/n)^3$. The figure of merit Q/V_{eff} in the weak coupling regime is about two times higher than the highest value reported so far for doubly-degenerated modes. Therefore, this cavity is very promising for the realization of entangled photon sources. The designed cavity has also been successfully applied to achieve high Q cavities for material with low index and for quantum cascade lasers, in which a lack of photonic bandgap

usually hinders them from applications. The results achieved in this chapter extend the scope of optical devices that can utilize photonic crystal cavities to improve their performances, while the photonic bandgap is no longer a preliminary requirement to achieve high Q .

In Chapter 6, three designs of high- Q cavities in three-dimensional photonic crystals with finite structural size that can be practically fabricated have been presented. High- Q cavity modes in square-shaped and rectangular-shaped nanocavities have been achieved by tuning their frequencies to midgap frequency of a complete photonic bandgap, where light confinement is strongest, by means of optimizing size of the defects to gain an advantage from the photonic bandgap effect as much as possible. Apart from tuning cavity modes to the midgap frequency, the Q factor can be further improved by modifying cavity structure through shifting of dielectric rods surrounding the cavity. 4.3-time improvement of Q with a value of 73,300 has been achieved compared with the structure without modification of the cavity structure. Importantly, this high Q cavity only needs 17 stacked layers to obtain such high Q . These designed cavities show a great promise in the realization of high Q cavities using current fabrication technologies.

In Chapter 7, experimental demonstrations of two high- Q cavities coupled with quantum dots in three-dimensional photonic crystals fabricated by using micromanipulation techniques have been presented. The structures have been shown to have very small stacking errors in order of 50 nm, in spite of their large number of the stacked layers. A square-shaped defect cavity in a 25-layer woodpile layer has exhibited a cavity mode with Q factor of more than 8,600, which is the highest Q among those for three-dimensional photonic crystal cavities reported so far. The high- Q nature of the cavity has been confirmed to be originated not only from a large number of the stacked layers, but also from the strong localization of the cavity mode when it was tuned to the midgap frequency of the complete photonic bandgap. The obtained cavity- Q can still be improved to more than 10,000 by finer tuning the cavity mode to the exact midgap. For a rectangular-shaped cavity, a cavity mode with Q factor of more than 7,700 has been obtained by choosing a cavity mode with high theoretical Q and tuning it to the midgap. The cavity mode has been shown to have mode volume as small as 2 cubic half-wavelengths, approaching the diffraction limit value. These high Q/V_{eff} cavities will give three-dimensional photonic crystals a wide-

open opportunity for the realization of the applications concerning the full control of light-matter interaction.

In summary, all the key objectives of this thesis have been accomplished (See Section 1.2). High Q cavity, in which its principal parameter of design is fabrication-tolerant and can be precisely controlled, has been obtained. In addition, the freedom of designs and applications of photonic crystal nanocavities have been extended, because the photonic bandgap is no longer a preliminary requirement to achieve high Q . Finally, high Q nanocavities in three-dimensional photonic crystals have been demonstrated. This achievement is one important step towards the acquisition of complete manipulation of light-matter interaction.

8.2 Future outlook

The designs and demonstrations of high Q cavities that have been presented in this thesis have much room for future development. From the results of high Q cavities in three-dimensional photonic crystals, with proper excitation source, the first demonstration of lasing operation can be expected. In addition, as briefly discussed in Chapter 7, due to the flexibility of the micromanipulation techniques, structures that can be fabricated are not restricted to only the woodpile. By just changing patterns of plates, realization of more complicated structures, such as a rod-connected diamond photonic crystal structure [162], which has a larger photonic bandgap than the woodpile is possible. As a result, cavity modes with higher Q s but less sensitive to changes in cavity geometry can be expected from such structure because they can be located deeper inside the wide bandgap. Furthermore, in micromanipulation techniques all the unit plates are separately prepared, those used for constituting the upper layers can be designed to have graded index profile, and consequently can act like a lens to improve the outcoupling efficiency into a collection lens or fiber. In the two-dimensional photonic crystal cavities, both of the designed cavities possess high Q/V_{eff} doubly-degenerated cavity modes that are orthogonally-polarized. Therefore, they can be used to suppress nondegeneracy of an intermediate exciton level of a single quantum dot, which is crucial for the realization of polarization-entangled photon sources [101,102].

References

- [1] C. Kittel, Introduction to Solid State Physics (Wiley, New York, 1980), Chapter 7.
- [2] P. Vukusic and J. R. Sambles, *Nature* **424**, 852 (2003).
- [3] H. Ghiradella, *Appl. Opt.* **30**, 3492 (1991).
- [4] G. Tayeb, B. Gralak, and S. Enoch, *Opt. Photonics News* **14**, 38 (2003).
- [5] H. A. Haus and C. V. Shank, *IEEE J. Quantum Electron.* **12**, 532 (1976).
- [6] H. Kogelnik and C. V. Shank, *J. Appl. Phys.* **43**, 2327 (1972).
- [7] H. Ghafouri-Shiraz and G. S. K. Lo, *Distributed Feedback Laser Diodes* (Wiley, New York, 1996).
- [8] J. Jewell, J. Harbison, and A. Scherer, *Sci. Am.* **86**, 56 (1991).
- [9] C. Wilmsen, H. Temkin, and L. Coldren, *Vertical-Cavity Surface-Emitting Lasers: Design, Fabrication, Characterization, and Applications* (Cambridge Univ. Press, Cambridge, U.K., 1999).
- [10] E. Yablonovitch, *Phys. Rev. Lett.* **58**, 2059 (1987).
- [11] S. John, *Phys. Rev. Lett.* **58**, 2486 (1987).
- [12] K. M. Ho, C. T. Chan, C. M. Soukoulis, *Phys. Rev. Lett.* **65**, 3152 (1990).
- [13] E. Yablonovitch, T. J. Gmitter, and K. M. Leung, *Phys. Rev. Lett.* **67**, 2295 (1991).
- [14] E. Yablonovitch and K. M. Leung, *Nature* **351**, 278 (1991).
- [15] J. G. Fleming and S. Y. Lin, *Opt. Lett.* **24**, 49 (1999).
- [16] S. Y. Lin, J. G. Fleming, D. L. Hetherington, B. K. Smith, R. Biswas, K. M. Ho, M. M. Sigalas, W. Zubrzycki, S. R. Kurtz, and J. Bur, *Nature* **394**, 251 (1998).
- [17] S. Y. Lin and J. G. Fleming, *J. Lightwave Technol.* **17**, 1944 (1999).
- [18] S. Noda, K. Tomoda, N. Yamamoto, and A. Chutinan, *Science* **289**, 604 (2000).
- [19] N. Yamamoto, S. Noda, and A. Chutinan, *Jpn. J. Appl. Phys.* **37**, L1052

- (1998).
- [20] A. Chelnokov, K. Wang, S. Rowson, P. Garoche, and J. M. Lourtioz, *Appl. Phys. Lett.* **77**, 2943 (2000).
 - [21] S. Noda, M. Imada, M. Okano, S. Ogawa, M. Mochizuki, and A. Chutinan, *IEEE J. Quantum Electron.* **38**, 726 (2002).
 - [22] M. Imada, L. H. Lee, M. Okano, S. Kawashima, and S. Noda, *Appl. Phys. Lett.* **88**, 171107 (2006).
 - [23] S. A. Rinne, F. García-Santamaría, and P. V. Braun, *Nature Photon.* **2**, 52 (2008).
 - [24] P. Kohli, J. Chatterton, D. Stieler, G. Tuttle, M. Li, X. Hu, Z. Ye, and K. M. Ho, *Opt. Express* **16**, 19844 (2008).
 - [25] A. P. Philipse, *J. Mater. Sci. Lett.* **8**, 1371 (1989).
 - [26] O. D. Velev, T. A. Jede, R. F. Lobo, and A. M. Lenhoff, *Nature* **389**, 447 (1997).
 - [27] H. S. Sozuer, J. W. Haus, and R. Inguva, *Phys. Rev. B* **45**, 13962 (1992).
 - [28] R. D. Pradhan, I. I. Tarhan, and G. H. Watson, *Phys. Rev. B* **54**, 13721 (1996).
 - [29] J. B. Pendry and A. Mackinnon, *Phys. Rev. Lett.* **69**, 2772 (1992).
 - [30] B. Gates and Y. Xia, *Appl. Phys. Lett.* **78**, 3178 (2001).
 - [31] E. Palacios-Lidon, B. H. Juarez, E. Castillo-Martinez, and C. Lopez, *J. Appl. Phys.* **97**, 063502 (2005).
 - [32] N. Tétreault, G. von Freymann, M. Deubel, M. Hermatschweiler, F. Pérez-Willard, S. John, M. Wegener, and G. A. Ozin, *Adv. Mater.* **18**, 457 (2006).
 - [33] H. B. Sun, S. Matsuo, and H. Misawa, *Appl. Phys. Lett.* **74**, 786 (1999).
 - [34] M. Deubel, G. von Freymann, M. Wegener, S. Pereira, K. Busch, and C. M. Soukoulis, *Nat. Mater.* **3**, 444 (2004).
 - [35] M. Deubel, M. Wegener, A. Kaso, and S. John, *Appl. Phys. Lett.* **85**, 1895 (2004).
 - [36] M. Campbell, D. N. Sharp, M. T. Harrison, R. G. Denning, and A. J. Turberfield, *Nature* **404**, 53 (2000).
 - [37] V. Ramanan, E. Nelson, A. Brzezinski, P. V. Braun, and P. Wiltzius, *Appl. Phys. Lett.* **92**, 173304 (2008).
 - [38] Y. C. Chen, J. B. Geddes III, J. T. Lee P. V. Braun, and P. Wiltzius, *Appl. Phys. Lett.* **91**, 241103 (2007).
 - [39] D. Shir, E. C. Nelson, Y. C. Chen, A. Brzezinski, H. Liao, P. V. Braun, P.

- Wiltzius, K. H. A. Bogart, and J. A. Rogers, *Appl. Phys. Lett.* **94**, 011101 (2009).
- [40] M. H. Qi, E. Lidorikis, P. T. Rakich, S. G. Johnson, J. D. Joannopoulos, E. P. Ippen, and H. I. Smith, *Nature* **429**, 538 (2004).
- [41] S. Noda, N. Yamamoto, H. Kobayashi, M. Okano, and K. Tomoda, *Appl. Phys. Lett.* **75**, 905 (1999).
- [42] S. Kawashima, M. Imada, K. Ishizaki, and S. Noda, *J. Microelectromech. Syst.* **16**, 1140 (2007).
- [43] S. Ogawa, M. Imada, S. Yoshimoto, M. Okano, and S. Noda, *Science* **305**, 227 (2004).
- [44] S. Ogawa, K. Ishizaki, T. Furukawa, and S. Noda, *Electron. Lett.* **44**, 377 (2008).
- [45] K. Aoki, H. T. Miyazaki, H. Hirayama, K. Inoshita, T. Baba, K. Sakoda, N. Shinya, and Y. Aoyagi, *Nature Mater.* **2**, 117 (2003).
- [46] K. Aoki, H. T. Miyazaki, H. Hirayama, K. Inoshita, T. Baba, K. Sakoda, N. Shinya, and Y. Aoyagi, *Appl. Phys. Lett.* **81**, 3122 (2002).
- [47] K. Aoki, D. Guimard, M. Nishioka, M. Nomura, S. Iwamoto, and Y. Arakawa, *Nature Photon.* **2**, 688 (2008).
- [48] T. Baba, *IEEE J. Sel. Top. Quantum Electron.* **3**, 808 (1997).
- [49] Y. Arakawa and H. Sakaki, *Appl. Phys. Lett.* **40**, 939 (1982).
- [50] G. Khitrova, H. M. Gibbs, F. Jahnke, M. Kira, and S. W. Koch, *Rev. Mod. Phys.* **71**, 1591 (1999).
- [51] P. Berman, *Cavity Quantum Electrodynamics* (Academic, San Diego, 1994).
- [52] U. Grüning, V. Lehmann, and C. M. Engelhardt, *Appl. Phys. Lett.* **66**, 3254 (1995).
- [53] H. B. Lin, R. J. Tonucci, and A. J. Campillo, *Appl. Phys. Lett.* **68**, 2927 (1996).
- [54] S. Rowson, A. Chelnokov, C. Cuisin, and J. M. Lourtioz, *IEE Proc.: Optoelectron.* **145**, 403 (1998).
- [55] U. Grüning, V. Lehmann, S. Ottow, and K. Busch, *Appl. Phys. Lett.* **68**, 747 (1996).
- [56] H. W. Lau, G. J. Parker, R. Greef, and M. Hölling, *Appl. Phys. Lett.* **67**, 1877 (1995).
- [57] T. Krauss, R. DeLaRue, and S. Brand, *Nature* **383**, 699 (1996).

- [58] S. Fan, P. R. Villeneuve, J. D. Joannopoulos, and E. F. Schubert, *Phys. Rev. Lett.* **78**, 3294 (1997).
- [59] P. R. Villeneuve, S. Fan, S. G. Johnson, and J. D. Joannopoulos, *Proc. Inst. Elec. Eng. —Optoelectron.* **145**, 384 (1998).
- [60] S. G. Johnson, S. Fan, P. R. Villeneuve, and J. D. Joannopoulos, *Phys. Rev. B* **60**, 5751 (1999).
- [61] H. Y. Ryu, J. K. Hwang, and Y. H. Lee, *J. Appl. Phys.* **88**, 4941 (2000).
- [62] N. Kawai, K. Inoue, N. Carlsson, N. Ikeda, Y. Sugimoto, K. Asakawa, and T. Takemori, *Phys. Rev. Lett.* **86**, 2289 (2001).
- [63] O. Painter, R. K. Lee, A. Scherer, A. Yariv, J. D. O'Brien, P. D. Dapkus and I. Kim, *Science* **284**, 1819-1821 (1999).
- [64] K. S. Yee: *IEEE Trans. Antennas Propagat.* **AP-14**, 302 (1966).
- [65] Y. Akahane, T. Asano, B. S. Song and S. Noda *Nature* **425**, 944 (2003).
- [66] Y. Akahane, T. Asano, B. S. Song and S. Noda, *Opt. Express* **13**, 1202 (2005).
- [67] J. Vučković and Y. Yamamoto, *Appl. Phys. Lett.* **82**, 2374 (2003).
- [68] H. G. Park, J. K. Hwang, J. Huh, H. Y. Ryu, S. H. Kim, J. S. Kim and Y.H. Lee, *IEEE J. Quantum Electron.* **38**, 1353 (2002).
- [69] T. Yoshie, J. Vučković, A. Scherer, H. Chen and D. Deppe: *Appl. Phys. Lett.* **79** 4289 (2001).
- [70] H. Y. Ryu, H. G. Park, and Y. H. Lee, *IEEE J. Sel. Top. Quantum Electron.* **8**, 891 (2002).
- [71] H. Y. Ryu, M. Notomi, and Y. H. Lee, *Appl. Phys. Lett.* **83**, 4294 (2003).
- [72] B. S. Song, S. Noda, T. Asano and Y. Akahane, *Nature Mat.* **4**, 207 (2005).
- [73] E. Kuramochi, M. Notomi, S. Mitsugi, A. Shinya and T. Tanabe, *Appl. Phys. Lett.* **88**, 041112 (2006).
- [74] T. Asano, B. S. Song and S. Noda, *Opt. Express* **14**, 1996 (2006).
- [75] T. Tanabe, M. Notomi and E. Kuramochi, *Electron. Lett.* **43**, 187 (2007).
- [76] D. Englund and J. Vučković, *Opt. Express* **14**, 3472 (2006).
- [77] A. P. Alivisatos, *Science* **271**, 933 (1996).
- [78] L. Manna, E. C. Scher, A. P. Alivisatos, *J. Am. Chem. Soc.* **122**, 12700 (2000).
- [79] V. I. Klimov, A. A. Mikhailovsky, S. Xu, A. Malko, J. A. Hollingsworth, C. A. Leatherdale, H. J. Eisler, M. G. Bawendi, *Science* **290**, 314 (2000).
- [80] F. Capasso, *Science* **235**, 172 (1987).
- [81] J. Fasit, F. Capasso, D.L. Sivco, C. Sirtori, A.L. Hutchinson, A.Y. Cho,

- Science **264**, 553 (1994).
- [82] F. Capasso, R. Paiella, R. Martini, R. Colombelli, C. Gmachl, T. Myers, M. S. Taubman, R. M. Williams, C. G. Bethea, K. Unterrainer, H. Y. Hwang, D. L. Sivco, A. Y. Cho, H. C. Liu, and E. A. Whittaker, *IEEE J. Quan. Elec.* **38**, 511 (2002).
- [83] N. W. Ashcroft and N. D. Mermin, *Solid State Physics* (Holt Saunders, Philadelphia, 1976).
- [84] J. D. Joannopoulos *Photonic Crystals, Molding the Flow of Light* (Princeton University Press, Princeton, NJ, 1995).
- [85] P. J. S. Thomas, T. J. C. Hosea, D. Lancefield, and H. Meidia, *Semicond. Sci. Technol.* **107** (2001).
- [86] A. Birner, K. Busch, and F. Müller, *Phys. Blätter* **55**, 27 (1999).
- [87] S. Y. Lin, E. Chow, V. Hietala, P. R. Villeneuve, and J. D. Joannopoulos, *Science* **282**, 274 (1998).
- [88] P. Kramper, A. Birner, M. Agio, C. M. Soukoulis, F. Müller, U. Gösele, J. Mlynek, and V. Sangoghar, *Phys. Rev. B* **64**, 23102 (2001).
- [89] A. Birner, R. B. Wehrspohn, U. Gösele, and K. Busch, *Adv. Mater.* **13**, 377 (2001).
- [90] L. C. Andreani and M. Agio: *IEEE J. Quantum Electron.* **38**, 891 (2002).
- [91] K. M. Ho, C. T. Chan, C. M. Soukoulis, R. Biswas, and M. Sigalas, *Solid State Commun.* **89**, 413 (1994).
- [92] M. Maldovan and E. L. Thomas, *Nat. Mater.* **3**, 593 (2004).
- [93] A. Taflove, *Computational Electrodynamics: The Finite-Difference Time-Domain Method* (Artech House, Norwood, MA, 2000), 2nd ed.
- [94] J. P. Berenger: *J. Comput. Phys.* **114**, 185 (1994).
- [95] J. D. Jackson, *Classical Electrodynamics* (Wiley, New York, 1962).
- [96] O. Painter, J. Vučković and A. Sherer, *J. Opt. Soc. Am. B* **16**, 275 (1999).
- [97] E. M. Purcell, *Phys. Rev.* **69**, 681 (1946).
- [98] S. Foresi, P.R. Villeneuve, J. Ferrera, E.R. Thoen, G. Steinmeyer, S. Fan, J. D. Joannopoulos, L. C. Kimerling, H. I. Smith and E. P. Ippen, *Nature* **390**, 143 (1997).
- [99] Y. Ryu, J. K. Hwang and Y. H. Lee, *IEEE J. Quantum Electron.* **39**, 314 (2003).
- [100] D. Englund, D. Fattal, E. Waks, G. Solomon, B. Zhang, T. Nakaoka, Y.

- Arakawa, Y. Yamamoto and J. Vučković, *Phys. Rev. Lett.* **95**, 013904 (2005).
- [101] T. M. Stace, G. J. Milburn, and C. H. Barnes, *Phys. Rev. B* **67**, 085317 (2003).
- [102] F. Troiani, J. I. Perea, and C. Tejedor, *Phys. Rev. B* **74**, 235310 (2006).
- [103] Y. Akahane, T. Asano, B. S. Song, and S. Noda, *Appl. Phys. Lett.* **83**, 1512 (2003).
- [104] O. Painter, A. Husain, A. Scherer, P. T. Lee, I. Kim, J. D. O'Brien, and P. D. Dapkus, *IEEE Photonics Technol. Lett.* **12**, 1126 (2000).
- [105] O. Painter and K. Srinivasan, *Opt. Lett.* **27**, 339 (2002).
- [106] T. Yoshie, A. Scherer, J. Hendrickson, G. Khitrova, H. M. Gibbs, G. Rupper, C. Ell, O. B. Shchekin, and D. G. Deppe, *Nature* **432**, 200 (2004).
- [107] J. P. Reithmaier, G. Sęk, A. Löffler, C. Hofmann, S. Kuhn, S. Reitzenstein, L. V. Keldysh, V. D. Kulakovskii, T. L. Reinecke, A. Forchel, *Nature* **432**, 197 (2004).
- [108] E. Peter, P. Senellart, D. Martrou, A. Lemaître, J. Hours, J. M. Gérard, and J. Bloch, *Phys. Rev. Lett.* **95**, 067401 (2005).
- [109] C. Santori, D. Fattal, J. Vučković, G. S. Solomon, and Y. Yamamoto, *Nature (London)* **419**, 594 (2002).
- [110] O. Benson, C. Santori, M. Pelton, and Y. Yamamoto, *Phys. Rev. Lett.* **84**, 2513 (2000).
- [111] R. M. Stevenson, R. J. Young, P. Atkinson, K. Cooper, D. A. Ritchie, and A. J. Shields, *Nature (London)* **439**, 179 (2006).
- [112] N. Akopian, N. H. Lindner, E. Poem, Y. Berlatzky, J. Avron, D. Gershoni, B. D. Gerardot, and P. M. Petroff, *Phys. Rev. Lett.* **96**, 130501 (2006).
- [113] F. Bordas, M. J. Steel, C. Seassal, and A. Rahmani, *Opt. Express* **15**, 10890 (2007).
- [114] K. Srinivasan, and O. Painter, *Opt. Express* **10**, 670 (2002).
- [115] M. Shirane, S. Kono, J. Ushida, S. Ohkouchi, N. Ikeda, Y. Sugimoto, and A. Tomita, *J. Appl. Phys.* **101**, 073107 (2007).
- [116] L. Carbone, C. Nobile, M. De Giorgi, F. Della Sala, G. Morello, P. P. Pompa, M. Hytch, E. Snoeck, A. Fiore, I. R. Franchini, M. Nadasan, A. F. Silvestre, L. Chiodo, S. Kudera, R. Cingolani, R. Krahne, and L. Manna, *Nano Lett.* **7**, 2942 (2007).
- [117] D. V. Talapin, J. H. Nelson, E. V. Shevchenko, S. Aloni, B. Sadtler, A. P.

- Alivisatos, *Nano Lett.* **7**, 2951 (2007).
- [118] M. Bahriz, V. Moreau, R. Colombelli, O. Crisafulli, and O. Painter, *Opt. Express* **15**, 5948 (2007).
- [119] M. Nomura, S. Iwamoto, N. Kumagai, and Y. Arakawa, *Physica E* **40**, 1800 (2008).
- [120] M. Nomura, S. Iwamoto, K. Watanabe, N. Kumagai, Y. Nakata, S. Ishida, and Y. Arakawa, *Opt. Express* **14**, 6308 (2006).
- [121] K. Nozaki, S. Kita, and T. Baba, *Opt. Express* **15**, 7506 (2007).
- [122] K. Nozaki and T. Baba, *Appl. Phys. Lett.* **88**, 211101 (2006).
- [123] S. Laurent, S. Varoutsis, L. Le Gratiet, A. Lemaître, I. Sagnes, F. Raineri, A. Levenson, I. Robert-Phillip, and I. Abram, *Appl. Phys. Lett.* **87**, 163107 (2005).
- [124] W. H. Chang, W. Y. Chen, H. S. Chang, T. P. Hsieh, J. I. Chyi, and T. M. Hsu, *Phys. Rev. Lett.* **96**, 117401 (2006).
- [125] M. Nomura, Y. Ota, N. Kumagai, S. Iwamoto, and Y. Arakawa, *Appl. Phys. Express* **1**, 072102 (2008).
- [126] K. Hennessy, A. Badolato, M. Winger, D. Gerace, M. Atatüre, S. Gulde, S. Fält, E. L. Hu, and A. Imamoglu, *Nature* **445**, 896 (2007).
- [127] D. Englund, A. Faraon, I. Fushman, N. Stoltz, P. Petroff, and J. Vučković, *Nature* **450**, 857 (2007).
- [128] Y. Ota, M. Shirane, M. Nomura, N. Kumagai, S. Ishida, S. Iwamoto, S. Yoroazu, and Y. Arakawa, *Appl. Phys. Lett.* **94**, 033102 (2009).
- [129] E. Özbay, G. Tuttle, M. Sigalas, C. M. Soukoulis, and K. M. Ho, *Phys. Rev. B* **51**, 13961 (1995).
- [130] P. Lodahl, A. Floris van Driel, I. S. Nikolaev, A. Irman, K. Overgaag, D. Vanmaekelbergh, and W. L. Vos, *Nature* **430**, 654 (2004).
- [131] M. Okano, A. Chutinan, and S. Noda, *Phys. Rev. B* **66**, 165211 (2002).
- [132] M. Okano and S. Noda, *Phys. Rev. B* **70**, 125105 (2004).
- [133] M. M. Sigalas and R. Biswas, *Phys. Rev. B* **78**, 033101 (2008).
- [134] J. F. Chen, R. T. Hong, and J. Y. Yang, *J. Appl. Phys.* **104**, 063111 (2008).
- [135] L. Tang and T. Yoshie, *Opt. Express* **15**, 17254 (2007).
- [136] L. Tang and T. Yoshie, *Opt. Express* **17**, 1346 (2009).
- [137] S. Strauf, K. Hennessy, M. T. Rakher, Y. S. Choi, A. Badolato, L. C. Andreani, E. L. Hu, P. M. Petroff, and D. Bouwmeester, *Phys. Rev. Lett.* **96**, 127404

- (2006).
- [138] C. C. Cheng and A. Scherer, *J. Vac. Sci. Technol. B* **13**, 2696 (1995).
- [139] S. Takahashi, M. Okano, M. Imada, and S. Noda, *Appl. Phys. Lett.* **89**, 123106 (2006).
- [140] H. G. Park, S. H. Kim, S. H. Kwon, Y. G. Ju, J. K. Yang, J. H. Baek, S. B. Kim, and Y. H. Lee, *Science* **305**, 1444 (2004).
- [141] S. G. Romanov, A. V. Fokin, V. I. Alperovich, N. P. Johnson, and R. M. De La Rue, *Phys. Status Solidi a* **164**, 169 (1997).
- [142] Y. A. Vlasov, M. Deutsch, and D. J. Norris, *Appl. Phys. Lett.* **76**, 1627 (2000).
- [143] J. E. G. J. Wijnhoven and W. L. Vos, *Science* **281**, 802 (1998).
- [144] A. Blanco, E. Chomski, S. Grabtchak, M. Ibisate, S. John, S. W. Leonard, C. Lopez, F. Meseguer, H. Miguez, J. P. Mondia, G. A. Ozin, O. Toader, and H. M. van Driel, *Nature* **405**, 437 (2000).
- [145] B. H. Cumpston, S. P. Ananthavel, S. R. Marder, and J. W. Perry, *Nature* **398**, 51 (1999).
- [146] G. M. Gratson, M. Xu, and J. A. Lewis, *Nature* **428**, 386 (2004).
- [147] M. Campbell, D. N. Sharp, M. T. Harrison, R. G. Denning, and A. J. Turberfield, *Nature* **404**, 53 (2000).
- [148] S. Noda, N. Yamamoto, and A. Sasaki, *Jpn. J. Appl. Phys.* **35**, L909 (1996).
- [149] E. Yablonovitch, T. J. Gmitter, R. D. Meade, A. M. Rappe, K. D. Brommer, and J. D. Joannopoulos, *Phys. Rev. Lett.* **67**, 3380 (1991).
- [150] S. Y. Lin, J. G. Fleming, M. M. Sigalas, R. Biswas, and K. M. Ho, *Phys. Rev. B: Condens. Matter.* **59**, R15579 (1999).
- [151] M. Imada, L. H. Lee, M. Okano, S. Kawashima, and S. Noda, *Appl. Phys. Lett.* **88**, 171107 (2006).
- [152] H. T. Miyazaki and T. Sato, *Proceedings, 1996 IEEE International Conference on Robotics and Automation (IEEE, Minneapolis, 1996)*, p. 2535.
- [153] S. Saito, H. T. Miyazaki, T. Sato, K. Takahashi, *J. Appl. Phys.* **92**, 5140 (2002).
- [154] A. A. Busnaina and T. Elsayy, *J. Adhesion* **74**, 391 (2000).
- [155] G. Owen and P. Rissman, *J. Appl. Phys.* **54**, 3573 (1983).
- [156] D. Guimard, S. Tsukamoto, M. Nishioka, and Y. Arakawa, *Appl. Phys. Lett.* **89**, 083116 (2006).
- [157] D. Guimard, M. Nishioka, S. Tsukamoto, and Y. Arakawa, *Appl. Phys. Lett.*

- 89**, 183124 (2006).
- [158] D. Guimard, Y. Arakawa, M. Ishida, S. Tsukamoto, M. Nishioka, Y. Nakata, H. Sudo, T. Yamamoto, and M. Sugawara, *Appl. Phys. Lett.* **90**, 241110 (2007).
- [159] Z. Zhang and M. Qiu, *Opt. Express* **12**, 3988 (2004).
- [160] D. Englund, I. Fushman, and J. Vučković, *Opt. Express* **13**, 5961 (2005).
- [161] G. Khitrova, H. M. Gibbs, F. Jahnke, M. Kira, and S. W. Koch, *Rev. Mod. Phys.* **71**, 1591 (1999).
- [162] C. T. Chan, K. M. Ho, and C. M. Soukoulis, *Europhys. Lett.* **16**, 563 (1991).

List of Publications

Related Publications

International Journal Papers

- [1] A. Tандаеchanurat, S. Iwamoto, M. Nomura, N. Kumagai and Y. Arakawa, “Increase of Q -factor in photonic crystal H1-defect nanocavities after closing of photonic bandgap with optimal slab thickness,” *Optics Express* **16**, 448 (2008).
- [2] L. Martiradonna, L. Carbone, A. Tандаеchanurat, M. Kitamura, M. Nomura, M. Nishioka, S. Ishida, B. Antonazzo, T. Nakaoka, S. Iwamoto, C. Roberto and Y. Arakawa, “Two-dimensional photonic crystal resist membrane nanocavity embedding colloidal dot-in-a-rod nanocrystals,” *Nano Letters* **8**, 260 (2008).
- [3] A. Tандаеchanurat, S. Iwamoto, M. Nomura, N. Kumagai and Y. Arakawa, “Ultra-high (Q/V_{eff}) doubly-degenerated modes by modulating air hole radii in square lattice photonic crystal nanocavity,” Submitted.
- [4] A. Tандаеchanurat, S. Ishida, K. Aoki, D. Guimard, M. Nomura, S. Iwamoto, and Y. Arakawa, “Demonstration of high- Q (>8600) three-dimensional photonic crystal nanocavity,” Submitted.

International Conferences

- [5] A. Tандаеchanurat, S. Iwamoto, M. Nomura, N. Kumagai and Y. Arakawa, “Demonstration of high- Q photonic crystal H1-defect nanocavities after closing of photonic bandgap,” Pacific Rim Conference on Lasers and Electro-Optics (CLEO/Pacific Rim), TuF4-7, Seoul, Korea (2007).

- [6] A. Tандаеchanurat, S. Iwamoto, M. Nomura, N. Kumagai and Y. Arakawa, “High quality factor photonic crystal H1-defect nanocavities with optimized slab thickness,” International Nano-Optoelectronic Workshop, P55, Beijing, China (2007).
- [7] A. Tандаеchanurat, S. Iwamoto, M. Nomura, N. Kumagai and Y. Arakawa, “Experimental demonstration of high Q -factor photonic crystal H1-defect nanocavities after closing of photonic bandgap,” Frontiers in Nanoscale Science and Technology workshop (FNST), B9, Tokyo, Japan (2007).
- [8] A. Tандаеchanurat, S. Ishida, K. Aoki, D. Guimard, M. Nomura, S. Iwamoto, and Y. Arakawa, “Demonstration of high- Q ($> 7,700$) three-dimensional photonic crystal nanocavity,” International Photonic & Electromagnetic Crystal Structures Meeting (PECS), Sydney, Australia (2009).

Domestic Conferences

- [9] A. Tандаеchanurat, S. Iwamoto and Y. Arakawa, “High quality factor photonic crystal H1-defect nanocavities with optimized slab thickness,” 53rd Spring Meet, Japan Society of Applied Physics and Related Societies, 24p-L-5, Tokyo (2006).
- [10] A. Tандаеchanurat, S. Iwamoto, M. Nomura, N. Kumagai and Y. Arakawa, “Demonstration of high- Q photonic crystal H1-defect nanocavities after closing of photonic bandgap,” 68th Autumn Meet, Japan Society of Applied Physics and Related Societies, 6p-P11-8, Sapporo (2007).
- [11] A. Tандаеchanurat, S. Iwamoto and Y. Arakawa, “Design of polarization-degenerated modes in photonic crystal nanocavities in square lattice with modulated air hole radius,” 68th Autumn Meet, Japan Society of Applied Physics and Related Societies, 6p-P11-9, Sapporo (2007).
- [12] A. Tандаеchanurat, S. Iwamoto and Y. Arakawa, “Design of Nanocavity in Three-dimensional photonic crystal with finite structural size for enhancing Q -factor,” 55th Spring Meet, Japan Society of Applied Physics and Related Societies, 27a-ZX-5, Chiba (2008).

- [13] A. Tандаеchanurat, S. Ishida, K. Aoki, D. Guimard, M. Nomura, S. Iwamoto, and Y. Arakawa, “Three-dimensional photonic crystal nanocavity coupled with quantum dots~ Demonstration of the highest Q factor (> 8600),” 56th Spring Meet, Japan Society of Applied Physics and Related Societies, 30a-ZN-6, Tsukuba (2009).
- [14] L. Martiradonna, L. Carbone, A. Tандаеchanurat, M. Kitamura, M. Nomura, M. Nishioka, S. Ishida, B. Antonazzo, T. Nakaoka, S. Iwamoto, C. Roberto and Y. Arakawa, “Fabrication and optical characterization of photonic crystal nanocavities with colloidal nanocrystals,” 68th Autumn Meet, Japan Society of Applied Physics and Related Societies, 6p-P11-1, Sapporo (2007).

Other Publications

International Journal Papers

- [15] M. Nomura, S. Iwamoto, A. Tандаеchanurat, Y. Ota, N. Kumagai, and Y. Arakawa, “Photonic band-edge micro lasers with quantum dot gain,” Optics Express **17**, 640 (2009).

International Conferences

- [16] M. Nomura, A. Tандаеchanurat, S. Iwamoto, Y. Ota, N. Kumagai, and Y. Arakawa, “Direct observation of highly efficient coupling of spontaneous emission in quantum dot-photonic crystal nanocavity systems by momentum space imaging,” IEEE Nanotechnology Materials and Devices Conference (NMDC), MoC II-4, Kyoto, Japan (2008).
- [17] M. Nomura, S. Iwamoto, A. Tандаеchanurat, Y. Ota, N. Kumagai, and Y. Arakawa, “Quantum dot-based photonic bandedge lasers,” International Photonic & Electromagnetic Crystal Structures Meeting (PECS), Sydney, Australia (2009).

Domestic Conferences

- [18] M. Nomura, S. Iwamoto, A. Tандаеchanurat, Y. Ota, N. Kumagai, and Y. Arakawa, “Ultralow threshold photonic bandedge lasers with quantum dot

gain,” 56th Spring Meet, Japan Society of Applied Physics and Related Societies, 31p-ZN-2, Tsukuba (2009).